UNIVERSITY OF CALIFORNIA

Los Angeles

Feedback Control of Thin Film Micro-Structure Using Multiscale Distributed Systems

A dissertation submitted in partial satisfaction of the

requirements for the degree Doctor of Philosophy

in Chemical Engineering

by

Yiming Lou

2004

UMI Number: 3164277

INFORMATION TO USERS

The quality of this reproduction is dependent upon the quality of the copy submitted. Broken or indistinct print, colored or poor quality illustrations and photographs, print bleed-through, substandard margins, and improper alignment can adversely affect reproduction.

In the unlikely event that the author did not send a complete manuscript and there are missing pages, these will be noted. Also, if unauthorized copyright material had to be removed, a note will indicate the deletion.

UMI®

UMI Microform 3164277

Copyright 2005 by ProQuest Information and Learning Company.

All rights reserved. This microform edition is protected against unauthorized copying under Title 17, United States Code.

ProQuest Information and Learning Company
300 North Zeeb Road
P.O. Box 1346
Ann Arbor, MI 48106-1346

The dissertation of Yiming Lou is approved.

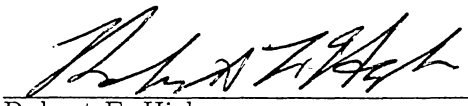

Robert F. Hicks

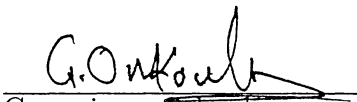

Gerassimos Orkoulas

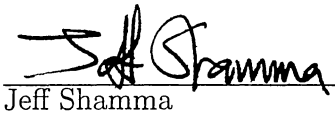

Jeff Shamma

Panagiotis D. Christofides, Committee Chair

University of California, Los Angeles

2004

Contents

1 Introduction 1

2 Estimation and Control of Surface Roughness in Thin Film Growth Using Kinetic Monte-Carlo Models 9

2.1 Introduction 9

2.2 Thin film growth process 11

2.2.1 Gas phase model 13

2.2.2 Surface micro-structure model 15

2.3 A roughness estimator 19

2.4 Feedback control of surface roughness 27

2.5 Conclusions 45

3 Feedback Control of Growth Rate and Surface Roughness in Thin Film Growth 46

3.1 Introduction 46

3.2 Thin film growth process 47

3.3 Real-time estimator for surface roughness and growth rate 47

3.4 Feedback control of surface roughness and growth rate 61

3.4.1 Feasibility of the control problem formulation 61
3.4.2 Effect of multivariable input/output interactions 66
3.4.3 Multivariable feedback control structure 70
3.5 Conclusions 78

4 Feedback Control of Surface Roughness of *GaAs* (001) Thin Films Using Kinetic Monte-Carlo Models 79

4.1 Introduction 79
4.2 Surface micro-structure model for GaAs thin film growth 81
4.2.1 Process description 82
4.2.2 Derivation of surface micro-structure model based on probability theory 84
4.2.3 Computation of kinetic Monte-Carlo model parameters using experimental data 91
4.3 Real-time estimation of thin film surface roughness 100
4.4 Feedback control of surface roughness 105
4.5 Conclusions 116

5 Feedback Control of Surface Roughness Using Stochastic PDEs 119

5.1 Introduction 119
5.2 Preliminaries 121
5.3 Feedback control 127
5.3.1 Model reduction 127
5.3.2 Feedback controller design 128
5.3.3 Analysis of the closed-loop infinite-dimensional system 130

5.4 Simulation results 133

5.5 Conclusions 140

6 Feedback Control of Surface Roughness in Sputtering Processes Using the Stochastic Kuramoto-Sivashinsky Equation 141

6.1 Introduction 141

6.2 Preliminaries 146

6.2.1 Process description 146

6.2.2 Stochastic PDE model of the sputtering process 147

6.3 Feedback control 153

6.3.1 Model reduction 153

6.3.2 Feedback control design 154

6.3.3 Analysis of the closed-loop infinite-dimensional system 155

6.4 Simulation results 158

6.4.1 Feedback control of surface roughness in process 6.1 159

6.4.2 Feedback control of surface roughness in Process 6.2 169

6.4.3 Feedback control of surface roughness in process 6.3 175

6.5 Conclusions 187

7 Optimal Actuator/Sensor Placement for Nonlinear Control of the Kuramoto-Sivashinsky Equation 188

7.1 Introduction 188

7.2 Preliminaries 191

7.3 Integrating nonlinear control and optimal actuator placement 196

7.3.1 Nonlinear state feedback controller synthesis 196

7.3.2 Computation of optimal actuator locations 197
7.3.3 Output feedback control and sensor placement 200
7.4 Numerical results 203
7.5 Conclusions 213

8 Fault-Tolerant Control of Fluid Dynamic Systems via Coordinated Feedback and Switching 214

8.1 Introduction 214
8.2 Preliminaries 217
8.2.1 Mathematical description 217
8.2.2 Problem formulation 220
8.3 Fault-tolerant control system design 222
8.3.1 Galerkin's method 222
8.3.2 Coordinating feedback and switching 223
8.4 Simulation results 229
8.5 Conclusions 241

9 Robust Stabilization of Infinite-Dimensional Systems Using Sliding-Mode Output Feedback Control 245

9.1 Introduction 245
9.2 Preliminaries 248
9.3 Sliding-Mode Feedback Synthesis 255
9.3.1 State Feedback Design 255
9.3.2 Output Feedback Design 268
9.4 Numerical results 275

9.4.1 Application to the linearized KSE without external disturbance 279

9.4.2 Application to the linearized KSE with non-vanishing external disturbance 284

9.5 Conclusions 299

10 Conclusions and Future Work **300**

10.1 Conclusions 300

10.2 Future work 302

Bibliography **303**

List of Figures

2.1 Illustration of the thin film growth process. 13

2.2 Comparison of the surface roughness profiles obtained from kinetic Monte-Carlo simulators which use 20×20, 50×50, 100×100 and 150×150 lattices. 21

2.3 Comparison of the surface roughness profiles from 3 independent kinetic Monte-Carlo simulations which utilize a 20×20 lattice. 21

2.4 Comparison of the surface roughness profiles from 3 independent kinetic Monte-Carlo simulations which utilize a 50×50 lattice. 22

2.5 Evolution of the roughness obtained directly from a kinetic Monte-Carlo simulator which uses a 20×20 lattice. 24

2.6 Filtered roughness from a kinetic Monte-Carlo simulator which uses a 20×20 lattice. 24

2.7 Filtered roughness from a kinetic Monte-Carlo simulator which uses a 20×20 lattice (dashed line) and roughness from a kinetic Monte-Carlo simulator which uses a 100×100 lattice (solid line). 26

2.8 Roughness profiles from the roughness estimator (dashed line) and from a kinetic Monte-Carlo simulator which uses a 100×100 lattice (solid line). 27

2.9 Diagram of the closed-loop system. 29

2.10 Evolution of the surface roughness under feedback control. 30

2.11 Evolution of the substrate temperature. 31

2.12 The micro-configuration of the surface for T=600K. 32

2.13 The micro-configuration of the surface at the end of the closed-loop simulation run. 32

2.14 Evolution of the surface roughness under feedback control - closed-loop system simulation under uncertainty. 33

2.15 Evolution of the substrate temperature - closed-loop system simulation under uncertainty. 33

2.16 Evolution of the surface roughness under feedback controller without roughness estimator. 34

2.17 Evolution of the substrate temperature under feedback controller without roughness estimator. 35

2.18 Evolution of the surface roughness under feedback controller without roughness estimator: controller is tuned such that significant oscillation is avoided. 36

2.19 Evolution of the substrate temperature under feedback controller without roughness estimator: controller is tuned such that significant oscillation is avoided. 36

2.20 Comparison of surface roughness profiles: (1) roughness profile under feedback control using roughness estimator, (2) roughness profile under feedback control without using roughness estimator with controller parameters shown in Table 2.1, and (3) roughness profile under feedback control without using roughness estimator with controller parameters tuned to avoid significant oscillation. 37

2.21 Evolution of the surface roughness under feedback controller without roughness estimator - delayed roughness measurements. 39

2.22 Evolution of the substrate temperature under feedback controller without roughness estimator - delayed roughness measurements. 39

2.23 Evolution of the surface roughness under feedback controller using the estimator/controller structure - delayed roughness measurements. . . 40

2.24 Evolution of the substrate temperature under feedback controller using the estimator/controller structure - delayed roughness measurements. 40

2.25 Evolution of the surface roughness under open-loop PI controller. . . 41

2.26 Evolution of the substrate temperature under open-loop PI controller. 42

2.27 Comparison of the evolution of surface roughness from: (1) a Monte-Carlo simulator which uses a 20×20 lattice, (2) the computation of the average of six independent Monte-Carlo simulations which utilize a 20×20 lattice, and (3) a Monte-Carlo simulator which uses a 100×100 lattice. 43

2.28 Comparison of the evolution of surface roughness from: (1) a Monte-Carlo simulator which uses a 30 × 30 lattice, (2) the computation of the average of six independent Monte-Carlo simulations which utilize a 20 × 20 lattice, and (3) a Monte-Carlo simulator which uses a 100 × 100 lattice. 44

2.29 Closed-loop surface roughness profile under feedback controller using a kinetic Monte-Carlo simulator that employs multiple small lattice models. 44

2.30 Closed-loop substrate temperature profile under feedback controller using a kinetic Monte-Carlo simulator that employs multiple small lattice models. 45

3.1 Growth rate from a kinetic Monte-Carlo simulation which uses a 20 × 20 lattice. 50

3.2 Growth rate from the computation of the average of six independent kinetic Monte-Carlo simulations which utilize a 20 × 20 lattice. . . . 51

3.3 Surface roughness from a kinetic Monte-Carlo simulation which uses a 20 × 20 lattice. 51

3.4 Surface roughness from the computation of the average of six independent kinetic Monte-Carlo simulations which utilize a 20 × 20 lattice. 52

3.5 Growth rate from a kinetic Monte-Carlo simulation which uses a 30 × 30 lattice. 53

3.6 Surface roughness from a kinetic Monte-Carlo simulation which uses a 30 × 30 lattice. 54

3.7 Growth rate profiles from the estimator (solid line) and from a kinetic Monte-Carlo simulation which uses a 120 × 120 lattice model (dashed line). 56

3.8 Surface roughness profiles from the estimator (solid line) and from a kinetic Monte-Carlo simulation which uses a 120 × 120 lattice model (dashed line). 57

3.9 Comparison of the surface roughness profiles from a kinetic Monte-Carlo simulator which uses an 80 × 80 lattice (dotted) and that from a kinetic Monte-Carlo simulator which uses a 120 × 120 lattice (solid). 58

3.10 Comparison of the growth rate profiles from a kinetic Monte-Carlo simulator which uses an 80 × 80 lattice (dotted) and that from a kinetic Monte-Carlo simulator which uses a 120 × 120 lattice (solid). 59

3.11 Evolution of the surface roughness during the formation of the first 10 monolayers. 60

3.12 Evolution of the growth rate during the formation of the first 200 monolayers. 60

3.13 Diagram of the estimator/controller structure using a kinetic Monte-Carlo simulator based on multiple small lattice models. 62

3.14 Closed-loop growth rate under single-loop feedback control using the estimator/controller structure of Figure 3.13. 64

3.15 Inlet precursor mole fraction under single-loop feedback control using the estimator/controller structure of Figure 3.13. 64

3.16 Closed-loop surface roughness under single-loop feedback control using the estimator/controller structure of Figure 3.13. 65

3.17 Substrate temperature under single-loop feedback control using the estimator/controller structure of Figure 3.13. 66

3.18 Closed-loop surface roughness under feedback control which does not account for multivariable input/output interactions. 67

3.19 Substrate temperature using feedback control which does not account for multivariable input/output interactions. 68

3.20 Closed-loop growth rate under feedback control which does not account for multivariable input/output interactions. 68

3.21 Precursor mole fraction using feedback control which does not account for multivariable input/output interactions. 69

3.22 Comparison of closed-loop growth rate profiles a) growth rate is the only controlled output and the structure of Figure 3.13 is used (solid line), b) simultaneous regulation of growth rate and surface roughness is considered and feedback control which does not account for multivariable input/output interactions is used (dotted line). 69

3.23 Growth rate (middle plot) and surface roughness (bottom plot) profiles for a step change in inlet precursor mole fraction (top plot) from 2.0×10^{-5} to 2.1×10^{-5} - substrate temperature is kept at $800K$. 71

3.24 Growth rate (middle plot) and surface roughness (bottom plot) with a step change in substrate temperature (top plot) from $800K$ to $840K$ - inlet precursor mole fraction is 2.0×10^{-5}. 72

3.25 Diagram of multivariable feedback control system with interaction compensation. 74

3.26 Comparison of the closed-loop growth rate under multivariable feedback control with interaction compensation (solid line) and under multiple single-loop control (dashed line). 75

3.27 Comparison of inlet precursor mole fraction under multivariable feedback control with interaction compensation (solid line) and under multiple single-loop control (dashed line). 75

3.28 Closed-loop surface roughness under multivariable feedback control with interaction compensation. 76

3.29 Substrate temperature under multivariable feedback control with interaction compensation. 76

3.30 Surface micro-configuration at the beginning of the closed-loop simulation run (roughness=1.8). 77

3.31 Surface micro-configuration at the end of the closed-loop simulation run (roughness=1.5) under multivariable feedback control with interaction compensation. 77

4.1 Surface roughness under different substrate temperatures when the parameters of migration rate are the same to those for $GaAs$ thin film growth by MBE reported in Shitara et al. (1992a). (a) T=713K, (b) T=750K, (c) T=775K and (d)=800K. 95

4.2 Surface roughness under different substrate temperatures when the parameters of migration rate are adjusted to match the experimental results reported in Law et al. (2000). (a) T=825K, (b) T=850K, (c) T=875K and (d)=900K. 98

4.3 Surface roughness profiles from the estimator (dotted line) and from a kinetic Monte-Carlo simulation which uses a 150 × 150 lattice model (solid line). 104

4.4 Diagram of the closed-loop system under the developed estimator/ controller structure. 107

4.5 Evolution of the surface roughness under feedback control based on the roughness estimator. 108

4.6 Evolution of the substrate temperature under feedback control based on the roughness estimator. 109

4.7 Evolution of the surface roughness under feedback control based on the roughness estimator - closed-loop simulation under uncertainty. . . . 110

4.8 Evolution of the substrate temperature under feedback control based on the roughness estimator - closed-loop simulation under uncertainty. 110

4.9 Evolution of the surface roughness under feedback control without roughness estimator. 111

4.10 Evolution of the substrate temperature under feedback control without roughness estimator. 112

4.11 Evolution of the surface roughness under feedback control without roughness estimator. 113

4.12 Evolution of the substrate temperature under feedback control without roughness estimator. 113

4.13 Comparison of roughness profiles: (1) roughness profile under feedback control based on the roughness estimator (solid line) and (2) roughness profile under feedback control without roughness estimator with controller parameters $K_c = 5K/\text{Å}$, $\tau_c = 1.0s$. 114

4.14 Evolution of the surface roughness under feedback control based on the roughness estimator - delayed roughness measurements. 115

4.15 Evolution of the substrate temperature under feedback control based on the roughness estimator - delayed roughness measurements. 115

4.16 Evolution of the surface roughness under open-loop implementation of the estimator/controller structure. 116

4.17 Evolution of the substrate temperature under open-loop implementation of the estimator/controller structure. 117

5.1 Schematic of the rules of the deposition. 122

5.2 Comparison of the open-loop profile of the expected surface roughness from the kinetic Monte-Carlo simulator (solid line) and that from the solution of the SPDE using 1000 modes (dotted line). 135

5.3 Comparison of the open-loop profile of the expected surface roughness from the kinetic Monte-Carlo simulator (solid line) and that from the solution of the SPDE, with adjusted covariance, using 1000 modes (dotted line). 136

5.4 Closed-loop simulation results by applying the controller designed based on the first 40 modes of the SPDE model to the kinetic Monte-Carlo model. (a) The closed-loop surface roughness profile from one simulation run (solid line), (b) the expected closed-loop surface roughness profile (dotted line), and (c) the open-loop surface roughness profile from one simulation run (dashed line). 138

6.1 Schematic of the rule to determine P_e. P_e is defined as $\frac{1}{7}$ times the number of occupied sites in a box of size 3×3 centered at the particle on the top of site i; $P_e = 1$ in the left figure and $P_e = \frac{4}{7}$ in the right figure, where the particle marked by $\bullet$ is on the top of site i. 147

6.2 The open-loop profile of the expected surface roughness in Process 6.1 computed from the Monte-Carlo simulations. 162

6.3 Evolution of $\langle \alpha_2^2 \rangle$, $\langle \alpha_3^2 \rangle$, $\langle \alpha_4^2 \rangle$ and $\langle \alpha_5^2 \rangle$ in Process 6.1. 163

6.4 $1/\langle \alpha_n(\infty)^2 \rangle$ versus n for $n = 2, 3, 4$, and 5 (marked by 'o') and the curve of $y = 23.07n^2$ (dotted line) in Process 6.1. 164

6.5 Plots of $-\ln\left[\frac{2\nu n^2}{\sigma^2}\langle \alpha_n(t)^2 \rangle + 1\right]/n^2$ versus t for $n = 2, 3, 4$, and 5 in Process 6.1. 165

6.6 Comparison of the open-loop profile of the expected surface roughness from the kinetic Monte-Carlo simulator (solid line) and that from the solution of the Edwards-Wilkinson equation with $\nu = -1.2 \times 10^{-4}$ and $\sigma = 3.4 \times 10^{-3}$ (dotted line) in Process 6.1. 166

6.7 Closed-loop surface roughness profiles in Process 6.1. (a) The closed-loop surface roughness profile from one simulation run (solid line), (b) The expected closed-loop surface roughness profile obtained from 200 independent simulation runs (dashed line), and (c) the open-loop surface roughness profile from one simulation run (dotted line). . . . 168

6.8 The open-loop profile of the expected surface roughness in Process 6.2 from the kinetic Monte-Carlo simulator. 172

6.9 Evolution of $\langle \alpha_1^2 \rangle$, $\langle \alpha_5^2 \rangle$, $\langle \alpha_{15}^2 \rangle$ and $\langle \alpha_{20}^2 \rangle$ in Process 6.2. 172

6.10 Closed-loop surface roughness profiles in Process 6.2. (a) The closed-loop surface roughness profile from one simulation run (solid line), (b) the expected closed-loop surface roughness profile (dotted line), and (c) the open-loop surface roughness profile from one simulation run (dashed line). 175

6.11 The open-loop profile of the expected surface roughness in Process 6.3 from the kinetic Monte-Carlo simulator. 179

6.12 Evolution of $\langle \alpha_{20}^2 \rangle$, $\langle \alpha_{22}^2 \rangle$, $\langle \alpha_{25}^2 \rangle$ and $\langle \alpha_{30}^2 \rangle$ in Process 6.3. 179

6.13 $1/\langle \alpha_n(\infty)^2 \rangle$ versus n for $n = 20, 21, \cdots, 30$ (marked by '$\circ$') and the curve of $y = 1.45 \times 10^{-3} n^4 - 0.26 n^2$ (dotted line) in Process 6.3. . . . 180

6.14 $\ln \left[\frac{2(\nu n^2 - \kappa n^4)}{\sigma^2} \langle \alpha_n(t)^2 \rangle + 1 \right] / 2n^2$ versus t for $n = 20, 22, 24, 26, 28,$ and 30 in Process 6.3. 181

6.15 The slopes of lines in Fig.6.14 versus n for $n = 20, \cdots, 30$ (marked by '$\circ$') and the curve of $y = 3.27 \times 10^{-6} - 1.34 \times 10^{-8} n^2$ (dotted line) in Process 6.3. 182

6.16 Comparison of the open-loop profile of the expected surface roughness from the kinetic Monte-Carlo simulator (solid line) and that from the solution of the linearized stochastic Kuramoto-Sivashinsky equation with $\nu = 3.27 \times 10^{-6}$, $\kappa = 1.34 \times 10^{-8}$ and $\sigma = 4.65 \times 10^{-3}$ (dotted line) in Process 6.3. 183

6.17 Closed-loop surface roughness profiles in Process 6.3. (a) The closed-loop surface roughness profile from one simulation run (solid line), (b) The expected closed-loop surface roughness profile obtained from 200 independent simulation runs (dotted line), and (c) the open-loop surface roughness profile from one simulation run (dashed line). . . . 186

7.1 Open-loop spatiotemporal profile of $U(z,t)$ for $\nu = 0.2$. 206

7.2 Closed-loop norm of the control effort, $\|u\|$, for $x_s(0) = [\phi_1\ 0]$, for the optimal case (solid line), case 2 (dashed-dotted line), case 3 (dashed line), case 4 (dotted line). 208

7.3 Closed-loop norm of the control effort,$\|u\|$, for $x_s(0) = [0\ \phi_2]$, for the optimal case (solid line), case 2 (dashed-dotted line), case 3 (dashed line), and case 4 (dotted line). 208

7.4 Closed-loop estimation error e versus time, for the optimal actuator/sensor locations, for $x_s(0) = [\phi_1\ 0]$ (solid line) and $x_s(0) = [0\ \phi_2]$ (dotted line). 209

7.5 Profile of KSE under output feedback control, for the optimal actuator/sensor locations, for $x_s(0) = [\phi_1\ 0]$. 210

7.6 Profile of KSE under output feedback control, for the optimal actuator/sensor locations, for $x_s(0) = [0\ \phi_2]$. 210

7.7 Profile of KSE under output feedback control, for the optimal actuator/sensor locations, for $x_s(0) = [\phi_1\ 0]$ and uncertainty in ν (top plot). Manipulated input profiles (bottom plot) - Solid line u_1 and dashed line u_2. 211

7.8 Profile of KSE under output feedback control, for the optimal actuator/sensor locations, for $x_s(0) = [0\ \phi_2]$ and uncertainty in ν (top plot). Manipulated input profiles (bottom plot) - Solid line u_1 and dashed line u_2. 212

8.1 Open-loop spatiotemporal profile of $U(z,t)$ for $\nu = 0.2$. 232

8.2 (a) Evolution of the norm of the fast modes, $a_f = [a_3, \cdots, a_{30}]$, and of the two dominant modes, a_1 and a_2, for $\nu = 1.2$. (b) Evolution of the norm of the fast modes (in deviation variable form), $a_f^d = [a_3^d, \cdots, a_{30}^d]$, and of the two dominant modes, a_1^d and a_2^d, for $\nu = 0.2$ (all modes are in deviation variable form). 233

8.3 (a) Stability regions for configuration A ($u_{max} = 2.0$, $z_1 = 0.3\pi$, $z_2 = 0.7\pi$) (solid ellipse) and for configuration B ($u_{max} = 2.0$, $z_1 = 0.1\pi$, $z_2 = 0.9\pi$) (dashed ellipse), (b) Closed-loop state profile (state feedback) for $(a_1(0), a_2(0)) = (0.2, 1.5)$ using configuration A without switching, (c) Corresponding manipulated input profiles for u_1 (solid) and u_2 (dashed). 235

8.4 (a) Closed-loop state profile (state feedback) for $(a_1(0), a_2(0)) = (0.2, 1.5)$ when configuration A fails at $t = 3.5$ and configuration B is activated, (b) Corresponding manipulated input profiles for u_1 (solid) and u_2 (dashed). 236

8.5 (a) Closed-loop state profile (state feedback) for $(a_1(0), a_2(0)) = (0.2, 1.5)$ when configuration A fails at $t = 5$ and configuration B is activated, (b) Corresponding manipulated input profiles for u_1 (solid) and u_2 (dashed). 237

8.6 (a) Stability regions for configuration A ($u_{max} = 2.0$, $z_1 = 0.3\pi$, $z_2 = 0.7\pi$) (solid ellipse), configuration B ($u_{max} = 2.0$, $z_1 = 0.1\pi$, $z_2 = 0.9\pi$) (dashed ellipse), and configuration C ($u_{max} = 0.5$, $z_1 = 0.2\pi$, $z_2 = 0.8\pi$), (b) Closed-loop state profile (state feedback) for $(a_1(0), a_2(0)) = (0.2, 1.5)$ when configuration A fails at $t = 3.5$ and configuration C is activated, (b) Corresponding manipulated input profiles for u_1 (solid) and u_2 (dashed). 239

8.7 (a) Closed-loop state profile (state feedback) for $(a_1(0), a_2(0)) = (0.2, 1.5)$ when configuration A fails at $t = 3.5$ and configuration B is activated, (b) Corresponding manipulated input profiles for u_1 (solid) and u_2 (dashed). 240

8.8 (a) Closed-loop state profile (output feedback) for $(a_1(0), a_2(0)) = (0.2, 1.5)$ when configuration A fails at $t = 3.5$ and configuration B is activated, (b) Corresponding manipulated input profiles for u_1 (solid) and u_2 (dashed). 242

8.9 (a) Closed-loop state profile (output feedback) for $(a_1(0), a_2(0)) = (0.2, 1.5)$ when configuration A fails at $t = 5$ and configuration B is activated, (b) Corresponding manipulated input profiles for u_1 (solid) and u_2 (dashed). 243

9.1 Eigenspectrum of the linearized KdVB equation with $a_1 = 0.05$ (left plot) and that of the linearized KSE with $\nu = 0.2$ (right plot). 254

9.2 Closed-loop spatio-temporal profile of $x(z,t)$ (left figure) and manipulated input profiles (right figure) under $\delta-$sliding-mode state feedback control. 282

9.3 Closed-loop spatio-temporal profile of $x(z,t)$ (left figure) and manipulated input profiles (right figure) under $\delta-$sliding-mode output feedback control. 285

9.4 Closed-loop spatio-temporal profile of $x(z,t)$ (left figure) and manipulated input profiles (right figure) under $\delta-$sliding-mode output feedback control for 25% uncertainty in ν. 286

9.5 Closed-loop spatio-temporal profile of $x(z,t)$ (left figure) and manipulated input profiles (right figure) under $\delta-$sliding-mode state feedback control with external disturbance ($d(z,t) = \frac{1}{\sqrt{\pi}}\sin(z)[4+\sin(10t)]$). . 289

9.6 Closed-loop spatio-temporal profile of $x(z,t)$ (left figure) and manipulated input profiles (right figure) under linear state feedback control with external disturbance ($d(z,t) = \frac{1}{\sqrt{\pi}}\sin(z)[4+\sin(10t)]$). 290

9.7 Closed-loop spatio-temporal profile of $x(z,t)$ (left figure) and manipulated input profiles (right figure) under linear state feedback control without external disturbance; $J(t_f) = \int_0^{t_f}\int_{-\pi}^{\pi} x^2(z,t)dzdt$=0.3567. . . 292

9.8 Closed-loop spatio-temporal profile of $x(z,t)$ (top figure) and manipulated input profiles (bottom figure) under $\delta-$sliding-mode state feedback control without external disturbance; $J(t_f) = \int_0^{t_f}\int_{-\pi}^{\pi} x^2(z,t)dzdt$ =0.3567. 293

9.9 Closed-loop spatio-temporal profile of $x(z,t)$ (top figure) and manipulated input profiles (bottom figure) under $\delta-$sliding-mode output feedback control with external disturbance. 295

9.10 Closed-loop spatio-temporal profile of $x(z,t)$ (top figure) and manipulated input profiles (bottom figure) under linear output feedback control with external disturbance. 296

9.11 Closed-loop spatio-temporal profile of $x(z,t)$ (left figure) and manipulated input profiles (right figure) under sliding-mode output feedback control. 298

List of Tables

2.1 Process and controller parameters. 30

3.1 Process parameters. 49

3.2 Growth rate estimator and controller parameters. 63

3.3 Roughness estimator and controller parameters. 65

4.1 Parameters for migration rate in $GaAs$ thin film growth by MBE (Shitara et al., 1992a). 94

4.2 Parameters for migration rate obtained by fitting kinetic Monte-Carlo simulation results to the experimental results reported in Law et al. (2000). 97

4.3 Roughness estimator and controller parameters. 108

6.1 Number of control actuators versus the lowest achievable closed-loop surface roughness. 169

7.1 Results for two control actuators. 209

7.2 Results for two control actuators and measurement sensors. 209

ACKNOWLEDGEMENTS

I would like to express my deepest gratitude to my advisor, Professor Panagiotis Christofides, for his guidance in my research and his encouragement and support throughout. I consider myself fortunate to become his student and to work with him during my time at UCLA.

I would like to thank Professor Robert Hicks, Professor Gerassimos Orkoulas, and Professor Jeff Shamma for agreeing to serve on my thesis committee.

The results included in Chapters 8 and 9 are joint works with Nael El-Farra at UCLA and Dr. Yuri Orlov at CICESE Research Center. Working with them was a real pleasure and I am thankful for their involvement and inspiration.

The feeling of gratitude and pride for my wife, Chengning, cannot be expressed in words. She has supported and encouraged my endeavor for the last four years, while nurturing our daughter through her first steps and pursuing a M.S. Degree in International Business.

Finally, I would also like to thank my parents in China, for their constant encouragement, support and love.

VITA

August 14, 1975	Born, Hangzhou, China
1997	B. Eng., Electrical Engineering Zhejiang University Hangzhou, China
1999	Rockwell Scholarship
2000	M. S., Control Science & Engineering Zhejiang University Hangzhou, China
2000	University Fellowship from University of California, Los Angeles, CA
2000-04	Research Assistant Department of Chemical Engineering University of California, Los Angeles, CA
2004	O. Hugo Shuck Best Paper Award from American Automatic Control Council

PUBLICATIONS AND PRESENTATIONS

El-Farra, N., Y. Lou and P. D. Christofides, "Fault-Tolerant Control of Fluid Dynamic Systems via Coordinated Feedback and Switching," *Computers & Chemical Engineering*, **27**, 1913-1924, 2003.

Lou, Y., M. Li and P. D. Christofides, "Feedback Control of Material Microstructure Using Multiscale Distributed Models," AIChE Annual Meeting, paper 278a, Reno, Nevada, 2001.

Lou, Y., P. Ray, A. Armaou and P. D. Christofides, "Optimal Actuator/Sensor Placement for Feedback Control of Fluids," AIChE Annual Meeting, paper 266e, Reno, Nevada, 2001.

Lou, Y. and P. D. Christofides, "Estimation and Control of Surface Roughness in Thin Film Growth Using Kinetic Monte-Carlo Models," AIChE Annual Meeting, paper 279c, Indianapolis, Indiana, 2002.

Lou, Y., D. Ni, P. D. Christofides and J. P. Chang, "Modeling and Control of Surface Roughness in a PECVD Reactor," AIChE Annual Meeting, paper 261g, Indianapolis, Indiana, 2002.

Lou, Y. and P. D. Christofides, "Estimation and Control of Surface Roughness in Thin Film Growth Using Kinetic Monte-Carlo Models," *Chemical Engineering Science*, **58**, 3115-3129, 2003.

Lou, Y. and P. D. Christofides, "Feedback Control of Growth Rate and Surface Roughness in Thin Film Growth Using Kinetic Monte-Carlo Models," *A.I.Ch.E Journal*, **49**, 2099-2113, 2003.

Lou, Y. and P. D. Christofides, "Modeling and Control of Surface Roughness and Growth Rate of GaAs (001) Thin Films Produced by MOCVD," AIChE Annual Meeting, paper 444b, San Francisco, California, 2003.

Lou, Y. and P. D. Christofides, "Optimal Actuator/Sensor Placement for Nonlinear Control of the Kuramoto-Sivashinsky Equation," *IEEE Transactions on Control Systems Technology*, **11**, 737-745, 2003.

Lou, Y. and P. D. Christofides, "Feedback Control of Surface Roughness Using Stochastic PDEs," *A.I.Ch.E Journal*, in press, 2004.

Lou, Y. and P. D. Christofides, "Feedback Control of Surface Roughness of GaAs(001) Thin Films Using Kinetic Monte-Carlo Models," *Computers & Chemical Engineering*, in press, 2004.

Lou, Y. and P. D. Christofides, "Feedback Control of the Stochastic Kuramoto-Sivashinsky Equation," Conference on Decision and Control, to be presented, Atlantis, Paradise Island, Bahamas, 2004.

Lou, Y., P. D. Christofides and G. Orkoulas, "Feedback Control of Surface Roughness in a Sputtering Process Using the Stochastic Kuramoto-Sivashinsky Equation," AIChE Annual Meeting, to be presented, Austin, Texas, 2004.

Lou, Y., M. Li and P. D. Christofides, "Covariance Control of Stochastic Infinite Dimensional Systems," AIChE Annual Meeting, to be presented, Austin, Texas, 2004.

Ni, D., Y. Lou, P. D. Christofides, L. Sha, S. Lao and J. P. Chang, "Real-Time Control of High-k Dielectric Thin Film Composition and Thickness," AIChE Annual Meeting, paper 176d, San Francisco, California, 2003.

Ni, D., Y. Lou, P. D. Christofides, L. Sha, S. Lao and J. P. Chang, "Real-Time Carbon Content Control for PECVD ZrO_2 Thin-Film Growth," *IEEE Transactions on Semiconductor Manufacturing*, **17**, 221-230, 2004.

Orlov, Y., Y. Lou and P. D. Christofides, "Robust Stabilization of Infinite-Dimensional Systems via Discontinuous Output Feedback Control," AIChE Annual Meeting, paper 442c, San Francisco, California, 2003.

Orlov, Y., Y. Lou and P. D. Christofides, "Robust Stabilization of Infinite-Dimensional Systems via Sliding-Mode Output Feedback Control," *International Journal of Control*, in press, 2004.

ABSTRACT OF THE THESIS

Feedback Control of Thin Film Micro-Structure Using Multiscale Distributed Systems

by

Yiming Lou

Doctor of Philosophy in Chemical Engineering

University of California, Los Angeles, 2004

Professor Panagiotis D. Christofides, Chair

The research on feedback control of thin film growth is motivated by the strong dependence of the electrical and mechanical properties of thin films on their micro-structure and the desire to produce high quality thin films to meet the increasingly stringent requirements on the quality of such films. This thesis focuses on the development of a framework of feedback control of thin film micro-structure using multiscale distributed systems.

Initially, a methodology for feedback control of thin film growth using kinetic Monte-Carlo models is developed. The methodology leads to the design of (a) real-time roughness estimators by using multiple small lattice kinetic Monte-Carlo simulators, adaptive filters and measurement error compensators, and (b) feedback controllers based on the real-time roughness estimators. The method is successfully applied to the multiscale process model of a thin film growth process in a stagnation flow geometry and to an experimentally determined kinetic Monte-Carlo process

model of a $GaAs$ deposition process to regulate the surface roughness to desired levels.

Then, the problem of multivariable feedback control of thin film growth is studied. A multivariable feedback controller, which uses the state estimator and explicitly compensates for the effect of input/output interactions, is designed and is applied to the multiscale model of a thin film growth process in a stagnation flow geometry to simultaneously regulate the growth rate and surface roughness by manipulating substrate temperature and inlet precursor mole fraction.

The desire to further improve the closed-loop performance by designing feedback controllers directly on the basis of deposition process models motivates research on feedback control of deposition processes based on stochastic partial differential equation (PDE) process models. A method for feedback control of surface roughness in deposition processes described by stochastic PDEs is also developed. We formulate the stochastic PDE model into a system of infinite stochastic ordinary differential equations by using modal decomposition. A finite-dimensional approximation of the stochastic PDE model is then derived that captures the dominant mode contribution to the surface roughness. A state feedback controller is designed based on the finite-dimensional approximation to control the surface roughness. The developed method is employed to control surface roughness in a deposition process described by the Edwards-Wilkinson equation and in sputtering processes described by the stochastic Kuramoto-Sivashinsky equation.

Chapter 1

Introduction

Deposition of thin films from gas phase precursors has great industrial importance. The modern integrated circuit technology depends strongly on the uniformity and micro-structure of deposited thin films (Granneman, 1993). Due to the increasingly stringent requirements on the quality of such films including uniformity, composition and micro-structure and the desire to improve productivity by increasing wafer dimensions and reducing product variability, real-time feedback control of thin film deposition becomes important.

These trends have motivated significant research efforts on feedback control of film deposition processes with emphasis on control of film spatial uniformity in rapid thermal chemical vapor deposition (e.g., Baker and Christofides, 1999; Theodoropoulou et al., 1999) and plasma-enhanced chemical vapor deposition (e.g., Armaou and Christofides, 1999). From a control point of view, film spatial uniformity control is a distributed control problem that can be addressed on the basis of continuum type transport-reaction models by using controller design methods for nonlinear parabolic partial differential equations (PDEs); see the book (Christofides, 2001b) for results and references on this problem.

In addition to achieving spatially uniform deposition of thin films, one would like to control film properties such as micro-structure and composition that characterize film quality. This is motivated by the strong dependence of the electrical and mechanical properties of thin films on their micro-structure and composition (see, for example, Lee et al., 1999; Chang et al., 2001; Akiyama et al., 2002). A typical example of thin film growth where feedback control of film surface roughness could be useful is the deposition of thin films of materials with high dielectric constant (such as ZrO_2); such materials are expected to replace SiO_2 thin films to achieve higher performance and lower static-power operation in complementary metal oxide semiconductor (CMOS) devices (Chang et al., 2001). In this application, a rough ZrO_2 film surface would lead to silicidation of the interface between the ZrO_2 film and the polysilicon gate during rapid thermal annealing (Busch et al., 2002), which, in turn, would lead to an interfacial layer with low dielectric constant which would reduce the effective capacities of the gate dielectrics (Wallace and Wilk, 2002). Therefore, good control of surface roughness in the deposition of the ZrO_2 thin film is needed to achieve a smoother film surface with fewer reaction sites which would result in a suppression of the interfacial reactions. The study of feedback control of surface roughness is also motivated by the possibility to obtain roughness measurements in real-time using scanning tunnelling microscopy (Voigtländer, 2001), spectroscopic ellipsometry techniques (Zapien et al., 2001), grazing-incidence small-angle X-ray scattering (GISAXS) (Renaud et al., 2003) or by combination of on-line measurements techniques for measuring gas phase compositions with off-line measurement techniques for measuring surface roughness. An implementation of the latter approach was recently reported in Ni et al. (2004), where it was used to measure carbon composition of the films in plasma-enhanced chemical vapor deposition using combination of optical emission spectroscopy (OES) and X-ray photoelectron spectroscopy (XPS).

As the dimensions of the semiconductor devices are approaching the nanometer scale (Voigtländer, 2001), the desire to understand, model and control the micro-structure of thin films has motivated extensive research on fundamental mathematical models describing thin film growth and its interaction with the surrounding gas.

Thin film deposition is a typical process including very different time and length scales for dynamics of gas phase and that of film micro-structure. In gas phase, the continuum hypothesis is held and deterministic conservation equations can be developed to describe the macroscopic transport phenomena in the gas phase (e.g., Sharma and Sirignano, 1969; Coltrin et al., 1989; Tirtowidjojo and Pollard, 1988; Vlachos, 1996; Yun and Rhee, 1997). However, thin film micro-structure is directly shaped by random surface micro-processes such as adsorption, desorption, diffusion or reaction of surface atoms or molecules. At the time and length scales of these surface micro-processes, the continuum hypothesis is no longer held and stochastic modeling techniques are needed to capture the microscopic phenomena. A series of works on microscopic modeling and simulation of surface micro-structure in a variety of the deposition processes by using Monte-Carlo techniques (e.g., Shitara et al., 1992a; Adams et al., 1993; Meng and Weinberg, 1996; Itoh, 2001) or using stochastic partial differential equations (e.g., Edwards and Wilkinson, 1982; Villain, 1991; Vvedensky et al., 1993) have been reported.

The multiscale hybrid modeling approach proposed in Vlachos (1997) efficiently couples the continuum gas-phase PDE models with surface molecular models so that molecular level information can be integrated into the macroscopic systems. The multiscale modeling of materials growth is a rapidly evolving field (Christofides, 2001a) and results on multiscale models for a variety of processes have been reported. Some examples are: dendrite growth (Plapp and Karma, 2000), ionized physical vapor de-

position (Hansen et al., 2000), epitaxial growth of films (Lam and Vlachos, 2001) and film deposition within porous substrates (Gummalla et al., 2004).

Recently, we have developed a methodology for feedback control of surface roughness using kinetic Monte-Carlo models (Lou and Christofides, 2003a,b). The method was successfully applied to control surface roughness in a $GaAs$ deposition process using an experimentally determined kinetic Monte-Carlo process model (Lou and Christofides, 2004b). Kinetic Monte-Carlo methods are also used to study dynamics of complex deposition processes including multiple components with both short-range and long-range interactions (Ni and Christofides, 2004a) and to perform predictive control design to control final surface roughness in Ni and Christofides (2004b). Moreover, the desire to perform model-based controller design for thin film micro-structure leads to the development of the method for feedback control of surface roughness based on stochastic PDE process models (Lou and Christofides, 2004c) and the method was successfully applied to sputtering processes whose surface height fluctuations can be described by the stochastic Kuramoto-Sivashinsky equation (Lou and Christofides, 2004a). Other approaches have also been developed to: (a) identify linear models from outputs of kinetic Monte-Carlo simulators and perform controller design by using linear control theory (Siettos et al., 2003; Armaou et al., 2004), and (b) construct reduced-order approximations of the master equation (Gallivan and Murray, 2003).

This thesis includes all our works on feedback control of thin film micro-structure using multiscale distributed systems and it is organized as follows:

In Chapter 2, we present a methodology for estimation and control of surface roughness in thin film growth using kinetic Monte-Carlo models. A roughness estimator is initially constructed that allows computing estimates of the surface roughness at a time-scale comparable to the real-time evolution of the process using discrete

on-line roughness measurements. The roughness estimates are fed to a proportional-integral (PI) feedback controller. Application of the proposed estimator/controller structure to the multiscale process model demonstrates successful regulation of the surface roughness at the desired value.

Chapter 3 extends the methodology developed in Chapter 2 to multivariable feedback controller design so that surface roughness and growth rate can be regulated simultaneously in thin film growth. An estimator is first constructed that allows computing estimates of the surface roughness and growth rate at a time-scale comparable to the real-time evolution of the process. The multivariable control problem is then studied and a multivariable feedback control system, which directly uses the estimator and compensates for the effect of multivariable input/output interactions, is designed to simultaneously regulate the growth rate and surface roughness by manipulating substrate temperature and inlet precursor concentration. The proposed control system is applied to the multiscale process model and successful regulation of the surface roughness and growth rate to the desired set-point values is demonstrated through computer simulations.

In Chapter 4, we apply the methodology presented in Chapter 2 to study estimation and control of surface roughness of $GaAs$ (001) thin films during deposition in a horizontal-flow quartz reactor using triisobutylgallium ($TIBGa$) and tertiarybutylarsine ($TBAs$) as precursors and H_2 as the carrier gas. An experimentally determined kinetic Monte-Carlo model is used to construct an estimator/controller structure to control the surface roughness to a desired level. Application of the proposed estimator/controller structure to the process model based on a large-lattice kinetic Monte-Carlo simulator demonstrates successful regulation of the surface roughness to the desired level. The proposed approach is shown to be superior to PI control with

direct use of the discrete roughness measurements.

Chapter 5 presents a method for feedback control of surface roughness in deposition processes, based on stochastic PDEs which describe the fluctuation of surface height in the spatial domain. To demonstrate the method, we focus on control of surface roughness in a deposition process on a 1-dimensional lattice, whose fluctuation of surface height can be described by the Edwards-Wilkinson equation, a second-order stochastic PDE. We initially reformulate the stochastic PDE into a system of infinite stochastic ordinary differential equations by using modal decomposition. A finite-dimensional approximation of the Edwards-Wilkinson equation is then derived that captures the dominant mode contribution to the surface roughness. A state feedback controller is designed based on the finite-dimensional approximation to control the surface roughness. Analysis of the closed-loop system shows that the controller can drive the surface roughness governed by the infinite-dimensional system to desired levels. The effectiveness of the proposed method is demonstrated by numerical simulations.

In Chapter 6, we apply the method developed in Chapter 5 to control the surface roughness in sputtering processes including two surface micro-processes, diffusion and erosion. The fluctuation of surface height of such sputtering processes can be described by the stochastic Kuramoto-Sivashinsky equation (KSE), a fourth-order stochastic PDE. Feedback control of surface roughness in three different sputtering processes with different sputtering yield functions and different ratios of erosion and diffusion rates is studied. Monte-Carlo simulations are first performed to simulate the evolution of the surface height fluctuation in the three sputtering processes. Then, the parameters of the stochastic PDE models describing the sputtering processes are identified by using the surface height fluctuation data obtained from Monte-

Carlo simulations so that the evolution of the surface roughness computed from the stochastic PDE models is consistent to that computed from Monte-Carlo simulations. Feedback controllers are designed and applied to Monte-Carlo models of the sputtering processes to control the surface roughness to desired levels.

In Chapter 7, the problem of optimal actuator/sensor placement for nonlinear output feedback control of the Kuramoto-Sivashinsky equation is solved. We use the methodology proposed in Antoniades and Christofides (2001) to compute optimal locations of point control actuators and measurement sensors for nonlinear output feedback control of the KSE with periodic boundary conditions. The optimal actuator location problem is formulated as the one of minimizing a meaningful cost functional that includes penalty on the response of the closed-loop system and the control action. The optimal location of the measurement sensors is computed by minimizing a cost function of the estimation error in the closed-loop infinite-dimensional system. The theoretical results are successfully illustrated through computer simulations of the closed-loop system using a high-order discretization of the KSE.

Chapter 8 focuses on the problem of coupling feedback and switching between actuator configurations for fault-tolerant control of fluid dynamic systems modelled by highly-dissipative PDEs with constrained control actuators. The problem is addressed on the basis of finite-dimensional Galerkin approximations of the PDE system and entails the integrated synthesis, via Lyapunov techniques, of stabilizing nonlinear feedback controllers together with stabilizing switching laws that orchestrate the switching between the admissible control actuator configurations, in a way that respects actuator constraints, accommodates inherently conflicting control objectives, and guarantees closed-loop stability. Precise conditions that guarantee stability of the constrained closed-loop system under switching are provided. The proposed control

methodology is demonstrated through an application to the problem of suppression of wave formation, achieved via the stabilization of the zero solution, $U(z,t) = 0$, of the KSE with periodic boundary conditions, in the presence of control actuator constraints and faults.

In Chapter 9, an output feedback control method based on sliding modes is developed for a class of linear infinite-dimensional systems with finite-dimensional unstable part using finite-dimensional sensing and actuation. For these systems, our main results include: 1) the discontinuous output feedback controller synthesis based on sliding modes in the infinite-dimensional setting, and 2) the justification of the implementation of the discontinuous sliding-mode controller via its continuous approximation.

Chapter 10 summarizes the contributions of this thesis and proposes future directions.

Chapter 2

Estimation and Control of Surface Roughness in Thin Film Growth Using Kinetic Monte-Carlo Models

2.1 Introduction

Precise control of film properties requires models that predict how the film state (microscopic scale) is affected by changes in the controllable process parameters (macroscopic scale). The desire to understand and control the micro-structure of thin films has motivated extensive research on fundamental mathematical models describing thin film growth and its interactions with the surrounding gas. Thin film deposition is a typical process including multiple time and length scales and this has motivated the use of multiscale models to obtain modeling descriptions which can be simulated with reasonable computing power. Specifically, one approach to model thin film growth is to model the gas phase phenomena using a set of partial differential equations (PDEs) derived from mass, momentum and energy balances and to model the film growth using the kinetic Monte-Carlo simulation method with appropriate lattice

configurations (see, for example, Vlachos, 1997; Lam and Vlachos, 2001). The two models are coupled through the film surface boundary conditions. Other approaches have been also developed to study the growth of thin films including the level set method (Chen et al., 2001). While multiscale modeling provides a computationally attractive alternative with respect to direct modeling of the entire thin film growth process using a molecular model, it still leads to dynamic models that cannot be solved fast enough for real-time estimation and control purposes.

Mathematically, kinetic Monte-Carlo simulation methods provide a numerical solution to the master equation (Gillespie, 1976; Van Kampen, 1992), which is a partial differential equation describing the evolution of the probability that the thin film is at a certain micro-configuration. The kinetic Monte-Carlo simulation method can be used to predict average properties of the thin film (which are of interest from a control point of view, for example, surface roughness), by explicitly accounting for the micro-processes that directly shape thin film microstructure. As the lattice size used to perform the kinetic Monte-Carlo simulation increases, the average thin film properties, which are computed from the kinetic Monte-Carlo simulation, converge to the values obtained from the solution of the master equation. The accuracy of solutions of the kinetic Monte-Carlo simulation method depends on the size of the lattice used in the simulation which, in turn, determines the computational requirements of the simulation. The computational requirements for a solution with reasonable computing power make the direct use of kinetic Monte-Carlo simulators in an on-line feedback control scheme impossible. Motivated by this, recent research efforts have focused on the development of order reduction techniques for the master equation (Gallivan and Murray, 2003). Other approaches have also been developed to identify linear models from outputs of kinetic Monte-Carlo simulators and perform controller

design by using linear optimal control theory (Siettos et al., 2003; Armaou et al., 2004).

In this chapter, we present an approach to estimation and control of surface roughness in thin film growth using kinetic Monte-Carlo models. We use the process of thin film growth in a stagnation flow geometry and consider atom adsorption, desorption and surface migration as the three processes that shape film micro-structure. A multiscale model that involves coupled PDEs for the modeling of the gas phase and a kinetic Monte-Carlo simulator, based on a high-order lattice, for the modeling of the film micro-structure, is used to simulate the process. A roughness estimator is constructed that allows computing estimates of the surface roughness at a time-scale comparable to the real-time evolution of the process using discrete on-line roughness measurements. The estimator involves a kinetic Monte-Carlo simulator based on a small lattice, an adaptive filter used to reduce roughness stochastic fluctuations and an error compensator used to reduce the error between the roughness estimates and the discrete roughness measurements. The roughness estimates are fed to a PI controller. Application of the proposed estimator/controller structure to the multiscale process model demonstrates successful regulation of the surface roughness at the desired value. The proposed approach is shown to be superior to PI control with direct use of the discrete roughness measurements. The reason is that the available measurement techniques do not provide measurements at a frequency that is comparable to the time-scale of evolution of the dominant film growth dynamics.

2.2 Thin film growth process

We consider the growth of a thin film from a fluid in a vertical, stagnation flow geometry. The process is shown in Figure 2.1. In this geometry, inlet fluid flow forms

a uniform boundary layer adjacent to the surface of the substrate and precursor atoms diffuse through such a boundary and deposit a uniform thin film (Gadgil, 1993). Upon arrival at the surface, the precursor atoms are adsorbed onto the surface. Subsequently, adsorbed atoms may desorb to the gas phase or migrate on the surface.

From a modeling point of view, the major challenge is the integration of the wide range of length and time scales that the process encompasses (Vlachos, 1997). Specifically, in the gas phase, the processes of heat/mass transport can be adequately modeled under the hypothesis of continuum, thereby leading to PDE models for chamber temperature and species concentration. However, when the micro-structure of the surface is studied, microscopic events such as atom adsorption, desorption and migration have to be considered, and the length-scale of interest reduces dramatically to the order of that of several atoms. Under such a small length scale, the continuum hypothesis is no longer valid and deterministic PDEs can not be used to describe the microscopic phenomena. Different approaches, such as Monte-Carlo simulation or molecular dynamics, should be employed to model the evolution of surface micro-structure.

Although different modeling approaches are used to model the macroscopic and microscopic phenomena of the process, there are strong interactions between the macro- and micro-scale phenomena. For example, the concentration of the precursor in the inlet gas governs the rate of adsorption of atoms on the surface, which, in turn, influences the surface roughness. On the other hand, the density of the adatoms on the surface affects the rate of desorption of atoms from surface to the gas phase, which, in turn, influences the gas phase concentration of the precursor. A multiscale model (Vlachos, 1997) is employed in this work to capture the evolution of both macroscopic and microscopic phenomena of the thin film growth process as well as their interac-

tions. A set of PDEs derived from the mass, momentum and energy balances are used to describe the gas phase dynamics. Kinetic Monte-Carlo simulation (Fichthorn and Weinberg, 1991) is employed to capture the evolution of surface micro-structure. Furthermore, the parameters of Monte-Carlo simulation such as the temperature and precursor concentration are provided by the solution of PDEs and the results from the kinetic Monte-Carlo simulation are used to determine the boundary conditions of the PDEs of the macroscopic model.

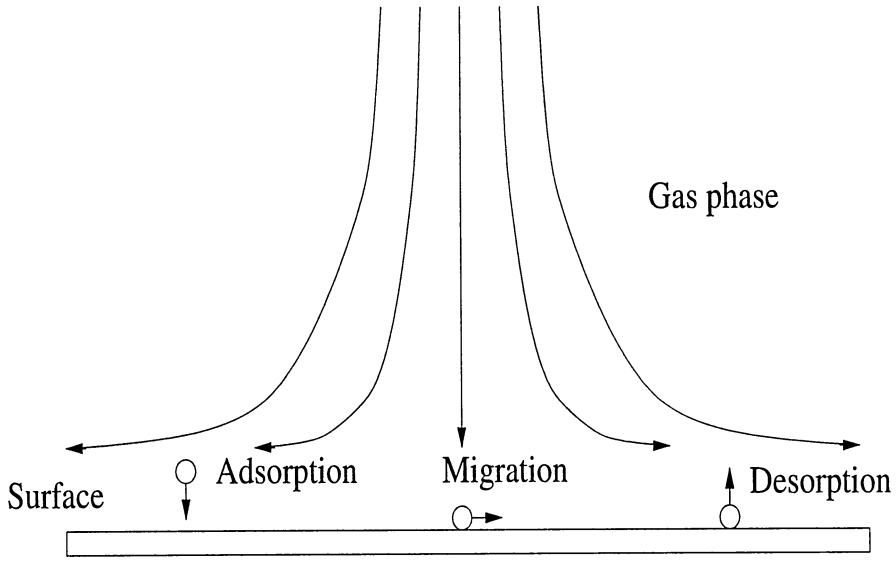

Figure 2.1: Illustration of the thin film growth process.

2.2.1 Gas phase model

Under the assumption of axisymmetric flow, the gas phase can be modeled through continuum type momentum, energy and mass balances as follows (Lam and Vlachos, 2001):

$$\frac{\partial}{\partial \tau}(\frac{\partial f}{\partial \eta}) = \frac{\partial^3 f}{\partial \eta^3} + f\frac{\partial^2 f}{\partial \eta^2} + \frac{1}{2}[\frac{\rho_b}{\rho} - (\frac{\partial f}{\partial \eta})^2] \tag{2.1}$$

$$\frac{\partial T}{\partial \tau} = \frac{1}{P_r}\frac{\partial^2 T}{\partial \eta^2} + f\frac{\partial T}{\partial \eta} \tag{2.2}$$

$$\frac{\partial y_i}{\partial \tau} = \frac{1}{Sc_j}\frac{\partial^2 y_i}{\partial \eta^2} + f\frac{\partial y_i}{\partial \eta} \tag{2.3}$$

The following boundary conditions are used for $\eta \rightarrow \infty$:

$$\begin{aligned} T &= T_{bulk} \\ \frac{\partial f}{\partial \eta} &= 1 \\ y_j &= y_{jb},\ j = 1, \ldots, N_g \end{aligned} \tag{2.4}$$

and for $\eta \rightarrow 0$ (surface) :

$$\begin{aligned} T &= T_{surface} \\ f &= 0 \\ \frac{\partial f}{\partial \eta} &= 0 \\ \frac{\partial y_j}{\partial \eta} &= 0, \text{ for } j \neq growing \\ \frac{\partial y_{growing}}{\partial \eta} &= \frac{Sc_{growing}(R_a - R_d)}{\sqrt{2a\mu_b\rho_b}} \end{aligned} \tag{2.5}$$

where f is the dimensionless stream function, R_a and R_d are the rates of adsorption and desorption, respectively, η is the dimensionless distance to the surface, ρ is the density of the mixture, P_r is the Prandtl number, y_j and Sc_j are the mole fraction and Schmidt number of the species j, respectively, μ_b and ρ_b are the viscosity and the density of the bulk, respectively, a is the hydrodynamic strain rate and $\tau = 2at$ is the dimensionless time.

Although the macroscopic model describes the spatio-temporal evolution of the precursor concentration and temperature (which influence the configuration of the growing surface), no direct information of the surface micro-structure is available from the macroscopic model. Furthermore, the boundary conditions for the mass transfer equation of the growing species depend on the rates of adsorption and desorption. Therefore, a microscopic model is necessary to model the micro-structure of the surface and to determine the boundary conditions of the mass transfer equation.

2.2.2 Surface micro-structure model

The thin film growth considered in this work encompasses of three kinds of processes, the adsorption of atoms from the gas phase to the surface, the desorption of atoms from the surface to the gas phase and the migration of atoms on the surface. The statistical properties of these processes can be studied by sampling a duration t into n identical time intervals δ. When $n \rightarrow \infty$, δ will be small enough so that each interval will contain one event at the most. The average of the rate can be defined as (Fichthorn and Weinberg, 1991):

$$r = \lim_{\delta \rightarrow 0} \frac{n_\delta}{t} \tag{2.6}$$

where n_δ is the number of time intervals containing events. Therefore, the probability that n_e events will occur in time t is:

$$P_{n_e} = \binom{n}{n_e} (r\delta)^{n_e} (1 - r\delta)^{n - n_e} \tag{2.7}$$

where n is the number of intervals in time duration t and $\binom{n}{n_e} = \frac{n!}{n_e!(n - n_e)!}$. When $n \rightarrow \infty$,

$$P_{n_e} = \frac{rt^{n_e}}{n_e!} e^{-rt} \tag{2.8}$$

which is a Poisson distribution (Van Kampen, 1992). Eq.2.8 can be readily applied to the adsorption, desorption and migration processes involved in the thin film growth process. Due to the fact that the ensemble of independent Poisson processes is also a Poisson process (Fichthorn and Weinberg, 1991), the thin film growth process is a Poisson process.

Due to that stochastic nature of the process, the probability that the surface is in the possible configuration α is described by the so-called master equation (Van Kam-

pen, 1992):

$$\frac{dP_\alpha}{dt} = \sum_\beta (W_{\alpha\beta} P_\beta - W_{\beta\alpha} P_\alpha) \tag{2.9}$$

where P_α is the probability of the surface being in configuration α and $W_{\alpha\beta}$ is the transition probability rate of the surface going from configuration β to configuration α, which can be computed from the probability distribution of adsorption, desorption and migration. It is hard to write down the explicit form of Eq.2.9 because the number of the possible states is extremely large for most systems of realistic size. For example, consider a system of 10×10 sites with a maximum height of 1, the number of configurations is $2^{100} \approx 10^{30}$. This makes the direct solution of Eq.2.9 using numerical methods for integration of ODEs (e.g., Runge-Kutta) impossible.

Monte-Carlo methods provide an approach to solve the master equation numerically. To capture the dynamic properties of the system, the Monte-Carlo algorithms must be able to satisfy the detailed balance criterion, appropriately calculate the life time of each Monte-Carlo event and guarantee the independence of events by using an appropriate random number generator (Fichthorn and Weinberg, 1991). The way to satisfy detailed balance criterion differs when different algorithms are used. In general, there are two groups of Monte-Carlo algorithms which have been developed to simulate processes governed by the master equation: (a) the null-event algorithm (Ziff et al., 1986), and (b) the kinetic Monte-Carlo method (Jansen, 1995) . When null-event algorithm is used, which tries to execute Monte-Carlo events on randomly selected sites with certain probabilities of success, the probabilities of successful trials should be appropriately constructed to satisfy the detailed balance criterion. On the other hand, if kinetic Monte-Carlo method is used, which selects the Monte-Carlo event before the selection of the site on which the Monte-Carlo event is going to be executed, the detailed balance criterion is satisfied by appropriately constructing the

probabilities of the different kinds of Monte-Carlo events to be selected. Upon a successful Monte-Carlo event, the time passed during the event is computed based on the total rates of all the micro-processes (Vlachos, 1997). In this way, the dynamic properties of the system can be captured. Since the kinetic Monte-Carlo method is computationally more efficient than the null-event algorithm, it is used to simulate the surface processes in the thin film growth process in this study (see Reese et al., 2001, for a detailed discussion on comparison of computational efficiency of the kinetic Monte-Carlo method to the null-event algorithm).

To run the Monte-Carlo simulation for the evolution of the surface micro-structure, an $N \times N$ lattice is initially constructed. The size of the lattice (or the value of N) is determined based on the desired accuracy and the need to obtain a numerically stable solution. Generally, a larger lattice can achieve higher accuracy (in terms of average properties and size of stochastic fluctuations) but requires larger solution time. When the lattice is ready, microscopic events are executed on the lattice based on the probabilities of the individual processes. To simplify the development, only first-nearest-neighbor interactions are considered, the solid-on-solid approximation of a simple cubic lattice is made and periodic boundary conditions are used.

In this study, we consider the multilayer growth and all the sites are available for the adsorption at all the time, therefore, the adsorption rate is treated as site independent. For an ideal gas, the adsorption rate is given by the kinetic theory (Lam and Vlachos, 2001):

$$r_a = \frac{s_0 P}{\sqrt{2\pi m k T} C_{tot}} \tag{2.10}$$

where s_0 is the sticking coefficient, k is the Boltzmann constant, P is the partial pressure of the precursor, C_{tot} is the concentration of sites on the surface, m is the molecular weight of the precursor, T is the gas-phase temperature above the surface.

The rate of desorption depends on the local activation energy. Under the consideration of only first nearest neighbor interactions, the desorption rate of an atom from the surface site with n first nearest neighbors is:

$$r_d(n) = \nu_0 \exp(-\frac{nE}{kT}) \tag{2.11}$$

where E is the energy associated with a single bond on the surface and ν_0 is the frequency of events, which is determined by the following expression:

$$\nu_0 = k_{d0} \exp(-\frac{E_d}{kT}) \tag{2.12}$$

where k_{d0} is an event frequency constant and E_d is the energy associated with desorption.

Surface migration is modeled as desorption followed by re-adsorption (Gilmer and Bennema, 1972), and the migration rate is given by:

$$r_m(n) = \nu_0 A \exp(-\frac{nE}{kT}) \tag{2.13}$$

where A is associated with the energy difference that an atom on a flat surface has to overcome in jumping from one lattice site to an adjacent one and A is given as:

$$A = \exp(\frac{E_d - E_m}{kT}) \tag{2.14}$$

where E_m is the energy associated with migration.

When the lattice is set and the rates of the three events are determined based on the corresponding rate expressions, a kinetic Monte-Carlo simulation is executed following the algorithm reported in Vlachos (1997). First, a random number is generated to select an event to be run based on the above rates, then, a second random number is generated to select the site where the event will be executed from the list of the sites that the event is possible to happen. Upon an executed event, a time

increment dt is computed by (Lam and Vlachos, 2001):

$$dt = \frac{-\ln \xi}{r_a \times N_T + \nu_0(1+A)\sum_{m=1}^{5} N_m \exp(\frac{-mE}{kT})} \tag{2.15}$$

where ξ is a random number in the $(0,1)$ interval, N_T is the total number of sites on the lattice and N_m is the number of atoms that have m neighbors on the surface.

2.3 A roughness estimator

The objective of this section is to present a systematic method for the design of a dynamic estimator to estimate surface roughness in real-time using on-line roughness measurements obtained at discrete time instants. Surface roughness is a property of interest from a control point of view since it directly influences device properties. The roughness, r, is represented by the number of broken bonds on the surface (Raimondeau and Vlachos, 2000):

$$r = 1 + \frac{\sum_{i,j}(|h_{i+1,j} - h_{i,j}| + |h_{i-1,j} - h_{i,j}| + |h_{i,j+1} - h_{i,j}| + |h_{i,j-1} - h_{i,j}|)}{2 \times N \times N} \tag{2.16}$$

where N is the size of the lattice and $h_{i,j}$ is the number of atoms at site (i,j).

In the kinetic Monte-Carlo simulation, the size of the lattice influences the accuracy of the result and the computational demand. Roughly speaking, the computational complexity of the algorithm we adopt in this work is $O(N^4)$ and the magnitude of the fluctuation in the solution is $O(\frac{1}{N^2})$ where N is the size of the lattice. The $4th$ order dependence on computational complexity and the $2nd$ order dependence of fluctuations on the size of the lattice leave room for reducing the solution time with relatively small loss of accuracy.

Figure 2.2 shows the evolution of the surface roughness at $T = 600$ from kinetic

Monte-Carlo simulators using different lattice sizes: 20×20, 50×50, 100×100 and 150×150. All the simulation results in this paper are plotted with respect to the dimensionless time τ ($\tau = 2at$, where t is the the real time and a is the hydrodynamic strain rate. The value of a in this work is shown in Table 2.1). The result from a kinetic Monte-Carlo simulator which uses 20×20 lattice contains significant fluctuations compared to the roughness profiles obtained from a kinetic Monte-Carlo simulator which uses a higher-order lattice. However, it gives the same trend of the evolution of surface roughness. Furthermore, the results from kinetic Monte-Carlo simulators which use 50×50, 100×100 and 150×150 lattices are very close, thereby implying that further increase of the lattice size does not improve the accuracy of the results. Due to the stochastic nature of the algorithm, it is not possible to obtain the same results from repeated runs starting from the same initial conditions (see Remark 2.5 for how to handle this problem). However, for sufficiently large lattice size, the results from different runs are consistent in the sense that they provide surface roughness profiles that are very close. Figures 2.3 and 2.4 show the results from 3 independent kinetic Monte-Carlo simulations which utilize a 20×20 lattice and a 50×50 lattice. Clearly, as the lattice size increases, the error among different runs decreases.

To implement on-line control of surface roughness, the size of the lattice has to be selected to make the model computations be at a time-scale comparable to the process real-time evolution (see also Remark 2.1 for a discussion on the issue of selecting the size of the small lattice). In our simulations, when the size of the lattice is reduced to 20×20, the time of simulation is comparable to the real time process evolution. To overcome the fluctuations introduced by the smaller lattice size, a second-order linear filter is used to reject the noise in the roughness values obtained from the

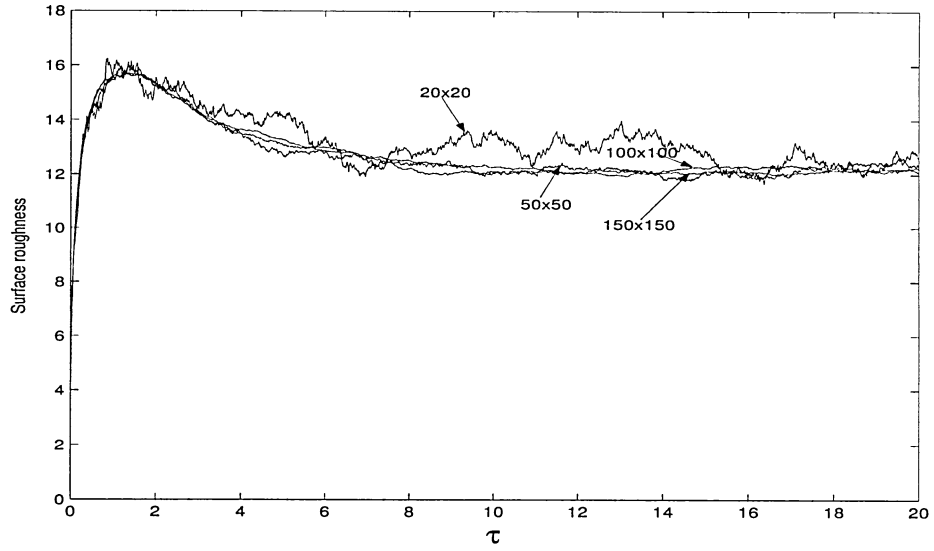

Figure 2.2: Comparison of the surface roughness profiles obtained from kinetic Monte-Carlo simulators which use 20×20, 50×50, 100×100 and 150×150 lattices.

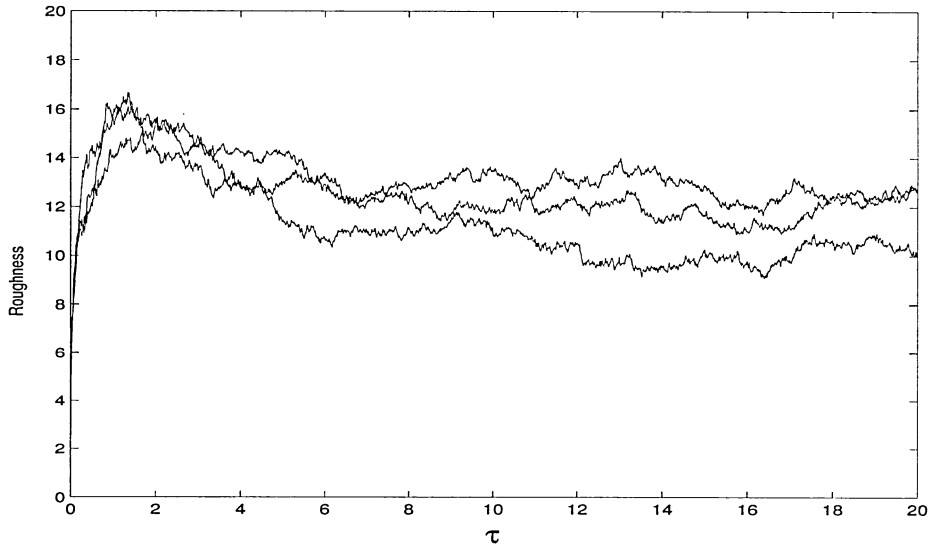

Figure 2.3: Comparison of the surface roughness profiles from 3 independent kinetic Monte-Carlo simulations which utilize a 20×20 lattice.

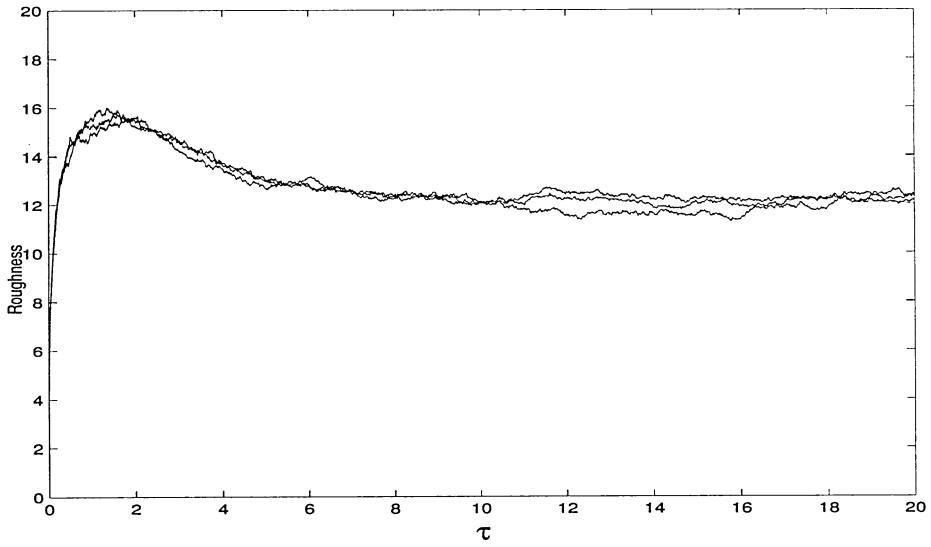

Figure 2.4: Comparison of the surface roughness profiles from 3 independent kinetic Monte-Carlo simulations which utilize a 50×50 lattice.

kinetic Monte-Carlo simulator which uses a small lattice model with the following state space representation:

$$\begin{aligned} \frac{d\hat{y}_r}{d\tau} &= y_1 \\ \frac{dy_1}{d\tau} &= \frac{K}{\tau_I}(y_r - \hat{y}_r) - \frac{1}{\tau_I} y_1 \end{aligned} \tag{2.17}$$

where y_r is the output of the kinetic Monte-Carlo simulator which uses small lattice and $\hat{y}_r$ is the filter output, K is the filter gain and τ_I is the time constant. To accelerate the response of the filter and avoid overshoot, $\tau_I = 0.5/K$.

Due to the Arrhenius-like dependence of the rate of desorption and surface migration on temperature, the dynamics of the roughness with respect to temperature variations is very fast. To this end, we need a filter that can both track the fast dynamics and reject the noise so that the noise will not deteriorate the controller performance. However, fast tracking and efficient noise rejection are two conflicting objectives that are very hard to be achieved simultaneously. Fortunately, during the

fast dynamic stage, the roughness is very large compared to the fluctuations and the effect of the fluctuations on the controller performance is insignificant. The fluctuations begin to deteriorate the controller performance significantly only when the controlled roughness is close to the set-point value. Motivated by this, an adaptive scheme is used to determine the gain of the filter on-line such that the filter focuses on tracking the growth dynamics at the fast dynamic stage and on noise rejection when the surface dynamics slow down. To achieve this, the gain of the filter is adjusted according to the following law:

$$K(\tau) = K_0 \frac{|\int_{\tau-\Delta\tau}^{\tau} y_r(t)dt - \int_{\tau-2\Delta\tau}^{\tau-\Delta\tau} y_r(t)dt|}{\Delta\tau^2} + K_s \tag{2.18}$$

where K_0 is a constant, K_s is the steady state gain for the adaptive filter and $\Delta\tau$ is the dimensionless time interval between two updates of K. To make the filter focus on tracking the growth dynamics at the fast dynamic stage and on noise rejection when the surface dynamics slow down, the K_0 and K_s in Eq.2.18 are tuned such that the first term in right hand side of Eq.2.18 is dominant during the fast dynamics stage and the second term in the right hand side of Eq.2.18 is dominant when the dynamics slow down. The filter parameters (K_0 and K_s) are determined from a step test of the process and are shown in Table 2.1. Regarding the choice of $\Delta\tau$, although a better tracking performance is expected when a smaller $\Delta\tau$ is used, a very small $\Delta\tau$ will introduce the effect of fluctuations on the filter gain and should be avoided. Figure 2.5 shows the roughness obtained directly from a kinetic Monte-Carlo simulator using a 20×20 lattice and Figure 2.6 shows the roughness from the same kinetic Monte-Carlo simulator and the adaptive filter. The results clearly show that the adaptive filter can reject most of the fluctuation in the roughness values while capturing the characteristics of the output of the kinetic Monte-Carlo simulator which uses the small lattice.

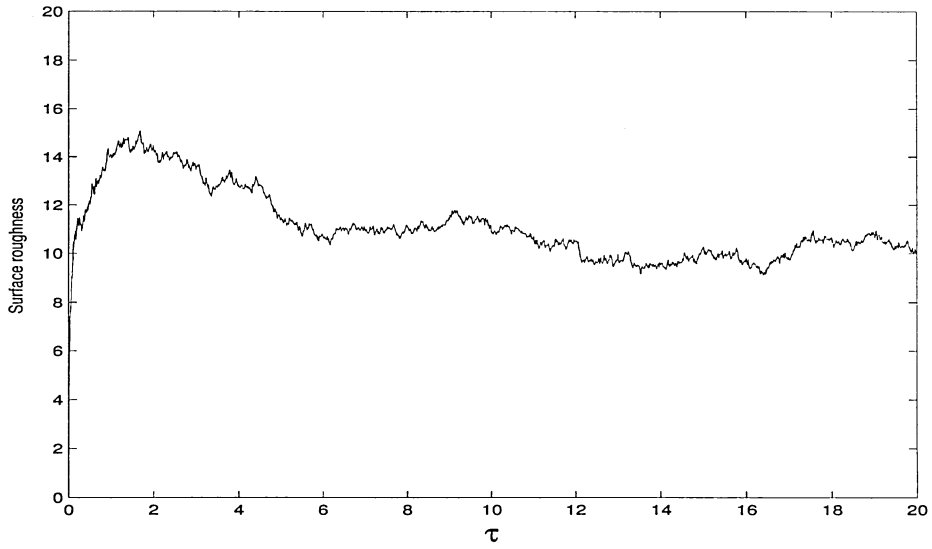

Figure 2.5: Evolution of the roughness obtained directly from a kinetic Monte-Carlo simulator which uses a 20×20 lattice.

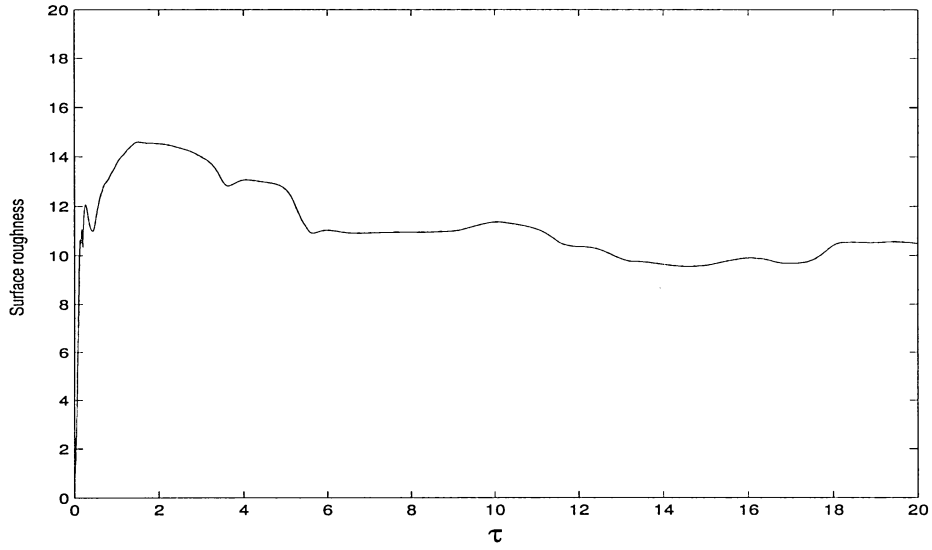

Figure 2.6: Filtered roughness from a kinetic Monte-Carlo simulator which uses a 20×20 lattice.

The significant fluctuation is not the only problem need to be fixed when a small lattice is used in the kinetic Monte-Carlo simulator. There is also model inaccuracy when the outputs of kinetic Monte-Carlo simulators which use a small lattice and a high-order lattice are compared. Figure 2.7 shows the output from a kinetic Monte-Carlo simulator which uses a 20×20 lattice after passing the filter and that from a kinetic Monte-Carlo simulator which uses a 100×100 lattice. Although the filtered roughness from the kinetic Monte-Carlo simulator which uses small lattice contains little fluctuation, the output of the kinetic Monte-Carlo simulator which uses a small lattice does not match that of the kinetic Monte-Carlo simulator which uses a high-order lattice. This can be corrected by using a measurement error compensator that uses the available roughness measurements obtained from a kinetic Monte-Carlo simulator which uses the high-order lattice model to produce an improved roughness estimate. The state-space representation of the measurement error compensator is:

$$\frac{de}{d\tau} = K_e(y_h(\tau_{m_i}) - \hat{y}(\tau_{m_i})); \quad \tau_{m_i} < \tau \leq \tau_{m_{i+1}}; \qquad i = 1, 2, \cdots \tag{2.19}$$

and the final roughness estimates are computed by:

$$\hat{y} = \hat{y}_r + e \tag{2.20}$$

In the above equations, K_e is the compensator gain, e is the estimated model error, which is used to compensate the model output, $\hat{y}$ is the roughness estimates, $\hat{y}_r$ is the filtered output from a kinetic Monte-Carlo simulator which uses a small lattice and y_h is the output of a kinetic Monte-Carlo simulator which uses the high-order lattice (in an experimental set-up y_h could be obtained from the measurement sensor). Since the roughness measurements are only available at discrete points in time $\tau_m = [\tau_{m_1}, \tau_{m_2}, \cdots]$, the right-hand side of Eq.2.19 is computed at the time a roughness measurement is available and is kept in this value in the time interval between two available roughness measurements.

The combination of the adaptive filter and the measurement error compensator functions as a roughness estimator, which is capable to accurately predict the evolution of roughness during the thin film growth by using measurements of the precursor concentration above the substrate and surface roughness. In this work, we assume that the estimate of precursor concentration above the substrate is available; the estimation of surface precursor concentration can be done by using estimation methods for continuum-type PDE models (Christofides, 2001b). Figure 2.8 illustrates the prediction of surface roughness by the roughness estimator and its comparison to the output from the kinetic Monte-Carlo model which uses a high-order lattice. The results clearly show that when measurements are used, the estimator based on a kinetic Monte-Carlo simulator which uses a small lattice can predict the evolution of surface roughness, while the computational requirements are kept within the limit that on-line control is possible.

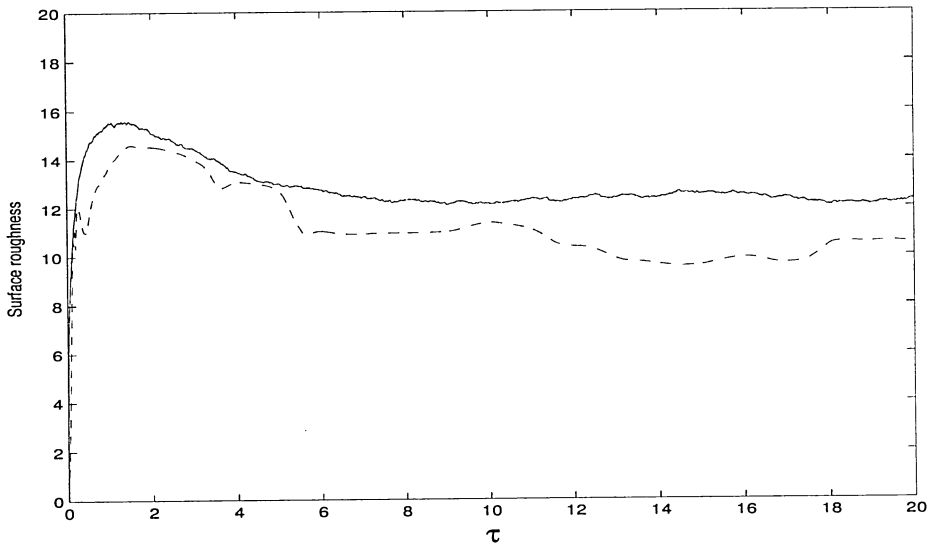

Figure 2.7: Filtered roughness from a kinetic Monte-Carlo simulator which uses a 20×20 lattice (dashed line) and roughness from a kinetic Monte-Carlo simulator which uses a 100×100 lattice (solid line).

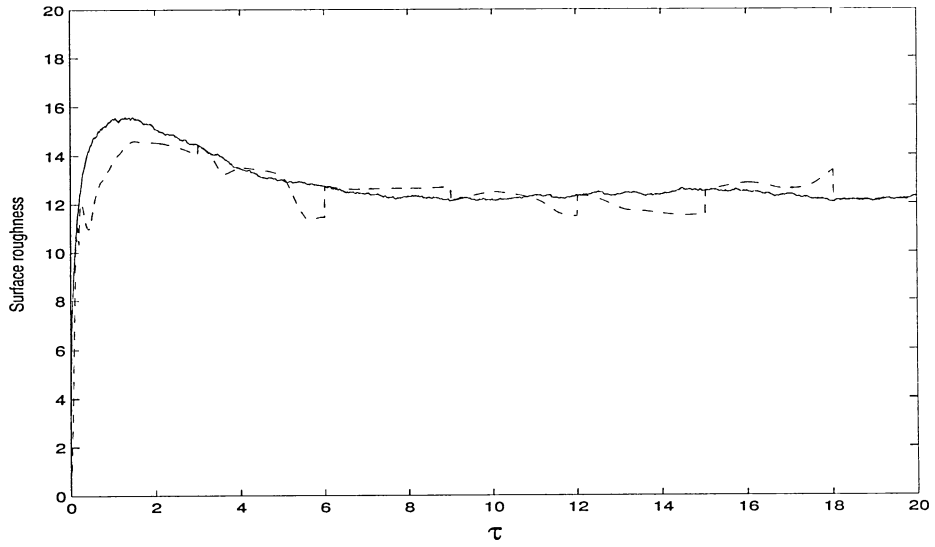

Figure 2.8: Roughness profiles from the roughness estimator (dashed line) and from a kinetic Monte-Carlo simulator which uses a 100×100 lattice (solid line).

Remark 2.1 *It is important to point out that while a* 20×20 *small lattice captures adequately the evolution of the surface roughness in this specific thin film growth problem, the dimension of the small lattice in general should be chosen so that the interactions between the surface atoms are adequately captured, and also that it is large enough to describe the spatio-temporal phenomena occurring (e.g., island formation) on the surface. The choice of the dimension of the small lattice can be guided by the study of the surface behavior obtained by simulating a very high order lattice; in this way, the proposed approach, based on reduction of lattice size, appears to be quite intuitive (see Gallivan and Murray, 2003, for reduction approaches based on the master equation).*

2.4 Feedback control of surface roughness

The production of high-quality thin films requires that the surface roughness is maintained at a desired level. In this work, we consider as manipulated variable the

substrate temperature (which is assumed to change only with respect to time) - this is a reasonable formulation for the manipulated input and is satisfied by many deposition processes including experimental systems at UCLA. With such a manipulated input formulation, the only variable that can be controlled is a spatially averaged roughness, as defined in Eq.2.16. We could have formulated a control problem under the assumption that a large number of manipulated inputs (control actuators) are available to control surface roughness with higher precision but such a control problem formulation would not be practically feasible at the present time. As we will see below, it is possible by manipulating substrate temperature (single input formulation) to achieve an overall very smooth surface configuration.

The fact that the model that describes the evolution of the thin film growth process is not available in closed form (Monte-Carlo model) motivates the use of a proportional-integral (PI) feedback controller to regulate the surface roughness. Specifically, the controller has the following form:

$$u(\tau) = K_c[(\hat{y} - y_{set}) + \frac{1}{\tau_c}\int_0^{\tau}(\hat{y} - y_{set})dt] \tag{2.21}$$

where y_{set} is the set-point of the output, $\hat{y}$ is the output of the roughness estimator, K_c is the proportional gain and τ_c is the integral time constant.

The PI controller is coupled with the roughness estimator presented in the previous section. A diagram of the closed-loop system under the proposed estimator/controller structure is shown in Figure 2.9. The roughness estimator includes the Monte-Carlo model that uses the small lattice, the adaptive filter and the measurement error compensator. The output of the Monte-Carlo model is sent to the adaptive filter (Eq.2.17) to eliminate the noise, and the measurement error compensator (Eq.2.19 and 2.20) updates the filtered roughness based on the measurements. Finally, the

roughness estimates are used in the controller to determine the substrate temperature.

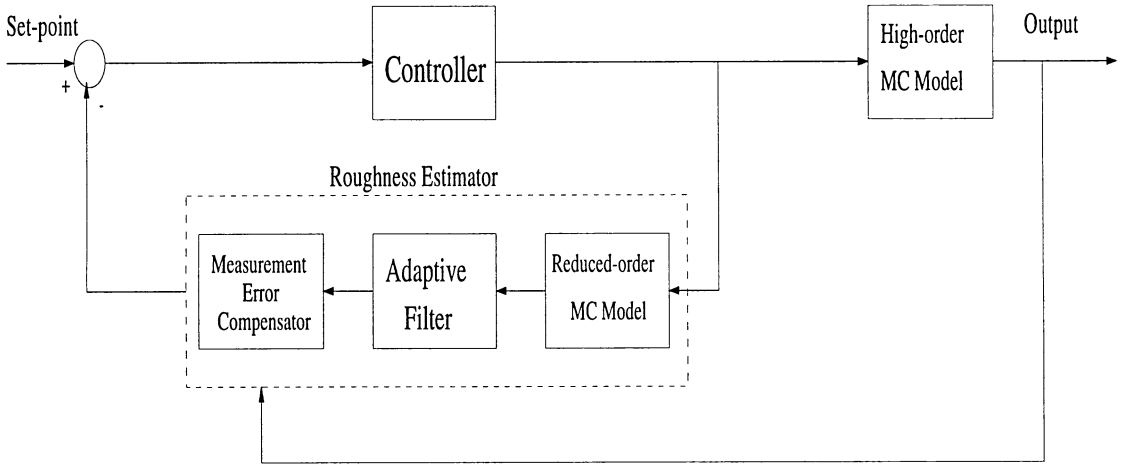

Figure 2.9: Diagram of the closed-loop system.

A closed-loop simulation was run to evaluate the effectiveness of the estimator/controller structure. The size of the small lattice is 20×20 and a 50×50 lattice Monte-Carlo model is used to describe the evolution of the process. The desired roughness is 1.5. The time interval between two available measurements is $0.3s$; this is consistent with spectroscopic ellipsometry techniques that can be used to measure surface roughness on-line (Zapien et al., 2001). Other parameters used in the simulation are shown in table 2.1.

Initially, the thin film grows on a perfect surface at $T = 600K$ and the roughness increases. Then, the controller is activated when the roughness reaches 15.5. Figure 2.10 shows the evolution of surface roughness under feedback control. Figure 2.11 shows the profile of the substrate temperature. The results clearly show that the proposed estimator/controller structure can successfully drive the surface roughness to the desired set-point value.

The micro-configurations of the surface before the controller is activated and at the end of the closed-loop simulation run are shown in Figure 2.12 and Figure 2.13,

P	$10^{-4}atm$	a	$5s^{-1}$
s_0	0.1	m	$0.028kg/mol$
C_{tot}	$10^{19}sites/m^2$	k_{d0}	$10^{13}s^{-1}$
E_d	$7.14 \times 10^4 J/mol$	E_m	$4.28 \times 10^4 J/mol$
E	$7.14 \times 10^4 J/mol$	K_0	0.5
K_s	1.0	K_e	0.08
K_c	30	τ_c	0.4
y_{set}	1.5		

Table 2.1: Process and controller parameters.

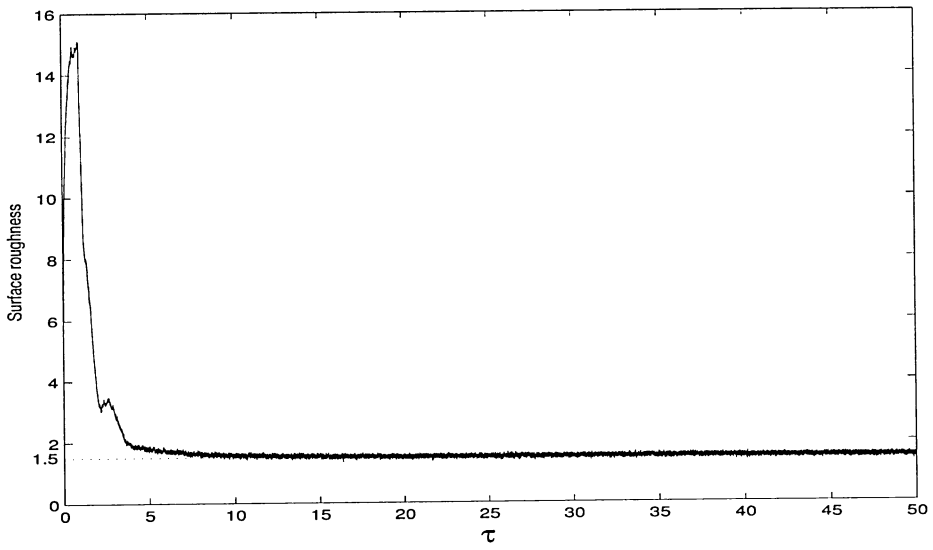

Figure 2.10: Evolution of the surface roughness under feedback control.

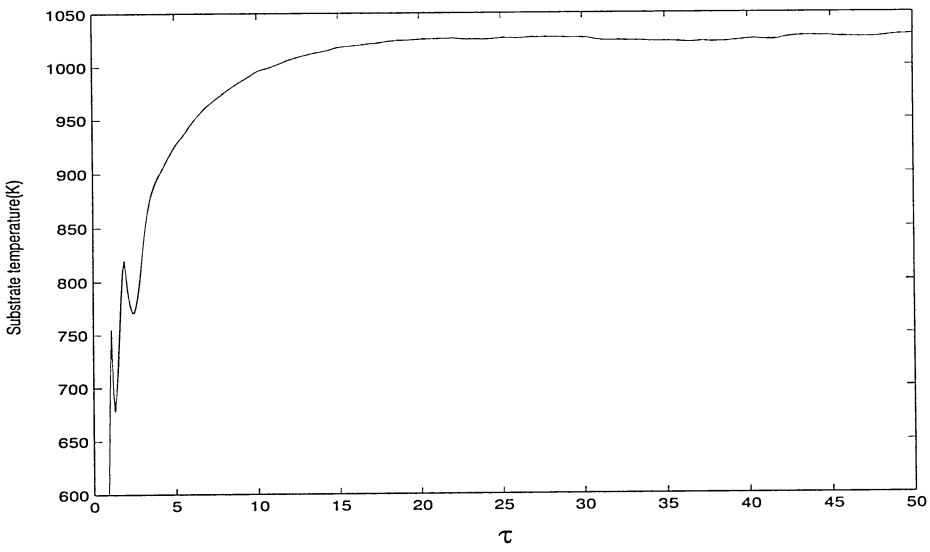

Figure 2.11: Evolution of the substrate temperature.

respectively. The controller successfully reduces the surface roughness of the thin film.

To test the robustness of the proposed estimator/controller structure, we considered controlling the thin film growth process in the presence of 10% uncertainty in the energy associated with a single bond on the surface. Figure 2.14 and Figure 2.15 show the corresponding output and input profiles, respectively. The controller exhibits very good robustness properties (compare Figures 2.10 and 2.14).

To show the importance of using the roughness estimator for feedback control and not relying exclusively on the roughness measurements (which are obtained every 0.3 seconds), we applied the PI controller (with the same parameters as in Table 2.1) to the multiscale process model assuming that new roughness measurements are fed into the controller every 0.3 seconds (this is consistent with our previous simulations). Also, to prevent the substrate temperature increasing to an unreasonable high value, the substrate temperature is constrained to be below $T_{max} = 1100K$. We note

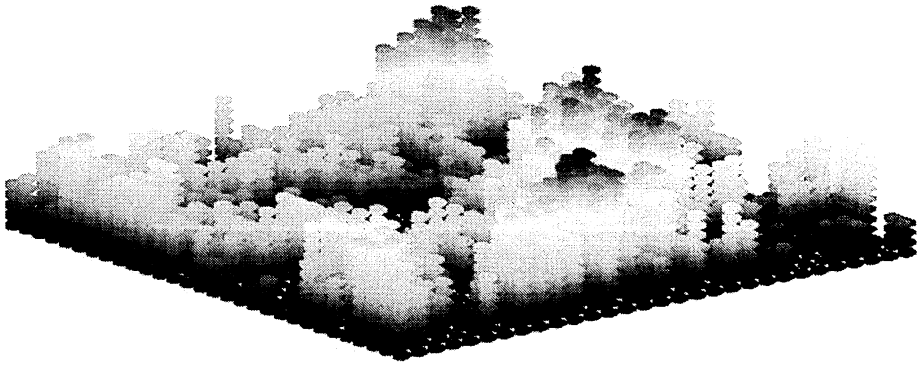

Figure 2.12: The micro-configuration of the surface for T=600K.

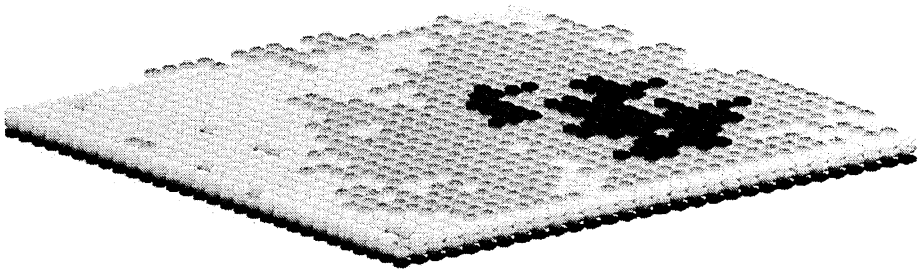

Figure 2.13: The micro-configuration of the surface at the end of the closed-loop simulation run.

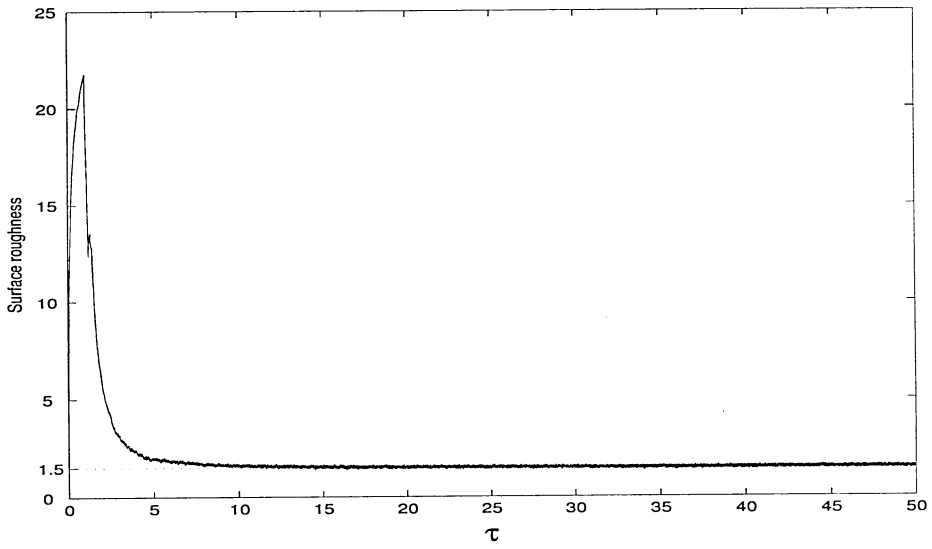

Figure 2.14: Evolution of the surface roughness under feedback control - closed-loop system simulation under uncertainty.

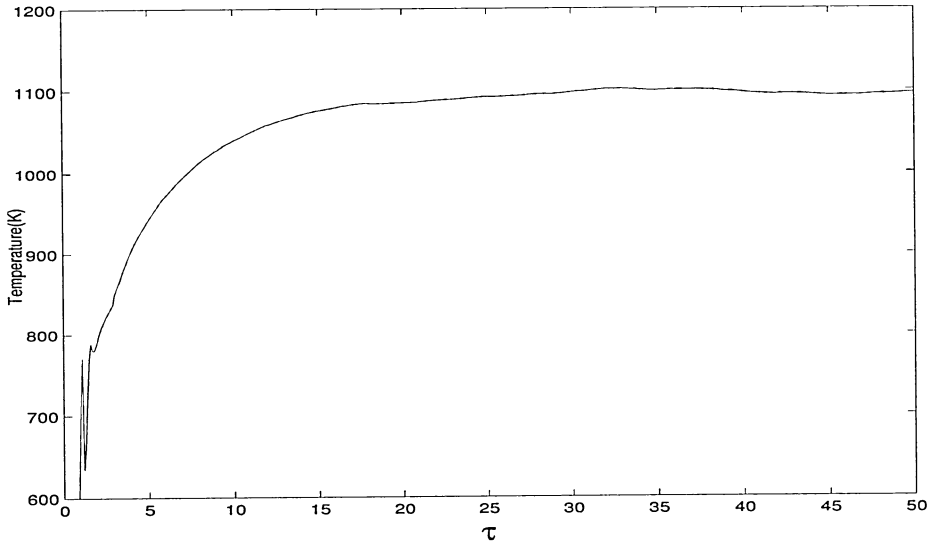

Figure 2.15: Evolution of the substrate temperature - closed-loop system simulation under uncertainty.

that when the roughness is controlled using the proposed controller/estimator structure, the substrate temperature is always lower than T_{max} (see Figure 2.11). Figures 2.16 and 2.17 show the evolution of surface roughness and substrate temperature, respectively. Due to the discrete measurements, we observe significant oscillations in the surface roughness profile; this simulation shows the usefulness of the proposed estimator/controller structure.

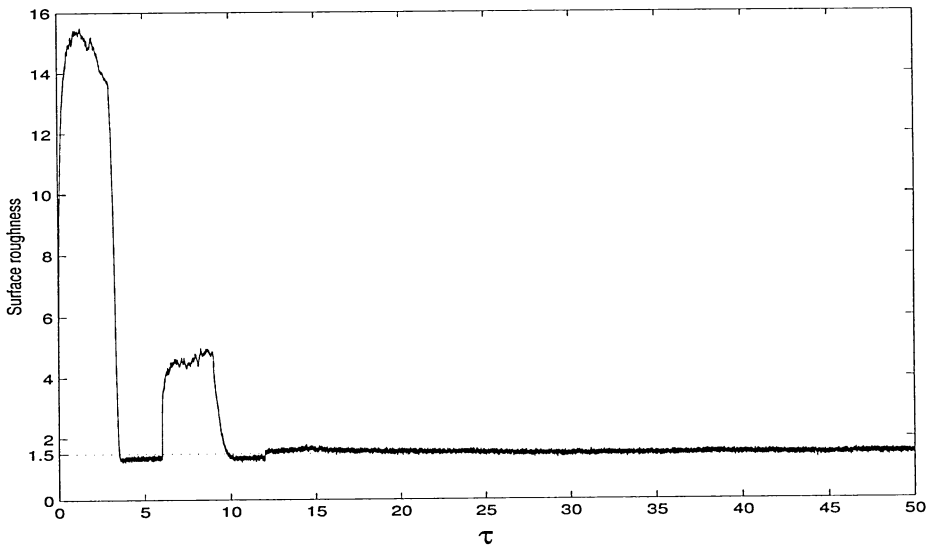

Figure 2.16: Evolution of the surface roughness under feedback controller without roughness estimator.

Remark 2.2 *We note that the fundamental reason for the poor performance shown in Figure 2.16 is that the discrete measurements can not capture the full dynamics of the system, which prevents efficient control actions to be computed by the controller. Tuning the controller can not achieve a control performance as good as that achieved under feedback control using the roughness estimator. As shown in Figure 2.16, when the controller is tuned to achieve fast dynamics in the output, significant oscillation can be seen in the roughness output. The oscillations could be reduced by tuning the controller, however, the result of this is that the time needed for the process to reach the steady state becomes much longer. To show this, we applied the PI controller*

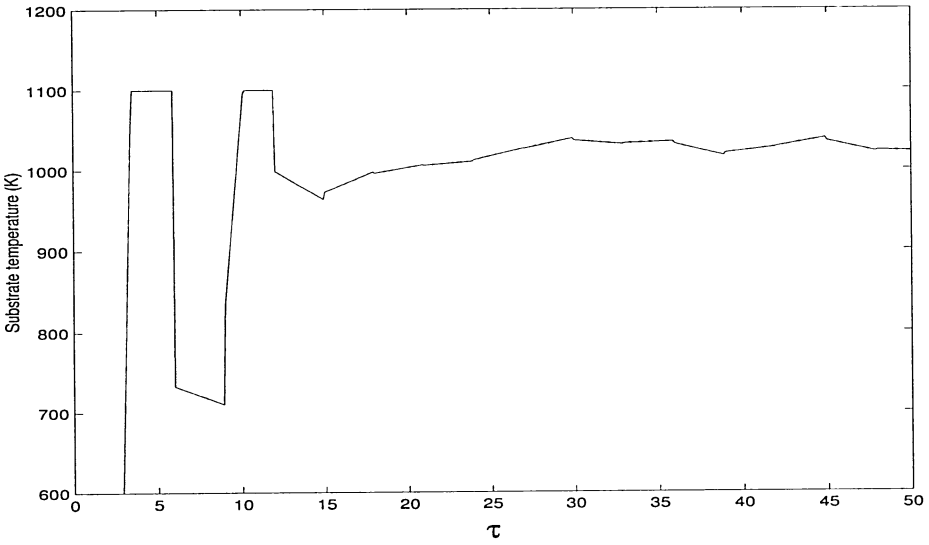

Figure 2.17: Evolution of the substrate temperature under feedback controller without roughness estimator.

with a set of new parameters ($K_c = 10$, $\tau_c = 1.0$) to the same multiscale process model assuming that new roughness measurements are fed into the controller every 0.3 *seconds. The parameters of the PI controller are tuned to avoid significant oscillation in the roughness profile under feedback control. Figures 2.18 and 2.19 show the profiles of surface roughness and substrate temperature, respectively. With the new controller parameters, fewer oscillations are observed, but the process takes significant longer time to reach the new steady state (compare Figure 2.11 and Figure 2.19, in Figure 2.11, the substrate temperature reaches the steady state value at around $\tau = 20$, but in Figure 2.19, the substrate temperature reaches the steady state value at around $\tau = 100$). To better compare the performance of the various control approaches, the roughness profiles shown in Figures 2.10, 2.16 and 2.18 are shown together in Figure 2.20. We tried different parameters of the PI controller but it turns out it is hard to achieve short transient time and less oscillation simultaneously when control the surface roughness exclusively relying on the discrete measurements.*

Remark 2.3 *Furthermore, when there is time-delay in the measurements of surface*

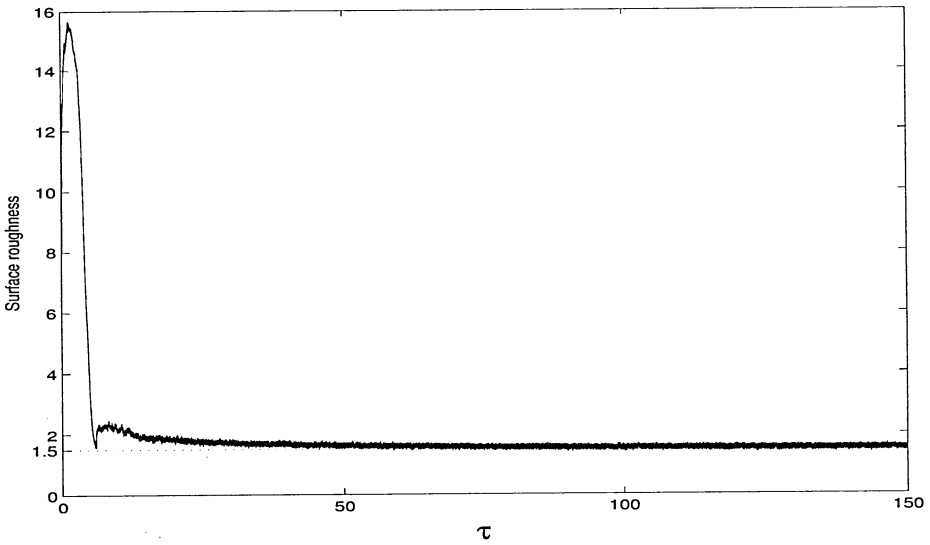

Figure 2.18: Evolution of the surface roughness under feedback controller without roughness estimator: controller is tuned such that significant oscillation is avoided.

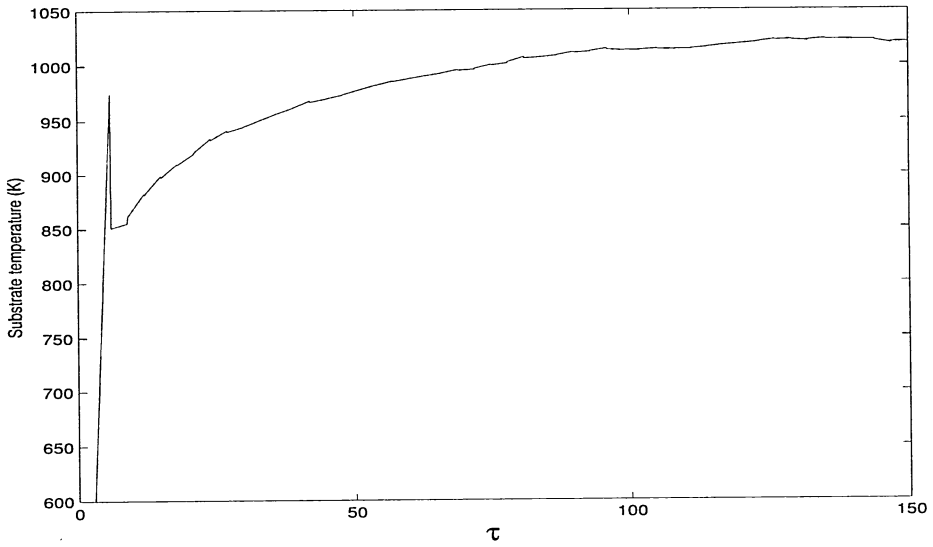

Figure 2.19: Evolution of the substrate temperature under feedback controller without roughness estimator: controller is tuned such that significant oscillation is avoided.

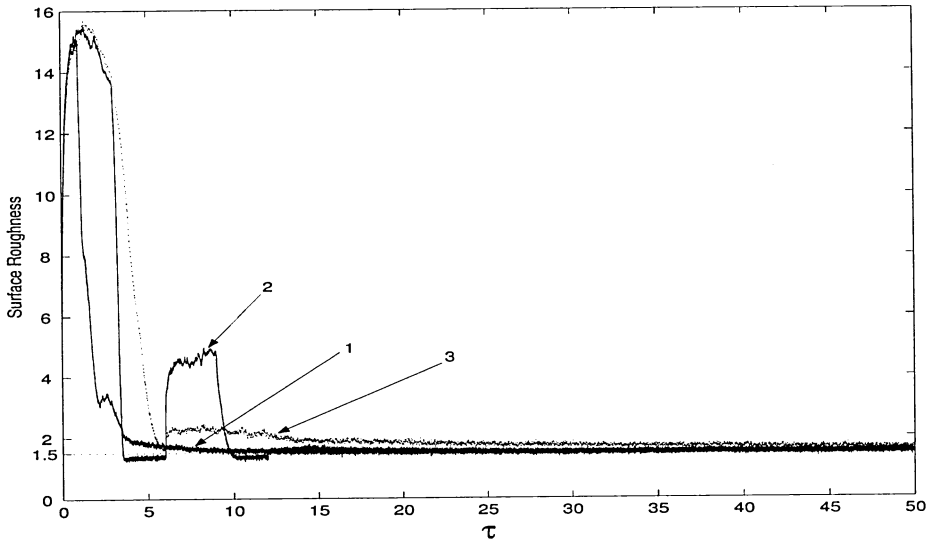

Figure 2.20: Comparison of surface roughness profiles: (1) roughness profile under feedback control using roughness estimator, (2) roughness profile under feedback control without using roughness estimator with controller parameters shown in Table 2.1, and (3) roughness profile under feedback control without using roughness estimator with controller parameters tuned to avoid significant oscillation.

roughness, the PI controller (with parameters shown in Table 2.1) is not able to drive the surface roughness to the set-point value. To show this, we applied the PI controller to the multiscale process model assuming that new roughness measurements are fed into the controller every 0.3 *seconds with a time-delay of* $\tau_d = 0.3s$. *Also, to prevent the substrate temperature reaching an unreasonable high or low value, the substrate temperature is constrained to be between* $T_{max} = 1100K$ *and* $T_{min} = 300K$. *We note that the lower limit of the substrate temperature* $T_{min} = 300K$ *was not reached in any of the previous simulations. Figures 2.21 and 2.22 show the profiles of surface roughness and substrate temperature under PI control using the discrete roughness measurements with time-delay. Due to the existence of time-delay in measurements, we observe that the PI controller can not stabilize the system. On the other hand, in the estimator/controller structure, the measurement-delay has very little effect to the control performance. To show this, we applied the estimator/controller structure (the parameters of the PI controller are the same to those shown in Table 2.1) to the multiscale process model assuming that new roughness measurements are fed into the controller every* 0.3 *seconds with a time-delay of* $\tau_d = 0.3s$. *The resulting profiles of surface roughness and substrate temperature are shown in Figures 2.23 and 2.24. It is clear that the proposed estimator/controller structure successfully drives the surface roughness to the set-point value in the presence of time-delay in the roughness measurements.*

Remark 2.4 *Furthermore, to show that the estimator/controller structure is able to control the surface roughness independently of the frequency at which the roughness measurements are available, we implemented the proposed structure without using roughness measurements, i.e. the controller determines the substrate temperature based only on the output of the kinetic Monte-Carlo simulator which uses the small lattice and the adaptive filter. Figures 2.25 and 2.26 show the resulting profiles of surface roughness and substrate temperature. Our simulation results show that this open-loop implementation of the proposed controller/estimator structure (with same*

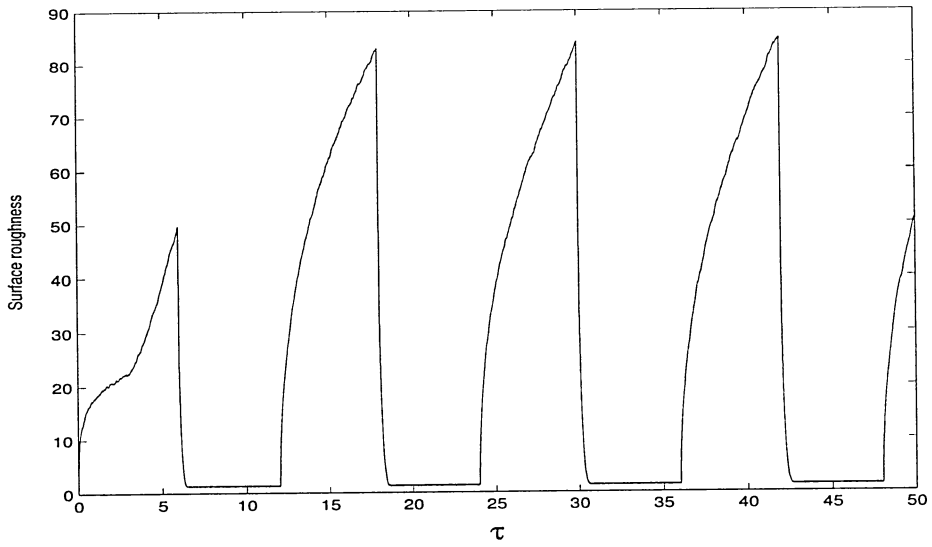

Figure 2.21: Evolution of the surface roughness under feedback controller without roughness estimator - delayed roughness measurements.

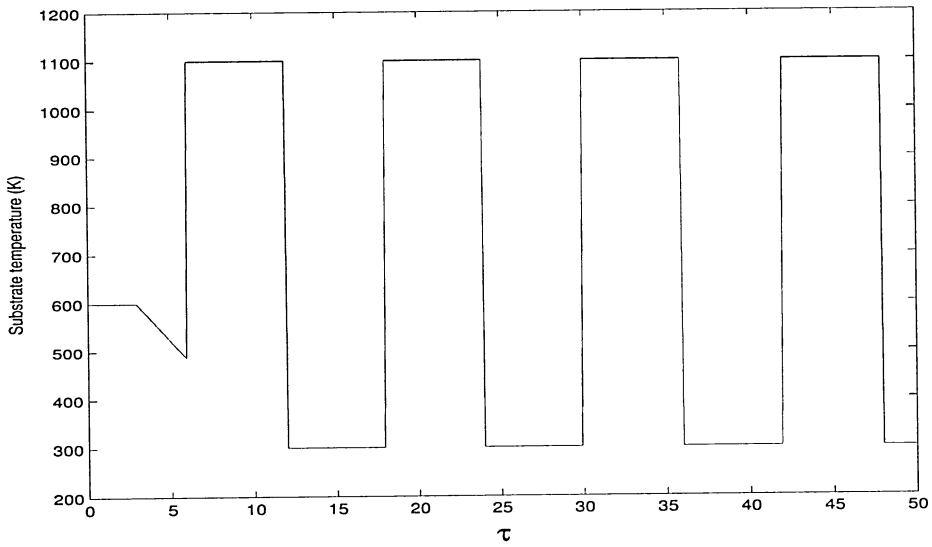

Figure 2.22: Evolution of the substrate temperature under feedback controller without roughness estimator - delayed roughness measurements.

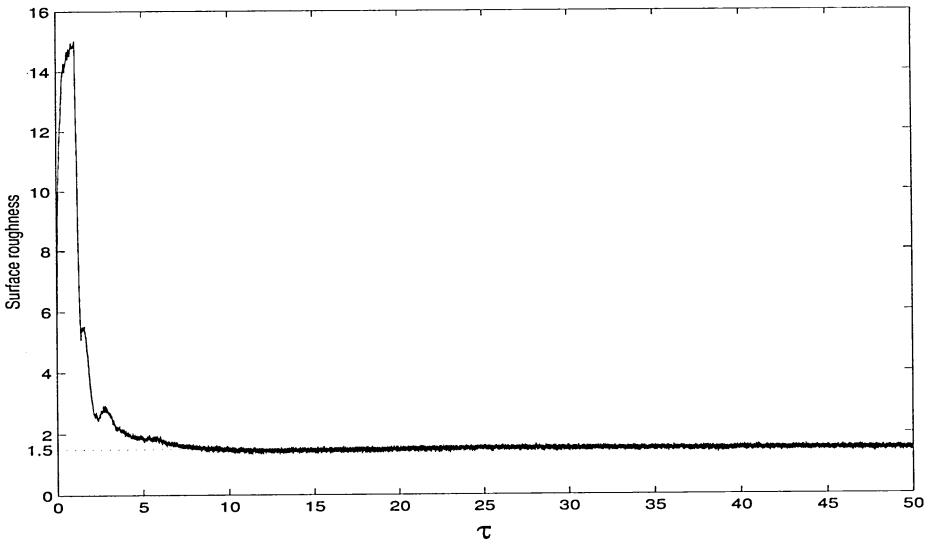

Figure 2.23: Evolution of the surface roughness under feedback controller using the estimator/controller structure - delayed roughness measurements.

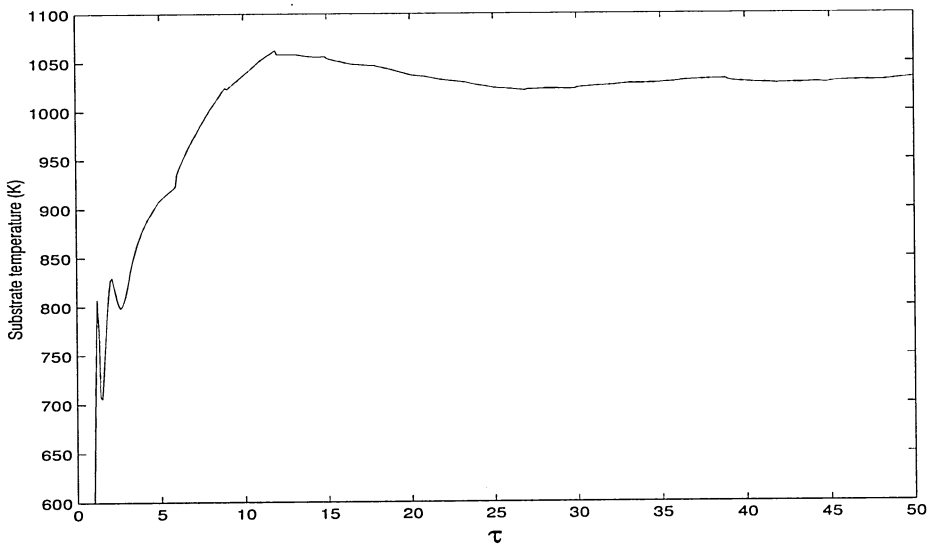

Figure 2.24: Evolution of the substrate temperature under feedback controller using the estimator/controller structure - delayed roughness measurements.

parameters as those shown in Table 2.1) successfully drives the surface roughness to the desired value.

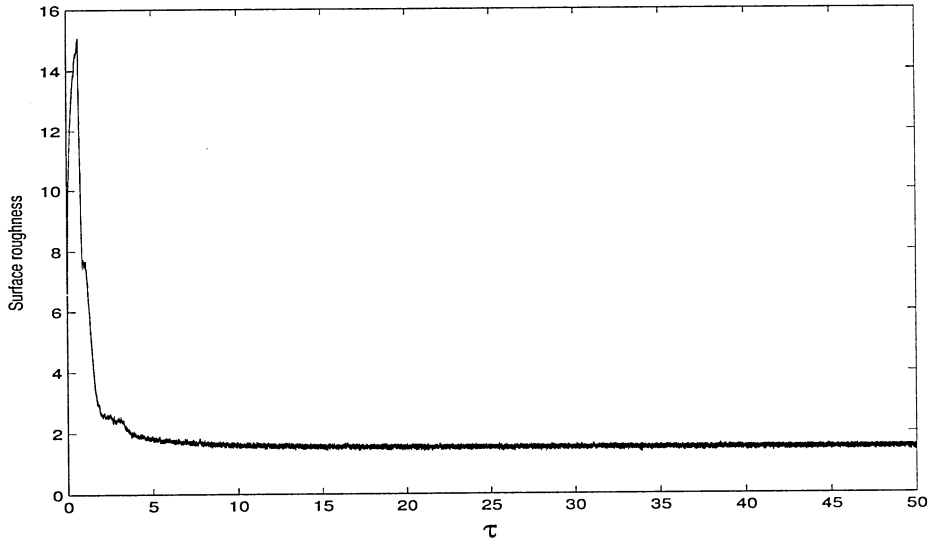

Figure 2.25: Evolution of the surface roughness under open-loop PI controller.

Remark 2.5 *The fluctuations of the roughness value obtained by using a small lattice Monte-Carlo model can be reduced by independently running several Monte-Carlo simulations using a small lattice with the same parameters and averaging the roughness values obtained from the different runs. Figure 2.27 shows a comparison of the evolution of surface roughness obtained from: a) a kinetic Monte-Carlo simulator which uses a* 20×20 *lattice, b) the computation of the average of six independent Monte-Carlo simulations which utilize a* 20×20 *lattice, and c) a Monte-Carlo simulator which uses a* 100×100 *lattice. These results show that when the outputs from multiple small lattice models are averaged, a more accurate calculation of surface roughness is obtained. However, by increasing the number of Monte-Carlo simulations, the computational requirement is also increasing. For the simulations of Figure 2.27, the computational time for the averaged roughness is six times as much as that needed to perform one Monte-Carlo simulation run and it is approximately equal to the computational time needed to run a Monte-Carlo simulation on a* 30×30 *lattice.*

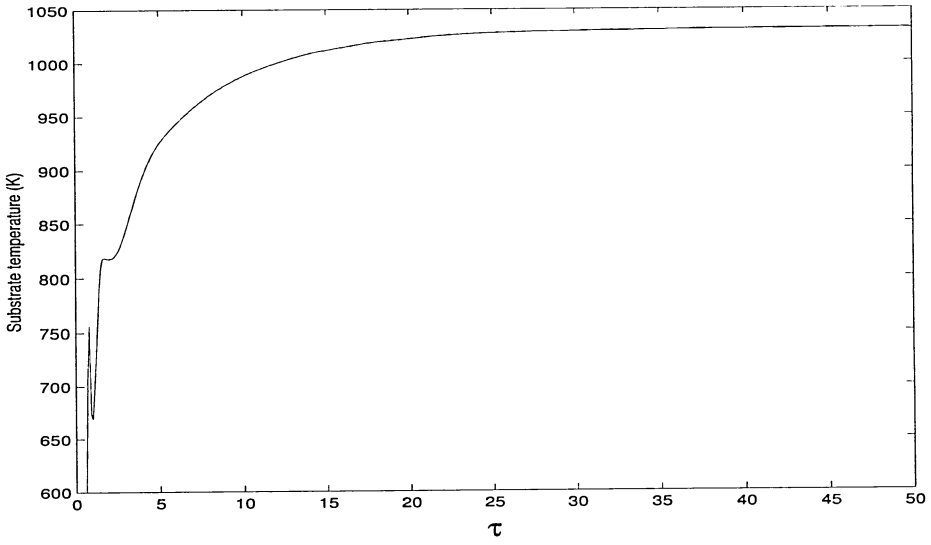

Figure 2.26: Evolution of the substrate temperature under open-loop PI controller.

Figure 2.28 shows a comparison of the evolution of roughness obtained from: a) a Monte-Carlo simulator which uses a 30×30 *lattice, b) the computation of the average of six independent Monte-Carlo simulations which utilize a* 20×20 *lattice, and c) a Monte-Carlo simulator which uses a* 100×100 *lattice. The results of Figure 2.28 show that the roughness obtained by averaging six Monte-Carlo simulations, which use a* 20×20 *lattice model, is close to the one obtained from the* 100×100 *lattice model and is superior to the one obtained from the* 30×30 *lattice model.*

Figure 2.29 shows the evolution of surface roughness under feedback control using multiple small lattice models. Figure 2.30 shows the corresponding profile of the substrate temperature. The results are comparable to the case of using a kinetic Monte-Carlo simulator which uses one 20×20 lattice in the controller (compare closed-loop roughness profiles in Figure 2.10 and Figure 2.29); which means that the feedback control system based on a kinetic Monte-Carlo simulator which uses a single small lattice performs very well.

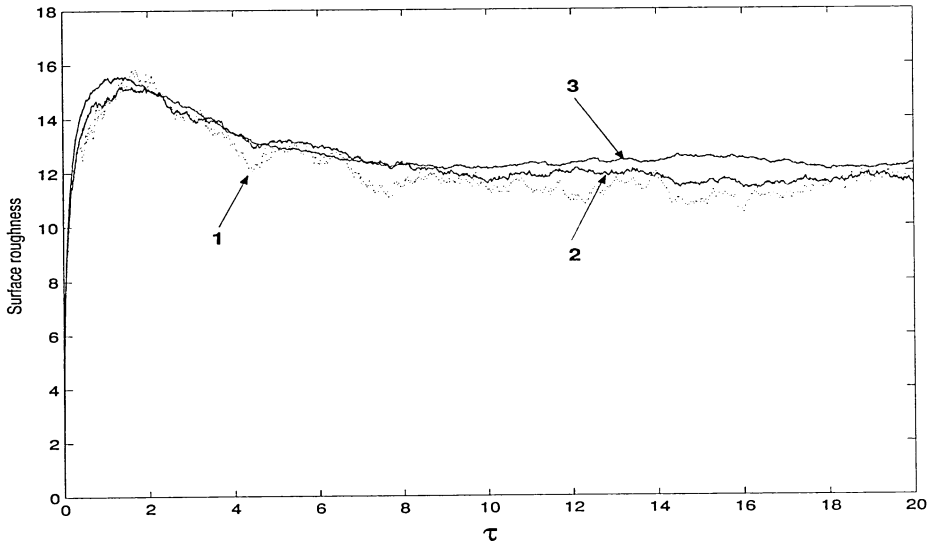

Figure 2.27: Comparison of the evolution of surface roughness from: (1) a Monte-Carlo simulator which uses a 20×20 lattice, (2) the computation of the average of six independent Monte-Carlo simulations which utilize a 20×20 lattice, and (3) a Monte-Carlo simulator which uses a 100×100 lattice.

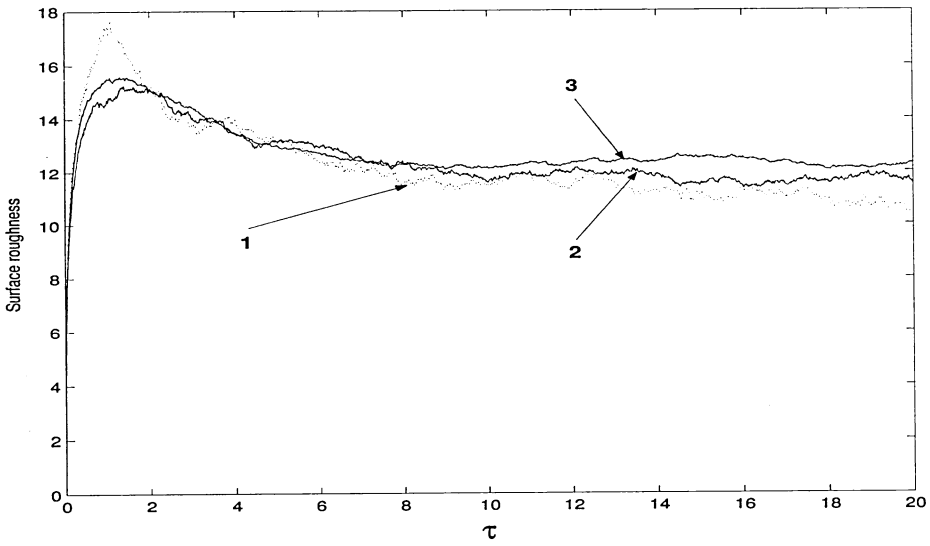

Figure 2.28: Comparison of the evolution of surface roughness from: (1) a Monte-Carlo simulator which uses a 30×30 lattice, (2) the computation of the average of six independent Monte-Carlo simulations which utilize a 20×20 lattice, and (3) a Monte-Carlo simulator which uses a 100×100 lattice.

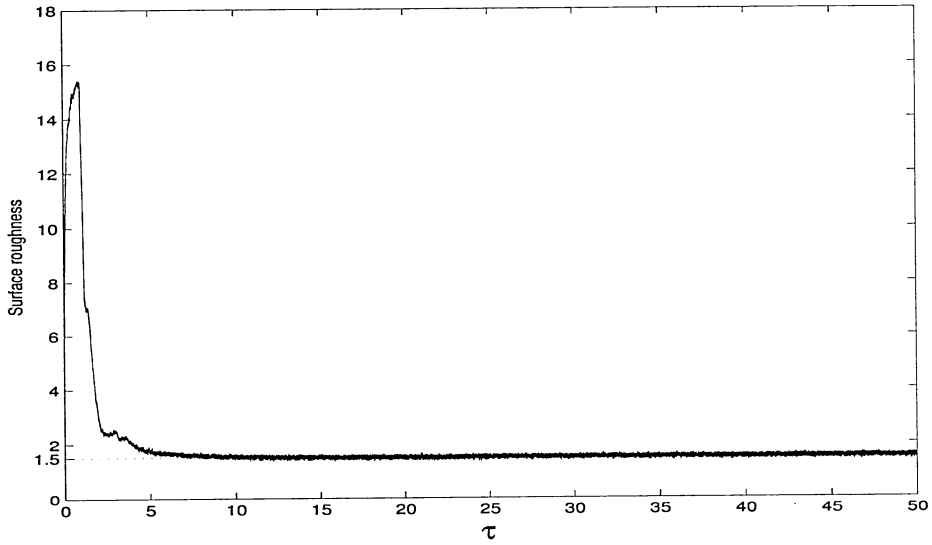

Figure 2.29: Closed-loop surface roughness profile under feedback controller using a kinetic Monte-Carlo simulator that employs multiple small lattice models.

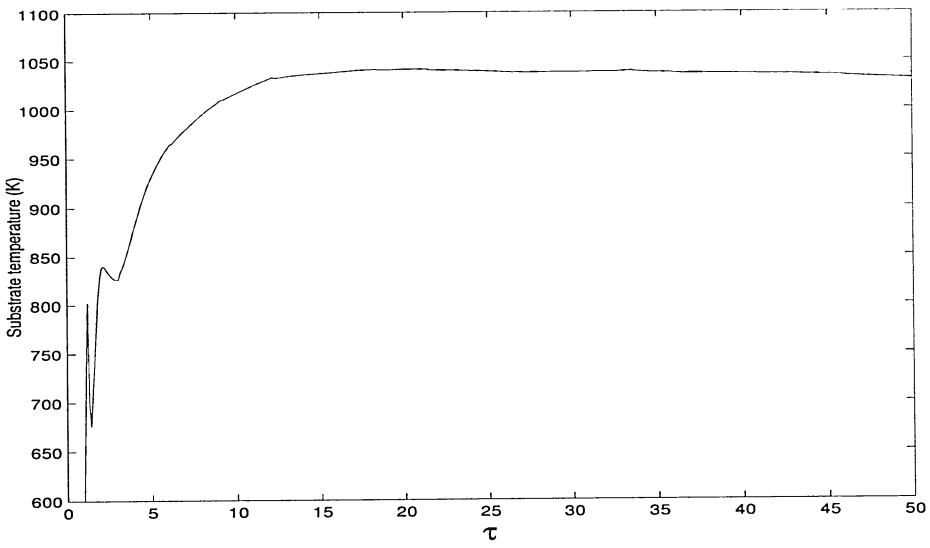

Figure 2.30: Closed-loop substrate temperature profile under feedback controller using a kinetic Monte-Carlo simulator that employs multiple small lattice models.

2.5 Conclusions

In this chapter, an approach to estimation and control of surface roughness in thin film growth was proposed. A feedback control system, which can be implemented in real-time, was developed and applied to a thin film growth process in a stagnation flow geometry. The control system consists of a roughness estimator and a proportional integral controller. The roughness estimator combines kinetic Monte-Carlo simulators that use small lattice models, a filter and a measurement error compensator that uses discrete roughness measurements. Application of the proposed estimator/controller structure to the multiscale process model demonstrates successful regulation of the surface roughness at the desired set-point value. The proposed approach is shown to be superior to PI control with direct use of the discrete roughness measurements. The reason is that the available measurement techniques do not provide measurements at a time-scale comparable to the evolution of the dominant film growth dynamics.

Chapter 3

Feedback Control of Growth Rate and Surface Roughness in Thin Film Growth

3.1 Introduction

In Chapter 2, we proposed a systematic method for the design of roughness estimators which consist of kinetic Monte-Carlo simulators based on small lattice models, an adaptive filter for noise reduction and a measurement error compensator. Based on the estimator, a single-loop feedback control system was developed and applied to the multiscale model of a thin film growth process to regulate surface roughness.

This chapter focuses on multivariable feedback control of surface roughness and growth rate in thin film growth. The objective is to understand the nature of this multivariable control problem and to develop a systematic method for the design of a multivariable feedback control system, which can be implemented in real-time. To proceed, the thin film growth process is first introduced and a multiscale model is presented. An estimator is then constructed that allows computing estimates of the sur-

face roughness and growth rate at a time-scale comparable to the real-time evolution of the process. The multivariable control problem is then studied and a multivariable feedback control system, which directly uses the estimator and compensates for the effect of multivariable input/output interactions, is designed to simultaneously regulate the growth rate and surface roughness by manipulating substrate temperature and inlet precursor concentration. Finally, the proposed control system is applied to the multiscale process model and successful regulation of the surface roughness and growth rate to the desired set-point values is demonstrated through computer simulations. While the proposed method for estimation/control using kinetic Monte-Carlo simulators is applied to the process of thin film growth in a stagnation flow geometry, the methodological approach presented in this chapter is applicable to other thin film growth processes.

3.2 Thin film growth process

We consider the same thin film growth process as the one presented in Chapter 2. Please refer to Section 2.2 for the mathematical descriptions of the multiscale model of this thin film growth process.

3.3 Real-time estimator for surface roughness and growth rate

Surface roughness and growth rate are properties of interest from a control point of view since they directly influence device properties and productivity. To be able to achieve good control of surface roughness and growth rate, it is important to develop an estimator that can provide estimates of these variables in real-time. In

this section, we develop such an estimator by following a methodology that was proposed in Chapter 2.

The roughness, r, is represented by the number of broken bonds on the surface and is computed according to the following expression (Raimondeau and Vlachos, 2000):

$$r = \frac{\sum(|h_{i+1,j} - h_{i,j}| + |h_{i-1,j} - h_{i,j}| + |h_{i,j+1} - h_{i,j}| + |h_{i,j-1} - h_{i,j}|)}{2 \times N \times N} + 1 \qquad (3.1)$$

where N is the size of the lattice and $h_{i,j}$ is the number of atoms at site (i, j).

The growth rate, gr, (units monolayer/second, ML/s), determines how fast the thin film grows. In this study, the growth rate is defined as the difference between the rate of adsorption and the rate of desorption on the surface, and is given by the following expression:

$$gr = \frac{\sum_{i,j} r_{ai,j} - r_{di,j}}{N \times N} \qquad (3.2)$$

where $r_{ai,j}$ and $r_{di,j}$, (units sec^{-1}), are the rates of adsorption and desorption at the site (i, j) of the surface, respectively and N is the size of the lattice. The rate $r_{di,j}$ depends on the number of nearest neighbors at site (i, j) and is obtained from the kinetic Monte-Carlo simulations.

In the kinetic Monte-Carlo simulation, the size of the lattice influences the accuracy of the result and the computational demand. In previous work (Lou and Christofides, 2003a), we discussed the dependence of simulation results on the lattice size used in the Monte-Carlo simulations. The simulation results show that when the lattice size is sufficient large, the roughness profiles obtained from kinetic Monte-Carlo simulations are independent of the lattice size. To implement real-time feedback control based on a model that captures the evolutions of surface roughness and growth rate, the size of the lattice has to be selected to make the model solution time com-

parable to the process real-time evolution, while capturing the dominant phenomena occurring on the surface. In our simulations, when the size of the lattice is reduced to 30×30, the solution time of the kinetic Monte-Carlo simulation is comparable to the real-time process evolution and the average values of the surface roughness and growth rate approximate well the average values of these variables, which are obtained by running the kinetic Monte-Carlo simulation on a 120×120 lattice (this is a sufficiently large lattice to ensure simulation results which are independent of the lattice size; see the discussion at the end of Remark 3.1). However, the outputs from a kinetic Monte-Carlo simulation using a 30×30 lattice contain significant stochastic fluctuations, and thus, they cannot be directly used for feedback control (such an approach would result to significant fluctuations of the control action which could perturb unmodeled (fast) process dynamics and should be avoided).

Table 3.1: Process parameters.

Sticking coefficient	s_0	0.1	
Precursor molecular weight	m	4.65×10^{-26}	kg
Surf. site concentration	C_{tot}	10^{19}	$sites/m^2$
Event freq. const	k_{d0}	10^{13}	s^{-1}
Bond energy	E	7.14×10^4	J/mol
Desorption energy	E_d	7.14×10^4	J/mol
Migration energy	E_m	4.28×10^4	J/mol
Chamber pressure	P	10^5	Pa
Strain rate	a	5	s^{-1}

The fluctuations on the values of the outputs (i.e., surface roughness and growth rate) obtained from the kinetic Monte-Carlo simulation using the 30×30 lattice can be reduced by independently running several small lattice kinetic Monte-Carlo

simulations with the same parameters and averaging the outputs of the different runs. Figure 3.1 shows the growth rate obtained from a kinetic Monte-Carlo simulation which uses a 20×20 lattice. Figure 3.2 shows the growth rate obtained from the computation of the average of six independent kinetic Monte-Carlo simulations which utilize a 20×20 lattice. These results show that when the outputs from multiple kinetic Monte-Carlo simulations that use small lattices are averaged, growth rate fluctuations can be significantly reduced. Figure 3.3 shows the surface roughness obtained from a Monte-Carlo simulation which uses a 20×20 lattice. Figure 3.4 shows the surface roughness obtained from the computation of the average of six independent kinetic Monte-Carlo simulations which utilize a 20×20 lattice. Again, less fluctuations are observed in the roughness profile obtained by averaging the outputs from multiple small lattice kinetic Monte-Carlo simulations.

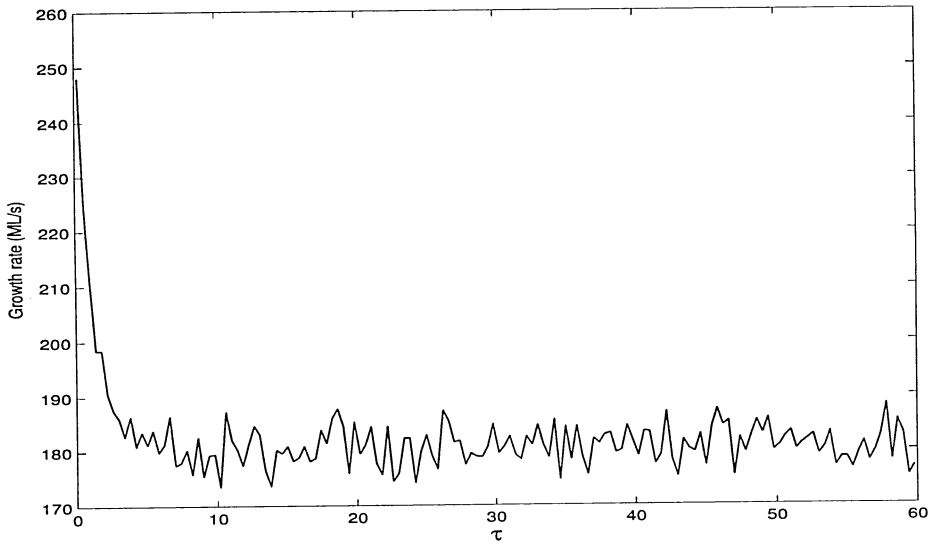

Figure 3.1: Growth rate from a kinetic Monte-Carlo simulation which uses a 20×20 lattice.

However, by increasing the number of kinetic Monte-Carlo simulations which run simultaneously, the computational time is also increasing (unless each simulation can

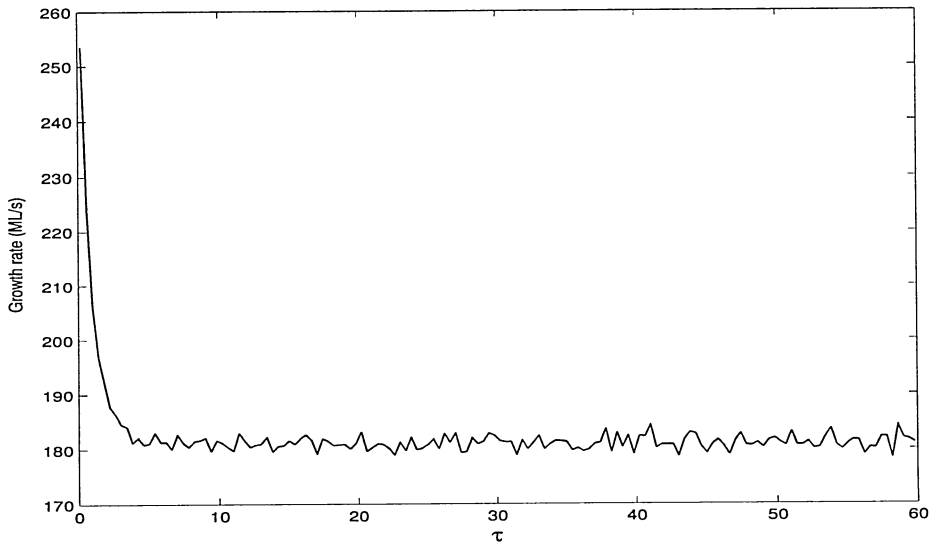

Figure 3.2: Growth rate from the computation of the average of six independent kinetic Monte-Carlo simulations which utilize a 20×20 lattice.

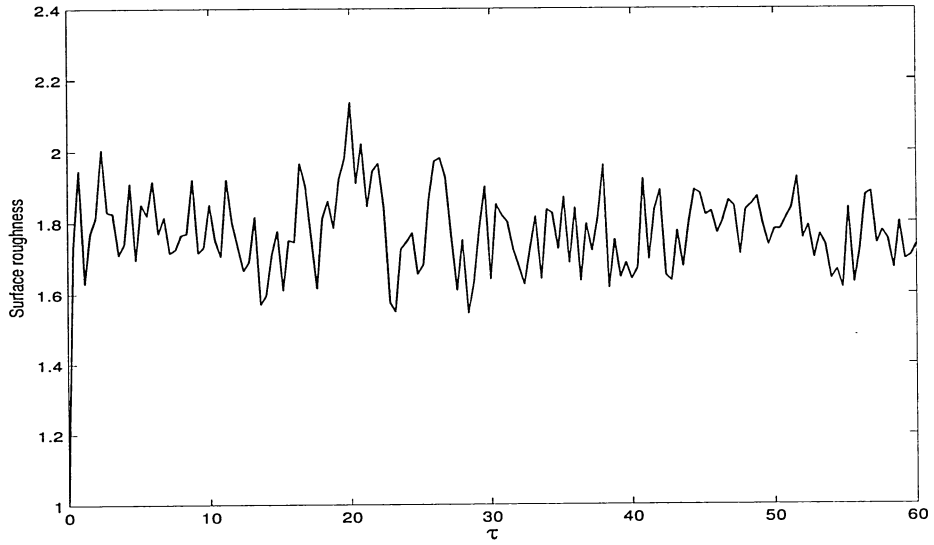

Figure 3.3: Surface roughness from a kinetic Monte-Carlo simulation which uses a 20×20 lattice.

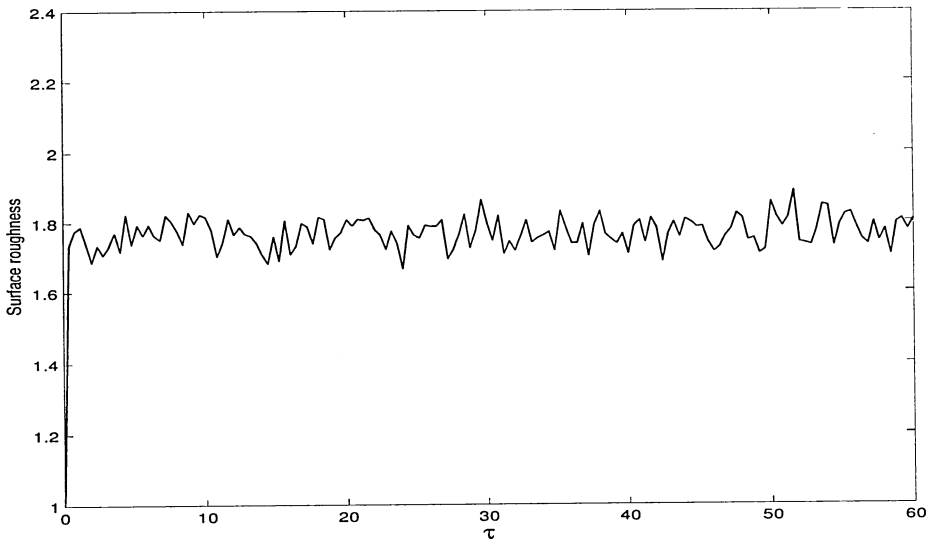

Figure 3.4: Surface roughness from the computation of the average of six independent kinetic Monte-Carlo simulations which utilize a 20 × 20 lattice.

run in a different processor which is possible because there is no interaction between the six simulations). For the results shown in Figures 3.2 and 3.4, the computational time is six times as much as that needed to perform one Monte-Carlo simulation run (Figures 3.1 and 3.3) and it is approximately equal to the computational time needed to run a Monte-Carlo simulation on a 30 × 30 lattice. Figures 3.5 and 3.6 show growth rate and roughness profiles obtained from a Monte-Carlo simulation which uses a 30 × 30 lattice. Comparing the simulation results shown in Figures 3.2 and 3.5 and Figures 3.4 and 3.6, we find that the roughness and growth rate obtained by averaging six independent kinetic Monte-Carlo simulations, which use a 20 × 20 lattice model, contain less fluctuations than those obtained from a kinetic Monte-Carlo simulation which uses a 30 × 30 lattice model. This demonstrates that, for a fixed computational time, the use of a kinetic Monte-Carlo simulator based on multiple small lattice models would yield growth rate and surface roughness profiles with fewer fluctuations compared to a kinetic Monte-Carlo simulator which uses a

single lattice with larger size.

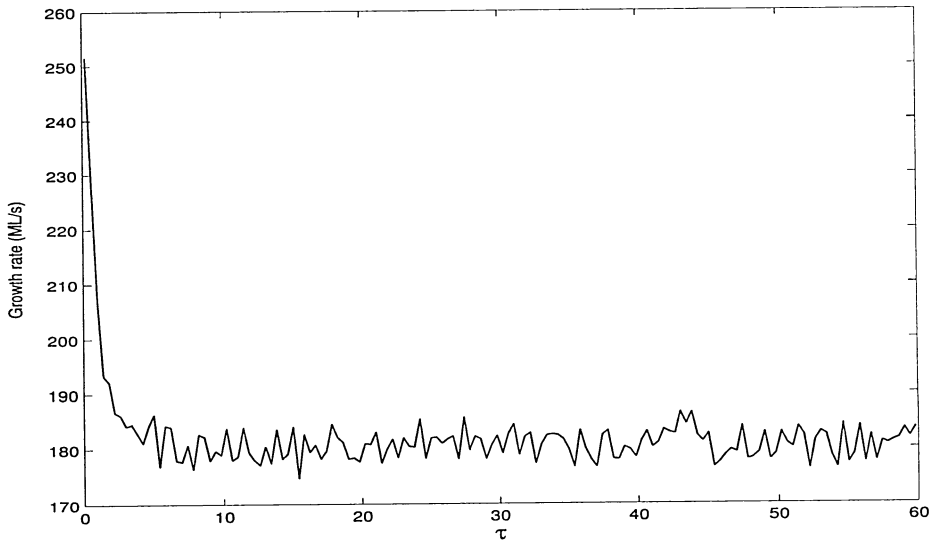

Figure 3.5: Growth rate from a kinetic Monte-Carlo simulation which uses a 30×30 lattice.

The predicted profiles of surface roughness and growth rate, which are obtained from kinetic Monte-Carlo simulation based on multiple small lattice models, still contain stochastic fluctuations and are not robust (due to the open-loop nature of the calculation) with respect to disturbances and variations in process parameters. To alleviate these problems, we follow the approach proposed in Lou and Christofides (2003a) and combine the small lattice kinetic Monte-Carlo simulator with an adaptive filter, to reject the stochastic fluctuations on the surface roughness and growth rate profiles, and a measurement error compensator to improve the estimates of these variables using on-line measurements. We use the same adaptive filter and measurement error compensator structure for both the surface roughness and the growth rate. To simplify the notation of the mathematical formulas, we only present the general structure of the adaptive filter and of the measurement error compensator. Specifically, the adaptive filter is a second-order dynamical system with the following state-space

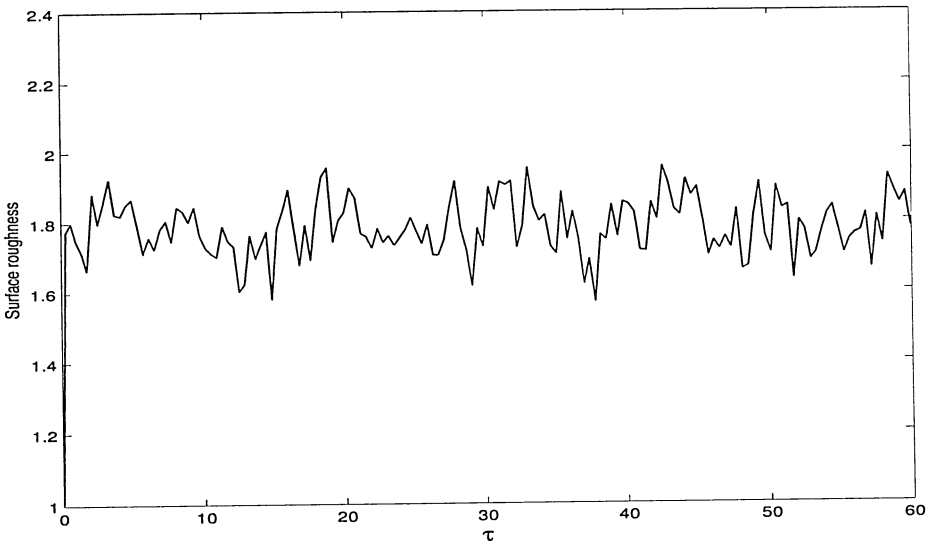

Figure 3.6: Surface roughness from a kinetic Monte-Carlo simulation which uses a 30×30 lattice.

representation:

$$\begin{aligned} \frac{d\hat{y}_r}{d\tau} &= y_1 \\ \frac{dy_1}{d\tau} &= \frac{K}{\tau_I}(y_r - \hat{y}_r) - \frac{1}{\tau_I} y_1 \end{aligned} \tag{3.3}$$

where y_r is the output of the kinetic Monte-Carlo simulation based on multiple small lattice models, $\hat{y}_r$ is the filter output, K is the filter gain and τ_I is the time constant. To accelerate the response of the filter and avoid large overshoot, $\tau_I = 0.5/K$. To achieve both fast tracking of the dynamics of the outputs and efficient noise rejection, the gain of the filter is adaptively adjusted according to the following law:

$$K(\tau) = K_0 \frac{|\int_{\tau-\Delta\tau}^{\tau} y_r(t)dt - \int_{\tau-2\Delta\tau}^{\tau-\Delta\tau} y_r(t)dt|}{\Delta\tau^2} + K_s \tag{3.4}$$

where K_0 is a constant, K_s is the steady state gain for the adaptive filter and $\Delta\tau$ is the dimensionless time interval between two updates of K. Although a better tracking performance is expected when a small $\Delta\tau$ is used, a very small $\Delta\tau$ will introduce the effect of fluctuations on the filter gain and should be avoided.

The measurement error compensator uses the available on-line measurements (in the numerical simulations the values of the surface roughness and growth rate obtained from the large lattice model are used) to produce improved estimates of the surface roughness and growth rate. The state-space representation of the measurement error compensator is:

$$\frac{de}{d\tau} = K_e(y_h(\tau_{m_i}) - \hat{y}(\tau_{m_i})); \quad \tau_{m_i} < \tau \leq \tau_{m_{i+1}}; \qquad i = 1, 2, \cdots \tag{3.5}$$

and the final roughness estimates are computed by:

$$\hat{y} = \hat{y}_r + e \tag{3.6}$$

In the above equations, K_e is the compensator gain, e is the estimated model error, which is used to compensate the model output, $\hat{y}$ is the roughness estimates, $\hat{y}_r$ is the filtered output from a kinetic Monte-Carlo simulator which uses a small lattice and y_h is the output of a kinetic Monte-Carlo simulator which uses the large lattice (in an experimental set-up y_h could be obtained from the measurement sensor). Since the roughness measurements are only available at discrete points in time $\tau_m = [\tau_{m_1}, \tau_{m_2}, \cdots]$, the right-hand side of Eq.3.5 is computed at the time a roughness measurement is available and is kept in this value in the time interval between two available roughness measurements.

The combination of the adaptive filter and the measurement error compensator functions as an estimator, which is capable to accurately predict the evolution of surface roughness and growth rate during the thin film growth by using measurements of the precursor concentration above the substrate. In this work, we assume that measurements of precursor concentration above the substrate are available; when such measurements are not available, a state estimator can be constructed on the basis of the PDE model that describes the gas phase species concentrations and

the temperature to obtain estimates of this quantity (see Christofides, 2001b, for estimator design methods for PDE systems). Figures 3.7 and 3.8 show the growth rate and surface roughness profiles computed by the estimator, which uses a kinetic Monte-Carlo simulator based on six 20×20 lattice models (solid lines); they are compared with the growth rate and surface roughness profiles obtained from a kinetic Monte-Carlo simulator which uses a 120×120 lattice model. The results clearly show that the developed estimator can accurately predict the evolution of growth rate and surface roughness. Note also that the developed estimator can be used for real-time feedback control since, the computational time needed to run kinetic Monte-Carlo simulation based on six 20×20 lattice models is comparable to the real-time process evolution.

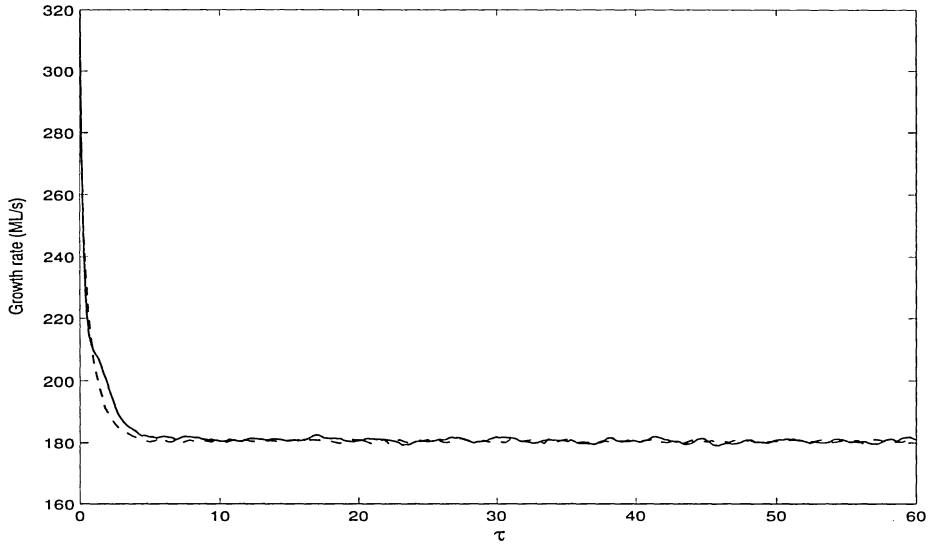

Figure 3.7: Growth rate profiles from the estimator (solid line) and from a kinetic Monte-Carlo simulation which uses a 120×120 lattice model (dashed line).

Remark 3.1 *Referring to the selection of the lattice size, it is important to point out that while kinetic Monte-Carlo simulation based on multiple* 20×20 *lattice models can adequately capture the evolution of surface roughness and growth rate in the specific*

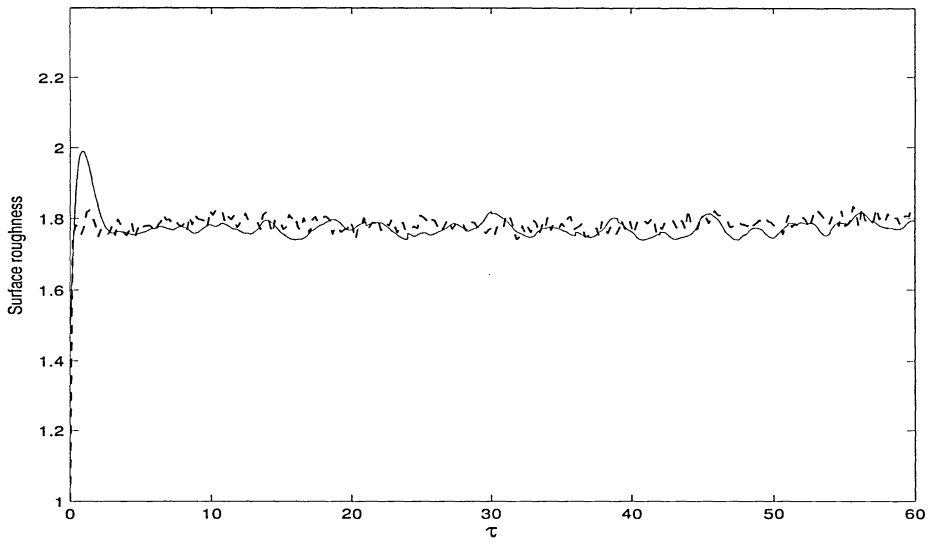

Figure 3.8: Surface roughness profiles from the estimator (solid line) and from a kinetic Monte-Carlo simulation which uses a 120×120 lattice model (dashed line).

thin film growth problem under consideration, the dimension of the small lattice in general should be chosen so that the interactions between the surface atoms are adequately captured, and also that it is large enough to describe all the spatio-temporal phenomena occurring on the surface (e.g., cluster formation). Furthermore, the small lattice should be chosen to provide accurate estimates of the desired properties to be controlled. For example in the case of surface roughness, this quantity is defined as the average number of broken bonds for every surface atoms and the microscopic unit involved is an individual atom. When a 20×20 *small lattice is used, the computation of surface roughness involves hundreds of surface atoms, which is adequate to obtain the expected value. However, when the property of interest is, for example, step density, a larger lattice is needed to obtain a convergent average value from the kinetic Monte-Carlo simulation. At this point, it is important to note that the proposed reduction of lattice size can be viewed as alternative (and quite intuitive) way to perform order reduction of the master equation (see Gallivan and Murray, 2003, for reduction approaches based directly on the master equation). In this work, when*

the surface roughness and growth rate are considered in the process with parameters shown in Table 3.1, we found out that an 80×80 *lattice is sufficient to capture the evolution of the process and that further increase of the lattice size leads to no observable improvement in the accuracy of the simulation results; this is shown in Figures 3.9 and 3.10, which show comparisons of surface roughness profiles and growth rate profiles from a kinetic Monte-Carlo simulator which uses an* 80×80 *lattice and those from a kinetic Monte-Carlo simulator which uses a* 120×120 *lattice. Therefore, in the remainder of this work, we use a kinetic Monte-Carlo simulator which uses an* 80×80 *lattice to describe the evolution of the thin film growth under open-loop and closed-loop conditions.*

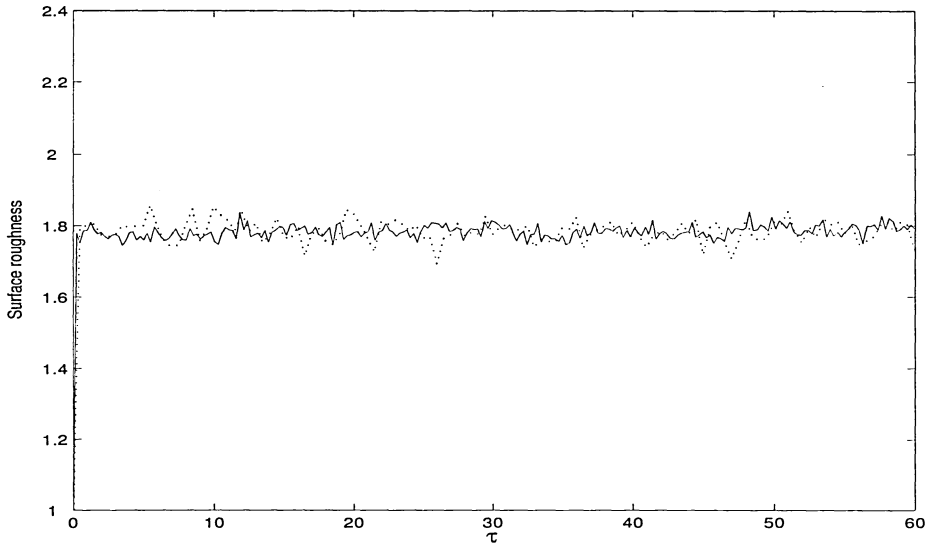

Figure 3.9: Comparison of the surface roughness profiles from a kinetic Monte-Carlo simulator which uses an 80×80 lattice (dotted) and that from a kinetic Monte-Carlo simulator which uses a 120×120 lattice (solid).

Remark 3.2 *We note that the surface roughness during the formation of a single monolayer slightly fluctuates around the surface roughness value of the completely formed monolayer. This can be observed in Figure 3.11, which shows the evolution of surface roughness during the formation of the first 10 layers in the deposition from*

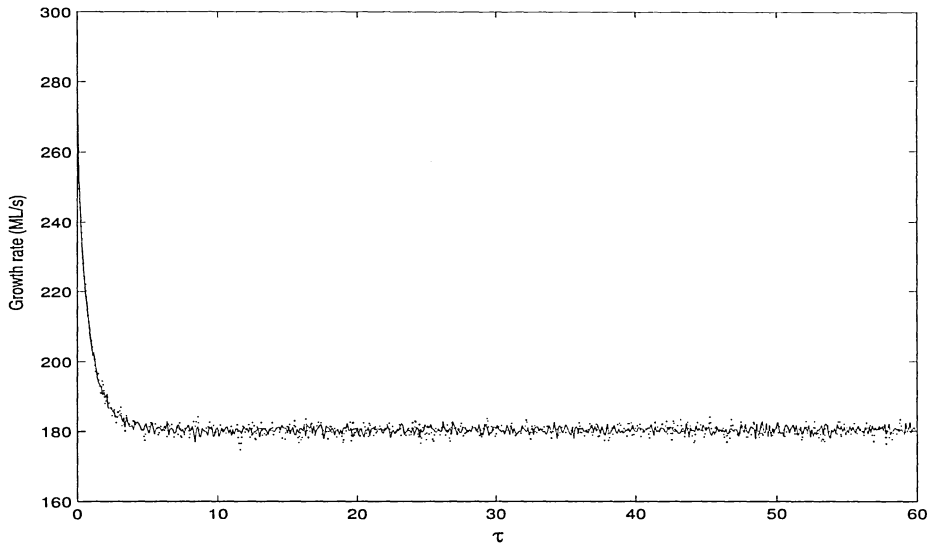

Figure 3.10: Comparison of the growth rate profiles from a kinetic Monte-Carlo simulator which uses an 80×80 lattice (dotted) and that from a kinetic Monte-Carlo simulator which uses a 120×120 lattice (solid).

a kinetic Monte-Carlo simulator using an 80×80 *lattice. However, this fluctuation is very small and does not influence the performance of the feedback control system. The same comment also applies to the evolution of the growth rate; Figure 3.12 shows the evolution of the growth rate during the formation of the first 200 layers from the same kinetic Monte-Carlo simulation.*

Remark 3.3 *It is important to note that because available techniques for real-time measurement of film properties (e.g., surface roughness) do not provide measurements at a large enough frequency to fully capture the film growth dynamics, the use of a roughness estimator within a feedback control scheme is needed to predict growth behavior at time instants in which on-line measurements are not available. In a recent study (Lou and Christofides, 2003a), we showed that feedback control which exclusively relies on infrequent on-line measurements leads to poor closed-loop performance (no matter the tuning of the controller) compared to feedback control which employs our estimator to compute roughness estimates.*

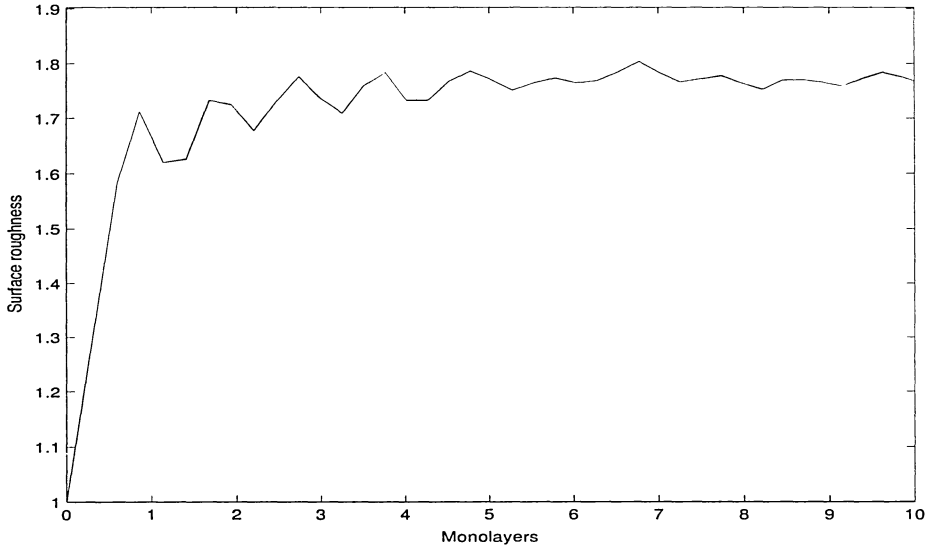

Figure 3.11: Evolution of the surface roughness during the formation of the first 10 monolayers.

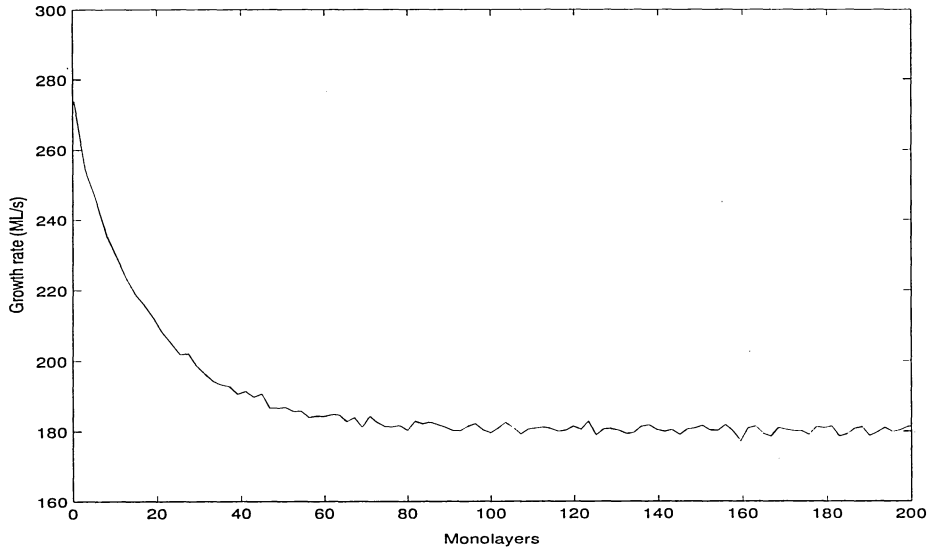

Figure 3.12: Evolution of the growth rate during the formation of the first 200 monolayers.

3.4 Feedback control of surface roughness and growth rate

The efficient production of high-quality thin films requires that the surface roughness and growth rate are maintained at desired levels. Therefore, the objective of this section is to study the nature of the multivariable control problem and to develop a systematic method for the design of a multivariable feedback control system, which can be implemented in real-time. The feedback control system makes use of the developed estimator which provides a computationally feasible approach to predict the growth rate and surface roughness of the thin film in real-time. Given the set of available manipulated inputs and the desired control objectives, the control problem is formulated as the one of regulating the surface roughness and growth rate by manipulating the substrate temperature and precursor mole fraction in inlet gases.

We will begin with a study of the feasibility of the control problem formulation, continue with an analysis and evaluation of the effect of input/output interactions on closed-loop performance, and close with the design and evaluation of the multivariable feedback control structure.

3.4.1 Feasibility of the control problem formulation

In this subsection, we establish that it is feasible to control surface roughness and growth rate by manipulating the substrate temperature and precursor mole fraction in inlet gases. To this end, we perform the following set of closed-loop simulations: 1) the growth rate is controlled by manipulating the precursor mole fraction in the inlet gas while the substrate temperature is kept constant, and 2) the surface roughness is controlled by manipulating the substrate temperature while the inlet precursor mole fraction is kept constant. The process parameters used in the simulations are shown in Table 3.1. In our calculations, since the precursor mole fraction is very small, we

assume that the chamber pressure is independent of the precursor mole fraction. In each simulation, a controller/estimator structure of the type shown in Figure 3.13 is used to control the process. In this structure, the estimator, which includes multiple kinetic Monte-Carlo simulators using small lattice models, an adaptive filter and a measurement error compensator, is used to provide estimates of the controlled variable (surface roughness or growth rate) in a time-scale comparable to the real-time evolution of the process. The estimates are used in the controller to determine the control action. Since the models that describe the evolution of surface roughness and growth rate are not available in closed form, a proportional integral controller is used to compute the control action:

$$u(\tau) = K_c[(y_{set} - \hat{y}) + \frac{1}{\tau_c}\int_0^{\tau}(y_{set} - \hat{y})dt] \tag{3.7}$$

where y_{set} is the set-point of the output, $\hat{y}$ is the output of the estimator, K_c is the proportional gain and τ_c is the integral time constant.

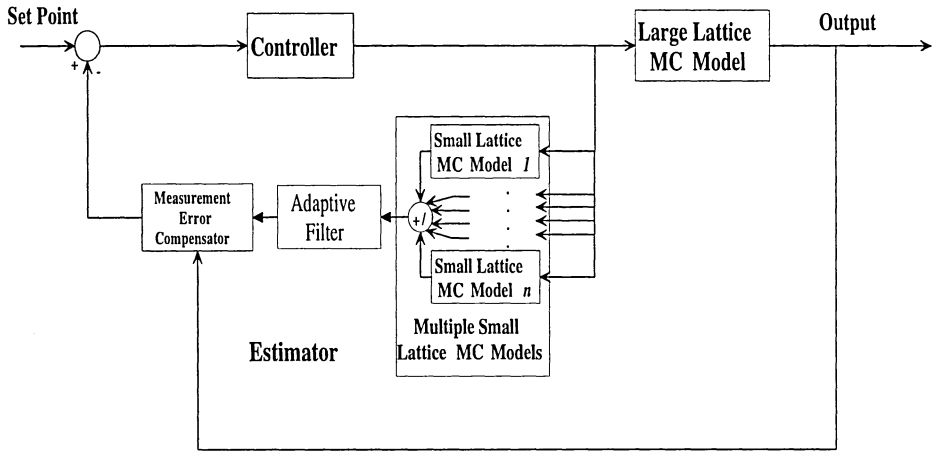

Figure 3.13: Diagram of the estimator/controller structure using a kinetic Monte-Carlo simulator based on multiple small lattice models.

In the case of controlling the growth rate, the size of the small lattice is 20×20 and the outputs of six small lattice kinetic Monte-Carlo simulators are averaged within

the estimator. A kinetic Monte-Carlo simulator based on an 80×80 lattice model is used to describe the evolution of the process. The time interval between two available measurements is taken to be $0.3s$, which is consistent with available techniques that can be used to measure growth rate in real-time (Pickering, 2001). The substrate temperature is kept constant at $800K$ and the initial inlet precursor mole fraction is 2.0×10^{-5}; these values correspond to a growth rate of about $180ML/s$. The desired set-point value for the growth rate is $220ML/s$. The parameters for the growth rate estimator and the PI controller used in this simulation are shown in Table 3.2. Figures 3.14 and 3.15 show the growth rate and the inlet precursor mole fraction under feedback control. The results clearly show that the growth rate can be successfully controlled to the desired set-point by manipulating the precursor mole fraction.

Table 3.2: Growth rate estimator and controller parameters.

K_0	K_s	K_e	K_c	τ_c
0.5	1.0	0.08	2.0×10^{-9}	0.4

In the second simulation run, the surface roughness is controlled by manipulating the substrate temperature while the inlet precursor mole fraction is kept constant. Figures 3.16 and 3.17 show the profiles of the surface roughness and substrate temperature in the closed-loop system. A kinetic Monte-Carlo simulator which uses an 80×80 lattice model is used to describe the evolution of the process. The inlet precursor mole fraction is kept constant at 2.0×10^{-5} and the substrate temperature is initially $800K$. The desired set-point value of surface roughness is 1.5. The parameters for the roughness estimator and controller are shown in Table 3.3. The controller successfully drives the surface roughness to the set-point by manipulating the substrate temperature.

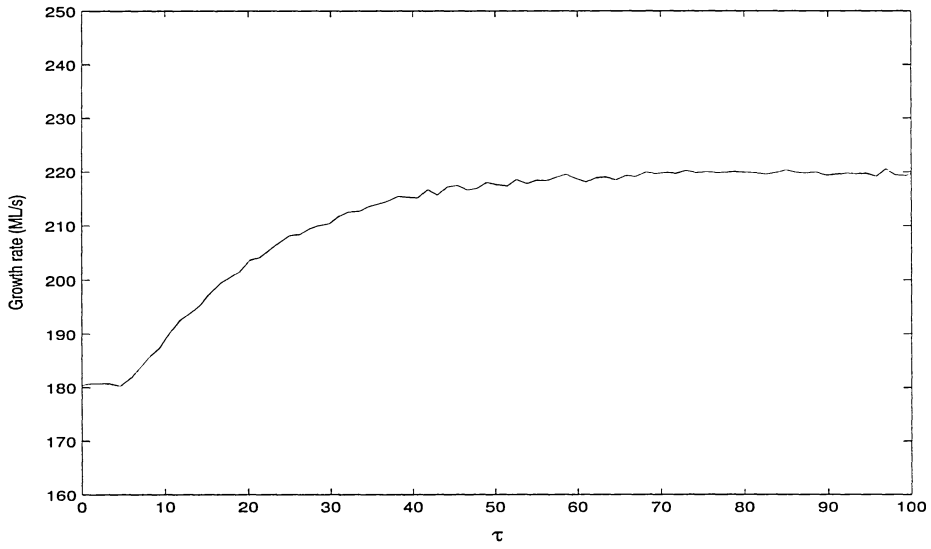

Figure 3.14: Closed-loop growth rate under single-loop feedback control using the estimator/controller structure of Figure 3.13.

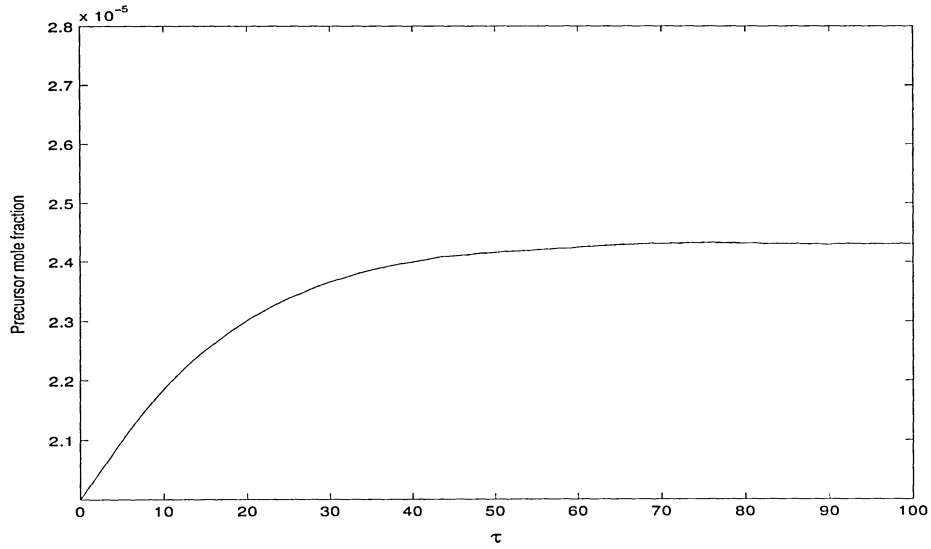

Figure 3.15: Inlet precursor mole fraction under single-loop feedback control using the estimator/controller structure of Figure 3.13.

Table 3.3: Roughness estimator and controller parameters.

K_0	K_s	K_e	K_c	τ_c
0.5	1.0	0.08	−15	0.3

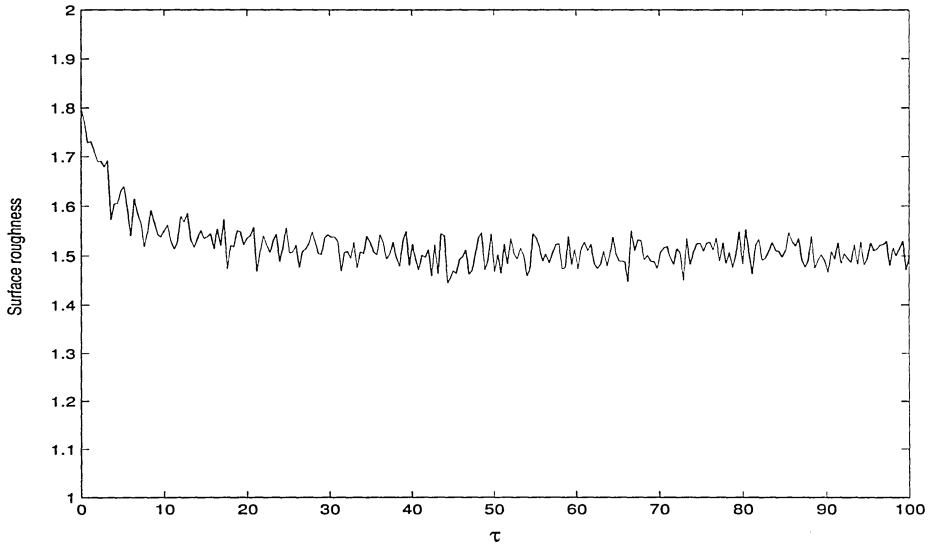

Figure 3.16: Closed-loop surface roughness under single-loop feedback control using the estimator/controller structure of Figure 3.13.

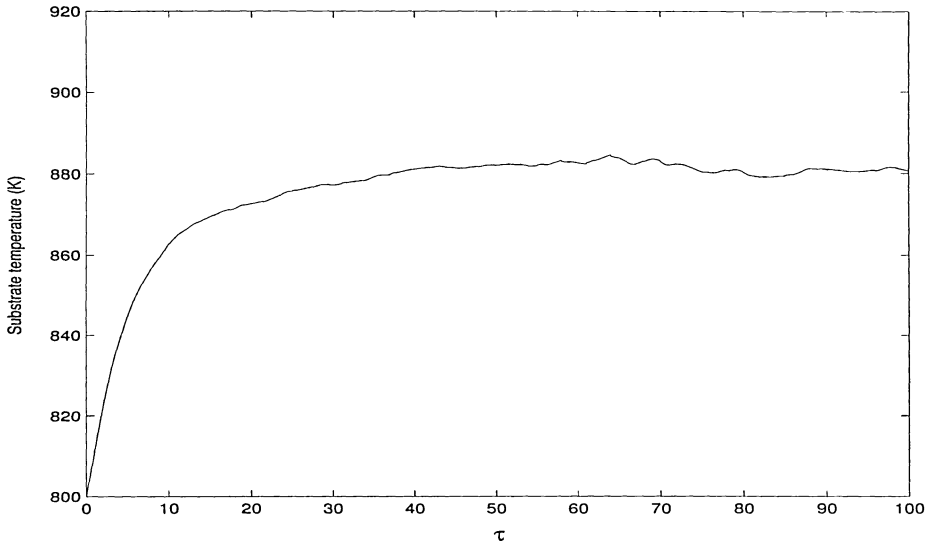

Figure 3.17: Substrate temperature under single-loop feedback control using the estimator/controller structure of Figure 3.13.

3.4.2 Effect of multivariable input/output interactions

The objective of this subsection is to understand the influence of multivariable input/output interactions on closed-loop performance and determine whether there is a need for the design and implementation of a multivariable controller which compensates for the effect of such interactions. To this end, we consider the problem of simultaneous regulation of the growth rate and of the surface roughness and use a feedback control system that comprises of the estimator and two $single - loop$ proportional integral controllers. Specifically, following up on the results of the previous subsection, the input/ouput pairs are substrate temperature (T) - surface roughness (r) and inlet precursor mole fraction (y) - growth rate (gr).

A closed-loop system simulation is carried out to evaluate this approach to simultaneous control of growth rate and surface roughness. In this simulation, the outputs from six kinetic Monte-Carlo simulators running on 20×20 lattice models are aver-

aged within the estimator. A kinetic Monte-Carlo simulator which uses an 80×80 lattice model is used to describe the evolution of the process. The parameters for the estimator and the controllers are those listed in Tables 3.2 and 3.3.

Figures 3.18 and 3.19 show the surface roughness and substrate temperature. Comparing Figures 3.16 and 3.18, we find very similar roughness profiles, which means that multivariable input/output interactions do not influence the profile of the surface roughness under single-loop control.

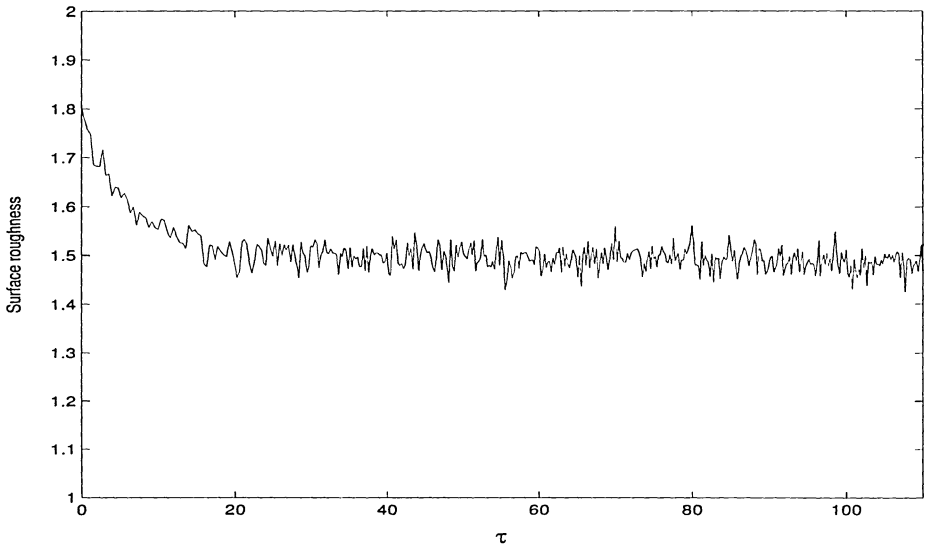

Figure 3.18: Closed-loop surface roughness under feedback control which does not account for multivariable input/output interactions.

Figures 3.20 and 3.21 show the profiles of the growth rate and inlet precursor mole fraction for the same simulation run. It is clear that the control system successfully drives the growth rate to the desired set-point values. However, the transient response of the growth rate in the case of simultaneous growth rate and surface roughness control is slower compared to the case where the growth rate is the only controlled output and the structure of Figure 3.13 is used (Figure 3.22).

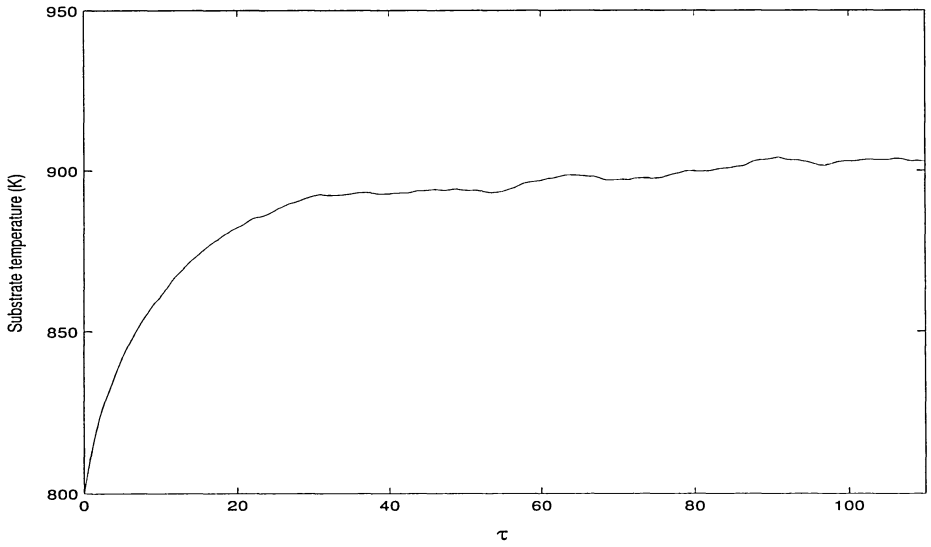

Figure 3.19: Substrate temperature using feedback control which does not account for multivariable input/output interactions.

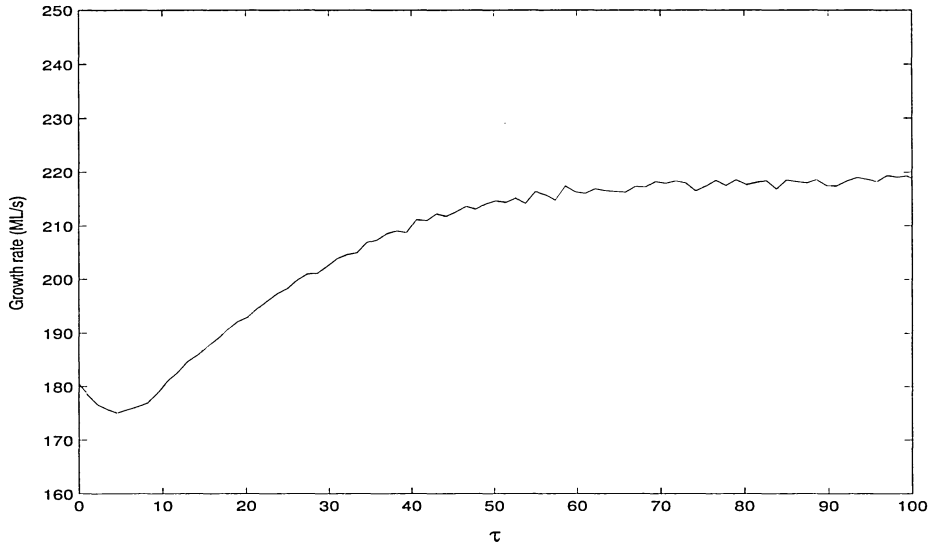

Figure 3.20: Closed-loop growth rate under feedback control which does not account for multivariable input/output interactions.

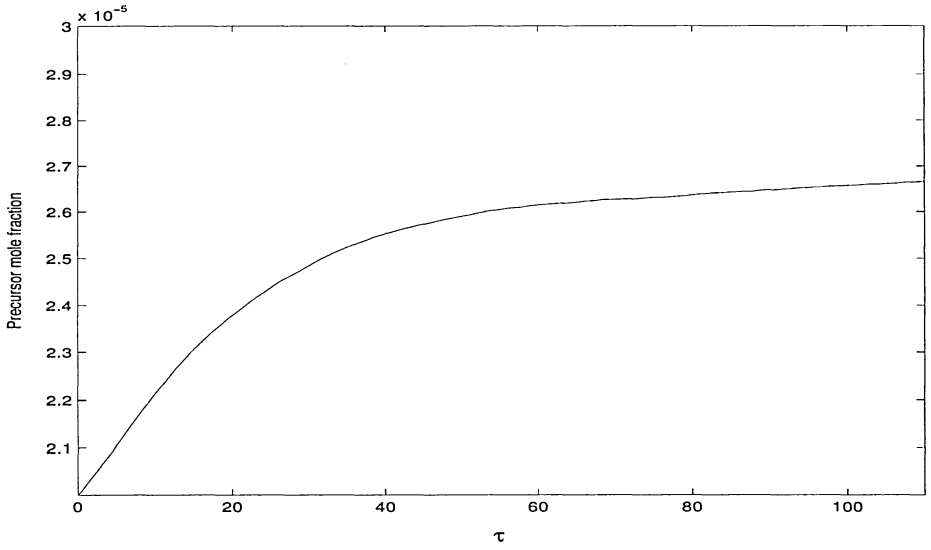

Figure 3.21: Precursor mole fraction using feedback control which does not account for multivariable input/output interactions.

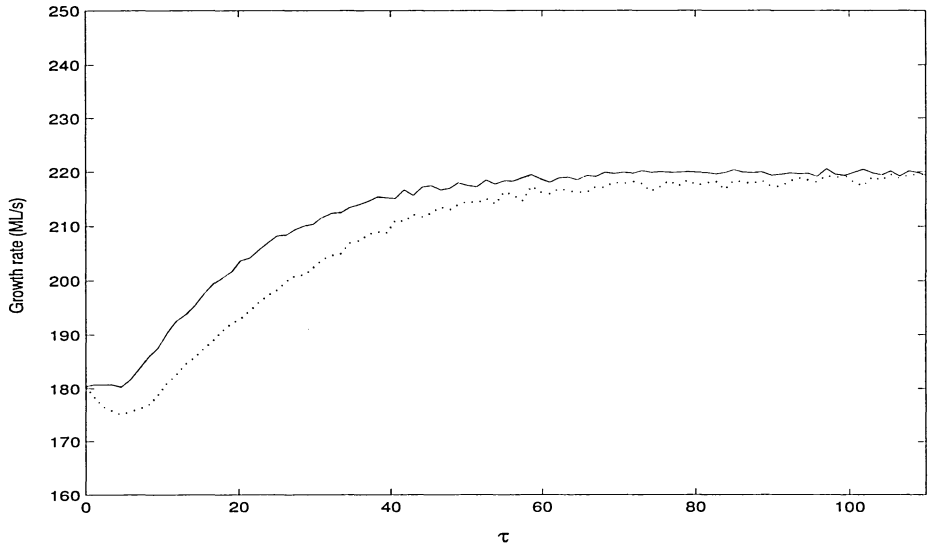

Figure 3.22: Comparison of closed-loop growth rate profiles a) growth rate is the only controlled output and the structure of Figure 3.13 is used (solid line), b) simultaneous regulation of growth rate and surface roughness is considered and feedback control which does not account for multivariable input/output interactions is used (dotted line).

The reason for the slower transient response of the growth rate is the effect of multivariable input/ouput interactions (i.e., the influence of the variation of substrate temperature on growth rate and the influence of the variation of inlet precursor mole fraction on surface roughness in the closed-loop system); these interactions need to be compensated for in order to speed up the growth rate response and improve closed-loop performance.

3.4.3 Multivariable feedback control structure

This subsection focuses on the design and evaluation of a multivariable feedback control structure. To this end, we need to understand and model the interactions between inputs and outputs; two simulations are carried out to observe the changes of the surface roughness and growth rate for: 1) a step change on substrate temperature with constant inlet precursor mole fraction, and 2) a step change on inlet precursor mole fractions with constant substrate temperature.

Figure 3.23 shows the growth rate and surface roughness when the substrate temperature is kept at $800K$ and the inlet precursor mole fraction changes form 2.0×10^{-5} to 2.1×10^{-5} at $\tau = 10$. The results show that the growth rate increases from around $180ML/s$ to $19ML/s$, but there is no observable change in the surface roughness, which means the change of the inlet precursor mole fraction has very little influence on the surface roughness.

The interactions between the substrate temperature and the surface roughness and growth rate are studied by keeping the inlet precursor mole fraction at 2.0×10^{-5} and increasing the substrate temperature from $800K$ to $840K$ at $\tau = 10$. Figure 3.24 shows the responses of growth rate and surface roughness to the substrate temperature change. The simulation results show that the growth rate drops from approximately

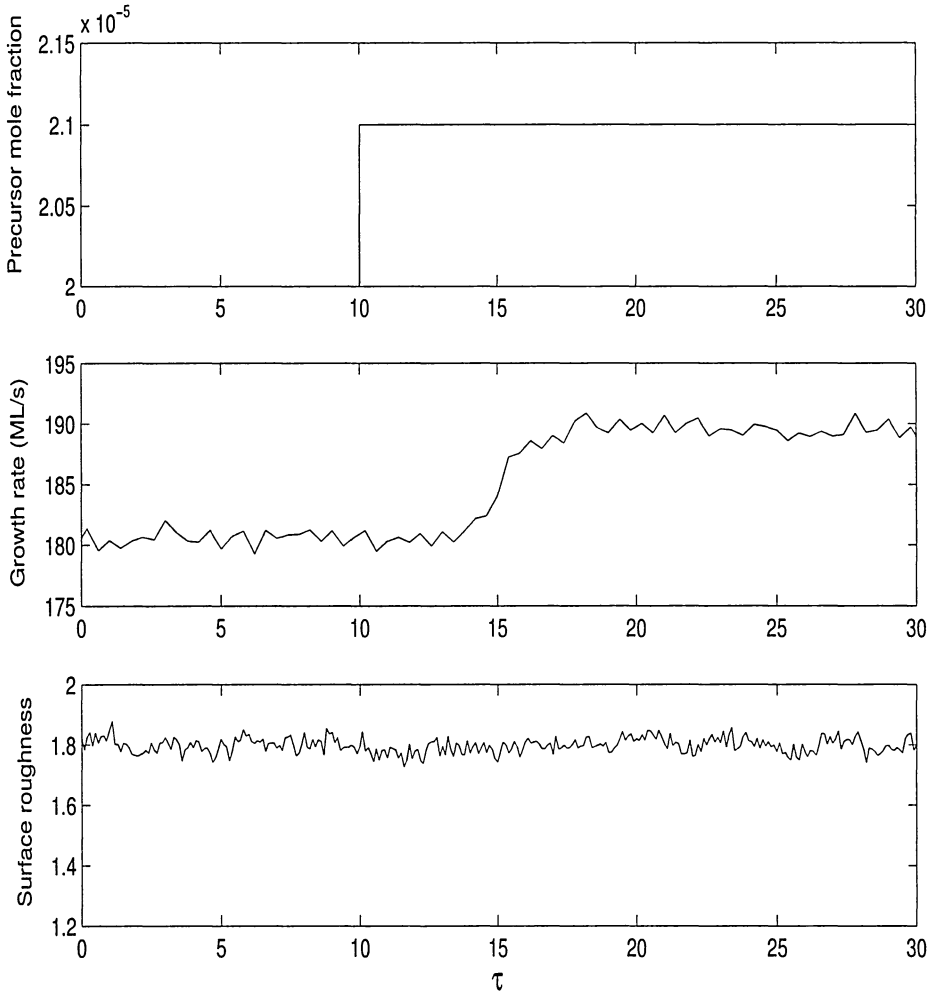

Figure 3.23: Growth rate (middle plot) and surface roughness (bottom plot) profiles for a step change in inlet precursor mole fraction (top plot) from 2.0×10^{-5} to 2.1×10^{-5} - substrate temperature is kept at $800K$.

$180ML/s$ to $175ML/s$ and the roughness drops from approximately 1.8 to 1.6; which indicates that variations on the substrate temperature influence both surface roughness and growth rate. It should be pointed out that this specific coupling pattern is valid only under the specific growth conditions used in this simulation.

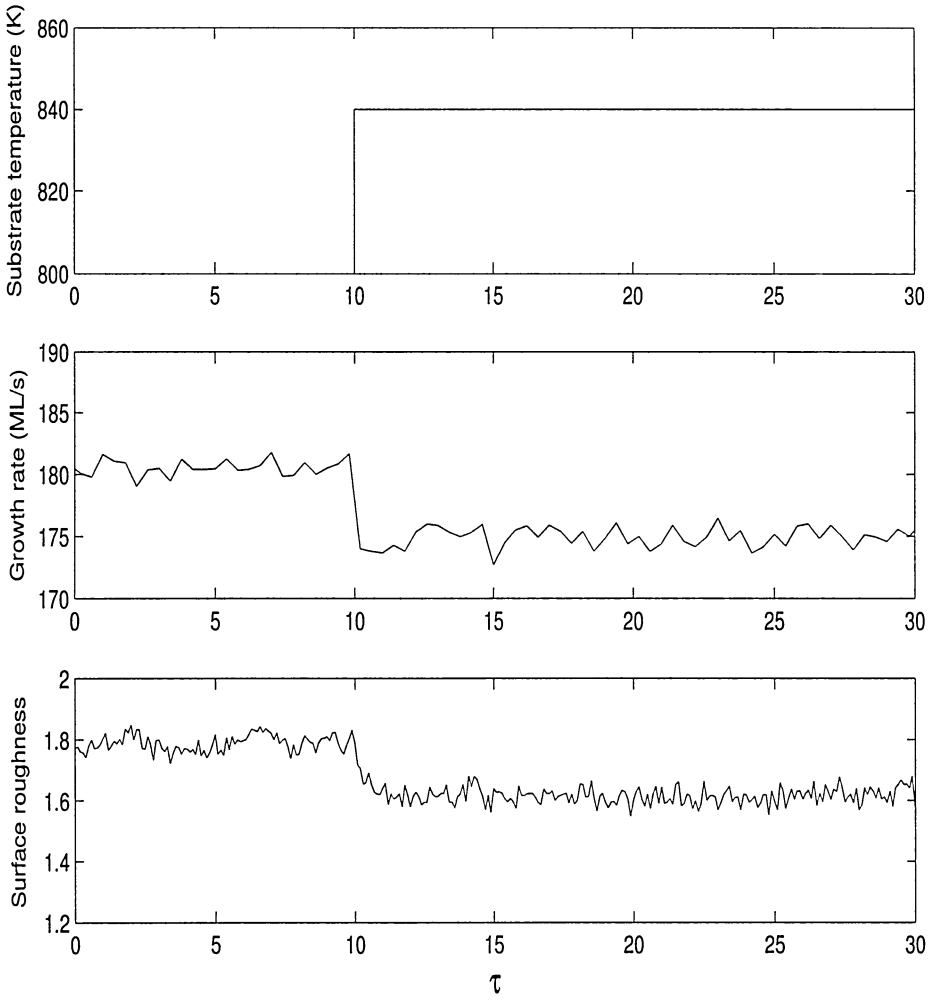

Figure 3.24: Growth rate (middle plot) and surface roughness (bottom plot) with a step change in substrate temperature (top plot) from $800K$ to $840K$ - inlet precursor mole fraction is 2.0×10^{-5}.

To improve the closed-loop performance, a multivariable feedback control struc-

ture is developed, which explicitly compensates for the effect of the multivariable interactions occurring in the process. The controller structure is obtained by introducing a compensation block between the multiple single-loop controllers and the process. Because the interactions between inlet precursor mole fraction and surface roughness are not significant (as shown in Figure 3.23 - bottom plot), only one compensator is needed in this example. A diagram of the multivariable control system using the estimator/controller structure with interaction compensation is shown in Figure 3.25. $G_1(s)$ is the transfer function between the substrate temperature and the growth rate and $G_2(s)$ is the transfer function between the inlet precursor mole fraction and the growth rate. Step tests are used to identify the expression and parameters of $G_1(s)$ and $G_2(s)$. Specifically, based on the simulation results shown in Figures 3.23 (middle plot) and Figure 3.24 (middle plot), G_1 and G_2 are taken to be constants with the following values $G_1(s) = 0.125$ and $G_2(s) = 1.0 \times 10^7$. The rest of the process and controller parameters used in the simulation are the same to those shown in Tables 3.2 and 3.3.

A closed-loop system simulation is performed to evaluate the effectiveness of the multivariable estimator/control structure with interaction compensation shown in Figure 3.25. The size of the small lattice is 20×20 and the outputs from six kinetic Monte-Carlo simulators based on 20×20 lattice models are averaged within the estimator. A kinetic Monte-Carlo simulator based on an 80×80 lattice model is used to describe the evolution of the process. The roughness set-point value is 1.5 and the growth rate set-point value is $220ML/s$. Initially, the substrate temperature is $T = 800K$ and the inlet precursor mole fraction is 2.0×10^{-5}; these conditions correspond to a growth rate of about $180ML/s$ and a surface roughness of about 1.8. The proposed multivariable control system (Figure 3.25) is applied to the process to regulate the

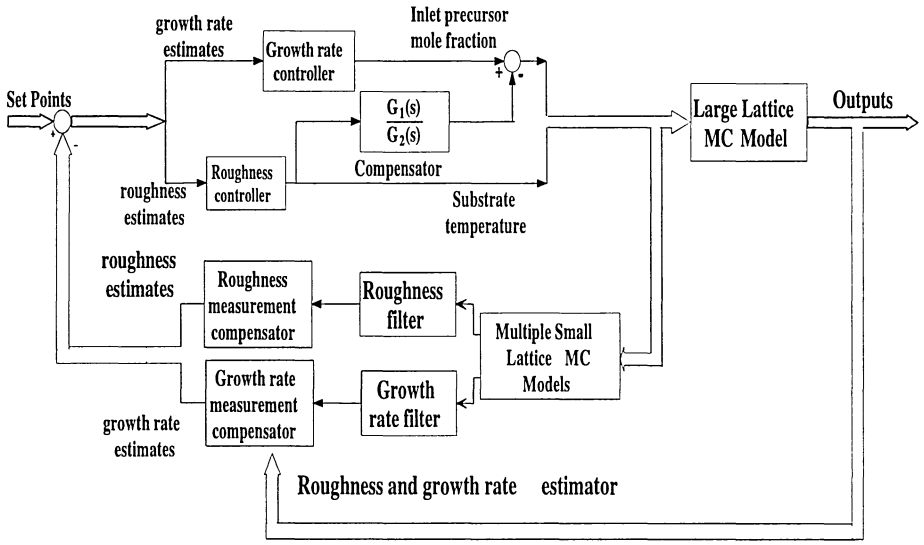

Figure 3.25: Diagram of multivariable feedback control system with interaction compensation.

growth rate and surface roughness to the desired set-point values. Figure 3.26 shows the comparison of the growth rate profiles under multivariable feedback control with interaction compensation and under multiple single-loop control without interaction compensation. By using the interaction compensator, the growth rate converges to the desired set-point value faster. Figure 3.27 shows the comparison of the inlet precursor mole fraction under multivariable control with interaction compensation and that obtained under multiple single-loop control. Figures 3.28 and 3.29 show the surface roughness under multivariable control with interaction compensation and the profile of the substrate temperature, respectively. The microstructure of the thin film at the beginning and at the end of the closed-loop system simulation run is shown in Figure 3.30 and Figure 3.31, respectively. These results show that the proposed multivariable control system with interaction compensation can simultaneously drive the growth rate and surface roughness to the desired set-point values and improve closed-loop response.

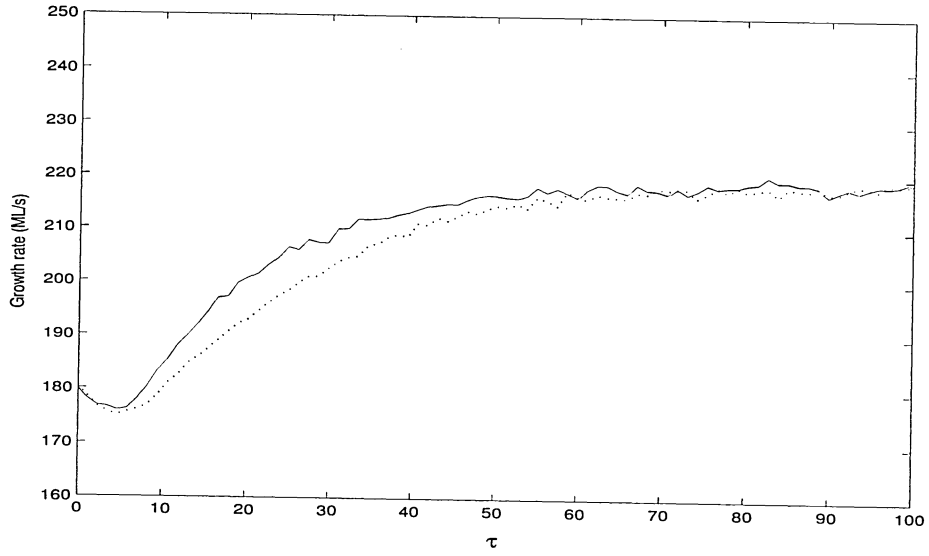

Figure 3.26: Comparison of the closed-loop growth rate under multivariable feedback control with interaction compensation (solid line) and under multiple single-loop control (dashed line).

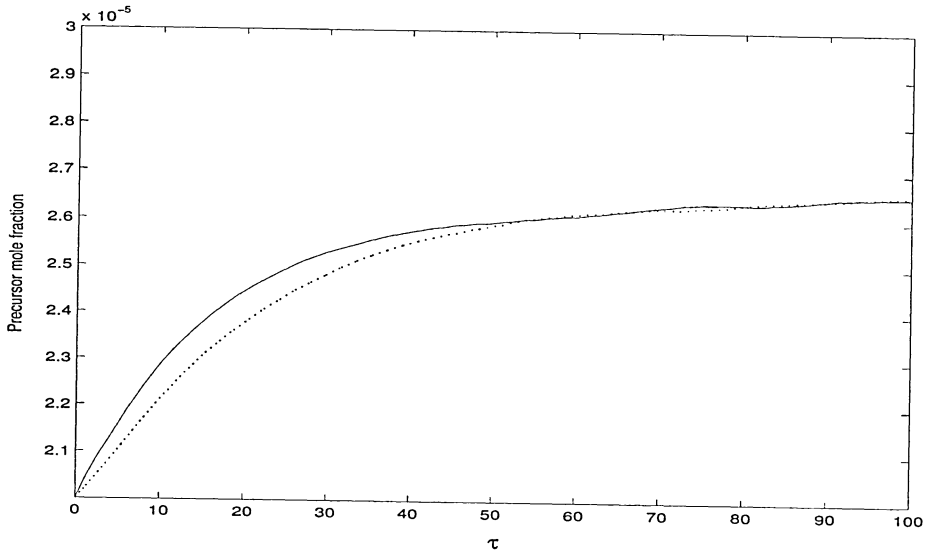

Figure 3.27: Comparison of inlet precursor mole fraction under multivariable feedback control with interaction compensation (solid line) and under multiple single-loop control (dashed line).

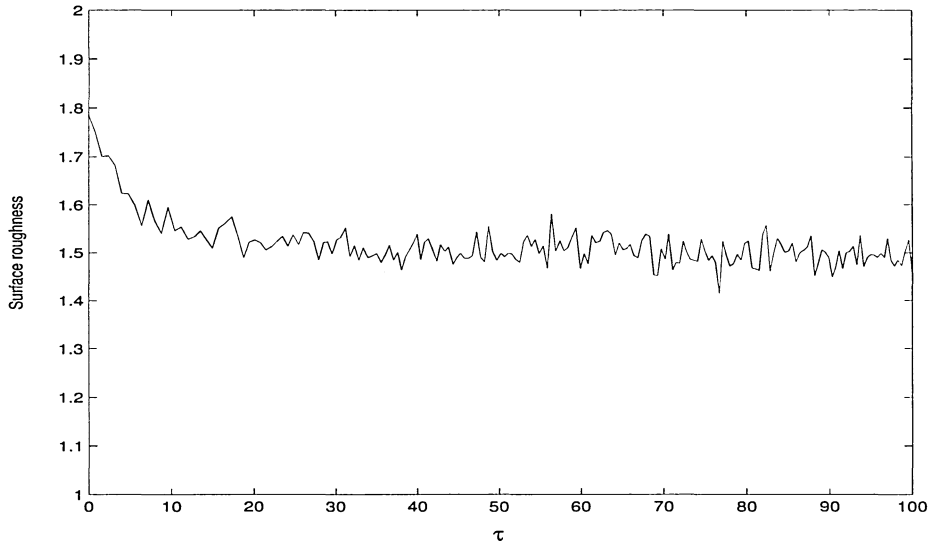

Figure 3.28: Closed-loop surface roughness under multivariable feedback control with interaction compensation.

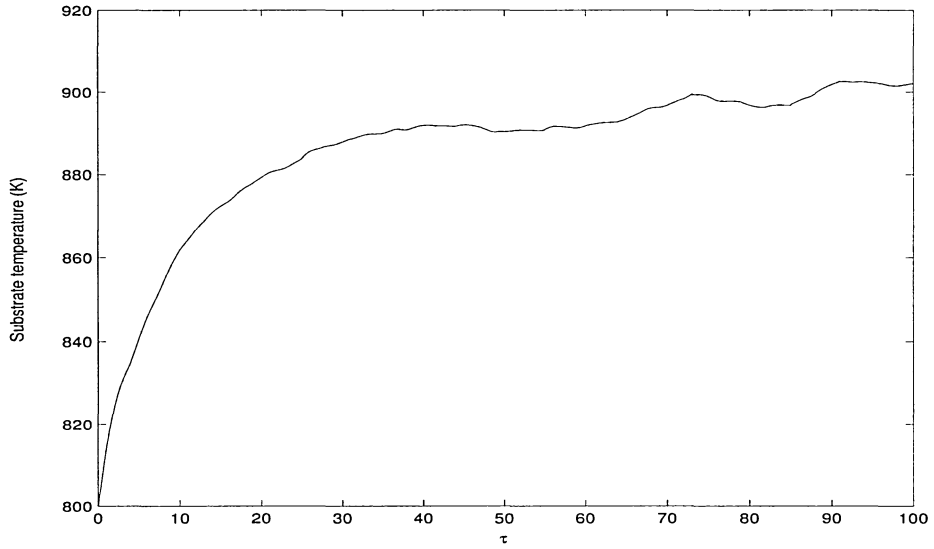

Figure 3.29: Substrate temperature under multivariable feedback control with interaction compensation.

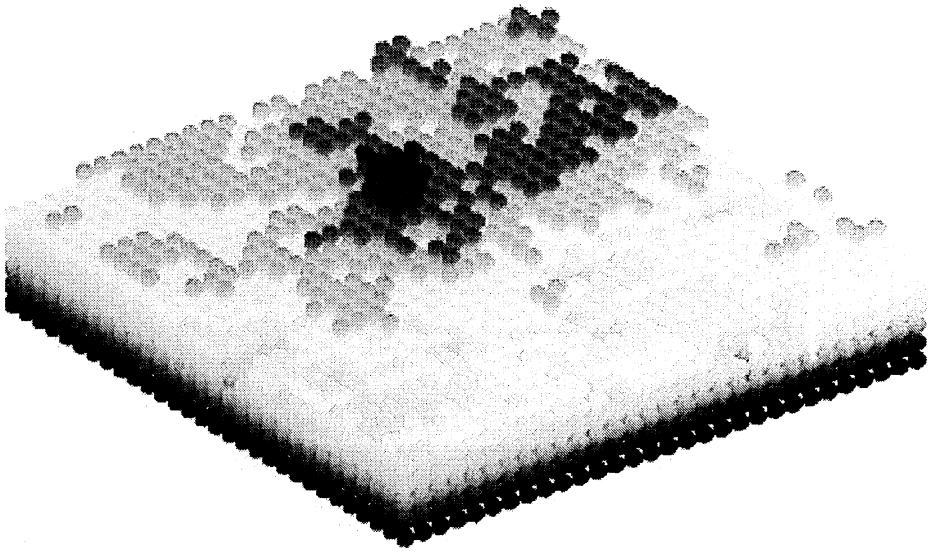

Figure 3.30: Surface micro-configuration at the beginning of the closed-loop simulation run (roughness=1.8).

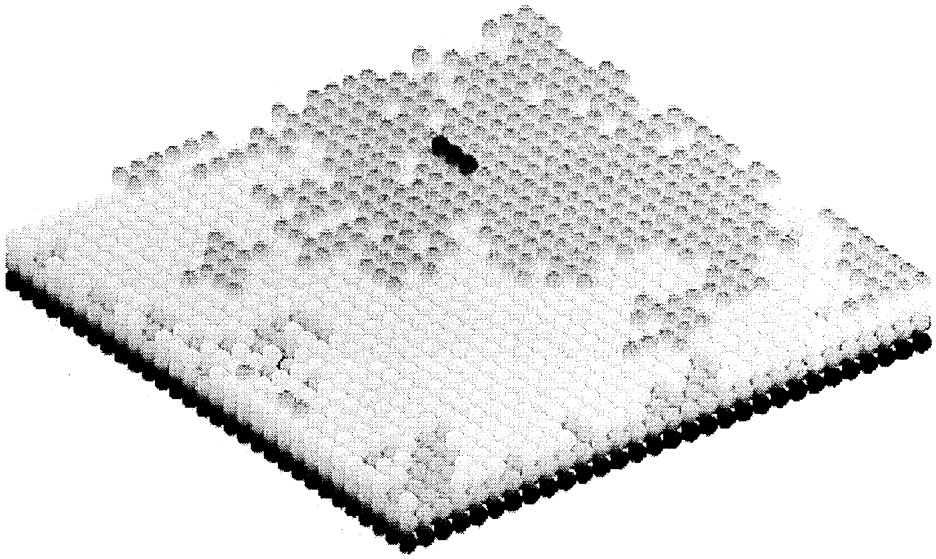

Figure 3.31: Surface micro-configuration at the end of the closed-loop simulation run (roughness=1.5) under multivariable feedback control with interaction compensation.

3.5 Conclusions

This chapter focused on multivariable feedback control of surface roughness and growth rate in thin film growth. The multivariable control problem was studied and a multivariable feedback control system, which can be implemented in real-time, was proposed. The proposed control system uses an estimator that provides estimates of the surface roughness and growth rate at a time-scale comparable to the real-time evolution of the process, a multivariable interaction compensation block and two proportional-integral feedback controllers. The control system was applied to the multiscale process model and was found to successfully regulate the surface roughness and growth rate to the desired set-point values. While the proposed method for estimation/control using kinetic Monte-Carlo simulators was applied to the process of thin film growth in a stagnation flow geometry, the methodological approach of this work is applicable to other thin film growth processes.

Chapter 4

Feedback Control of Surface Roughness of $GaAs$ (001) Thin Films Using Kinetic Monte-Carlo Models

4.1 Introduction

Gallium arsenide ($GaAs$) is an important compound semiconductor that has many applications including light-emitting diodes, microwave devices, broadband communications, and space solar cells (Fu et al., 2000). The $GaAs$ thin films can be deposited by either molecular-beam epitaxy (MBE) (e.g., Vanhove et al., 1983) or metal-organic chemical vapor deposition (MOCVD) (e.g., Tirtowidjojo and Pollard, 1988; Law et al., 2000). Extensive experiment has been done to study the surface roughness of $GaAs$ thin films under different deposition conditions using reflection high-energy electron diffraction (RHEED) (e.g., Shitara et al., 1992b,a), scanning tunnelling microscopy (STM) (e.g., Law et al., 2000; Kasu and Kobayashi, 1997) and atomic force microscopy

(AFM) (e.g., Tejedor et al., 1999).

Extensive research has been also carried out to study the $GaAs$ thin film growth by using kinetic Monte-Carlo simulations. Monte-Carlo simulation for $GaAs$ thin film growth by MBE was first performed by Shitara et al. (1992b,a). In this study, the authors explicitly modelled the adsorption onto the surface and migration of Ga atoms because these rate-limiting steps determine film growth and microstructure. The effects of all other surface processes (As-related surface processes and surface reconstruction) were incorporated into the model by computing an "effective" energy barrier to Ga surface migration rate based on experimental results. A more detailed kinetic Monte-Carlo model (which considers the kinetics of both Ga and As atoms) was recently developed by Ishii and Kawamura (1999). Furthermore, a theoretical investigation of the adsorption and migration on $GaAs$ surface using density functional theory was performed in Shiraishi (1996). By using Monte-Carlo models to simulate the formation of $GaAs$ thin films, phenomena such as atomic nucleation, growth, island formation and structural transformation can be studied (e.g., Ito and Shiraishi, 1996; Meng and Weinberg, 1996; Itoh et al., 2000; Shiraishi, 2001).

In this chapter, we follow the methodology presented in Chapter 2 to study estimation and control of surface roughness of $GaAs$ (001) thin films during deposition in a horizontal-flow quartz reactor using triisobutylgallium ($TIBGa$) and tertiarybutylarsine ($TBAs$) as precursors and H_2 as the carrier gas. The adsorption of $TIBGa$ onto the surface and the migration of Ga atoms on the surface are considered as the two rate-limiting steps in the film growth and are explicitly modelled within a kinetic Monte-Carlo simulation framework. The energy barrier and the pre-exponential factor of the migration rate of Ga atoms on the surface used in the simulations are initially determined by fitting the simulation results to the experimental data re-

ported by Law et al. (2000). Then, a roughness estimator is constructed that allows computing estimates of the surface roughness of the $GaAs$ thin films at a time-scale comparable to the real-time evolution of the process using discrete on-line roughness measurements. The estimator involves a kinetic Monte-Carlo simulator based on multiple small-lattice models, an adaptive filter used to reduce roughness stochastic fluctuations and an error compensator used to reduce the error between the roughness estimates and the roughness measurements. The roughness estimates are fed to a proportional-integral (PI) feedback controller which is used to control the surface roughness to a desired level by manipulating the substrate temperature. Application of the proposed estimator/controller structure to the process model based on a large-lattice kinetic Monte-Carlo simulator demonstrates successful regulation of the surface roughness to the desired level. The proposed approach is shown to be superior to PI control with direct use of the discrete roughness measurements. The reason is that the available measurement techniques do not provide measurements at a frequency that is comparable to the time constant of the dominant film growth process dynamics.

4.2 Surface micro-structure model for GaAs thin film growth

We use the Monte-Carlo model presented in Shitara et al. (1992a) to model the surface micro-processes during the growth of $GaAs$ thin films. Although the $GaAs$ thin film is a two-component film, the simulation only considers the adsorption and migration of Ga atoms because in an As-rich environment (which is the case for the process considered in this work), As-related kinetics are not rate-limiting and can be incorporated into the model by using an "effective" energy barrier to model the surface migration rate of Ga atoms. We note that the Monte-Carlo model in

Shitara et al. (1992a) is for growth of $GaAs$ thin film by MBE. However, based on the experimental results presented in Law et al. (2000), the rate-limiting processes in $GaAs$ thin film growth by MOCVD are the same to those in $GaAs$ thin film growth by MBE. Therefore, we can use the same model but with a different "effective" energy barrier for the migration rate of Ga atoms, to model $GaAs$ thin film growth by MOCVD.

In subsection 4.2.1, we describe the process of $GaAs$ thin film growth by MOCVD considered in this study and show the similarity of the rate-limiting processes involved in this process to that in $GaAs$ thin film growth by MBE.

4.2.1 Process description

For purposes of this study, the MOCVD growth of GaAs occurs in a horizontal-flow quartz reactor, with precursors of triisobutylgallium ($TIBGa$)/tertiarybutylarsine ($TBAs$) and the carrier gas is H_2. The pressures of the precursors and of the carrier gas are 0.25 mTorr for $TIBGa$, 25 mTorr for $TBAs$ and 20 for Torr H_2. Therefore, the growth occurs in an As-rich environment. Under these precursor pressures, the growth rate is $0.5\mu m/hr$, which is independent of the substrate temperature when the substrate temperature varies from $825K$ to $900K$ (Law et al., 2000).

During the deposition, the precursor molecules, $TIBGa$ and $TBAs$ first adsorb onto the surface. The $TIBGa$ molecules adsorb onto the surface sites occupied by As atoms and $TBAs$ molecules adsorb onto the surface sites occupied by Ga atoms. Upon adsorption of precursor molecules onto the surface, surface reactions occur; specifically, Ga atoms and As atoms are generated by the decompositions of $TIBGa$ and $TBAs$ on the surface. The butyl groups from the decomposition of $TIBGa$ or $TBAs$ desorb rapidly back to the gas phase at the high temperatures considered in

this study (750K-950K) (Cui et al., 1998). Due to the fact that the pressure of $TBAs$ is much higher than that of $TIBGa$ (the As/Ga ratio is 100), the diffusing species controlling the epitaxial growth is the Ga atoms (Law et al., 2000).

The rate-limiting steps are the adsorption of $TIBGa$ and the migration of Ga atoms. Because the decomposition of $TIBGa$ is very fast, the adsorption of $TIBGa$ onto the surface can be simply modelled by the adsorption of Ga atoms onto the surface. Therefore, to model the surface micro-structure, we only consider adsorption of Ga atoms and migration of surface Ga atoms.

During deposition, Ga atoms must adsorb onto surface sites occupied by As atoms and As atoms must adsorb onto surface sites occupied by Ga atoms. Because the As/Ga ratio is very high (about 100), we assume that right after a Ga atom adsorb onto the surface, it is immediately covered by an As atom. Therefore, the same site is immediately available for the adsorption of next Ga atom. Consequently, all the surface sites are available for adsorption of Ga atoms at all times and the adsorption rate of Ga atoms is treated as site independent. Furthermore, when the growth rate is fixed, the adsorption rate on each surface site is a constant, Eq.4.1:

$$w_a = F \tag{4.1}$$

The migration rate of each surface Ga atom depends on its local environment. Assuming only first nearest neighbor interactions, the migration rate of a surface Ga atom from a surface site with n first nearest neighbors is (Shitara et al., 1992b,a):

$$w_m(n) = \nu_0 \exp(-\frac{E_s + nE_n}{k_B T}) \tag{4.2}$$

where E_s is the energy barrier associated with migration due to surface effects, E_n is the energy barrier associated with migration due to nearest neighbor interactions, k_B is the Boltzmann's constant, and ν_0 is the pre-exponential factor.

4.2.2 Derivation of surface micro-structure model based on probability theory

The formation of $GaAs$ thin films by adsorption and migration of Ga atoms is a stochastic process because: (a) the exact time and location of the occurrence of one specific surface micro-process (adsorption or migration) are unknown, and (b) the probability with which each surface micro-process may occur is only available. Therefore, the surface evolution model should be established based on probability theory. A rigorous derivation of kinetic Monte-Carlo algorithm for chemical reactions was first developed in Gillespie (1976). In the present study, we follow the same methodology to derive the Monte-Carlo model for surface micro-structure of $GaAs$ thin film growth by MOCVD.

Specifically, we treat the surface micro-processes (adsorption and migration of Ga atoms) as Poisson processes, which means that the following assumptions are made (e.g., Melsa and Sage, 1973; Feller, 1975; Gillespie, 1976; Fichthorn and Weinberg, 1991):

Assumption 4.1: *The probability that k events occur in the time interval $(t, t+T)$ is independent of t.*

Assumption 4.2: *The probability that k events occur in the time interval $(t, t+T)$ is independent of the number of events occurring in any non-overlapping time interval.*

Assumption 4.3: *The probability that an event occurs in an infinitesimal time interval $[t, t+dt)$ is equal to $W \cdot dt$ (where W is the mean count rate of the event), and the probability of more than one event occurring in an infinitesimal time interval is negligible.*

Based on these three assumptions, the time evolution of probabilities that the surface is in one specific configuration can be derived. The configuration of a surface

is characterized as the height of each surface atom at each surface site. If $P(\alpha, t)$ represents the probability that the system is in configuration α at time t, based on Assumptions 4.2 and 4.3, we have the following equation for $P(\alpha, t + dt)$:

$$P(\alpha, t + dt) = P(\alpha, t)P_{0\alpha} + \sum_{\beta} P(\beta, t)P_{1\beta} \tag{4.3}$$

where $P_{0\alpha}$ is the probability that no event occurs in the time interval $(t, t + dt)$ given that the surface is in configuration α at t, $P(\beta, t)$ is the probability that the surface is in configuration β at t and $P_{1\beta}$ is the probability that one event occurs in the time interval $(t, t + dt)$ given that the surface is in configuration β at t, and the occurrence of this event results to a transition from configuration β to configuration α.

$P_{0\alpha}$ and $P_{1\beta}$ have the following expressions (a detailed proof can be found in Gillespie (1992)). Specifically,

$$P_{0\alpha} = 1 - \sum_{\beta} W_{\beta\alpha} dt \tag{4.4}$$

where $W_{\beta\alpha}dt$ is the probability that an event occurs in the time interval $[t, t + dt)$ which results in a transition from configuration α to a configuration β, therefore, $\sum_{\beta} W_{\beta\alpha}dt$ is the probability that any one event occurs in the time interval $(t, t + dt)$ provided that the surface configuration is α at t. Moreover,

$$P_{1\beta} = W_{\alpha\beta}dt \tag{4.5}$$

where $W_{\alpha\beta}dt$ is the probability that an event happens in the time interval $[t, t + dt)$ and the occurrence of this event results to a transition from configuration β to configuration α.

By substituting Eq.4.4 and 4.5 into Eq.4.3 and setting $dt \longrightarrow 0$, we obtain a differential equation describing the time evolution of the probability that the surface is in

configuration α, Eq.4.6:

$$\frac{dP(\alpha,t)}{dt} = \sum_{\beta} P(\beta,t)W_{\alpha\beta} - \sum_{\beta} P(\alpha,t)W_{\beta\alpha} \tag{4.6}$$

Eq.4.6 is the so-called "master equation" (ME) for a stochastic process. The ME has a simple, linear structure, however, it is difficult to write the explicit form of Eq.4.6 for any realistic system because the number of the possible states is extremely large for most systems of a realistic size. For example, for a system with 10×10 sites and a maximum height of 1, the number of configurations is $2^{100} \approx 10^{30}$. This makes the direct solution of Eq.4.6, for any system of meaningful size, using numerical methods for integration of ordinary differential equations (e.g., Runge-Kutta) impossible.

Monte-Carlo techniques provide a way to obtain unbiased realizations of a stochastic process, which is consistent with the ME. The consistency of the Monte-Carlo simulation to the ME is based on the fact that in a Monte-Carlo simulation, the time sequence of Monte-Carlo events is constructed following a probability density function which is derived based on the same assumptions (Assumptions 4.1 - 4.3) as those used in the derivation of the master equation (Gillespie, 1976).

A Monte-Carlo event is characterized by both the type of the event (adsorption or migration of Ga atoms in our application) and the site in which the event is executed. We use $e(x;i,j)$ to represent a Monte-Carlo event of type x executed on the site (i,j), where $x \in \{a,m\}$, where $x = a$ corresponds to an adsorption event and $x = m$ corresponds to a migration event, $1 \leq i,j \leq N$, and $N \times N$ is the size of the lattice.

The sequence of Monte-Carlo events can be constructed based on the probability density function, $F(\tau,e)$, defined as follows:

Definition 4.1: *$F(\tau,e)d\tau$ is the probability at time t that event e will occur in the infinitesimal time interval $(t+\tau, t+\tau+d\tau)$.*

We now compute the expression of $F(\tau, e)$ based on Assumptions 4.1 and 4.2, Eq.4.7:

$$F(\tau, e)d\tau = P_{0\tau}P_e \tag{4.7}$$

where $P_{0\tau}$ is the probability that no event occurs in $[t, t+\tau)$, and P_e is the probability that event e occurs in the time interval $(t+\tau, t+\tau+d\tau)$. P_e can be determined by using Assumption 4.3 as follows:

$$P_e = W_e d\tau \tag{4.8}$$

$P_{0\tau}$ can be calculated by sampling the duration $(t, t+\tau)$ into M identical time intervals $\delta\tau = \tau/M$. When $M \to \infty$, $\delta\tau$ is small enough so that each time interval of size $\delta\tau$ contains one event at most. Based on Assumption 4.3, the probability that one event e occurs in $\delta\tau$ is $W_e\delta\tau$ and based on Assumption 4.2, the probability that any one event occurs in $\delta\tau$ is $\sum_e W_e\delta\tau$. Therefore, the probability that no events will occur in $\delta\tau$ is

$$P_{0\delta\tau} = 1 - \sum_e W_e\delta\tau \tag{4.9}$$

where $P_{0\delta\tau}$ is the probability that no event occurs in one $\delta\tau$ interval and $W_e\delta\tau$ is the probability that one event e will occur in the $\delta\tau$ interval.

Eq.4.9 can be applied to all the $\delta\tau$ time intervals in the duration $(t, t+\tau)$. Therefore, the probability that no events will occur in the duration τ is:

$$P_{0\tau} = \lim_{N\to\infty} P_{0\delta\tau}^N = \lim_{N\to\infty} \left(1 - \frac{\sum_e W_e\tau}{N}\right)^N = \exp(-\sum_e W_e\tau) \tag{4.10}$$

By substituting Eq.4.10 and 4.8 into Eq.4.7 and using $W_{tot} = \sum_e W_e$, the probability density function, $F(\tau, e)$, is as follows:

$$F(\tau, e) = W_e \exp(-W_{tot}\tau) \tag{4.11}$$

Monte-Carlo simulation constructs the sequence of events following the probability density function shown in Eq.4.11. Note, that Eq.4.11 is based on the same assumptions as the master equation (Eq.4.6), therefore, the Monte-Carlo simulation is able to provide an unbiased realization of a stochastic process which is consistent with that described by the master equation. There are many Monte-Carlo algorithms available to simulate a stochastic dynamic process. In this study, the kinetic Monte-Carlo simulation algorithm developed by Vlachos (1997) to simulate the surface roughness of the $GaAs$ surface was used. This algorithm is a modification of the so-called "direct" method developed by Gillespie (1976). In the remainder of this section, we discuss in detail the theoretical foundation and steps in the "direct" method and of the algorithm used in the calculations. The "direct" method is based on the fact that the two-variable probability density function, Eq.4.11, can be written as the product of two one-variable probability functions, Eq. 4.12:

$$F(\tau, e)d\tau = F_1(\tau)d\tau \cdot P(e|\tau) \tag{4.12}$$

where $F(\tau, e)d\tau$ is the probability that event e will occur in the time interval $(t + \tau, t + \tau + d\tau)$, $F_1(\tau)d\tau$ is the probability that an event will occur in the time interval $(t + \tau, t + \tau + d\tau)$, and $P(e|\tau)$ is the probability that the next event will be event e, given that the next event will occur in $(t + \tau, t + \tau + d\tau)$.

Based on the addition theorem (Melsa and Sage, 1973), $F_1(\tau)d\tau$ is the sum of $F(\tau, e)d\tau$ over all events:

$$F_1(\tau)d\tau = \sum_e F(\tau, e)d\tau \tag{4.13}$$

$P(e|\tau)$ can be obtained by substituting Eq.4.13 into Eq.4.12:

$$P(e|\tau) = \frac{F(\tau, e)}{\sum_e F(\tau, e)} \tag{4.14}$$

By substituting Eq.4.11 into Eqs.4.13 and 4.14, we obtain:

$$F_1(\tau) = W_{tot} \exp(-W_{tot}\tau) \tag{4.15}$$

$$P(e|\tau) = \frac{W_e}{W_{tot}} \tag{4.16}$$

In the Monte-Carlo simulation, Eq.4.15 is used to determine the life time of a Monte-Carlo event and Eq.4.16 is used to determine the Monte-Carlo event to be executed. To execute a Monte-Carlo simulation, a pseudo-random number generator is used which generates random numbers following the uniform distribution in the interval $(0, 1)$. It has been proven by Gillespie (1976) that if a random number, ξ, follows the uniform distribution in the unit interval, then the life time of a Monte-Carlo event, τ, can be computed by:

$$\tau = -\frac{\ln \xi}{W_{tot}} \tag{4.17}$$

To demonstrate that the τ obtained by using Eq.4.17 follows the probability density function in Eq.4.15, we first compute the probability that $\tau < T$, $(P(\tau < T))$, using Eq.4.17. Specifically, we have:

$$P(\tau < T) = P(-\frac{\ln \xi}{W_{tot}} < T) = P(\exp(-W_{tot}T) < \xi < 1) \tag{4.18}$$

Because ξ follows the uniform distribution in the interval $(0, 1)$, from Eq.4.18 we have that:

$$P(\tau < T) = P(\exp(-W_{tot}T) < \xi < 1) = 1 - \exp(-W_{tot}T) \tag{4.19}$$

whose corresponding probability density function, $F_1'(\tau)$, is:

$$F_1'(\tau) = \frac{dP(\tau < T)}{dT} = W_{tot} \exp(-W_{tot}T) \tag{4.20}$$

which is the probability density function in Eq.4.15. Therefore, the life time of each Monte-Carlo event, τ, calculated using Eq.4.17 follows the probability density function in Eq.4.15, which is consistent to the master equation.

The Monte-Carlo algorithm picks an event to be executed based on the probability of Eq.4.16. In this study, we assume that the probability of adsorption in an infinitesimal time interval $\delta\tau$ is site independent and the probability of migration is only dependent on the number of immediate side neighbors. Therefore, the following algorithm presented in Lam and Vlachos (2001) is used to pick a Monte-Carlo event, which is consistent with Eq.4.16. First, the surface atoms are grouped into five classes based on the number of side neighbors (e.g., surface atoms have 0, 1, 2, 3 and 4 side neighbors), in each class, the atoms have the same migration probabilities (adsorption probability is site independent). The total rate of adsorption, W_a is computed as follows:

$$W_a = N^2 w_a \tag{4.21}$$

where N is the size of the lattice and w_a is the adsorption rate of Ga atoms on each surface site.

The total rate of migration, W_m is given by:

$$W_m = \sum_{i=0}^{4} W_{m_i} \tag{4.22}$$

$$W_{m_i} = M_i \nu_0 \exp(-\frac{E_s + iE_n}{k_B T}) \tag{4.23}$$

where M_i is the number of surface Ga atoms that have i side neighbors and the value of M_i is equal to the number of atoms in each of the five classes.

Then, a random number following the uniform distribution in the unit interval, ζ, is generated to select an event based on the rates. Specifically, if $0 < \zeta < W_a/(W_a + W_m)$, the event is adsorption; if $W_a/(W_a+W_m) < \zeta < 1$, the event is migration. If the event is migration, the k^{th} class in which the migration event will occur can be selected by finding out an integer, $k \in \{0, 1, 2, 3, 4\}$ such that $(W_a + \sum_{i=0}^{k-1} W_{m_i})/(W_a + W_m) < \zeta < (W_a + \sum_{i=0}^{k} W_{m_i})/(W_a + W_m)$. After that, a second random number is generated

to select the site where the event will be executed; if the event is adsorption, the site is randomly picked from sites in the entire lattice, if the event is migration, the site is randomly picked from the list of the sites in the selected class.

After the site is selected, the Monte-Carlo event is executed. If the event is adsorption, it is executed by adding one atom on the selected site, if the event is migration, a third random number is generated to randomly pick a neighboring site that has a lower height (target site), and move the atom from the original site to the target site. After an Monte-Carlo event is executed, the five classes are updated and the next step of the simulation can be performed. Upon an executed event, a real-time increment Δt is computed by applying Eq.4.17 to our process:

$$\Delta t = \frac{-\ln \xi}{W_a + W_m} \tag{4.24}$$

where ξ is a random number in the $(0, 1)$ interval. This algorithm guarantees that every trial is successful and is efficient compared to traditional null event algorithms (Reese et al., 2001).

4.2.3 Computation of kinetic Monte-Carlo model parameters using experimental data

The predictions of the Monte-Carlo simulation depend on the rates of adsorption and migration used in the calculations. When the film growth rate is fixed (which is the case in our process), the rate of adsorption can be directly calculated based on the growth rate. However, there are three parameters in the expression for the migration rate, ν_0, E_s and E_n, in Eq.4.2 that need to be determined. In this study, the values for these parameters will be calculated using experimental data. In the case of $GaAs$ thin film growth by MBE, values for the E_s and E_n have been obtained from the measurements of reflection high-energy electron diffraction (RHEED) specular

intensities so that the transition temperature predicted by the Monte-Carlo simulation matches that of the measured data (Shitara et al., 1992a). Furthermore, we adjust the values for the three parameters in Eq.4.2 so that the dependence of surface roughness on the substrate temperature measured in the experimental work of Law et al. (2000) can be predicted by the Monte-Carlo simulations.

To compare the roughness from Monte-Carlo simulations to experimental values reported in Law et al. (2000), we first give a description of the definition of surface roughness used in that paper. Surface roughness is a measure of fluctuation of surface height and can be defined as (Sinha et al., 1988; Tanenbaum et al., 1997):

$$\begin{aligned} r'(L) &= \sqrt{G(L)} \\ G(L) &= \langle [h(x_i, y_i) - h(x_j, y_j)]^2 \rangle \end{aligned} \tag{4.25}$$

where $G(L)$ is the height-height correlation function, $h(x_i, y_i)$ and $h(x_j, y_j)$ are the surface heights at locations i and j separated by a lateral distance, L, and $r'(L)$ is the roughness. The notation $\langle \cdot \rangle$ denotes an ensemble average over all possible pairs of surface points.

The surface roughness defined in this way follows a power-law dependence on the lateral separation up to a certain value denoted as the critical length, L_c, and saturates when the lateral separation is larger than the critical length (Sinha et al., 1988; Palasantzas, 1993). This leads to the following expressions for surface roughness:

$$\begin{aligned} r'(L) &= kL^{\alpha} \quad for \quad L < L_c \\ r'(L) &= r'(\infty) \quad for \quad L > L_c \end{aligned} \tag{4.26}$$

where α the roughness exponent, k is a constant, and $r'(\infty)$ is the saturated roughness value.

The values for $r'(\infty)$, α and L_c are measured in Law et al. (2000). In our simulation, a power-law dependence of surface roughness on the lateral separation up to a certain critical length is also observed. The value for the saturated roughness

from our Monte-Carlo simulations is tuned to fit the experimental data reported in Law et al. (2000) by adjusting the parameters of the migration rate. Note, that the Monte-Carlo simulation can not predict the values for critical length and roughness exponent reported in the experimental data.

To determine the parameters for migration rate to match the experimental results, we use the parameters reported in Shitara et al. (1992a) for $GaAs$ thin film growth by MBE as our initial estimate for the parameters of Eq.4.2 and run Monte-Carlo simulations for the evolution of surface roughness of $GaAs$ (001) surface. The parameters used as initial estimate are listed in Table 4.1, where k_B is the Boltzmann's constant, h is the Planck's constant and $\nu_0 = 2k_BT/h$, where T is the substrate temperature. We employ a cubic lattice in all kinetic Monte-Carlo simulations. Note, that the crystal structure of $GaAs$ is a Zinc-Blend type structure, but the (001) surface of Zinc-Blend structure is identical to a cubic lattice except from the fact that there is a shift of a half unit of the lattice at each atomic layer in the Zinc-Blend structure (Blakemore, 1982). This shift is not considered in this study. The thickness of one layer of $GaAs$ is 2.8Å and the lattice constant of the cubic lattice used in our simulations is 3.99Å. The growth rate is $0.5\mu m/h$, which corresponds to $w_a = 0.49/s$. Monte-Carlo simulations are performed on an 80×80 lattice at four different substrate temperatures (T=713K, 750K, 775K and 800K). Note, in the experimental work of Law et al. (2000), the $GaAs$ thin film surface roughness is measured by STM after cooling down the film to room temperature, the cooling down process is also simulated. During the cooling down process, there is no supply of precursors, but the surface migration still takes place. Therefore, during the cooling process, we set the adsorption rate, $w_a = 0$ and use the same migration rate (Eq.4.2) in all the simulations. The film is cooled down at a rate of $2K/s$, which is reported in Law et al. (2000). Fig.4.1 (a) shows the

evolution of surface roughness when $T = 713K$. During growth, the surface roughness is $\sim$ 3.3Å. The growth stops at $t = 400s$ and the surface roughness declines to 3.0Å after the cooling down process. Fig.4.1 (b) shows the evolution of surface roughness when $T = 750K$. During growth, the surface roughness is $\sim$ 2.3Å. The growth stops at $t = 200s$ and the surface roughness declines to $\sim$ 1.7Å after the cooling down process. Fig.4.1 (c) and (d) show the evolution of surface roughness when $T = 775K$ and $800K$. During growth, the surface roughness fluctuates between 1.5Å and 2.0Å. The growth stops at $t = 100s$ and the surface roughness stays at $\sim$ 2.0Å after the cooling down process. The experimental results of saturated surface roughness after the growth of a $0.5\mu m$-thick $GaAs$ film are (Law et al., 2000): $r'(\infty) = 2.8$Å when $T = 825K$ and $r'(\infty) \approx 1.3$Å when $T = 850K$, $875K$ and $900K$.

Table 4.1: Parameters for migration rate in $GaAs$ thin film growth by MBE (Shitara et al., 1992a).

E_s	1.58	eV
E_n	0.28	eV
k_B	1.38×10^{-23}	J/K
h	6.63×10^{-34}	$J \cdot s$

Comparing the simulation results for saturated surface roughness to the experimental data, we find that the saturated roughness obtained from Monte-Carlo simulation when $T = 713K$ is very close to the experimental data for saturated surface roughness when $T = 825K$, and the saturated roughness obtained from Monte-Carlo simulation when $T = 775K$ and $T = 800K$ is very close to the experimental data for saturated surface roughness when $T = 900K$. Therefore, we compute the parameters for migration rate in $GaAs$ thin film growth by MOCVD using the following method.

Let ν_0', E_s' and E_n' be the parameters of the migration rate in $GaAs$ thin film growth

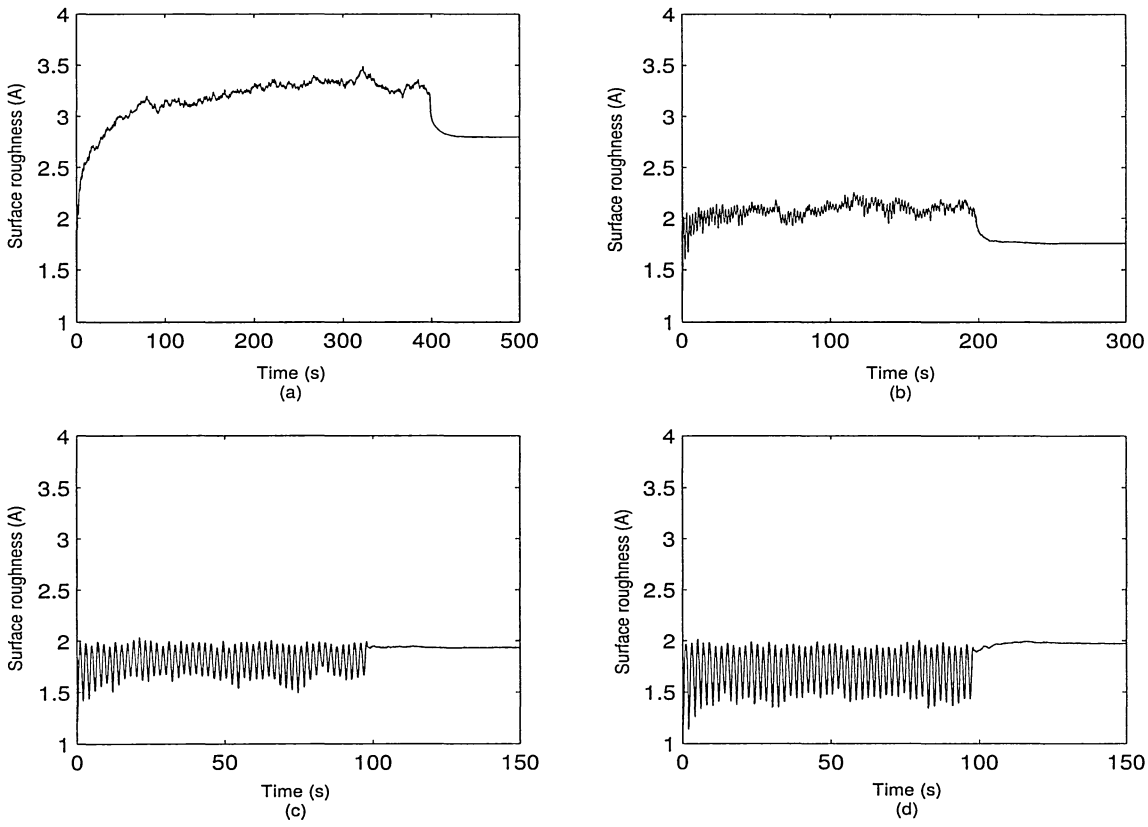

Figure 4.1: Surface roughness under different substrate temperatures when the parameters of migration rate are the same to those for $GaAs$ thin film growth by MBE reported in Shitara et al. (1992a). (a) T=713K, (b) T=750K, (c) T=775K and (d)=800K.

by MOCVD. First, compute ν_0' and E_s' then construct two equations for ν_0' and E_s'. To construct these two equations, set the migration rate of adatoms (surface atoms without side-neighbor) in MOCVD, when substrate temperature is $T = 825K$, equal to the migration rate of adatoms in MBE when substrate temperature is $T = 713K$. Also, set the migration rate of adatoms in MOCVD, when substrate temperature is $T = 900K$, equal to the migration rate of adatoms in MBE when substrate temperature is $T = 788K$ ($T = 788K$ is the average of $T = 775K$ and $T = 800K$). This averaged temperature is used because the experimental data for saturated roughness when $T = 900K$ in MOCVD is very close to the saturated roughness obtained from Monte-Carlo simulations under both $T = 775K$ and $T = 800K$ (when the parameters in Table 4.1 are used). Therefore, we have the following equations for ν_0' and E_s':

$$\nu_0' \exp(-\frac{E_s'}{k_B T_1'}) = \frac{2k_B T_1}{h} \exp(-\frac{E_s}{k_B T_1}) \tag{4.27}$$

$$\nu_0' \exp(-\frac{E_s'}{k_B T_2'}) = \frac{2k_B T_1}{h} \exp(-\frac{E_s}{k_B T_2}) \tag{4.28}$$

where the values of E_s, k_B and h are listed in Table 4.1, and T_1=713K, $T_2 = 788K$, $T_1' = 825K$ and $T_2' = 900K$.

By solving Eqs.4.27 and 4.28, $E_s' = 1.83eV$ and $\nu_0' = 2.9 \times 10^{13} s^{-1}$. Finally, the value of E_n' can be computed by setting the migration rate of surface atoms with 1 side-neighbor in MOCVD, when the substrate temperature is $T = 825K$, equal to the migration rate of surface atoms with 1 side-neighbor in MBE when the substrate temperature is $T = 713K$, resulting in Eq.4.29 for E_n':

$$\nu_0' \exp(-\frac{E_s' + E_n'}{k_B T_1'}) = \frac{2k_B T_1}{h} \exp(-\frac{E_s + E_n}{k_B T_1}) \tag{4.29}$$

where the values of E_s, k_B and h are listed in Table 4.1, $\nu_0' = 2.9 \times 10^{13} s^{-1}$, $E_s' = 1.83eV$, T_1=713K, and $T_1' = 825K$.

By solving Eq.4.29, $E'_n = 0.27eV = 0.15E'_s$, and this relationship is similar to the one reported in Shitara et al. (1992a) (specifically, $E_n = 0.15E_s$) in $GaAs$ thin film growth by MBE. The value of E'_s obtained following this method is also reasonably close to the value of E_s in MBE (Shitara et al., 1992a) and to those reported for MOCVD of $GaAs$ thin films (Law et al., 2000). Furthermore, by comparing the simulation results for the saturated roughness for $T = 850K$ and $T = 875K$ to experimental data, and increasing the pre-exponential factor, ν'_0 from $2.9 \times 10^{13}s^{-1}$ to $5.8 \times 10^{13}s^{-1}$ a better match of all the simulation results, for $T = 825K$, $850K$, $875K$ and $900K$, to the experimental data in Law et al. (2000) can be achieved.

The values of the migration rate parameters, obtained by following the above method and used in all the simulations are given in Table 4.2. Fig.4.2 (a) and (b) show the evolutions of surface roughness after $400s$ of deposition time when the substrate temperatures are $T = 825K$ and $850K$, respectively. Fig.4.2 (c) and (d) show the evolutions of surface roughness after $100s$ of deposition time when the substrate temperatures are $875K$ and $900K$, respectively. The saturated roughness from all the simulations are very close to the experimental data reported in Law et al. (2000).

Table 4.2: Parameters for migration rate obtained by fitting kinetic Monte-Carlo simulation results to the experimental results reported in Law et al. (2000).

ν_0	5.8×10^{13}	s^{-1}
E_s	1.82	eV
E_n	0.27	eV

Remark 4.1 *Note, that the critical length and the roughness exponent measured in Law et al. (2000) can not be obtained from our kinetic Monte-Carlo simulation by adjusting the simulation parameters. We believe that the critical length and roughness*

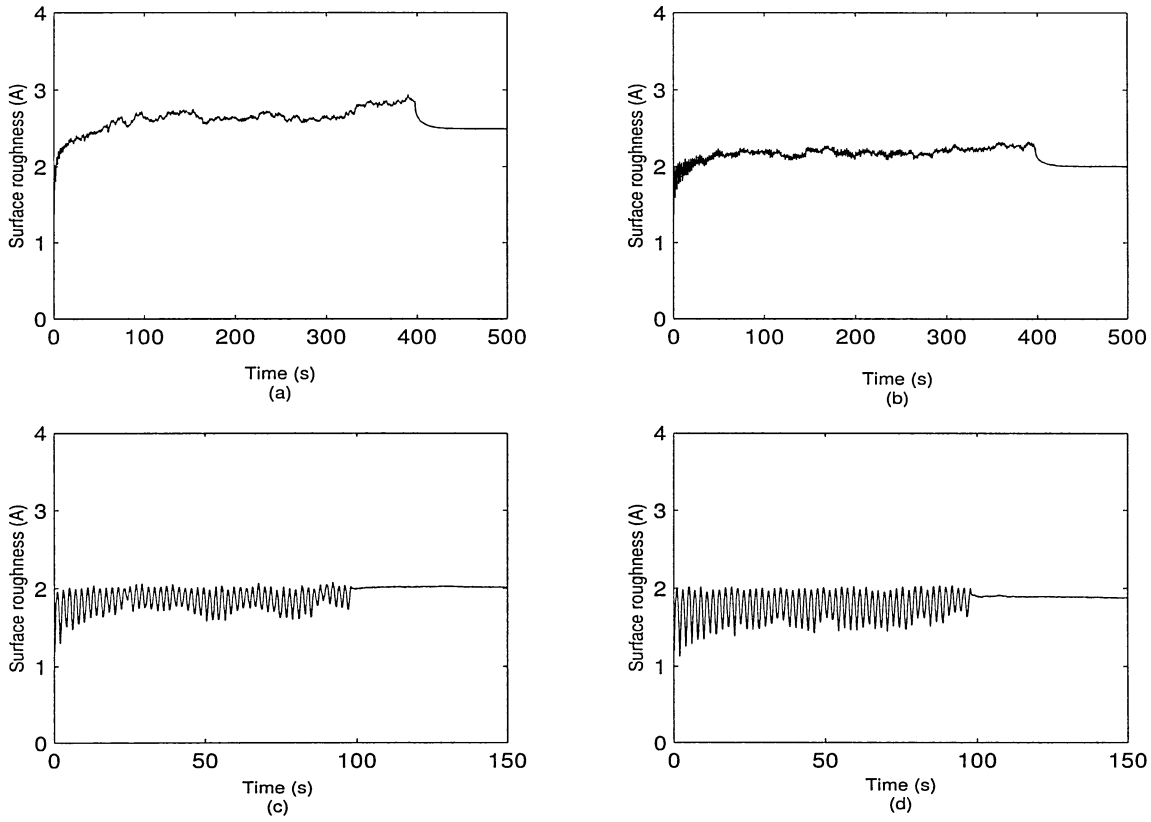

Figure 4.2: Surface roughness under different substrate temperatures when the parameters of migration rate are adjusted to match the experimental results reported in Law et al. (2000). (a) T=825K, (b) T=850K, (c) T=875K and (d)=900K.

exponent are related to the actual island-size on the surface. In the simulation, the sizes of surface islands have to be smaller than the size of the simulation lattice. Limited by the available computing power, the size of simulation lattice is not comparable to the size of the wafer, so the actual island-size can not be adequately captured within the small simulation lattice ($320\mathring{A}\times320\mathring{A}$) used in the present study. However, the saturated surface roughness, $r'(\infty)$, can be considered as a measure of the fluctuation of height of the surface because it is independent of the influence of the size of surface islands (the lateral separation is much larger than the sizes of surface islands and each surface pair picked in the height-height correlation are on different islands on the surface). We use the roughness defined in Eq.4.26 because this is the roughness used in Law et al. (2000) to compare and fit the simulation results to experimental data.

Remark 4.2 *Note, that in experimental studies, the surface roughness of GaAs thin films was measured after a deposition of $0.5\mu m$-thick film, which corresponds to a deposition time of about $1hr$. Owing to computational limitations, the simulated deposition time is much shorter that $1hr$. However, from the simulation results presented in Figs.4.1 and 4.2, it can be seen that after an initial transient of $\sim 100s$, the roughness either converges to some fixed value (see plots (a) and (b) of Figs.4.1 and 4.2) or oscillates around some fixed value (see plots (c) and (d) of Figs.4.1 and 4.2). Therefore, it can be concluded that further increase in the simulation time will lead to the same surface roughness for the GaAs thin film.*

Remark 4.3 *Note, that in Shitara et al. (1992a), the pre-exponential factor, ν_0, has a linear dependence on substrate temperature ($\nu_0 = 2k_BT/h$). However, this is a weak temperature dependence compare to the Arrhenius-like dependence of the migration rate of the substrate temperature. Therefore, we assume that the pre-exponential factor in Eq.4.2 is a constant. The same assumption can be also found in other Monte-Carlo simulation studies of GaAs thin film growth reported in the literature (see, for example, Meng and Weinberg, 1996; Heyn et al., 1999). Furthermore, the simulation*

results show that by assuming that the pre-exponential factor in Eq.4.2 is a constant, the saturated roughness predicted by kinetic Monte-Carlo simulations under different substrate temperatures is very close to the experimental data.

4.3 Real-time estimation of thin film surface roughness

Surface roughness is the property of interest from a control point of view since it directly influences device properties. To be able to achieve real-time control of surface roughness of $GaAs$ thin films, it is important to develop an estimator that can provide estimates of surface roughness in real-time. In this section, we develop such an estimator by following a methodology that was recently proposed in Lou and Christofides (2003a).

For consistency with the previous work, the roughness, r, is represented by the standard deviation of the surface from its average height and is computed as follows:

$$r = \sqrt{\frac{\sum_{i=1}^{N}\sum_{j=1}^{N}[h_{i,j} - \bar{h}]^2}{N \times N}} \tag{4.30}$$

where N is the size of the lattice, $\bar{h}$ is the average height of the surface and $h_{i,j}$ is the height of the surface at site (i, j); note that estimation and control of surface roughness using alternative surface roughness definitions can be readily studied within this framework.

In the kinetic Monte-Carlo simulation, the size of the lattice influences the quality of the predictions and the computational demand. In a previous work Lou and Christofides (2003a) discussed the dependence of simulation results on the lattice size used in the Monte-Carlo simulations. The simulation results show that when the lattice size is sufficiently large, the roughness profiles obtained from kinetic Monte-Carlo

simulations are independent of the lattice size. To implement real-time feedback control based on a model that captures the evolution of surface roughness, a small lattice must be used in the simulation to make the model solution time comparable to the process real-time. However, the roughness profiles from a kinetic Monte-Carlo simulation using a small lattice contain significant stochastic fluctuations, and thus, they cannot be directly used for feedback control (Lou and Christofides, 2003a,b) such an approach would result in significant fluctuations in the control action which could perturb unmodeled (fast) process dynamics and should be avoided.

Because each kinetic Monte-Carlo simulation run provides one realization of a stochastic process, by averaging the simulation results from different runs, the roughness obtained by averaging multiple kinetic Monte-Carlo simulations is closer to the expected roughness value obtained from the solution of the master equation, when compared to the roughness profile obtained from a single simulation run with a same size lattice. This result points to reducing the fluctuations on the surface roughness obtained from the kinetic Monte-Carlo simulation by independently running several small lattice kinetic Monte-Carlo simulations with the same parameters and averaging the outputs of the different runs. In the simulations, when the surface roughness profiles are computed by averaging six independent runs of kinetic Monte-Carlo simulations which use a 30×30 lattice, the solution time of the kinetic Monte-Carlo model is comparable to the real-time process evolution and the average values of the surface roughness approximate well their expected values computed from the solution of the master equation, which are obtained by running the kinetic Monte-Carlo simulation on a 150×150 lattice. This is a sufficiently large lattice to ensure simulation results which are independent of the lattice size.

The predicted profile of surface roughness, which is obtained from a kinetic Monte-

Carlo simulation based on multiple small lattice models, still contains stochastic fluctuations and is not robust (due to the open-loop nature of the calculation) with respect to disturbances and variations in process parameters. To mitigate these problems, the approach proposed by Lou and Christofides (2003a) that combined the kinetic Monte-Carlo simulator, based on multiple small lattice models, with an adaptive filter, to reject the stochastic fluctuations on the surface roughness profile, and a measurement error compensator to improve the estimates of surface roughness using on-line measurements was followed. Specifically, the adaptive filter is a second-order dynamical system with the following state-space representation:

$$\begin{aligned} \frac{d\hat{y}_r}{d\tau} &= y_1 \\ \frac{dy_1}{d\tau} &= \frac{K}{\tau_I}(y_r - \hat{y}_r) - \frac{1}{\tau_I} y_1 \end{aligned} \tag{4.31}$$

where y_r is the output of the kinetic Monte-Carlo simulation based on multiple small lattice models, $\hat{y}_r$ is the filter output, K is the filter gain and τ_I is the filter time constant. To accelerate the response of the filter and avoid a large overshoot, $\tau_I = 0.5/K$. To achieve both fast tracking of the dynamics of the outputs and efficient noise rejection, the gain of the filter is adaptively adjusted as follows:

$$K(\tau) = K_0 \frac{|\int_{\tau-\Delta\tau}^{\tau} y_r(t)dt - \int_{\tau-2\Delta\tau}^{\tau-\Delta\tau} y_r(t)dt|}{\Delta\tau^2} + K_s \tag{4.32}$$

where K_0 is a constant, K_s is the steady-state gain for the adaptive filter and $\Delta\tau$ is the time interval between two updates of K. Although a better tracking performance is expected when a small $\Delta\tau$ is used, a very small $\Delta\tau$ will not significantly reduce the effect of fluctuations on the filter output and should be avoided.

The measurement error compensator uses the available on-line measurements (in the numerical simulations the values of the surface roughness are obtained from the large lattice kinetic Monte-Carlo simulator) to produce improved estimates of the sur-

face roughness. The state-space representation of the measurement error compensator is:

$$\frac{de}{d\tau} = K_e(y_h(\tau_{m_i}) - \hat{y}(\tau_{m_i})); \quad \tau_{m_i} < \tau \leq \tau_{m_{i+1}}; \qquad i = 1, 2, \cdots \tag{4.33}$$

and the final roughness estimates are computed using Eq.4.34:

$$\hat{y} = \hat{y}_r + e \tag{4.34}$$

In the above equations, K_e is the compensator gain, e is the estimated model error, which is used to compensate the model output, $\hat{y}$ is the roughness estimates, $\hat{y}_r$ is the filtered output from a kinetic Monte-Carlo simulator which uses multiple small lattice models and y_h is the output of a kinetic Monte-Carlo simulator which uses a large lattice. In an experimental set-up, y_h could be obtained from the measurement sensor. Since the roughness measurements are only available at discrete points in time $\tau_m = [\tau_{m_1}, \tau_{m_2}, \cdots]$, the right-hand side of Eq.4.33 is computed at the time a roughness measurement is available and is kept at this value for the time interval between two available roughness measurements.

The combination of the adaptive filter and the measurement error compensator functions as an estimator, which is capable of accurately predicting the evolution of surface roughness during the thin film growth. Fig.4.3 shows the surface roughness profile computed by the estimator, which uses a kinetic Monte-Carlo simulator based on six 30×30 lattice models (solid lines). This profile is compared to the surface roughness profile obtained from a kinetic Monte-Carlo simulator which uses a 150×150 lattice model. This comparison clearly shows that the developed estimator can accurately predict the evolution of surface roughness. Note, that the developed estimator can be used for real-time feedback control, since the computational time needed to run kinetic Monte-Carlo simulation based on six 30×30 lattice models is comparable to the real-time process dynamics.

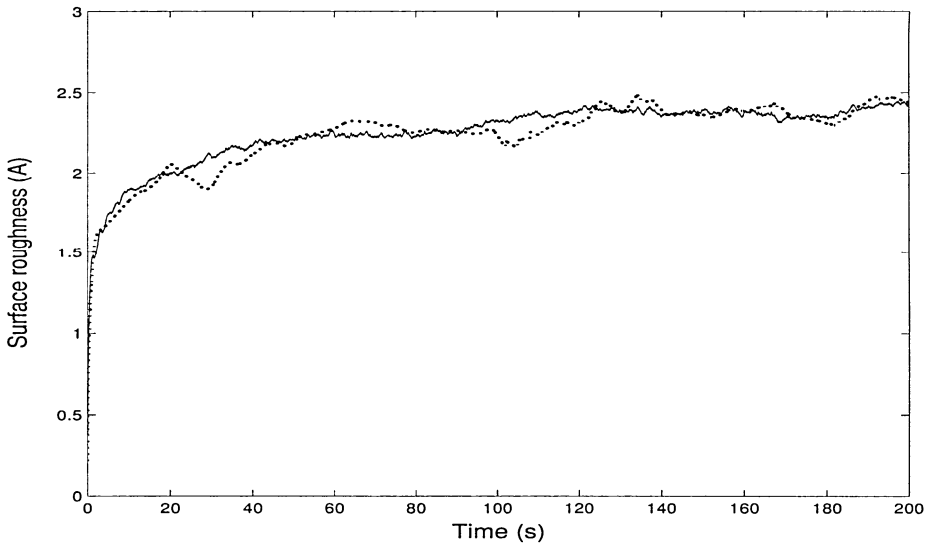

Figure 4.3: Surface roughness profiles from the estimator (dotted line) and from a kinetic Monte-Carlo simulation which uses a 150×150 lattice model (solid line).

Remark 4.4 *Referring to the selection of the lattice size, it is important to point out that while kinetic Monte-Carlo simulations based on multiple* 30×30 *lattice models can adequately capture the evolution of surface roughness in the specific thin film growth problem under consideration, the dimension of the small lattice in general should be chosen so that the interactions between the surface atoms are adequately captured, and also that it is large enough to describe all the spatio-temporal phenomena occurring on the surface (e.g., cluster formation). Furthermore, the small lattice should be chosen to provide accurate estimates of the desired controlled properties. For example in the case of surface roughness, this quantity is defined as the standard deviation of the surface from its average height. When a* 30×30 *small lattice is used, the computation of surface roughness involves hundreds of surface atoms, which is adequate to obtain the expected value. However, when the property of interest is, for example, step density, a larger lattice is needed to obtain a convergent average value from the kinetic Monte-Carlo simulation. At this point, it is important to note that the proposed reduction of lattice size can be viewed as an alternative way to perform*

order reduction of the master equation (see Gallivan and Murray, 2003, for reduction approaches based directly on the master equation). Finally, note that through extensive simulations for our process, a 150×150 *lattice is of sufficient size to capture the evolution of the film growth and that further increase of the lattice size leads to no observable improvement in the accuracy of the simulation results. Therefore, in the remainder of this study, a kinetic Monte-Carlo simulator which uses a* 150×150 *lattice to describe the evolution of the thin film growth in the closed-loop system is used.*

4.4 Feedback control of surface roughness

The production of high-quality thin films requires that the surface roughness is maintained at a desired level. In this study, we consider feedback control of surface roughness of $GaAs$ thin films by manipulating the substrate temperature, which is assumed to change only with respect to time. This is a reasonable formulation for the manipulated input and is practically feasible for many experimental and industrial deposition processes. With such a manipulated input formulation, however, it is only possible to achieve control of a spatially-averaged surface roughness, for example, the one defined in Eq.4.30. We could have formulated a control problem under the assumption that a large number of manipulated inputs (control actuators) are available to control surface roughness with higher precision but such a control problem formulation would not be practically feasible at the present time. As will be shown, it is possible by manipulating the substrate temperature (single input formulation) to achieve an overall very smooth film surface configuration.

The fact that the model that describes the evolution of the thin film growth process is not available in closed-form (available only as a kinetic Monte-Carlo model) motivates the use of a proportional-integral (PI) feedback controller to regulate the

surface roughness. Furthermore, from simulation results shown in Fig.4.2, even when the substrate temperature is fixed, the surface roughness oscillates around a fixed value. This oscillatory behavior is an intrinsic characteristic of the film growth process and is not the control objective to eliminate this oscillation, rather to control the surface roughness at a desired level (range). To eliminate unnecessary control actions, which may lead to poor closed-loop performance, the control objective is to stabilize the surface roughness value close to a desired level tolerance ϵ. For this purpose, a proportional integral (PI) feedback control algorithm is used in the following form:

$$u(\tau) = K_c[\hat{e} + \frac{1}{\tau_c}\int_0^{\tau} \hat{e}(t) \cdot dt] \tag{4.35}$$

$$\hat{e}(t) = \begin{cases} \hat{y} - y_{set}, & for \quad |\hat{y} - y_{set}| > \epsilon \\ 0, & for \quad |\hat{y} - y_{set}| \leq \epsilon \end{cases} \tag{4.36}$$

where y_{set} is the desired level of surface roughness, $\hat{y}$ is the output of the roughness estimator, K_c is the proportional gain and τ_c is the integral time constant.

The PI controller is coupled with the roughness estimator as shown in Fig.4.4. The roughness estimator includes a kinetic Monte-Carlo simulator which uses multiple small-lattice models, the adaptive filter and the measurement error compensator. The output of the kinetic Monte-Carlo simulator is sent to the adaptive filter (Eq.4.31) to suppress the noise, and then, the measurement error compensator (Eqs.4.33 and 4.34) further corrects the filtered roughness based on the measurements and the roughness estimates are used in the PI controller to determine the substrate temperature.

Several closed-loop simulation runs were performed to evaluate the effectiveness of the developed estimator/controller structure shown in Fig.4.4. In these simulations, the outputs from six kinetic Monte-Carlo simulators using 30×30 lattice models are averaged within the estimator. A 150×150 lattice Monte-Carlo model is used

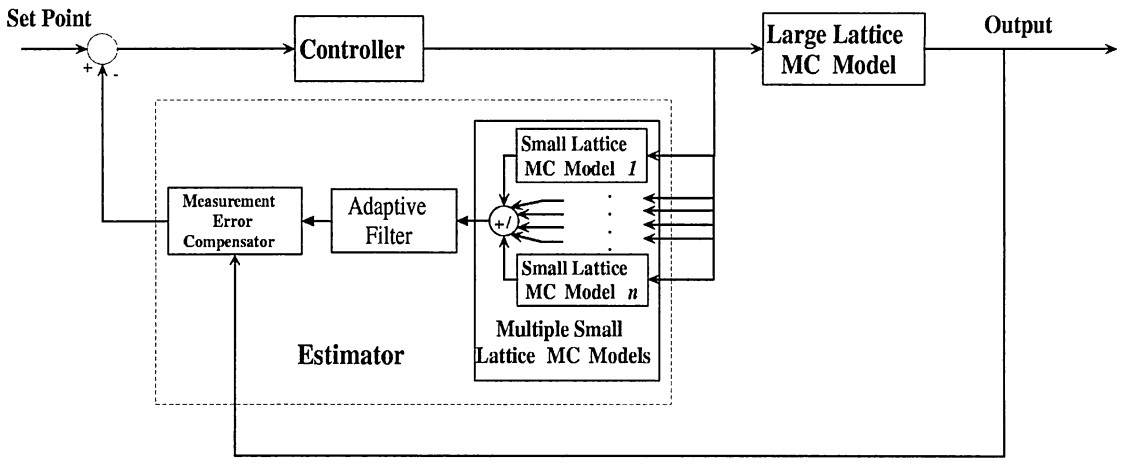

Figure 4.4: Diagram of the closed-loop system under the developed estimator/ controller structure.

to describe the evolution of the process, which corresponds to a 600Å×600Å $GaAs$ (001) surface. The desired roughness is 1.5Å and the tolerance is 0.1Å. The time interval between two available measurements is taken to be $3.0s$. This specification is made based on the fact that high-speed scanning tunnelling microscopy (STM) (Curtis et al., 1997) is able to measure the morphology of a 600Å×600Å surface with an acquisition time of $3s$ and the fact that it is feasible to perform STM measurement during epitaxial growth of $GaAs$ layers (Voigtländer, 2001). The parameters for the roughness estimator and the PI controller used in the simulations are given in Table 4.3. Initially, the $GaAs$ thin film grows on a perfect surface at $T = 800K$ with the roughness increasing. The controller is activated when the roughness reaches 2.3Å. Fig.4.5 shows the evolution of surface roughness under feedback control. Fig.4.6 shows the profile of the substrate temperature. The results clearly show that the developed estimator/controller structure can successfully drive the surface roughness to the desired level.

To test the robustness of the proposed estimator/controller structure, the $GaAs$

Table 4.3: Roughness estimator and controller parameters.

K_0	0.05	$s/\text{Å}$
K_s	0.1	
K_e	0.08	s^{-1}
K_c	15	$K/\text{Å}$
τ_c	0.2	s
ϵ	0.1	Å

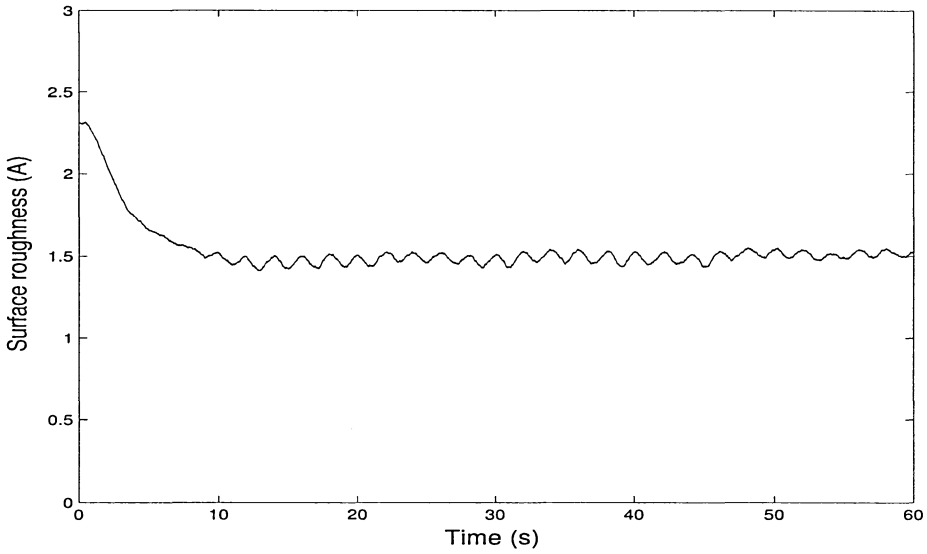

Figure 4.5: Evolution of the surface roughness under feedback control based on the roughness estimator.

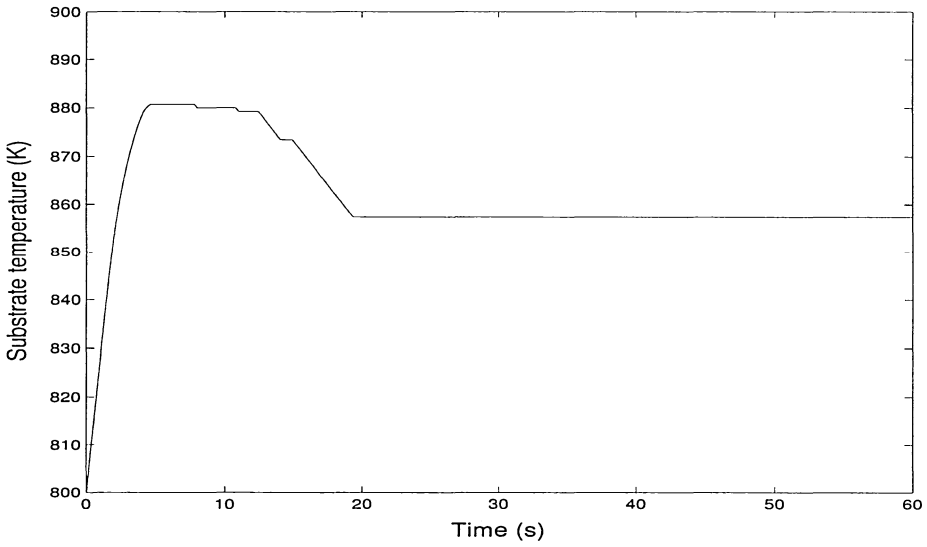

Figure 4.6: Evolution of the substrate temperature under feedback control based on the roughness estimator.

thin film growth process is assumed to have a 10% uncertainty in the energy associated with a single bond on the surface, i.e., the E_s used in the roughness estimator is $1.82eV$ but the E_s used in the kinetic Monte-Carlo model based on the large lattice is $2.0eV$. Figs.4.7 and 4.8 show the corresponding output and input profiles, respectively. Note, the controller does exhibit very good robustness behavior (compare also Figs.4.5 and 4.7).

To show the importance of using the roughness estimator for feedback control and not relying exclusively on the roughness measurements (which are obtained only every 3.0 seconds), the PI controller (parameters as Table 4.3) is applied to the kinetic Monte-Carlo model assuming that new roughness measurements are fed to the controller every 3.0 seconds, which is consistent with the previous simulations. Also, to prevent the substrate temperature from obtaining unreasonably high or low values, the substrate temperature is constrained to be $750K \leq T \leq 950K$. Note, that when

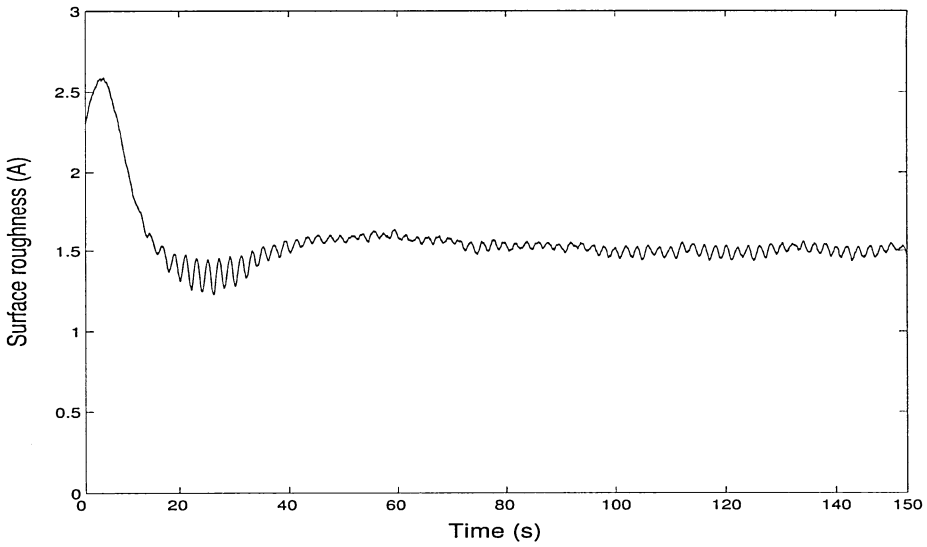

Figure 4.7: Evolution of the surface roughness under feedback control based on the roughness estimator - closed-loop simulation under uncertainty.

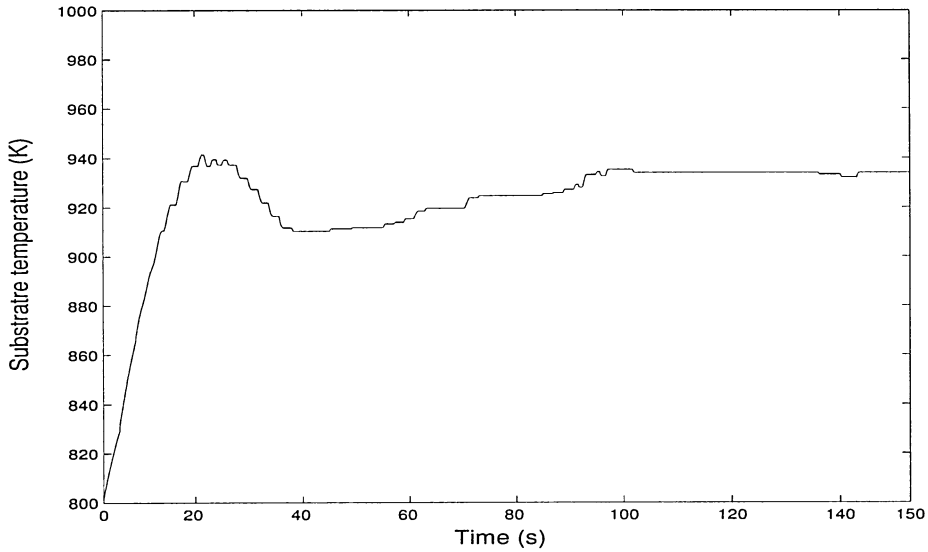

Figure 4.8: Evolution of the substrate temperature under feedback control based on the roughness estimator - closed-loop simulation under uncertainty.

the roughness is controlled using the proposed controller/estimator structure, the substrate temperature is always within $750K \leq T \leq 950K$ (see Fig.4.6). Figs.4.9 and 4.10 show the evolution of surface roughness and substrate temperature, respectively. We can see that the PI controller, based on discrete roughness measurements, is not able to control the surface roughness to the desired level which demonstrates the applicability of the proposed estimator/controller structure.

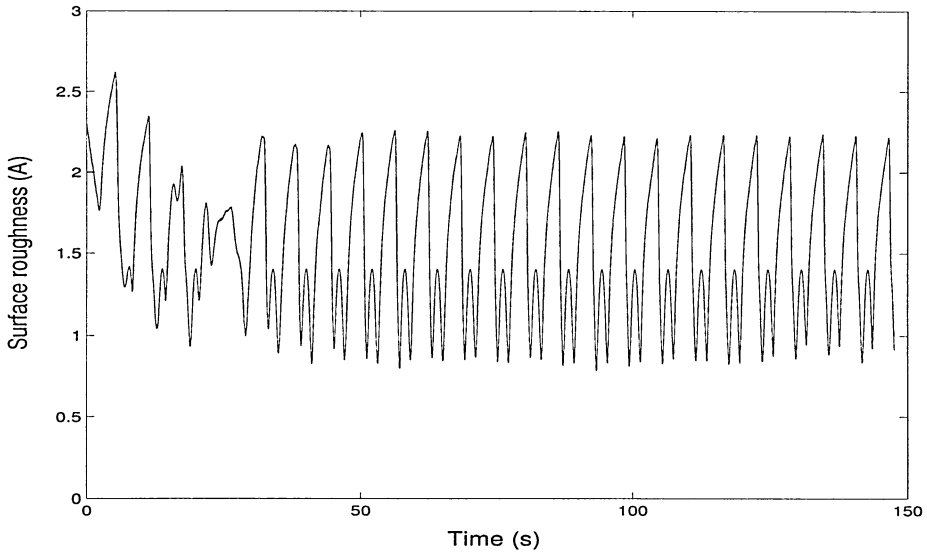

Figure 4.9: Evolution of the surface roughness under feedback control without roughness estimator.

Remark 4.5 *Note, that by tuning the PI controller, the surface roughness could be controlled to the desired level by using only the on-line roughness measurements. However, further controller tuning can not achieve a closed-loop performance as good as that achieved under feedback control using the roughness estimator. To show this, we applied the PI controller with a new set of parameters ($K_c = 5K/\AA$, $\tau_c = 1.0s$) to the same kinetic Monte-Carlo model for the GaAs thin film growth process, assuming that new roughness measurements are fed into the controller every* 3.0 *seconds. The parameters of the PI controller are tuned to make the controller drive the surface roughness to the desired level. Figs.4.11 and 4.12 show the profiles of surface*

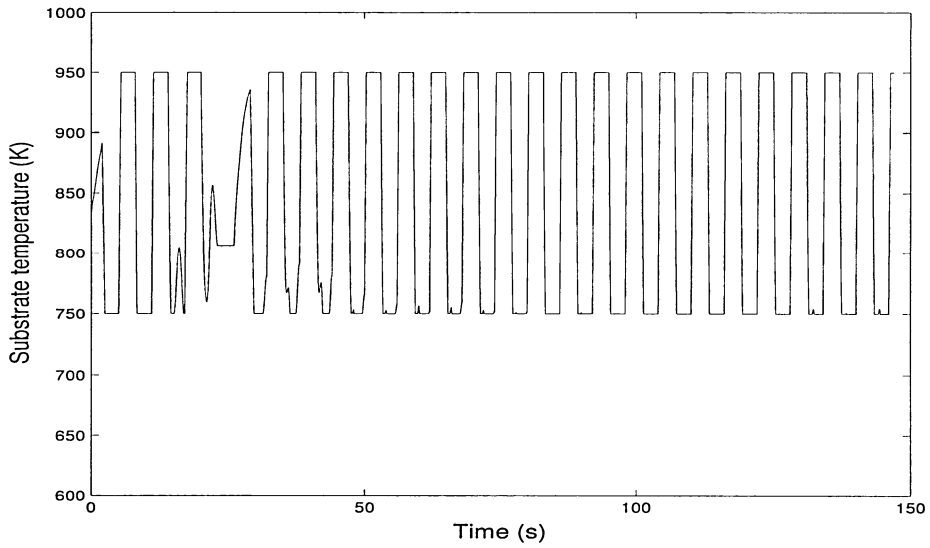

Figure 4.10: Evolution of the substrate temperature under feedback control without roughness estimator.

roughness and substrate temperature, respectively. With the new controller parameters, the surface roughness is eventually controlled to the desired level, but significant oscillations can be observed in the closed-loop roughness profile and the process takes significantly longer time to reach the desired level (compare Fig.4.5 and Fig.4.11; in Fig.4.5, the surface roughness in the closed-loop simulation reaches the desired level at about $t = 10s$*, but in Fig.4.11, the surface roughness in the closed-loop simulation reaches the desired level at about* $t = 30s$*). To better compare the closed-loop performance using different tuning parameters, the closed-loop roughness profiles shown in Figs.4.5 and 4.11 are shown together in Fig.4.13. Also, many other sets of tuning parameters for the PI controller were tested and it is difficult to simultaneously achieve short transient time and reduced oscillation when control of the surface roughness is performed using discrete roughness measurements.*

Remark 4.6 *The effect of time delays in the measurements of surface roughness on the closed-loop system performance under the developed estimator/controller structure was also evaluated. To this end, we applied the estimator/controller structure (the pa-*

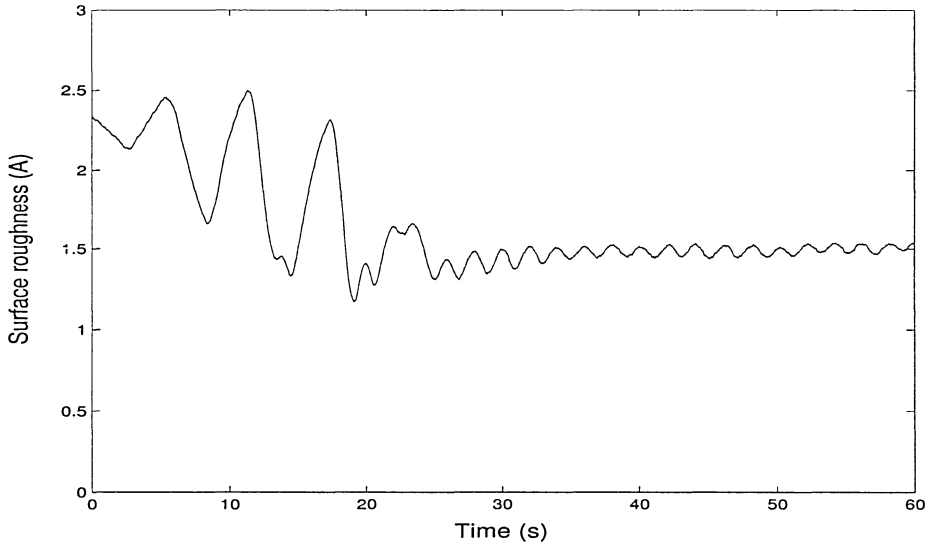

Figure 4.11: Evolution of the surface roughness under feedback control without roughness estimator.

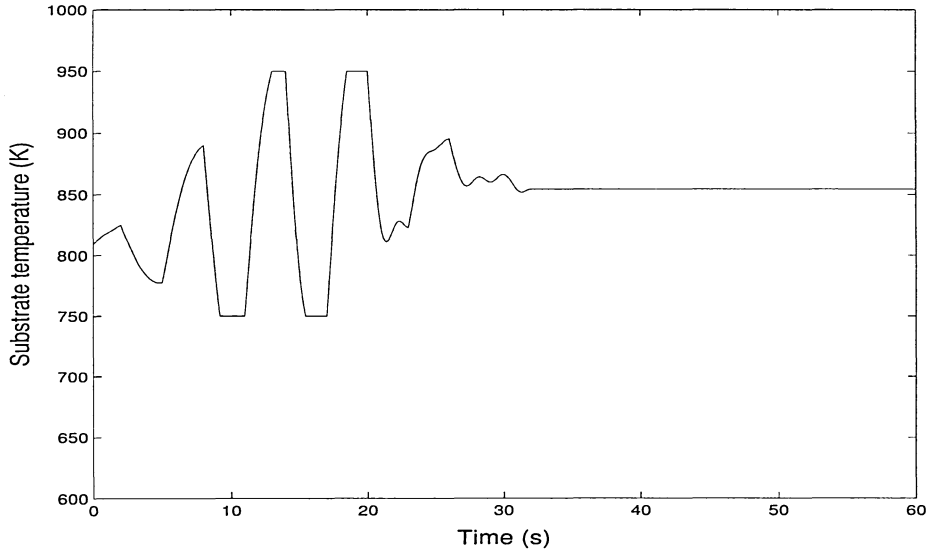

Figure 4.12: Evolution of the substrate temperature under feedback control without roughness estimator.

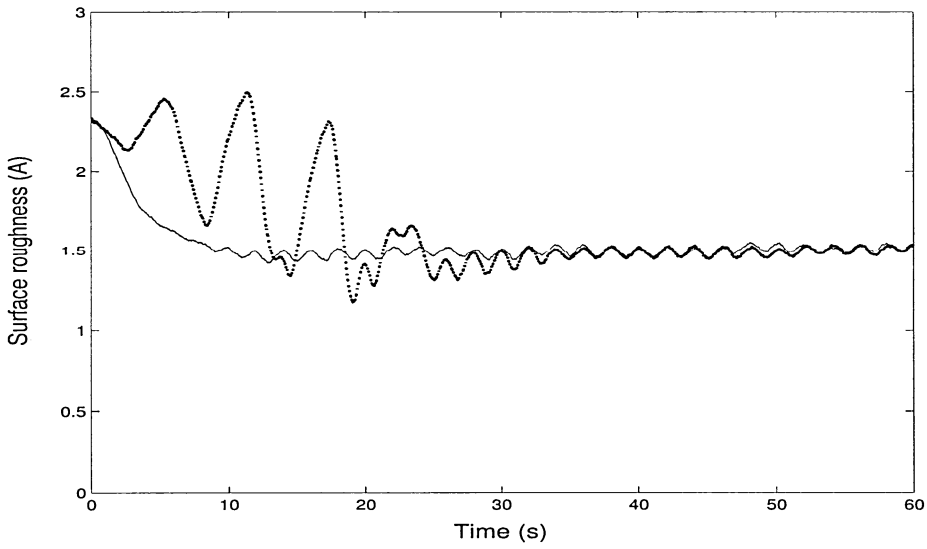

Figure 4.13: Comparison of roughness profiles: (1) roughness profile under feedback control based on the roughness estimator (solid line) and (2) roughness profile under feedback control without roughness estimator with controller parameters $K_c = 5K/\text{Å}$, $\tau_c = 1.0s$.

rameters of the roughness estimator and the PI controller are shown in Table 4.3) to the process model based on a 150×150*-lattice kinetic Monte-Carlo simulator assuming that the new roughness measurements are available every* 3.0 *seconds but with a time-delay of* $t_d = 3.0s$*. The resulting profiles of surface roughness and substrate temperature are shown in Figs.4.14 and 4.15. The developed estimator/controller structure successfully drives the surface roughness to the desired level in the presence of a large time-delay in the roughness measurements.*

Remark 4.7 *To show that the estimator/controller structure is able to control the surface roughness independently of the frequency at which the roughness measurements are available, the developed estimator/controller structure was implemented without using roughness measurements, i.e. the controller determines the substrate temperature based only on the output of the kinetic Monte-Carlo simulator which uses six small-lattice models and the adaptive filter. Figs.4.16 and 4.17 show the resulting profiles of surface roughness and substrate temperature. The simulation results show that*

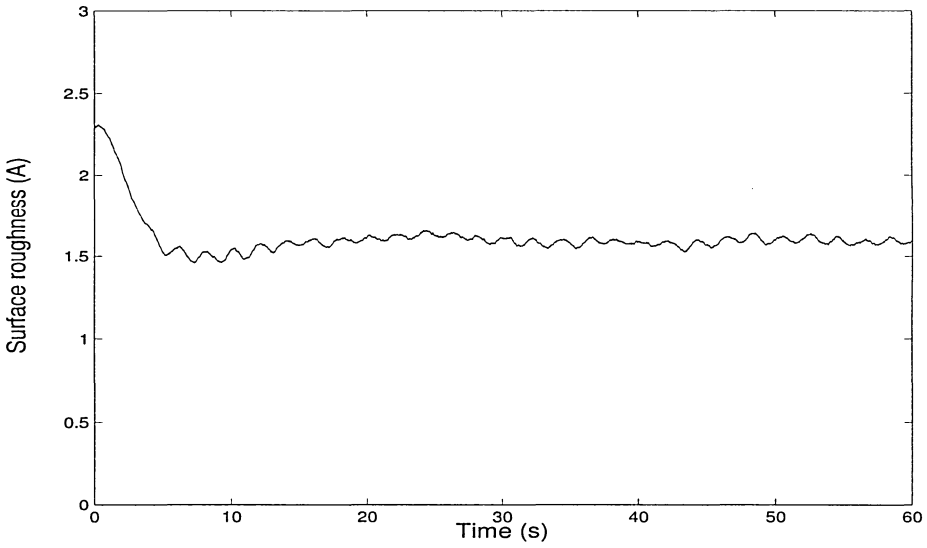

Figure 4.14: Evolution of the surface roughness under feedback control based on the roughness estimator - delayed roughness measurements.

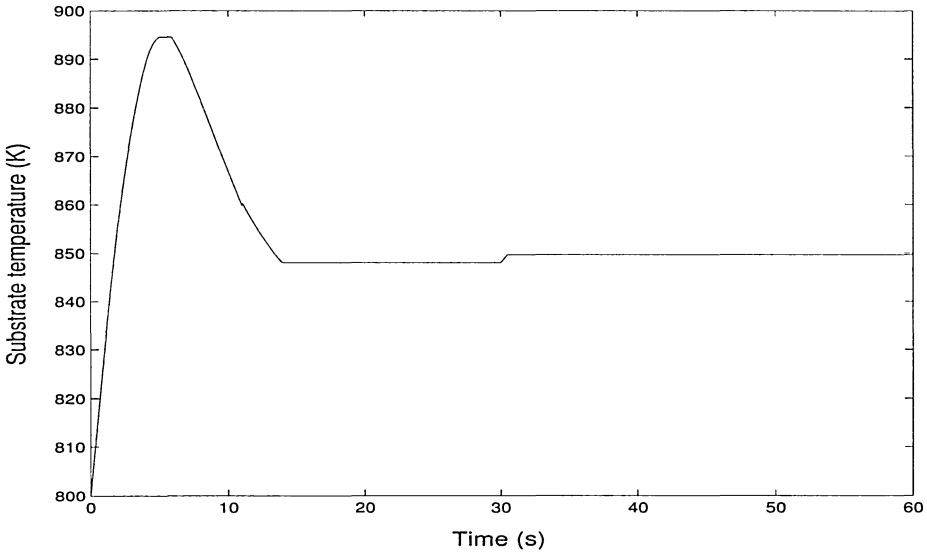

Figure 4.15: Evolution of the substrate temperature under feedback control based on the roughness estimator - delayed roughness measurements.

this open-loop implementation of the controller/estimator structure (with parameters shown in Table 4.3) successfully drives the surface roughness to the desired level.

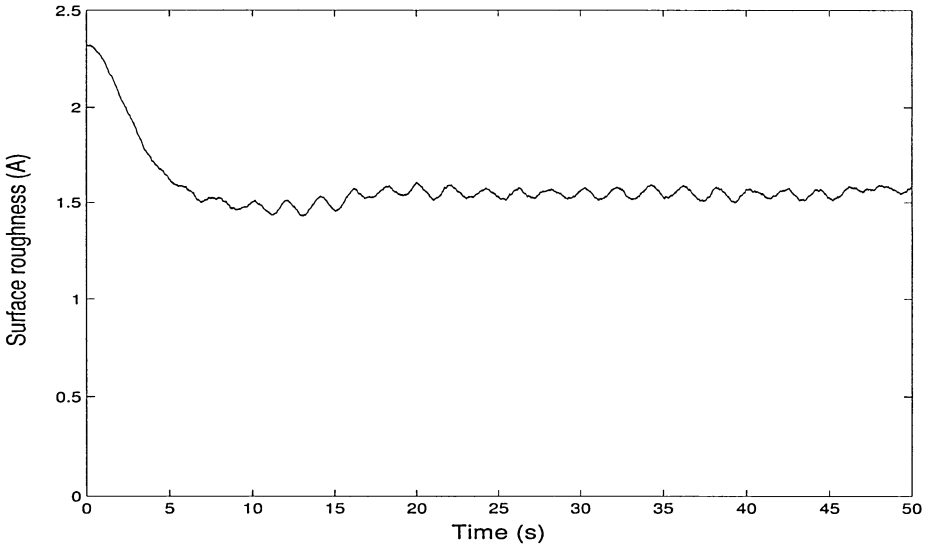

Figure 4.16: Evolution of the surface roughness under open-loop implementation of the estimator/controller structure.

Remark 4.8 *Note, although we demonstrate the effectiveness of the estimator/controller structure by applying it to a kMonte-Carlo process model using a large lattice, the results obtained from our numerical simulations are indicative of the application of the proposed estimator/controller structure to actual GaAs MOCVD processes. The reasons are: 1) the kMonte-Carlo model is validated by using experimental data, and 2) the estimator/controller structure has very good robustness properties with respect to significant model parameter uncertainty, therefore, possible unmodelled dynamics will not significantly deteriorate the closed-loop performance.*

4.5 Conclusions

In this chapter, the methodology presented in Chapter 2 was used to study estimation and control of surface roughness of $GaAs$ (001) thin films during deposition in

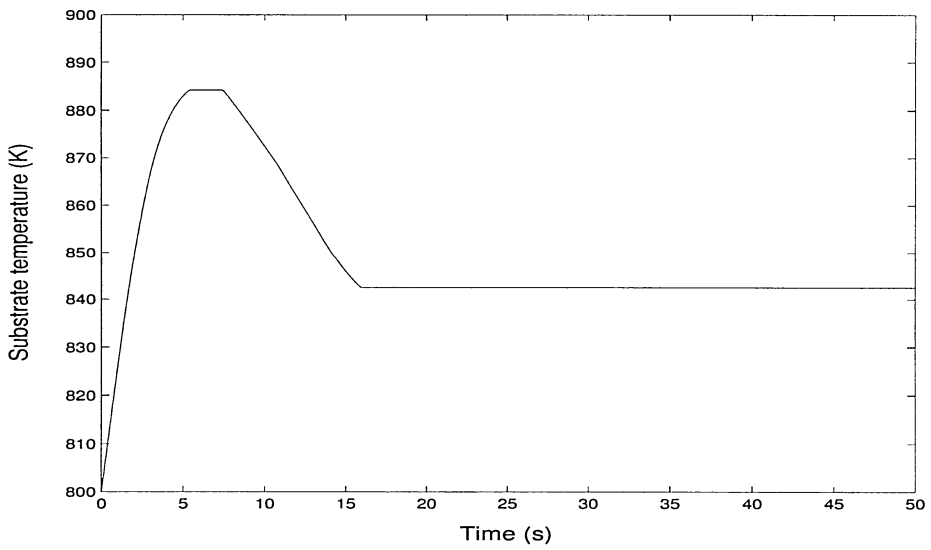

Figure 4.17: Evolution of the substrate temperature under open-loop implementation of the estimator/controller structure.

a horizontal-flow quartz reactor using $TIBGa$ and $TBAs$ as precursors and H_2 as the carrier gas. The adsorption of $TIBGa$ onto the surface and the migration of Ga atoms on the surface were considered as the two rate-limiting steps in the film growth and were explicitly modelled within a kinetic Monte-Carlo simulation framework. The energy barrier and the pre-exponential factor of the migration rate of Ga atoms on the surface used in the simulations were initially determined by fitting the simulation results to experimental data reported in Law et al. (2000). Then, a roughness estimator was constructed that provided estimates of the surface roughness of the $GaAs$ thin films at a time-scale comparable to the real-time evolution of the process using discrete on-line roughness measurements. The estimator involves a kinetic Monte-Carlo simulator based on multiple small-lattice models, an adaptive filter used to reduce roughness stochastic fluctuations and an error compensator used to reduce the error between the roughness estimates and the roughness measurements. The roughness estimates are then used as input to a PI feedback controller that controls

the surface roughness to a desired level by manipulating the substrate temperature. Application of the proposed estimator/controller structure to the process model based on a large-lattice kinetic Monte-Carlo simulator demonstrated successful control of the surface roughness. The proposed approach was shown to be superior to only PI control with direct use of the measured discrete roughness. The reason being that the available measurement techniques do not provide measurements at a frequency that is comparable to the time constant of evolution of the dominant film growth dynamics.

Chapter 5

Feedback Control of Surface Roughness Using Stochastic PDEs

5.1 Introduction

In a thin film growth process, the film is directly formed from microscopic random processes (e.g., particle adsorption, desorption, migration and surface reaction). Therefore, the stochastic nature of thin film growth processes must be fully considered in the modeling and control of the surface roughness of thin films. The desire to understand and control the thin film micro-structure has motivated extensive research on fundamental mathematical models describing the deposition processes, which include 1) kinetic Monte-Carlo methods (e.g., Gillespie, 1976; Fichthorn and Weinberg, 1991; Lam and Vlachos, 2001), and 2) stochastic partial differential equations (PDEs) (e.g., Edwards and Wilkinson, 1982; Villain, 1991; Vvedensky et al., 1993).

In Chapter 2 and 3, a methodology for feedback control of thin film growth using kinetic Monte-Carlo models has been developed. The methodology leads to the design of (a) real-time roughness estimators by using multiple small lattice kinetic

Monte-Carlo simulators, adaptive filters and measurement error compensators, and (b) feedback controllers based on the real-time roughness estimators. In Chapter 4, the method was successfully applied to control surface roughness in a $GaAs$ deposition process using an experimentally determined kinetic Monte-Carlo process model.

However, the fact that kinetic Monte-Carlo models are not available in closed-form makes very difficult to perform model-based controller design directly on the basis of kinetic Monte-Carlo models. To achieve better closed-loop performance, it is desirable to design feedback controllers on the basis of deposition process models. This motivates research on feedback control of deposition processes based on stochastic PDE models of thin film growth.

Stochastic PDE models have been developed to describe the evolution of the height profile for surfaces in a variety of physical and chemical processes. Examples include deposition processes including adsorption and surface relaxation (Edwards and Wilkinson, 1982; Vvedensky, 2003), crystal growth from atomic-beams with and without desorption (Villain, 1991), epitaxial growth processes with adsorption, desorption and surface migration (Vvedensky et al., 1993), surface erosion by ion sputtering (Cuerno et al., 1995) and ZrO_2 thin film growth by reactive ion beam sputtering (Qi et al., 2003).

This chapter presents a method for feedback control of surface roughness in deposition processes, based on stochastic PDEs which describe the fluctuation of surface height in the spatial domain. To demonstrate the method, we focus on control of surface roughness in a deposition process on a 1-dimensional lattice, whose fluctuation of surface height can be described by the Edwards-Wilkinson equation, a second-order stochastic PDE. We initially reformulate the stochastic PDE into a system of infinite stochastic ordinary differential equations by using modal decomposition. A finite-

dimensional approximation of the Edwards-Wilkinson equation is then derived that captures the dominant mode contribution to the surface roughness. A state feedback controller is designed based on the finite-dimensional approximation to control the surface roughness. Analysis of the closed-loop system shows that the controller can drive the surface roughness governed by the infinite-dimensional system to desired levels. The effectiveness of the proposed method is demonstrated by numerical simulations.

5.2 Preliminaries

We consider a deposition process on a 1-dimensional lattice. In this process, particles land on the surface at a rate, r_a. The rules for the deposition are as follows: a site, l, is first randomly picked among the sites of the whole lattice and the deposition site is determined according to the following rules: 1) if the height of this site is lower than or equal to that of both each nearest neighbors, this site is picked as the deposition site; 2) if the height of only one of the two nearest neighbor sites is lower than that of the original site, deposition is on that site; 3) if the height of each one of the nearest neighbor sites is lower than that of the original site, the deposition site is randomly picked with equal probability between the two nearest neighbor sites. A schematic of the rules of the deposition is shown in Fig.5.1. There is no particle migration and desorption taking place on this process (see Lou and Christofides, 2003a,b, for film growth processes that involve these phenomena).

The deposition process is a stochastic process. Kinetic Monte-Carlo simulation can be used to predict the evolution of the surface configuration in this process. The kinetic Monte-Carlo model of the deposition process is a first-principle model in the sense that the deposition rules can be explicitly considered in the model. Mathe-

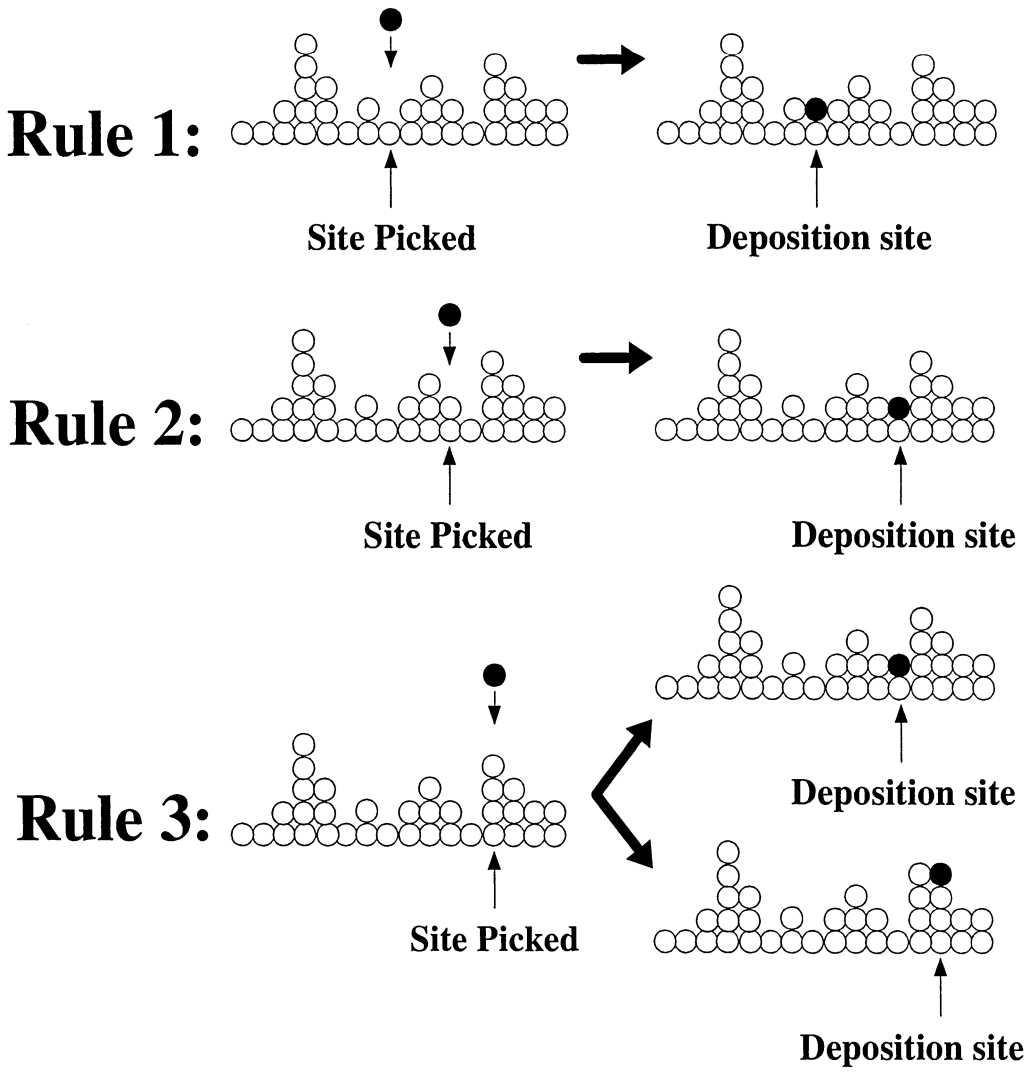

Figure 5.1: Schematic of the rules of the deposition.

matically, kinetic Monte-Carlo simulation methods provide an unbiased realization of the master equation (Gillespie, 1976; Van Kampen, 1992), which describes the evolution of the probability that the surface is at a certain configuration. Kinetic Monte-Carlo simulation can predict average properties of the surface from a deposition process (which are of interest from a control point of view, like, for example, surface roughness). Since a kinetic Monte-Carlo simulation run constitutes a realization of a stochastic process, simulation results from different simulation runs are not identical. However, by averaging the results from different simulation runs, the averaged properties of the surface converge to the values obtained from the solution of the master equation.

However, kinetic Monte-Carlo models are not available in closed-form, which prohibits their use for model-based control design. As an alternative, closed-form stochastic PDE models can be derived based on the deposition rules to describe the evolution of the surface configuration, which is consistent to that predicted by kinetic Monte-Carlo models. In this work, we focus on model-based feedback control design for surface roughness control using a stochastic PDE model of the deposition process described in Fig.5.1. The equation for the height fluctuations of the surface in this deposition process was first developed by (Edwards and Wilkinson, 1982). Recently, the same equation was derived directly from the microscopic transition rules of the process (Vvedensky, 2003).

Specifically, the height fluctuation of the surface is described by the following stochastic partial differential equation:

$$\frac{\partial h}{\partial t} = a^2 r_a \frac{\partial^2 h}{\partial x^2} + \xi(x,t) \tag{5.1}$$

where $x \in [-\pi, \pi]$ is the spatial coordinate, t is the time, $h(x,t)$ is the height of the surface at position x and time t, a is the lattice size and $\xi(x,t)$ is a Gaussian noise

with zero mean and covariance:

$$\langle \xi(x,t)\xi(x',t') \rangle = \varsigma^2 \delta(x-x')\delta(t-t') \tag{5.2}$$

where $\varsigma^2 = a^3 r_a$, $\delta(\cdot)$ is the dirac function, and $\langle \cdot\cdot \rangle$ denotes the average. Note that the noise covariance depends on both space x and time t.

The surface roughness, r, is given by the following expression:

$$r(t) = \sqrt{\frac{1}{2\pi}\int_{-\pi}^{\pi} [h(x,t) - \bar{h}(t)]^2 dx} \tag{5.3}$$

where $\bar{h}(t) = \frac{1}{2\pi}\int_{-\pi}^{\pi} h(x,t)dx$ is the average surface height.

Our objective is to control the surface roughness of the deposition process described by Fig.5.1. The controller design is based on the SPDE model of the process (Eqs.5.1 and 5.2). To do this, we formulate a distributed control problem in the spatial domain $[-\pi, \pi]$. The control problem is described by the following stochastic partial differential equation:

$$\frac{\partial h}{\partial t} = \nu \frac{\partial^2 h}{\partial x^2} + \sum_{i=1}^{p} b_i(x) u_i(t) + \xi(x,t) \tag{5.4}$$

subject to periodic boundary conditions:

$$\frac{\partial^j h}{\partial x^j}(-\pi, t) = \frac{\partial^j h}{\partial x^j}(\pi, t), \quad j = 0, 1 \tag{5.5}$$

and the initial condition:

$$h(x,0) = h_0(x) \tag{5.6}$$

where $\nu = a^2 r_a$, u_i is the ith manipulated input, p is the number of manipulated inputs and b_i is the ith actuator distribution function (i.e., b_i determines how the control action computed by the ith control actuator, u_i, is distributed (e.g., point or distributed actuation) in the spatial interval $[-\pi, \pi]$).

To study the dynamics of Eq.5.4, we initially consider the eigenvalue problem of the linear operator of Eq.5.4, which takes the form:

$$\begin{aligned} A\bar{\phi}_n(x) &= \nu\frac{d^2\bar{\phi}_n(x)}{dx^2} = \lambda_n\bar{\phi}_n(x), \quad n = 1, \cdots, \infty, \\ \frac{d^j\bar{\phi}_n}{dx^j}(-\pi) &= \frac{d^j\bar{\phi}_n}{dx^j}(\pi), \qquad\qquad j = 0, 1 \end{aligned} \tag{5.7}$$

where λ_n denotes an eigenvalue and $\bar{\phi}_n$ denotes an eigenfunction. A direct computation of the solution of the above eigenvalue problem yields $\lambda_0 = 0$ with $\psi_0 = 1/\sqrt{2\pi}$, and $\lambda_n = -\nu n^2$ (λ_n is an eigenvalue of multiplicity two) with eigenfunctions $\phi_n = (1/\sqrt{\pi})\sin(nx)$ and $\psi_n = (1/\sqrt{\pi})\cos(nx)$ for $n = 1, \cdots, \infty$. From the solution of the eigenvalue problem shown in Eq.5.7, it follows that for a fixed value of $\nu > 0$ the distance between two consecutive eigenvalues (i.e., λ_n and λ_{n+1}) increases as n increases. Furthermore, the eigenspectrum of operator A in Eq.5.7, $\sigma(A)$ can be partitioned as $\sigma(A) = \sigma_1(A) \bigcup \sigma_2(A)$, where $\sigma_1(A)$ contains the first m (with m finite) eigenvalues (i.e., $\sigma_1(A) = \{\lambda_1, \ldots, \lambda_m\}$) and $\sigma_2(A)$ contains the remaining eigenvalues (i.e., $\sigma_2(A) = \{\lambda_{m+1}, \ldots, \}$.

To present the method that we use to control the stochastic PDE of Eq.5.4, we first derive stochastic ODE approximations of Eq.5.4 using modal decomposition. To this end, we first expand the solution of Eq.5.4 in an infinite series in terms of the eigenfunctions of the operator of Eq.5.7 as follows:

$$h(x,t) = \sum_{n=1}^{\infty} \alpha_n(t)\phi_n(x) + \sum_{n=0}^{\infty} \beta_n(t)\psi_n(x) \tag{5.8}$$

where $\alpha_n(t)$, $\beta_n(t)$ are time-varying coefficients. Substituting the above expansion for the solution, $h(x,t)$, into Eq.5.4 and taking the inner product with the adjoint eigenfunctions, $\phi_n^*(z) = (1/\sqrt{\pi})\sin(nz)$ and $\psi_n^*(z) = (1/\sqrt{\pi})\cos(nz)$, the following

system of infinite stochastic ODEs is obtained:

$$\begin{aligned}\frac{d\alpha_n}{dt} &= -\nu n^2\alpha_n + \sum_{i=1}^{p} b_{i\alpha_n} u_i(t) + \xi_\alpha^n(t) \\ \frac{d\beta_n}{dt} &= -\nu n^2\beta_n + \sum_{i=1}^{p} b_{i\beta_n} u_i(t) + \xi_\beta^n(t); \quad n = 1, \ldots, \infty\end{aligned} \tag{5.9}$$

where $b_{i\alpha_n} = \int_{-\pi}^{\pi} \phi_n(x) b_i(x) dx$, $b_{i\beta_n} = \int_{-\pi}^{\pi} \psi_n(x) b_i(x) dx$, $\xi_\alpha^n(t) = \int_{-\pi}^{\pi} \xi(x,t)\phi_n(x) dx$, $\xi_\beta^n(t) = \int_{-\pi}^{\pi} \xi(x,t)\ \psi_n(x) dx$.

The covariances of $\xi_\alpha^n(t)$ and $\xi_\beta^n(t)$ can be computed by using the following result (Åström, 1970):

Result 5.1 *If (1) $f(x)$ is a deterministic function, (2) $\eta(x)$ is a random variable with $\langle \eta(x) \rangle = 0$ and covariance $\langle \eta(x)\eta(x') \rangle = \sigma^2\delta(x-x')$, and (3) $\epsilon = \int_a^b f(x)\eta(x)dx$, then ϵ is a random number with $\langle \epsilon \rangle = 0$ and covariance $\langle \epsilon^2 \rangle = \sigma^2 \int_a^b f^2(x)dx$.*

Using Result 5.1, we obtain $\langle \xi_\alpha^n(t)\xi_\alpha^n(t') \rangle = \varsigma^2\delta(t-t')$ and $\langle \xi_\beta^n(t)\xi_\beta^n(t') \rangle = \varsigma^2\delta(t-t')$.

In this work, the controlled variable is the expected value of surface roughness, $\sqrt{\langle r^2 \rangle}$. According to Eq.5.8, we have $\bar{h}(t) = \beta_0(t)\psi_0$. Therefore, $\sqrt{\langle r^2 \rangle}$ can be rewritten in terms of α_n and β_n as follows:

$$\begin{aligned}\sqrt{\langle r^2 \rangle} &= \sqrt{\frac{1}{2\pi}\langle \int_{-\pi}^{\pi} (h(x,t) - \bar{h}(t))^2 dx \rangle} \\ &= \sqrt{\frac{1}{2\pi}\langle \int_{-\pi}^{\pi} \sum_{i=1}^{\infty} \left[\alpha_i(t)^2\phi_i(x)^2 + \beta_i(t)^2\psi_i(x)^2\right] dx \rangle} \\ &= \sqrt{\frac{1}{2\pi}\langle \sum_{i=1}^{\infty} (\alpha_i^2 + \beta_i^2) \rangle} = \sqrt{\frac{1}{2\pi}\sum_{i=1}^{\infty} \left[\langle \alpha_i^2 \rangle + \langle \beta_i^2 \rangle\right]}\end{aligned} \tag{5.10}$$

Therefore, the surface roughness control problem for the stochastic PDE system of Eq.5.4 is formulated as the one of controlling the covariance of the states α_n and β_n of the system of infinite stochastic ODEs of Eq.5.9.

Remark 5.1 *Note that in practice, the control action, u_i, can be implemented by manipulating the gas composition across the surface in a deposition process. Spatially*

controllable CVD reactors have been developed to enable across-wafer spatial control of surface gas composition during deposition (Adomaitis et al., 2003). In such a control problem formulation, the rate that particles land on the surface is spatially distributed and is computed by the controller. However, the value of r_a, which is used to calculate the values of ν and the covariance, ς in the system of Eq. 5.4, corresponds to the adsorption rate under open-loop operation, and thus, it is a constant. The contribution of the spatially distributed adsorption rate to the fluctuations of the surface height profile (e.g., the surface roughness) is captured by the term $\sum_{i=1}^{p} b_i(x)u_i(t)$. This control problem formulation is further supported by our simulation results that the controller designed based on the stochastic PDE model of the deposition process can be applied to the kinetic Monte-Carlo model of the same deposition process to control the surface roughness to desired levels (see simulation results section).

5.3 Feedback control

In this section, we design a linear state feedback controller for the system of Eq.5.9 to regulate the surface roughness defined in Eq.5.10 to a desired level.

5.3.1 Model reduction

Owing to its infinite-dimensional nature, the system of Eq.5.9 cannot be directly used for the design of controllers that can be implemented in practice (i.e., the practical implementation of controllers which are designed on the basis of this system will require the computation of infinite sums which cannot be done by a computer). Instead, we base the controller design on finite-dimensional approximations of this system. Subsequently, we will show that the resulting controller will enforce the desired control objective in the closed-loop infinite-dimensional system.

Specifically, we rewrite the system of Eq.5.9 as follows:

$$\begin{aligned} \frac{dx_s}{dt} &= \Lambda_s x_s + B_s u + \xi_s \\ \frac{dx_f}{dt} &= \Lambda_f x_f + B_f u + \xi_f \end{aligned} \tag{5.11}$$

where $x_s = [\ \alpha_1 \ \cdots \ \alpha_m \ \ \beta_1 \ \cdots \ \beta_m\ ]^T$, x_f=$[\alpha_{m+1}\ \beta_{m+1} \cdots\ ]^T$, Λ_s=$diag[-\nu \cdots -m^2\nu\ -\nu \cdots -m^2\nu]$, Λ_f=$diag[-(m+1)^2\nu\ -(m+1)^2\nu \cdots]$, $u = [\ u_1 \ \cdots \ u_p\ ]$, $\xi_s = [\ \xi_\alpha^1 \ \cdots \ \xi_\alpha^m \ \ \xi_\beta^1 \ \cdots \ \xi_\beta^m\ ]$, and $\xi_f = [\xi_\alpha^{m+1}\ \xi_\beta^{m+1} \cdots]$.

$$B_s = \begin{bmatrix} b_{1_{\alpha_1}} & \cdots & b_{p_{\alpha_1}} \\ \vdots & \ddots & \vdots \\ b_{1_{\alpha_m}} & \cdots & b_{p_{\alpha_m}} \\ b_{1_{\beta_1}} & \cdots & b_{p_{\beta_1}} \\ \vdots & \ddots & \vdots \\ b_{1_{\beta_m}} & \cdots & b_{p_{\beta_m}} \end{bmatrix} \quad B_f = \begin{bmatrix} b_{1_{\alpha_{m+1}}} & \cdots & b_{p_{\alpha_{m+1}}} \\ b_{1_{\beta_{m+1}}} & \cdots & b_{p_{\beta_{m+1}}} \\ b_{1_{\alpha_{m+2}}} & \cdots & b_{p_{\alpha_{m+2}}} \\ b_{1_{\beta_{m+2}}} & \cdots & b_{p_{\beta_{m+2}}} \\ \vdots & \vdots & \vdots \end{bmatrix} \tag{5.12}$$

We note that the subsystem x_f in Eq.5.11 is infinite-dimensional.

Neglecting the x_f subsystem, the following $2m$-dimensional system is obtained:

$$\frac{d\tilde{x}_s}{dt} = \Lambda_s \tilde{x}_s + B_s u + \xi_s \tag{5.13}$$

where the tilde symbol in $\tilde{x}_s$ denotes that this state variable is associated with a finite-dimensional system.

5.3.2 Feedback controller design

We design the state feedback controller on the basis of the finite-dimensional system of Eq.5.13. To simplify our development, we assume that $p = 2m$ and pick the actuator distribution functions such that B_s^{-1} exists. The state feedback control law then takes the form:

$$u \ = \ B_s^{-1} \left(\Lambda_{cs} - \Lambda_s\right) \tilde{x}_s \tag{5.14}$$

where the matrix Λ_{cs} contains the desired poles of the closed-loop system; $\Lambda_{cs} = diag[\lambda_{c\alpha 1} \cdots \lambda_{c\alpha m} \ \lambda_{c\beta 1} \cdots \lambda_{c\beta m}]$, $\lambda_{c\alpha i}$ and $\lambda_{c\beta i}$ $(1 \leq i \leq m)$ are desired poles of the closed-loop finite-dimensional system, which can be computed from the desired closed-loop surface roughness level.

We first analyze the dependence of the covariances of the states α_n and β_n $(n = 1, \cdots, m)$ on the poles of the finite-dimensional system of Eq.5.13. Then, we will show in the next subsection that the surface roughness of the infinite-dimensional system of Eq.5.9 can be controlled to a desired level by using the state feedback controller of Eq.5.14, which only uses a finite number of actuators.

By applying the controller of Eq.5.14 to the system of Eq.5.13, the closed-loop system takes the form:

$$\frac{d\tilde{x}_s}{dt} = \Lambda_{cs}\tilde{x}_s + \xi_s(t) \tag{5.15}$$

To analyze the effect of the feedback controller on the covariance of the state $\tilde{x}_s$, we discretize Eq.5.15 in the time domain, using Δt as time step, as follows:

$$X_s(k+1) \ = \ G_{cs}X_s(k) + \zeta_s(k); \quad k = 0, \cdots, \infty \tag{5.16}$$

where $X_s(k) = \tilde{x}_s(k\Delta t)$, $G_{cs} = e^{\Lambda_{cs}\Delta t}$, $\zeta_s(k) = \int_{k\Delta t}^{(k+1)\Delta t} e^{\Lambda_{cs}((k+1)\Delta t - t)}\xi_s(t)dt$. According to (Åström, 1970, Chapter 3), if all eigenvalues of G_{cs} are within the unit circle on the complex plane, the covariance matrix of $X_s(k)$, $P(k) = \langle X_s(k)X_s(k)^T \rangle$ converges to $P(\infty)$, which is the solution of the following equation:

$$P(\infty) = G_{cs}P(\infty)G_{cs}^T + R_1 \tag{5.17}$$

where $R_1 = \langle \zeta_s \zeta_s^T \rangle$. Eq.5.17 can not be solved, in general, analytically. However, for the specific deposition system considered in this work, the analytical solution for $P(\infty)$ can be obtained as follows:

$$P(\infty) = \begin{bmatrix} P_\alpha(\infty) & 0 \\ 0 & P_\beta(\infty) \end{bmatrix} \tag{5.18}$$

where $P_\alpha(\infty) = diag[\ \langle\alpha_1(\infty)^2\rangle \ \cdots \ \langle\alpha_m(\infty)^2\rangle\ ]$, $P_\beta(\infty) = diag[\ \langle\beta_1(\infty)^2\rangle \cdots \langle\beta_m(\infty)^2\rangle]$. Using Result 1, $\langle\alpha_n(\infty)^2\rangle$ and $\langle\beta_n(\infty)^2\rangle$ $(n = 1, \cdots, m)$ can be computed by using the following expressions:

$$\langle\alpha_n(\infty)^2\rangle = -\frac{\varsigma^2}{2\lambda_{c\alpha_n}}; \quad \langle\beta_n(\infty)^2\rangle = -\frac{\varsigma^2}{2\lambda_{c\beta_n}} \tag{5.19}$$

From Eq.5.19, we can see that by assigning the closed-loop poles $\lambda_{c\alpha_n}$ and $\lambda_{c\beta_n}$ $(n = 1, \cdots, m)$ at desired locations, the covariances of the states α_n and β_n $(n = 1, \cdots, m)$ can be controlled to desired levels. Therefore, according to Eq.5.10, the contribution to the surface roughness from the finite-dimensional system of Eq.5.13 can be controlled to the desired level.

5.3.3 Analysis of the closed-loop infinite-dimensional system

In this subsection, we show that when the state feedback controller of Eq.5.14 is used to manipulate the poles of the finite-dimensional system of Eq.5.13, the contribution to the surface roughness from the α_f and β_f subsystem of the system of Eq.5.11 is bounded and can be made arbitrarily small by increasing the dimension of the x_s subsystem.

By applying the feedback controller of Eq.5.14 into the infinite-dimensional system of Eq.5.11, we obtain the following closed-loop system:

$$\begin{aligned} \frac{dx_s}{dt} &= \Lambda_{cs}x_s + \xi_s \\ \frac{dx_f}{dt} &= \Lambda_\epsilon x_s + \Lambda_f x_f + \xi_f \end{aligned} \tag{5.20}$$

where $\Lambda_\epsilon = B_f B_s^{-1}(\Lambda_{cs} - \Lambda_s)$.

The boundedness of the state of the above system follows directly from the stability of the matrices Λ_{cs} and Λ_f and the structure of the system, where the x_s subsystem is

independent of the x_f state (see Christofides and Daoutidis, 1997; Christofides, 2001b, for results and techniques for analyzing the stability properties of such systems).

Due to the structure of the eigenspectrum of operator A (Section 2), the effect of the control action computed from Eq.5.14 to the poles of the x_f subsystem can be reduced by increasing m. Therefore, by picking m sufficiently large, the $\Lambda_\epsilon x_s$ term can be made very small compared to the $\Lambda_f x_f$ term and thus, the closed-loop system of Eq.5.20 can be adequately described by the following system:

$$\begin{aligned} \frac{dx_s}{dt} &= \Lambda_{cs} x_s + \xi_s \\ \frac{dx_f}{dt} &= \Lambda_f x_f + \xi_f \end{aligned} \tag{5.21}$$

On the basis of the above system, it can be shown that the covariance of the state of the x_f subsystem converges to $[\ \langle \alpha_{m+1}(\infty)^2 \rangle \quad \langle \beta_{m+1}(\infty)^2 \rangle \quad \cdots \quad \cdots\ ]$, where

$$\langle \alpha_n(\infty)^2 \rangle = \frac{\varsigma^2}{2n^2\nu}; \quad \langle \beta_n(\infty)^2 \rangle = \frac{\varsigma^2}{2n^2\nu}; \quad n > m \tag{5.22}$$

Therefore, for m sufficiently large, the overall contribution to the surface roughness from the x_f subsystem in Eq.5.11 can be computed as follows:

$$\frac{\varsigma}{\sqrt{2\pi(m+1)\nu}} < \sqrt{\frac{1}{2\pi} \sum_{n=m+1}^{\infty} \left[\frac{\varsigma^2}{\nu n^2} \right]} < \frac{\varsigma}{\sqrt{2\pi m \nu}} \tag{5.23}$$

Clearly, as $m \to \infty$, the contribution to the surface roughness from the α_f and β_f subsystem goes to zero.

In summary, under the controller of Eq.5.14, the closed-loop surface roughness, for m sufficiently large, can be adequately described by the following expression:

$$\sqrt{\langle r^2 \rangle} = \varsigma \sqrt{\frac{1}{2\pi} \left(\lambda^* + \sum_{n=m+1}^{\infty} \frac{1}{\nu n^2} \right)} \tag{5.24}$$

where $\lambda^* = \sum_{i=1}^{m} \left(-\frac{1}{2\lambda_{c\alpha_i}} - \frac{1}{2\lambda_{c\beta_i}} \right)$.

Remark 5.2 *Note that in order to regulate the surface roughness to a desired level,* $\langle\sqrt{r_d^2}\rangle$*, the number of actuators should be large enough so that the value of* $\langle\sqrt{r_d^2}\rangle$ *is achievable. Specifically, the number of actuators,* m *should be selected such that the following inequality holds:*

$$\sqrt{\langle r_d^2\rangle} > \varsigma\sqrt{\frac{1}{2\pi}\left(\sum_{n=m+1}^{\infty}\frac{1}{\nu n^2}\right)} \tag{5.25}$$

This is because the closed-loop stability requires that $\lambda_{c\alpha_i} < 0$ *and* $\lambda_{c\beta_i} < 0$ *(for* $i = 1, \cdots, m$*), and thus,* $\lambda^* > 0$ *in Eq.5.24.*

Remark 5.3 *Note that to control the closed-loop surface roughness to* $\sqrt{\langle r_d^2\rangle}$*, we need to design a controller to assign the poles of the finite-dimensional system of Eq.5.15 to appropriate values so that the following equation holds:*

$$\lambda^* = \frac{2\pi(\langle r_d^2\rangle - \langle r_f^2\rangle)}{\varsigma^2} \tag{5.26}$$

The controller which assigns the poles of the system of Eq.5.15 to satisfy Eq.5.26 is not unique. Consequently, for a fixed number of actuators, p*, the controller that can regulate the closed-loop surface roughness to a desired level is also not unique. Furthermore, we note that robust control methods (Christofides, 1998; Christofides and Baker, 1999), which utilize bounds of the noise terms, can be employed to design controller that can achieve arbitrary degree of attenuation of the effect of noise on the PDE system state.*

Remark 5.4 *Note that the expected value of the open-loop surface roughness converges to its steady-state value,* $\sqrt{\langle r_{ol}^2\rangle}$*, which can be computed as follows:*

$$\sqrt{\langle r_{ol}^2\rangle} = \sqrt{\frac{\varsigma^2}{2\pi\nu}\left(\sum_{k=1}^{\infty}\frac{1}{k^2}\right)} \tag{5.27}$$

If the closed-loop poles of the finite-dimensional system of Eq.5.15 are written as $\lambda_{c\alpha_k} = -\nu n_{\alpha_k}^2$ *and* $\lambda_{c\beta_k} = -\nu n_{\beta_k}^2$ *for* $k = 1, \cdots, m$*, the ratio of the expected value of the steady-state closed-loop surface roughness,* $\sqrt{\langle r_{cl}^2\rangle}$ *to that of the steady-state*

open-loop surface roughness, $\sqrt{\langle r_{ol}^2 \rangle}$ *can be computed as follows:*

$$\frac{\sqrt{\langle r_{cl}^2 \rangle}}{\sqrt{\langle r_{ol}^2 \rangle}} = \sqrt{\frac{\sum_{k=1}^{m} \left(\frac{1}{n_{\alpha_k}^2} + \frac{1}{n_{\beta_k}^2} \right) + \sum_{k=m+1}^{\infty} \frac{1}{k^2}}{\sum_{k=1}^{\infty} \frac{1}{k^2}}} \tag{5.28}$$

This ratio is independent of the lattice size of the deposition system. Therefore, if the control objective is to achieve a certain percentage of reduction of the value of surface roughness from that under open-loop operation, the number of actuators needed is independent of the lattice size of the deposition process.

Remark 5.5 *Note that it is possible to apply the proposed method to control the surface roughness of deposition processes taking place in 2-dimensional surfaces. In a 2-dimensional process, the feedback control design and the analysis of the closed-loop system will be based on the model of Eq.5.11. Moreover, Eq.5.11 will be obtained by solving the eigenvalue/eigenfunctin problem of the operator A in the 2-dimensional spatial domain with appropriate boundary conditions. After Eq.5.11 is obtained, the method for control design and closed-loop analysis presented above can be applied to control the surface roughness for 2-dimensional surfaces described by stochastic PDEs.*

5.4 Simulation results

In this section, we present an application of the proposed state feedback controller to the deposition process described in Fig.5.1 to regulate the surface roughness to a desired level. Specifically, the deposition occurs on a lattice containing 1000 sites. Therefore, $a = 0.00628$. The open-loop deposition rate for each site is $\bar{r}_a = 1s^{-1}$. A $1000th$ order stochastic ordinary differential equation approximation of the system of Eq.5.4 is used to simulate the process (the use of higher-order approximations led to identical numerical results, thereby implying that the following simulation runs are

independent of the discretization). The δ function involved in the covariances of ξ_α^n and ξ_β^n is approximated by $\frac{1}{\delta t}$.

In the first simulation, we compare the expected value of the open-loop surface roughness of the deposition process from the solution of the stochastic PDE model of Eq.5.1 to that from a kinetic Monte-Carlo simulation. We use the kinetic Monte-Carlo algorithm developed in Gillespie (1976) to simulate the process. First, a random number is generated to pick a site among all the sites on the 1-D lattice. If the height of this site is lower than or equal to that of both each nearest neighbors, this site is picked as the deposition site and the height of this site increases by a; if the height of only one of the two nearest neighbor sites is lower than that of the original site, deposition is on that site and the height of that site increases by a; if the height of each one of the nearest neighbor sites is lower than that of the original site, a second random number is generated to randomly pick one of the two nearest neighbors with equal probability and the height of the picked site increases by a. Upon an executed event, a time increment, dt, is computed by $dt = \frac{-\ln \zeta}{N \times r_a}$, where ζ is a random number in the $(0, 1)$ interval and N is the total number of sites on the lattice.

The profiles of expected surface roughness are obtained by averaging surface roughness profiles (either from the stochastic PDE or the kinetic Monte-Carlo simulations) from 1000 independent simulation runs by using the same simulation parameters. Fig.5.2 shows the simulation results. The two profiles reflect the same tendency of the evolution of the surface roughness. However, the expected surface roughness from the solution of the stochastic PDE model of Eq.5.1 is about 9% lower than that from the kinetic Monte-Carlo simulation. This difference of expected surface roughness from the two models is due to approximations made during the derivation of the stochastic PDE model of the deposition process based on the master equation and

the transition rules (see Remark 5.6 for a discussion on this problem). However, this model error can be compensated by appropriately adjusting the value of covariance of Eq.5.2. In the second simulation run, we increase the value of ς in Eq.5.2 by 9% (ς is increased from 4.98×10^{-4} to 5.43×10^{-5}) and show the comparison of the profiles of expected surface roughness from the kinetic Monte-Carlo simulation and from the solution of the stochastic PDE model in Fig.5.3. We can see that with this adjustment of ς, the two profiles are almost identical. Therefore, by slightly adjusting the covariance of the stochastic PDE model of Eq.5.1, the model can adequately capture the evolution of surface roughness of the deposition process described in Fig.5.1 obtained by the kinetic Monte-Carlo simulations. Therefore, our control design will be based on the stochastic PDE model of the process with adjusted ς.

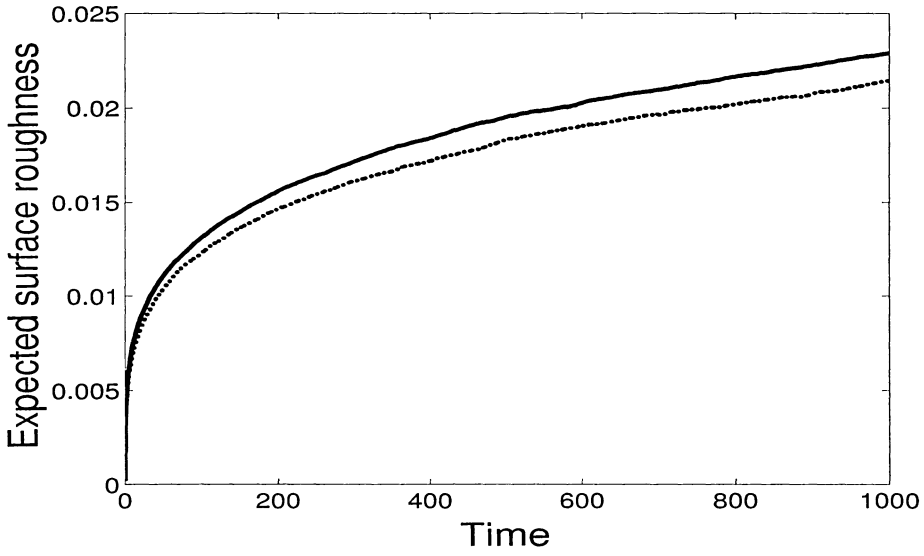

Figure 5.2: Comparison of the open-loop profile of the expected surface roughness from the kinetic Monte-Carlo simulator (solid line) and that from the solution of the SPDE using 1000 modes (dotted line).

Subsequently, we design a state feedback controller based on a $40th$ order stochastic ODE approximation constructed by using the first 40 eigenmodes of the system of

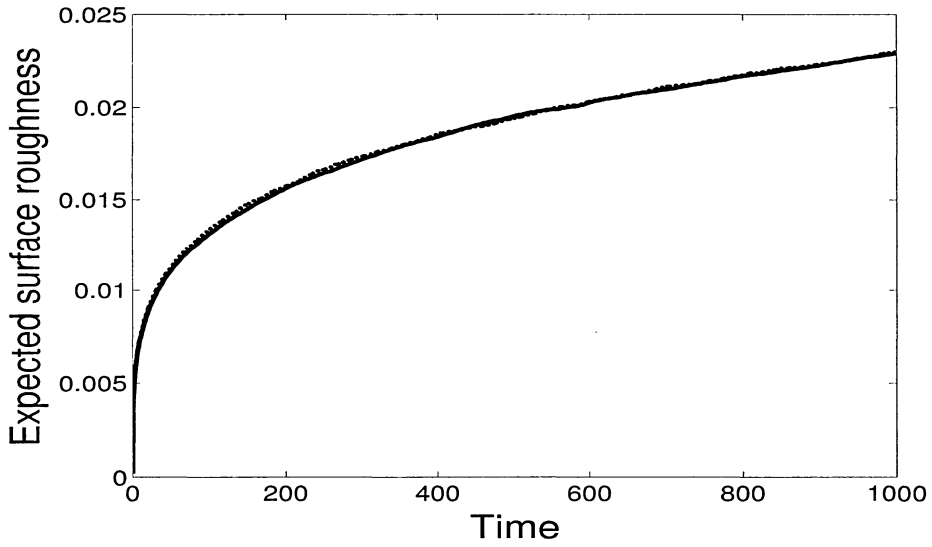

Figure 5.3: Comparison of the open-loop profile of the expected surface roughness from the kinetic Monte-Carlo simulator (solid line) and that from the solution of the SPDE, with adjusted covariance, using 1000 modes (dotted line).

Eq.5.9 with adjusted value of the covariance. 40 control actuators are used to control the system. The ith actuator distribution function is taken to be:

$$b_i(z) = \begin{cases} \frac{1}{\sqrt{\pi}} \sin(iz); & i = 1, \cdots, 20 \\ \frac{1}{\sqrt{\pi}} \cos[(i-20)z]; & i = 21, \cdots, 40 \end{cases} \tag{5.29}$$

The expected open-loop surface roughness converges to 0.045, which can be computed using Eq.5.27. The desired closed-loop surface roughness is 0.01 in this simulation, which is a 78% reduction compared to the open-loop surface roughness. Using Eq.5.24, we design the state feedback controller such that $\lambda_{c\alpha_i} = \lambda_{c\beta_i} = -0.023$, for $i = 1, \cdots, 20$. Then, we apply the designed controller to the kinetic Monte-Carlo model of the deposition process to control the surface roughness to the desired level. In this simulation, the controller is implemented by manipulating the adsorption rate of particles across the surface. Specifically, the adsorption rate on site i at time t is

determined according to the following expression:

$$r_a(i,t) = \bar{r}_a + \left(\sum_{j=1}^{40} b_j(z_i) u_j(t) \right) / a \tag{5.30}$$

The following simulation algorithm is used to run the kinetic Monte-Carlo simulations for the closed-loop system. First, a random number is generated to pick a site among all the sites on the 1-D lattice; the probability that a surface site is picked is proportional to the adsorption rate on this site, which is computed using Eq.5.30. If the height of this site is lower than or equal to that of both each nearest neighbors, this site is picked as the deposition site and the height of this site increases by a; if the height of only one of the two nearest neighbor sites is lower than that of the original site, deposition is on that site and the height of that site increases by a; if the height of each one of the nearest neighbor sites is lower than that of the original site, a second random number is generated to randomly pick one of the two nearest neighbors with equal probability and the height of the picked site increases by a. Upon an executed event, a time increment, dt, is computed by $dt = -\ln\zeta / \left(\sum_{i=1}^{N} \times r_a(i) \right)$, where ζ is a random number in the $(0,1)$ interval and N is the total number of sites on the lattice. Once a particle is deposited, the first 40 states ($\alpha_1, \cdots, \alpha_{20}$ and $\beta_1, \cdots, \beta_{20}$) are updated and new control actions are computed to update the spatially distributed adsorption rate across the surface. The closed-loop system simulation results are shown in Fig.5.4. The dotted line shows the expected surface roughness, which is the average of surface roughness profiles obtained from 200 independent runs, under feedback control. We can see that the controller successfully drives the expected surface roughness to the desired level. The solid line shows the surface roughness profile under feedback control from one simulation run; due to the stochastic nature of the deposition process, stochastic fluctuations can be observed in the closed-loop surface roughness profile, but the surface roughness is very close to the set-point

value under feedback control. For the sake of comparison, the dashed-line shows a surface roughness profile from one open-loop simulation run. We can see that under feedback control, a much lower surface roughness can be achieved. Finally, we note that the proposed approach for controller design can be, in principle, applied to larger scale deposition processes to control surface roughness. In such a case, the stochastic PDE model can be constructed by initially deriving a stochastic PDE model based on the transition rules and then fitting the model parameters based on experimental roughness data of the specific deposition process (see also the discussion in Remark 5.4).

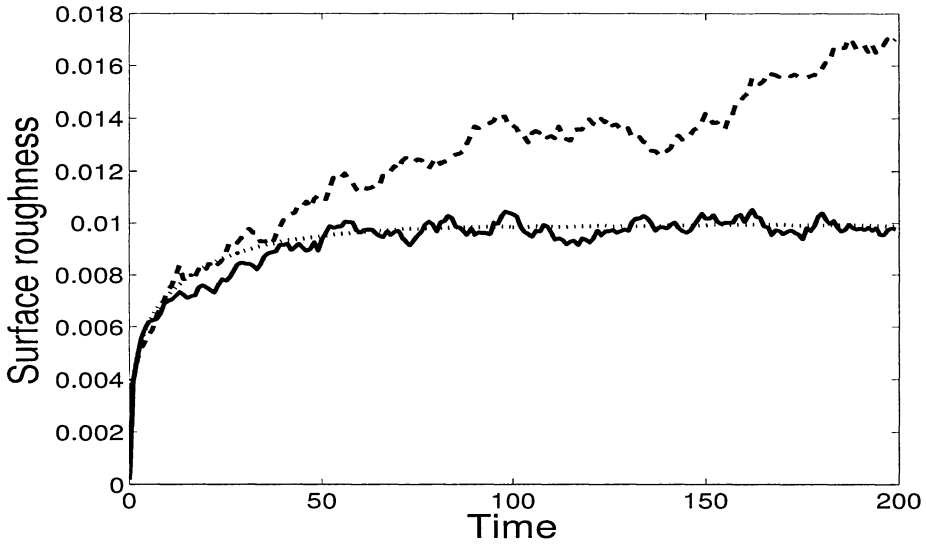

Figure 5.4: Closed-loop simulation results by applying the controller designed based on the first 40 modes of the SPDE model to the kinetic Monte-Carlo model. (a) The closed-loop surface roughness profile from one simulation run (solid line), (b) the expected closed-loop surface roughness profile (dotted line), and (c) the open-loop surface roughness profile from one simulation run (dashed line).

Remark 5.6 *The stochastic PDE models for many deposition processes can be derived based on the corresponding master equations, which describes the evolution of*

the probability that the surface is at a certain configuration. Two major assumptions are made to derive the stochastic PDE models based on the master equation. Specifically, if $\boldsymbol{H} = \{h_1, h_2, \cdots\}$ *represents the surface configuration,* $\boldsymbol{r} = \{r_1, r_2, \cdots\}$ *is the array of jump lengths at each site and* $W(\boldsymbol{H}; \boldsymbol{r})$ *is the transition rate from* $\boldsymbol{H}$ *to* $\boldsymbol{H}+\boldsymbol{r}$*, it is assumed that there exists a quantity* δ *such that (1)* $W(\boldsymbol{H}; \boldsymbol{r}) \approx 0$*, for* $|\boldsymbol{r}| > \delta$*, and (2)* $W(\boldsymbol{H} + \Delta\boldsymbol{H}; \boldsymbol{r}) \approx W(\boldsymbol{H}; \boldsymbol{r})$*, for* $|\Delta\boldsymbol{H}| < \delta$ *(Van Kampen, 1992). Because the difference in successive configurations is one height unit on a single site, the first assumption can be satisfied by increasing the number of lattice sites in the deposition process (equivalently, reducing the size of a single lattice on a fixed spatial domain as considered in this work). However, due to the dependence of the final deposition site on the local surface configuration, a change in a surface site by one height unit can produce a step change in* W*, which violates the second assumption; increasing the number of sites in the deposition process cannot alleviate this problem (Haselwandter and Vvedensky, 2002). Therefore, increase of the lattice sites can reduce the error of the solution of the stochastic PDE and of the kinetic Monte-Carlo simulation due to the first assumption, however, it cannot completely eliminate the model error between the expected roughness value obtained from the discrete microscopic kinetic Monte-Carlo simulation and from the stochastic PDE (which is a continuous approximation of the discrete process) due to the fact that the second assumption cannot be fully satisfied. As a result, to design feedback controllers based on stochastic PDE models, it is necessary to adjust the model parameters to compensate for this model error.*

Remark 5.7 *Note that the controller design method developed in this work can be applied to other deposition processes modeled by stochastic PDEs (see, for example, Lou and Christofides, 2004a, for an application of this method to control the stochastic Kuramoto-Sivashinsky equation which describes the evolution of the height profile for surfaces in a variety of physical and chemical processes including surface erosion by ion sputtering (Cuerno et al., 1995) and* ZrO_2 *thin film growth by reactive ion beam sputtering (Qi et al., 2003)).*

5.5 Conclusions

This chapter presented a method for feedback control of surface roughness in deposition processes based on stochastic PDEs which describe the fluctuation of surface height in the spatial domain. We focused on control of surface roughness in a deposition process on a 1-dimensional lattice, whose fluctuation of surface height can be described by the Edwards-Wilkinson equation. We initially reformulated the stochastic PDE into a system of infinite stochastic ordinary differential equations by using modal decomposition. A finite-dimensional approximation of the Edwards-Wilkinson equation was then derived that captures the dominant mode contribution to the surface roughness. A state feedback controller was designed based on the finite-dimensional approximation to control the surface roughness. Analysis of the closed-loop system showed that the controller can drive the surface roughness governed by the infinite-dimensional system to desired levels. The effectiveness of the proposed method was demonstrated by numerical simulations.

Chapter 6

Feedback Control of Surface Roughness in Sputtering Processes Using the Stochastic Kuramoto-Sivashinsky Equation

6.1 Introduction

Sputtering processes are widely used in the thin film and semiconductor fabrication to remove material from the surface of solids through the impact of energetic particles. In many cases sputtering is used to smooth out surface features. The surface morphology of thin films after the sputter erosion strongly depends on conditions such as incident ion energy, sputtered substrate temperature and material composition (Makeev et al., 2002). The surface roughness of thin films of advanced materials is an important variable to control because it strongly affects the quality of such films. Due to the increasingly stringent requirements on the quality of such films, feedback control of surface roughness of sputtering processes becomes important.

In a sputtering process, the surface is directly shaped by the microscopic surface processes (e.g., erosion, diffusion and surface reaction), which are stochastic processes. Therefore, the stochastic nature of sputtering processes must be fully considered in the modeling and control of the surface roughness of such processes. The desire to understand and control the thin film micro-structure has motivated extensive research on fundamental mathematical models describing the microscopic features of surfaces formed by surface micro-processes, which include 1) dynamical Monte-Carlo methods (e.g., Gillespie, 1976; Fichthorn and Weinberg, 1991; Shitara et al., 1992a; Kersch et al., 1994; Gilmer et al., 2000; Reese et al., 2001; Chen et al., 2003), and 2) stochastic partial differential equations (PDEs) (e.g., Edwards and Wilkinson, 1982; Villain, 1991; Vvedensky et al., 1993; Cuerno et al., 1995; Lauritsen et al., 1996). Furthermore, the study of feedback control of surface roughness is also motivated by the possibility to obtain roughness measurements in real-time using scanning tunneling microscopy (Voigtländer, 2001), spectroscopic ellipsometry techniques (Zapien et al., 2001), grazing-incidence small-angle X-ray scattering (GISAXS) (Renaud et al., 2003) or by combination of on-line measurements techniques for measuring gas phase compositions with off-line measurement techniques for measuring surface roughness. An implementation of the latter approach was recently reported in Ni et al. (2004), where it was used to measure carbon composition of thin films in plasma-enhanced chemical vapor deposition using combination of optical emission spectroscopy (OES) and X-ray photoelectron spectroscopy (XPS).

The Monte-Carlo simulation methods can be used to predict average properties of thin films (which are of interest from a control point of view, for example, surface roughness), by explicitly accounting for the micro-processes that directly shape thin film microstructure. Recently, a methodology for feedback control of surface rough-

ness using kinetic Monte-Carlo models has been developed in Lou and Christofides (2003a,b). The methodology leads to the design of (a) real-time roughness estimators by using multiple small lattice kinetic Monte-Carlo simulators, adaptive filters and measurement error compensators, and (b) feedback controllers based on the real-time roughness estimators. The method was successfully applied to control surface roughness in a $GaAs$ deposition process using an experimentally determined kinetic Monte-Carlo process model (Lou and Christofides, 2004b). Moreover, kinetic Monte-Carlo methods are also used to study dynamics of complex deposition processes including multiple components with both short-range and long-range interactions (Ni and Christofides, 2004a) and to perform predictive control design to control final surface roughness in Ni and Christofides (2004b).

However, the fact that kinetic Monte-Carlo models are not available in closed form makes very difficult to perform model-based controller design directly on the basis of kinetic Monte-Carlo models. To achieve better closed-loop performance, it is desirable to design feedback controllers on the basis of process models. This has motivated recent research on the development of a method for feedback control of surface roughness based on stochastic PDE process models (Lou and Christofides, 2004c). This method involves reformulation of the stochastic PDE into a system of infinite stochastic ordinary differential equations by using modal decomposition, derivation of a finite dimensional approximation that captures the dominant mode contribution to the surface roughness, and state feedback controller design based on the finite-dimensional approximation.

Both the deterministic and the stochastic Kuramoto-Sivashinsky equation (KSE) are important PDEs which describe a variety of chemical and physical processes. Some examples of processes that are described by the deterministic KSE are falling

liquid films (Chen and Chang, 1986), unstable flame fronts (Sivashinsky, 1977) and interfacial instabilities between two viscous fluids (Hooper and Grimshaw, 1985). Analytical and numerical studies of the dynamics of the deterministic KSE have revealed that the dominant dynamics of the KSE can be adequately characterized by a small number of degrees of freedom (e.g., Temam, 1988). This has motivated extensive research focusing on the design of linear/nonlinear finite-dimensional output feedback controllers (Armaou and Christofides, 2000a,b) for stabilization of the zero solution of the KSE on the basis of ordinary differential equation (ODE) approximations, obtained through linear (Armaou and Christofides, 2000a) and nonlinear (Armaou and Christofides, 2000b) Galerkin's method, that accurately describe the dominant dynamics of the KSE for a given value of the instability parameter. The global stabilization of the KSE has also been addressed via distributed static output feedback control (Christofides and Armaou, 2000). A nonlinear boundary feedback controller was also proposed in Liu and Krstić (2001) that enhances the rate of convergence to the spatially uniform steady-state of the KSE, for values of the instability parameter for which this steady state is open-loop stable. The issue of optimal actuator/sensor placement for the KSE was also addressed in Lou and Christofides (2003c) so that the desired control objectives are achieved with minimal energy use.

The stochastic KSE can be used to model the evolution of the height profile for surfaces in a variety of sputtering processes including surface erosion by ion sputtering (Cuerno et al., 1995; Lauritsen et al., 1996), surface smoothing by energetic clusters (Insepov et al., 1997) and ZrO_2 thin film growth by reactive ion beam sputtering (Qi et al., 2003). The long-time behavior of the stochastic KSE was studied through renormalization-group analysis (Cuerno and Lauritsen, 1995) and its numerical solution was obtained in Drotar et al. (1999). The problem of the existence and

uniqueness of the solution to the stochastic KSE was also investigated in Duan and Ervin (2001). Even though the above works have led to fundamental understanding of the physical meaning of the various terms and mathematical properties of the stochastic KSE, the problem of feedback controller design for systems described by the stochastic KSE has not been addressed.

This chapter focuses on control of surface roughness in sputtering processes including two surface micro-processes, diffusion and erosion. The fluctuation of surface height of such sputtering processes can be described by the stochastic KSE, a fourth-order stochastic PDE. Specifically, we consider a sputtering process, including surface diffusion and erosion, on a 1-dimensional lattice and use the method proposed in Chapter 5 to design a feedback controller to regulate the surface roughness at a desired level. We initially reformulate the stochastic KSE into a system of infinite stochastic ordinary differential equations by using modal decomposition. A finite-dimensional approximation of the stochastic KSE is then derived that captures the dominant mode contribution to the surface roughness. A state feedback controller is designed based on the finite-dimensional approximation to control the surface roughness. Feedback control of surface roughness in three different sputtering processes with different sputtering yield functions and different ratios of erosion and diffusion rates is subsequently studied. Monte-Carlo simulations are first performed to simulate the evolution of the surface height fluctuation in the three sputtering processes. Then, the parameters of the stochastic PDE models describing the sputtering processes are identified by using the surface height fluctuation data obtained from Monte-Carlo simulations so that the evolution of the surface roughness computed from the stochastic PDE models is consistent to that computed from Monte-Carlo simulations. Feedback controllers are designed and applied to Monte-Carlo models of the sputtering processes to control

the surface roughness to desired levels.

6.2 Preliminaries

6.2.1 Process description

We consider a sputtering process on a 1-dimensional lattice, which includes two surface micro-processes, erosion and diffusion. The rules are as follows: a site, i, is first randomly picked among the sites of the whole lattice and the particle at the top of this site is subject to: a) erosion with probability f, or b) diffusion with probability $1-f$.

If the particle at the top of site i is subject to erosion, the particle is removed from the site i with probability $P_e \cdot Y(\phi_i)$. P_e is determined as $\frac{1}{7}$ times the number of occupied sites in a box of size 3×3 centered at the site i (see Fig. 6.1). $Y(\phi_i)$ is the sputtering yield function defined as follows:

$$Y(\phi_i) = y_0 + y_1\phi_i^2 + y_2\phi_i^4 \tag{6.1}$$

where y_0, y_1 and y_2 are constants and ϕ_i is the local slope defined as follows:

$$\phi_i = \tan^{-1}\left(\frac{h_{i+1} - h_{i-1}}{2a}\right) \tag{6.2}$$

where a is the lattice size and h_{i+1} and h_{i-1} are the values of surface height at sites $i+1$ and $i-1$, respectively.

If the particle at the top of site i is subject to diffusion, one of its two nearest neighbors, j ($j = i+1$ or $i-1$) is randomly chosen and the particle is moved to the nearest neighbor column with probability $w_{i\to j}$ as follows:

$$w_{i\to j} = \frac{1}{1 + \exp\left(\beta \Delta H_{i\to j}\right)} \tag{6.3}$$

where $\Delta H_{i\to j}$ is the energy difference between the final and initial states of the move, $\beta = \frac{1}{k_B T}$ and H is computed as follows:

$$H = \left(\frac{J}{a^2}\right) \sum_{k=1}^{L} (h_k - h_{k+1})^2 \tag{6.4}$$

where J is a constant and L is the total number of sites in the lattice.

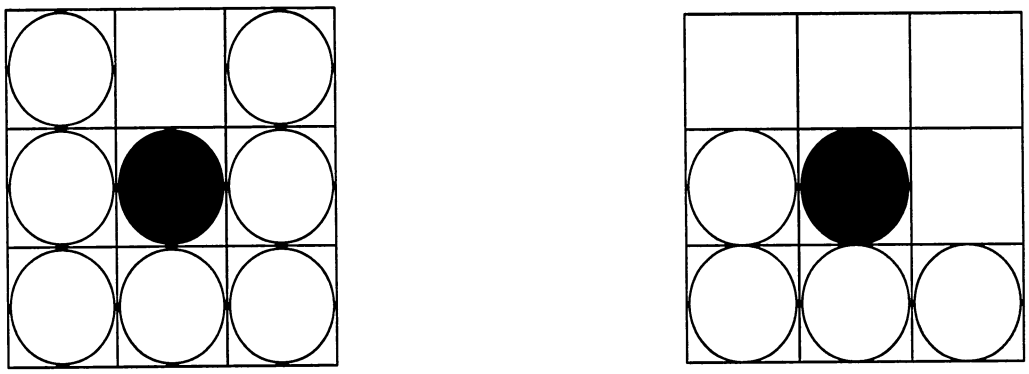

Figure 6.1: Schematic of the rule to determine P_e. P_e is defined as $\frac{1}{7}$ times the number of occupied sites in a box of size 3×3 centered at the particle on the top of site i; $P_e = 1$ in the left figure and $P_e = \frac{4}{7}$ in the right figure, where the particle marked by $\bullet$ is on the top of site i.

6.2.2 Stochastic PDE model of the sputtering process

The sputtering process is a stochastic process. Kinetic Monte-Carlo simulation can be used to predict the evolution of the surface configuration in this process. The kinetic Monte-Carlo model is a first-principle model in the sense that the erosion rules are explicitly considered in the model. Mathematically, kinetic Monte-Carlo simulation methods provide an unbiased realization of the master equation (Gillespie, 1976; Van Kampen, 1992), which describes the evolution of the probability that the surface is at a certain configuration. Kinetic Monte-Carlo simulation can predict average properties of the surface of a sputtering process (which are of interest from a control

point of view, for example, surface roughness). Since a kinetic Monte-Carlo simulation run constitutes a realization of a stochastic process, simulation results from a large number of different simulation runs are not identical. However, by averaging the results from different simulation runs, the averaged properties of the surface converge to the values obtained from the solution of the master equation.

Kinetic Monte-Carlo models are not available in closed-form, which makes very difficult to perform model-based control design on the basis of Monte-Carlo models. As an alternative, closed-form stochastic PDE models can be derived based on the erosion rules to describe the evolution of the surface configuration in a way that is consistent to that predicted by kinetic Monte-Carlo models. In this work, we focus on model-based feedback control design for surface roughness control using a stochastic PDE model of the sputtering process under consideration. The equation for the height fluctuations of the surface in this sputtering process was derived in Lauritsen et al. (1996) and is a stochastic Kuramoto-Sivashinsky equation of the following form:

$$\frac{\partial h}{\partial t} = -\nu\frac{\partial^2 h}{\partial x^2} - \kappa\frac{\partial^4 h}{\partial x^4} + \frac{\lambda}{2}\left(\frac{\partial h}{\partial x}\right)^2 + \xi(x,t) \tag{6.5}$$

where $x \in [-\pi, \pi]$ is the spatial coordinate, t is the time, $h(x,t)$ is the height of the surface at position x and time t, ν and κ are two constants, and $\xi(x,t)$ is a Gaussian noise with zero mean and covariance:

$$\langle \xi(x,t)\xi(x',t')\rangle = \sigma^2\delta(x-x')\delta(t-t') \tag{6.6}$$

where σ is a constant, $\delta(\cdot)$ is the dirac function, and $\langle\cdot\cdot\rangle$ denotes the expected value. Note that the noise covariance depends on both space x and time t.

The surface roughness, r, is given by the following expression:

$$r(t) = \sqrt{\frac{1}{2\pi}\int_{-\pi}^{\pi}[h(x,t) - \bar{h}(t)]^2 dx} \tag{6.7}$$

where $\bar{h}(t) = \frac{1}{2\pi}\int_{-\pi}^{\pi} h(x,t)dx$ is the average surface height.

Our objective is to control the surface roughness of the sputtering process to a desired level. In the process model of Eq.6.5, the nonlinear term $\frac{\lambda}{2}\left(\frac{\partial h}{\partial x}\right)^2$ corresponds to the effect of $Y(\phi)$ on the surface fluctuations, which is a nonlinear function of the local slope, and the nonlinearities become more significant in the model of Eq.6.5 at the late stage of the evolution of the surface when large slopes develop (Cuerno et al., 1995). In this work, we focus on the problem of feedback control of the sputtering process using linearizations of the stochastic KSE with appropriately identified parameters. To proceed, we formulate the linearized KSE with distributed control in the spatial domain $[-\pi, \pi]$ as follows:

$$\frac{\partial h}{\partial t} = -\nu\frac{\partial^2 h}{\partial x^2} - \kappa\frac{\partial^4 h}{\partial x^4} + \sum_{i=1}^{p} b_i(x)u_i(t) + \xi(x,t) \tag{6.8}$$

subject to periodic boundary conditions:

$$\frac{\partial^j h}{\partial x^j}(-\pi, t) = \frac{\partial^j h}{\partial x^j}(\pi, t), \quad j = 0, \cdots, 3 \tag{6.9}$$

and the initial condition:

$$h(x, 0) = h_0(x) \tag{6.10}$$

where u_i is the ith manipulated input, p is the number of manipulated inputs and b_i is the ith actuator distribution function (i.e., b_i determines how the control action computed by the ith control actuator, u_i, is distributed (e.g., point or distributed actuation) in the spatial interval $[-\pi, \pi]$).

To study the dynamics of Eq.6.8, we initially consider the eigenvalue problem of the linear operator of Eq.6.8, which takes the form:

$$\begin{aligned} A\bar{\phi}_n(x) &= -\nu\frac{d^2\bar{\phi}_n(x)}{dx^2} - \kappa\frac{d^4\bar{\phi}_n(x)}{dx^4} = \lambda_n\bar{\phi}_n(x), \quad n = 1, \cdots, \infty, \\ \frac{d^j\bar{\phi}_n}{dx^j}(-\pi) &= \frac{d^j\bar{\phi}_n}{dx^j}(\pi), \qquad\qquad\qquad\qquad j = 0, \cdots, 3 \end{aligned} \tag{6.11}$$

where λ_n denotes an eigenvalue and $\bar{\phi}_n$ denotes an eigenfunction. A direct computation of the solution of the above eigenvalue problem yields $\lambda_0 = 0$ with $\psi_0 = 1/\sqrt{2\pi}$, and $\lambda_n = \nu n^2 - \kappa n^4$ (λ_n is an eigenvalue of multiplicity two) with eigenfunctions $\phi_n = (1/\sqrt{\pi})\sin(nx)$ and $\psi_n = (1/\sqrt{\pi})\cos(nx)$ for $n = 1, \cdots, \infty$. From the solution of the eigenvalue problem shown in Eq.6.11, it follows that for fixed values of $\nu > 0$ and $\kappa > 0$, the number of unstable eigenvalues of A is finite and the distance between two consecutive eigenvalues (i.e., λ_n and λ_{n+1}) increases as n increases. Furthermore, the eigenspectrum of the operator A in Eq.6.11, $\sigma(A)$ can be partitioned as $\sigma(A) = \sigma_1(A) \bigcup \sigma_2(A)$, where $\sigma_1(A)$ contains the first m (with m finite) eigenvalues (i.e., $\sigma_1(A) = \{\lambda_1, \ldots, \lambda_m\}$) and $\sigma_2(A)$ contains the remaining eigenvalues (i.e., $\sigma_2(A) = \{\lambda_{m+1}, \ldots, \}$.

To present the method that we use to design a feedback controller on the basis of the stochastic KSE of Eq.6.8, we first derive stochastic ODE approximations of Eq.6.8 using modal decomposition. To this end, we first expand the solution of Eq.6.8 in an infinite series in terms of the eigenfunctions of the operator of Eq.6.11 as follows:

$$h(x,t) = \sum_{n=1}^{\infty} \alpha_n(t)\phi_n(x) + \sum_{n=0}^{\infty} \beta_n(t)\psi_n(x) \tag{6.12}$$

where $\alpha_n(t)$, $\beta_n(t)$ are time-varying coefficients. Substituting the above expansion for the solution, $h(x,t)$, into Eq.6.8 and taking the inner product with the adjoint eigenfunctions, $\phi_n^*(z) = (1/\sqrt{\pi})\sin(nz)$ and $\psi_n^*(z) = (1/\sqrt{\pi})\cos(nz)$, the following system of infinite stochastic ODEs is obtained:

$$\begin{aligned} \frac{d\alpha_n}{dt} &= (\nu n^2 - \kappa n^4)\alpha_n + \sum_{i=1}^{p} b_{i\alpha_n} u_i(t) + \xi_\alpha^n(t) \\ \frac{d\beta_n}{dt} &= (\nu n^2 - \kappa n^4)\beta_n + \sum_{i=1}^{p} b_{i\beta_n} u_i(t) + \xi_\beta^n(t); \quad n = 1, \ldots, \infty \end{aligned} \tag{6.13}$$

where

$$b_{i\alpha_n} = \int_{-\pi}^{\pi} \phi_n(x) b_i(x) dx, \qquad b_{i\beta_n} = \int_{-\pi}^{\pi} \psi_n(x) b_i(x) dx$$
$$\xi_\alpha^n(t) = \int_{-\pi}^{\pi} \xi(x,t)\phi_n(x)dx, \quad \xi_\beta^n(t) = \int_{-\pi}^{\pi} \xi(x,t)\psi_n(x)dx \tag{6.14}$$

The covariances of $\xi_\alpha^n(t)$ and $\xi_\beta^n(t)$ can be computed by using the following result (Åström, 1970):

Result 6.1 *If (1) $f(x)$ is a deterministic function, (2) $\eta(x)$ is a random variable with $\langle \eta(x) \rangle = 0$ and covariance $\langle \eta(x)\eta(x') \rangle = \sigma^2 \delta(x-x')$, and (3) $\epsilon = \int_a^b f(x)\eta(x)dx$, then ϵ is a random number with $\langle \epsilon \rangle = 0$ and covariance $\langle \epsilon^2 \rangle = \sigma^2 \int_a^b f^2(x)dx$.*

Using Result 6.1, we obtain $\langle \xi_\alpha^n(t)\xi_\alpha^n(t') \rangle = \sigma^2\delta(t-t')$ and $\langle \xi_\beta^n(t)\xi_\beta^n(t') \rangle = \sigma^2\delta(t-t')$.

In this work, the controlled variable is the expected value of surface roughness, $\sqrt{\langle r^2 \rangle}$. According to Eq.6.12, we have $\bar{h}(t) = \beta_0(t)\psi_0$. Therefore, $\sqrt{\langle r^2 \rangle}$ can be rewritten in terms of α_n and β_n as follows:

$$\begin{aligned}
\sqrt{\langle r^2 \rangle} &= \sqrt{\frac{1}{2\pi} \langle \int_{-\pi}^{\pi} (h(x,t) - \bar{h}(t))^2 dx \rangle} \\
&= \sqrt{\frac{1}{2\pi} \langle \int_{-\pi}^{\pi} \sum_{i=1}^{\infty} \left[\alpha_i(t)^2 \phi_i(x)^2 + \beta_i(t)^2 \psi_i(x)^2 \right] dx \rangle} \\
&= \sqrt{\frac{1}{2\pi} \langle \sum_{i=1}^{\infty} (\alpha_i^2 + \beta_i^2) \rangle} = \sqrt{\frac{1}{2\pi} \sum_{i=1}^{\infty} \left[\langle \alpha_i^2 \rangle + \langle \beta_i^2 \rangle \right]}
\end{aligned} \tag{6.15}$$

Therefore, the surface roughness control problem for the stochastic KSE system of Eq.6.8 is formulated as the one of controlling the covariance of the states α_n and β_n of the system of infinite stochastic ODEs of Eq.6.13.

Remark 6.1 *While the parameters of stochastic PDE models for many deposition processes and sputtering processes can be derived based on the corresponding master equations, which describe the evolution of the probability that the surface is at a*

certain configuration (see, for example Lauritsen et al., 1996; Vvedensky, 2003); for all practical purposes, the stochastic PDE model parameters should be identified by matching the prediction of the stochastic PDE model to that of Monte-Carlo simulations. The reason for this is the two major assumptions which are made in the derivation of the stochastic PDE models from the master equation. Specifically, if $\boldsymbol{H} = \{h_1, h_2, \cdots\}$ *represents the surface configuration,* $\boldsymbol{r} = \{r_1, r_2, \cdots\}$ *is the array of jump lengths at each site and* $W(\boldsymbol{H}; \boldsymbol{r})$ *is the transition rate from* $\boldsymbol{H}$ *to* $\boldsymbol{H}+\boldsymbol{r}$*, it is assumed that there exists a quantity* δ *such that (1)* $W(\boldsymbol{H}; \boldsymbol{r}) \approx 0$*, for* $|\boldsymbol{r}| > \delta$*, and (2)* $W(\boldsymbol{H} + \Delta\boldsymbol{H}; \boldsymbol{r}) \approx W(\boldsymbol{H}; \boldsymbol{r})$*, for* $|\Delta\boldsymbol{H}| < \delta$ *(Van Kampen, 1992). Because the difference in successive configurations is one height unit on a single site, the first assumption can be satisfied by increasing the number of lattice sites in the deposition process (equivalently, reducing the size of a single lattice on a fixed spatial domain as considered in this work). However, due to the dependence of the final deposition site on the local surface configuration, a change in a surface site by one height unit can produce a step change in* W*, which violates the second assumption; increasing the number of sites in the deposition process cannot alleviate this problem (Haselwandter and Vvedensky, 2002). Therefore, increase of the lattice sites can reduce the error between the solution of the stochastic PDE and that of the Monte-Carlo simulation due to the first assumption, however, it cannot completely eliminate the model error between the expected roughness value obtained from the discrete microscopic Monte-Carlo simulation and from the stochastic PDE (which is a continuous approximation of the discrete process) due to the fact that the second assumption cannot be fully satisfied. As a result, to design feedback controllers based on stochastic PDE models, it is necessary to identify PDE model parameters based on the surface height data obtained from Monte-Carlo simulations to compensate for this model error.*

6.3 Feedback control

In this section, we design a linear state feedback controller for the system of Eq.6.13 so that the surface roughness defined in Eq.6.15 can be controlled to a desired level.

6.3.1 Model reduction

Owing to its infinite-dimensional nature, the system of Eq.6.13 cannot be directly used for the design of controllers that can be implemented in practice (i.e., the practical implementation of controllers which are designed on the basis of this system will require the computation of infinite sums which cannot be done by a computer). Instead, we will base the controller design on finite-dimensional approximations of this system. Subsequently, we will show that the resulting controller will enforce the desired control objective in the closed-loop infinite-dimensional system.

Specifically, we rewrite the system of Eq.6.13 as follows:

$$\begin{aligned} \frac{dx_s}{dt} &= \Lambda_s x_s + B_s u + \xi_s \\ \frac{dx_f}{dt} &= \Lambda_f x_f + B_f u + \xi_f \end{aligned} \tag{6.16}$$

where x_s=$[\alpha_1 \cdots \alpha_m \ \beta_1 \cdots \beta_m]^T$, x_f=$[\alpha_{m+1} \ \beta_{m+1} \cdots \ ]^T$, $\Lambda_s = diag[\lambda_1 \cdots \lambda_m \ \lambda_1 \cdots \lambda_m]$, Λ_f=$diag[\lambda_{m+1} \ \lambda_{m+1} \ \lambda_{m+2} \ \lambda_{m+2} \cdots]$, u=$[u_1 \cdots u_p]$, $\xi_s = [\xi_\alpha^1 \cdots \xi_\alpha^m \ \xi_\beta^1 \cdots \xi_\beta^m]$, and $\xi_f = [\xi_\alpha^{m+1} \ \xi_\beta^{m+1} \cdots]$,

$$B_s = \begin{bmatrix} b_{1_{\alpha_1}} & \cdots & b_{p_{\alpha_1}} \\ \vdots & \ddots & \vdots \\ b_{1_{\alpha_m}} & \cdots & b_{p_{\alpha_m}} \\ b_{1_{\beta_1}} & \cdots & b_{p_{\beta_1}} \\ \vdots & \ddots & \vdots \\ b_{1_{\beta_m}} & \cdots & b_{p_{\beta_m}} \end{bmatrix}; \quad B_f = \begin{bmatrix} b_{1_{\alpha_{m+1}}} & \cdots & b_{p_{\alpha_{m+1}}} \\ b_{1_{\beta_{m+1}}} & \cdots & b_{p_{\beta_{m+1}}} \\ b_{1_{\alpha_{m+2}}} & \cdots & b_{p_{\alpha_{m+2}}} \\ b_{1_{\beta_{m+2}}} & \cdots & b_{p_{\beta_{m+2}}} \\ \vdots & \vdots & \vdots \end{bmatrix} \tag{6.17}$$

We note that in the system of Eq.6.16, by selecting m sufficiently large, Λ_f is an unbounded differential operator which is exponentially stable.

Neglecting the x_f subsystem, the following $2m$-dimensional system is obtained:

$$\frac{d\tilde{x}_s}{dt} = \Lambda_s \tilde{x}_s + B_s u + \xi_s \tag{6.18}$$

where the tilde symbol in $\tilde{x}_s$ denotes that this state variable is associated with a finite-dimensional system.

6.3.2 Feedback control design

We design the state feedback controller on the basis of the finite-dimensional system of Eq.6.18. To simplify our development, we assume that $p = 2m$ and pick the actuator distribution functions such that B_s^{-1} exists. The state feedback control law then takes the form:

$$u = B_s^{-1} \left[\left(\Lambda_{cs} - \Lambda_s \right) \tilde{x}_s \right] \tag{6.19}$$

where the matrix Λ_{cs} contains the desired poles of the closed-loop system; $\Lambda_{cs} = diag[\lambda_{c\alpha 1} \cdots \lambda_{c\alpha m} \ \lambda_{c\beta 1} \cdots \lambda_{c\beta m}]$, $\lambda_{c\alpha i}$ and $\lambda_{c\beta i}$ $(1 \leq i \leq m)$ are desired poles of the closed-loop finite-dimensional system, which can be determined from the desired closed-loop surface roughness level.

We first analyze the dependence of the covariances of the states α_n and β_n $(n = 1, \cdots, m)$ on the poles of the finite-dimensional system of Eq.6.18. Then, we will show in subsection 6.3.3 that the surface roughness of the infinite-dimensional system of Eq.6.13 can be controlled to the desired level by using the state feedback controller of Eq.6.19, which only uses a finite number of actuators.

By applying the controller of Eq.6.19 to the system of Eq.6.18, the closed-loop system takes the form:

$$\frac{d\tilde{x}_s}{dt} = \Lambda_{cs} \tilde{x}_s + \xi_s(t) \tag{6.20}$$

If all eigenvalues of Λ_{cs} have negative real part, the covariance matrix of $\tilde{x}_s(t)$, $P(t) = \langle \tilde{x}_s(t) \tilde{x}_s(t)^T \rangle$ converges to $P(\infty)$, which is the unique positive definite solution to the

Lyapunov equation (Hotz and Skelton, 1987):

$$\Lambda_{cs}P + P\Lambda_{cs} + R_1 = 0 \tag{6.21}$$

where $R_1 = \langle \xi_s(t)\xi_s(t)^T \rangle$. Eq.6.21 cannot be solved, in general, analytically. However, for the specific deposition system considered in this work, the analytical solution for $P(\infty)$ can be obtained as follows:

$$P(\infty) = \begin{bmatrix} P_\alpha(\infty) & 0 \\ 0 & P_\beta(\infty) \end{bmatrix} \tag{6.22}$$

where $P_\alpha(\infty) = diag[\ \langle \alpha_1(\infty)^2 \rangle \ \cdots \ \langle \alpha_m(\infty)^2 \rangle\ ]$, $P_\beta(\infty) = diag[\ \langle \beta_1(\infty)^2 \rangle \ \cdots \ \langle \beta_m(\infty)^2 \rangle]$. $\langle \alpha_n(\infty)^2 \rangle$ and $\langle \beta_n(\infty)^2 \rangle$ $(n = 1, \cdots, m)$ can be computed by using the following expressions:

$$\langle \alpha_n(\infty)^2 \rangle = -\frac{\sigma^2}{2\lambda_{c\alpha_n}}; \quad \langle \beta_n(\infty)^2 \rangle = -\frac{\sigma^2}{2\lambda_{c\beta_n}} \tag{6.23}$$

From Eq.6.23, we can see that by assigning the closed-loop poles $\lambda_{c\alpha_n}$ and $\lambda_{c\beta_n}$ $(n = 1, \cdots, m)$ at desired locations, the covariances of the states α_n and β_n $(n = 1, \cdots, m)$ can be controlled to desired levels. Therefore, according to Eq.6.15, the contribution to the surface roughness from the finite-dimensional system of Eq.6.18 can be controlled to the desired level.

6.3.3 Analysis of the closed-loop infinite-dimensional system

In this subsection, we show that when the state feedback controller of Eq.6.19 is used to manipulate the poles of the finite-dimensional system of Eq.6.18, the contribution to the surface roughness from the α_f and β_f subsystem of the system of Eq.6.16 is bounded and can be made arbitrarily small by increasing the dimension of the x_s subsystem.

By applying the feedback controller of Eq.6.19 into the infinite-dimensional system of Eq.6.16, we obtain the following closed-loop system:

$$\begin{aligned} \frac{dx_s}{dt} &= \Lambda_{cs} x_s + \xi_s \\ \frac{dx_f}{dt} &= \Lambda_\epsilon x_s + \Lambda_f x_f + \xi_f \end{aligned} \tag{6.24}$$

where $\Lambda_\epsilon = B_f B_s^{-1}(\Lambda_{cs} - \Lambda_s)$.

The boundedness of the state of the above system follows directly from the stability of the matrices Λ_{cs} and Λ_f and the structure of the system, where the x_s subsystem is independent of the x_f state (see Christofides, 2001b, for results and techniques for analyzing the stability properties of such systems).

Due to the structure of the eigenspectrum of operator A (Section 6.2.2), the effect of the control action computed from Eq.6.19 to the poles of the x_f subsystem can be reduced by increasing m. Therefore, by picking m sufficiently large, the $\Lambda_\epsilon x_s$ can be made very small compared to $\Lambda_f x_f$ and thus, the closed-loop system of Eq.6.24 can be adequately described by the following system:

$$\begin{aligned} \frac{dx_s}{dt} &= \Lambda_{cs} x_s + \xi_s \\ \frac{dx_f}{dt} &= \Lambda_f x_f + \xi_f \end{aligned} \tag{6.25}$$

On the basis of the above system, it can be shown that the covariance of the state of the x_f subsystem converges to $[\ \langle \alpha_{m+1}(\infty)^2 \rangle \quad \langle \beta_{m+1}(\infty)^2 \rangle \quad \cdots \quad \cdots\ ]$, where

$$\begin{aligned} \langle \alpha_n(\infty)^2 \rangle &= \frac{\sigma^2}{2n^2(\kappa n^2 - \nu)}; \\ \langle \beta_n(\infty)^2 \rangle &= \frac{\sigma^2}{2n^2(\kappa n^2 - \nu)}; \quad n > m \end{aligned} \tag{6.26}$$

Therefore, for m sufficiently large, the overall contribution to the surface roughness

from the x_f subsystem in Eq.6.16, $\sqrt{\langle r_f^2 \rangle}$ can be computed as follows:

$$\sqrt{\langle r_f^2 \rangle} = \sqrt{\frac{1}{2\pi} \sum_{n=m+1}^{\infty} \left[\frac{\sigma^2}{n^2(\kappa n^2 - \nu)} \right]} \tag{6.27}$$

Clearly, as $m \rightarrow \infty$, the contribution to the surface roughness from the x_f subsystem goes to zero.

In summary, under the controller of Eq.6.19, the closed-loop surface roughness, for m sufficiently large, can be adequately described by the following expression:

$$\sqrt{\langle r^2 \rangle} = \sigma \sqrt{\frac{1}{2\pi} \left\{ \lambda^* + \sum_{n=m+1}^{\infty} \left[\frac{1}{n^2(\kappa n^2 - \nu)} \right] \right\}} \tag{6.28}$$

where $\lambda^* = \sum_{i=1}^{m} \left(-\frac{1}{2\lambda_{c\alpha_i}} - \frac{1}{2\lambda_{c\beta_i}} \right)$ and $\lambda_{c\alpha_i}$ and $\lambda_{c\beta_i}$ are closed-loop poles of the finite-dimensional system of Eq.6.20.

Remark 6.2 *Note that in order to regulate the surface roughness to a desired level, $\langle \sqrt{r_d^2} \rangle$, the number of actuators should be large enough so that the value of $\langle \sqrt{r_d^2} \rangle$ is achievable. Specifically, the number of actuators, m should be selected such that the following inequality holds:*

$$\sqrt{\langle r_d^2 \rangle} > \sigma \sqrt{\frac{1}{2\pi} \left\{ \sum_{n=m+1}^{\infty} \left[\frac{1}{n^2(\kappa n^2 - \nu)} \right] \right\}} \tag{6.29}$$

This is because the closed-loop stability requires that $\lambda_{c\alpha_i} < 0$ and $\lambda_{c\beta_i} < 0$ (for $i = 1, \cdots, m$), and thus, $\lambda^* > 0$ in Eq.6.28.

Remark 6.3 *Note that to control the closed-loop surface roughness to $\sqrt{\langle r_d^2 \rangle}$, we need to design a controller to assign the poles of the finite-dimensional system of Eq.6.20 to appropriate values so that the following equation holds:*

$$\lambda^* = \frac{2\pi(\langle r_d^2 \rangle - \langle r_f^2 \rangle)}{\sigma^2} \tag{6.30}$$

The controller which assigns the poles of the system of Eq.6.20 to satisfy Eq.6.30 is not unique. Consequently, for a fixed number of actuators, p, the controller that

can regulate the closed-loop surface roughness to a desired level is also not unique. Furthermore, we note that robust control methods (Christofides, 1998; Christofides and Baker, 1999), which utilize bounds of the noise terms, can be employed to design controllers that can achieve arbitrary degree of attenuation of the effect of noise on the PDE system state.

Remark 6.4 *Note that it is possible to apply the proposed method to control the surface roughness of sputtering processes taking place in 2-dimensional surfaces. In a 2-dimensional process, the feedback control design and the analysis of the closed-loop system will be based on the model of Eq.6.16. Moreover, Eq.6.16 will be obtained by solving the eigenvalue/eigenfunctin problem of the operator A in the 2-dimensional spatial domain with appropriate boundary conditions. After Eq.6.16 is obtained, the method for control design and closed-loop analysis presented above can be applied to control the surface roughness for 2-dimensional surfaces described by stochastic PDEs.*

6.4 Simulation results

In this section, we present applications of the method followed for the design of the state feedback controller to control three different sputtering processes. In all processes, the sputtering occurs on a lattice containing 200 sites. Therefore, $a = 0.0314$. The rate of bombardment for each surface site is $\bar{r}_b = 1s^{-1}$ in the open-loop system. Specifically, the following three processes are studied in this work.

Process 6.1 *Only surface erosion is considered, which is corresponding to $f = 1$ in the sputtering process model in Section 6.2.1. Plus, we set $Y(\phi) \equiv 1$ and the probability with which a particle is removed from a surface site is $1 - P_e$, where P_e is determined by the box rule shown in Fig.6.1.*

Process 6.2 *Both erosion and surface diffusion are considered with $\bar{f} = 0.5$. The sputtering yield function, $Y(\phi_i) \equiv 1$. If a randomly selected surface site is subject to*

erosion, the probability with which a particle is removed from a surface site is P_e, where P_e is determined by the box rule shown in Fig.6.1. If a randomly selected surface site is subject to diffusion, the diffusion probability, $w_{i\to j}$ is computed according to Eq.6.3 with $\beta J = 2.0$.

Process 6.3 *Both erosion and surface diffusion are considered with $\bar{f} = 0.5$. The sputtering yield function, $Y(\phi_i)$ is a nonlinear function of ϕ_i, which takes the form of Eq.6.1. y_0, y_1 and y_2 are chosen such that $Y(0) = 0.5$, $Y(\frac{\pi}{2}) = 0$ and $Y(1) = 1$ (Cuerno et al., 1995). If a randomly selected surface site is subject to erosion, the probability with which a particle is removed from a surface site is $Y(\phi_i) \cdot P_e$, where P_e is determined by the box rule shown in Fig. 6.1. If a randomly selected surface site is subject to diffusion, the diffusion probability, $w_{i\to j}$ is computed according to Eq.6.3 with $\beta J = 2.0$.*

6.4.1 Feedback control of surface roughness in process 6.1

According to Cuerno et al. (1995), in the stochastic KSE model of Eq.6.5, the nonlinear term corresponds to the effect of the nonlinear function $Y(\phi)$ and κ accounts for the surface diffusion. By setting $Y(\phi) \equiv 1$ and $f = 1$, the surface roughness has the scaling properties of the Edwards-Wilkinson equation (Edwards and Wilkinson, 1982). The open-loop surface roughness converges to a finite value (see Fig.6.2). This is because by setting the erosion probability equal to $1 - P_e$, one favors the erosion of peaks as compared to valleys, which is a smoothing mechanism preventing the instability of surface roughness in the sputtering process.

The problem of controlling surface roughness of a deposition process whose surface height fluctuations are described by the Edwards-Wilkinson equation has been solved in Lou and Christofides (2004c). In this case study, we design a feedback controller based on the stochastic PDE model, which takes the form of the Edwards-Wilkinson

equation, of the sputtering process. The model parameters are identified by using data of the evolution of surface height obtained from Monte-Carlo simulations so that the prediction of the surface roughness from the solution of the stochastic PDE model of the process is consistent to that from the Monte-Carlo simulations. Then, we apply the designed controller to the Monte-Carlo model of the sputtering process to control the surface roughness of this process to a desired level.

Model identification

Since the surface roughness in this sputtering process has the same scaling properties to that of the Edwards-Wilkinson equation (Edwards and Wilkinson, 1982), the following stochastic PDE model is used to describe height fluctuation of the surface in Process 6.1:

$$\begin{aligned} \frac{\partial h}{\partial t} &= -\nu \frac{\partial^2 h}{\partial x^2} + \xi(x,t) \\ \langle \xi(x,t)\xi(x',t') \rangle &= \sigma^2 \delta(x-x')\delta(t-t') \end{aligned} \tag{6.31}$$

where $\nu < 0$. By expanding h in an infinite series in terms of $\phi(x)$ and $\psi(x)$ as in Eq.6.12, the following system of infinite stochastic ODEs is obtained:

$$\begin{aligned} \frac{d\alpha_n}{dt} &= \nu n^2 \alpha_n + \xi_\alpha^n(t) \\ \frac{d\beta_n}{dt} &= \nu n^2 \beta_n + \xi_\beta^n(t); \quad n = 1, \ldots, \infty \end{aligned} \tag{6.32}$$

Based on Eq.6.32, we can obtain the following expressions for $\alpha_n(t)$ and $\beta_n(t)$:

$$\begin{aligned} \alpha_n(t) &= \alpha_n(0) e^{\nu n^2 t} + \int_0^t e^{\nu n^2 (t-\tau)} \xi_\alpha^n(\tau) d\tau \\ \beta_n(t) &= \beta_n(0) e^{\nu n^2 t} + \int_0^t e^{\nu n^2 (t-\tau)} \xi_\beta^n(\tau) d\tau; \quad n = 1, \ldots, \infty \end{aligned} \tag{6.33}$$

If the initial surface is flat, e.g., $\alpha_n(0) = 0$ and $\beta_n(0) = 0$ for $n = 1, \cdots, \infty$, the covariance of $\alpha_n(t)$ and $\beta_n(t)$ can be computed as follows by using Result 6.1, :

$$\langle \alpha_n(t)^2 \rangle = \langle \beta_n(t)^2 \rangle = \sigma^2 \left(\frac{e^{2\nu n^2 t} - 1}{2\nu n^2} \right); \quad n = 1, \ldots, \infty \tag{6.34}$$

Based on Eq.6.34, the values of ν and σ can be identified by using the data of $\langle \alpha_n(t)^2 \rangle$ or $\langle \beta_n(t)^2 \rangle$, which can be obtained from Monte-Carlo simulations of the same sputtering process. The Monte-Carlo simulation algorithm used to simulate the sputtering process is described as follows. In this algorithm, a trial to execute an event may or may not be successful (Ziff et al., 1986). Upon successful realization of an event, the time is advanced by an increment, δt (Fichthorn and Weinberg, 1991).

Monte-Carlo algorithm for Process 6.1:

- A random number, ζ_1 is first generated to pick a site, i, among all the sites on the 1-D lattice.
- P_e is computed by using the box rule shown in Fig.6.1 and the center of the box is the surface particle on site i.
- The second random number, ζ_2 in the $(0, 1)$ interval is generated.
- If $\zeta_2 > 1 - P_e$, no Monte-Carlo event is executed and the trial is not successful.
- If $\zeta_2 < 1 - P_e$ the surface particle on site i is removed and a time increment, δt is computed by using the following expression:

$$\delta t = -\frac{\ln \zeta_3}{\sum_{i=1}^{N} (1 - P_{e_i})} \tag{6.35}$$

  where ζ_3 is a random number in the $(0, 1)$ interval and P_{e_i} is computed by using the box rule shown in Fig.6.1 in which the center of the box is the surface particle at site i.

- Upon the successful realization of one Monte-Carlo event (a surface particle is

removed from site i), α_n or β_n can be updated by using the following expression:

$$\begin{aligned} \alpha_n^{new} &= \alpha_n^{old} + \frac{a\left[\psi(n, z_i - a/2) - \psi(n, z_i + a/2)\right]}{n} \\ \beta_n^{new} &= \beta_n^{old} + \frac{a\left[\phi(n, z_i + a/2) - \phi(n, z_i - a/2)\right]}{n} \end{aligned} \tag{6.36}$$

where a is the lattice size and z_i is the coordinate of the center of site i.

Fig.6.2 shows the open-loop profile of the expected surface roughness in Process 6.1 from Monte-Carlo simulations. The expected surface roughness is obtained by averaging surface roughness profiles from 1000 independent simulation runs by using the same simulation parameters. The expected surface roughness converges to about 0.15 after about 2500 monolayers are eroded.

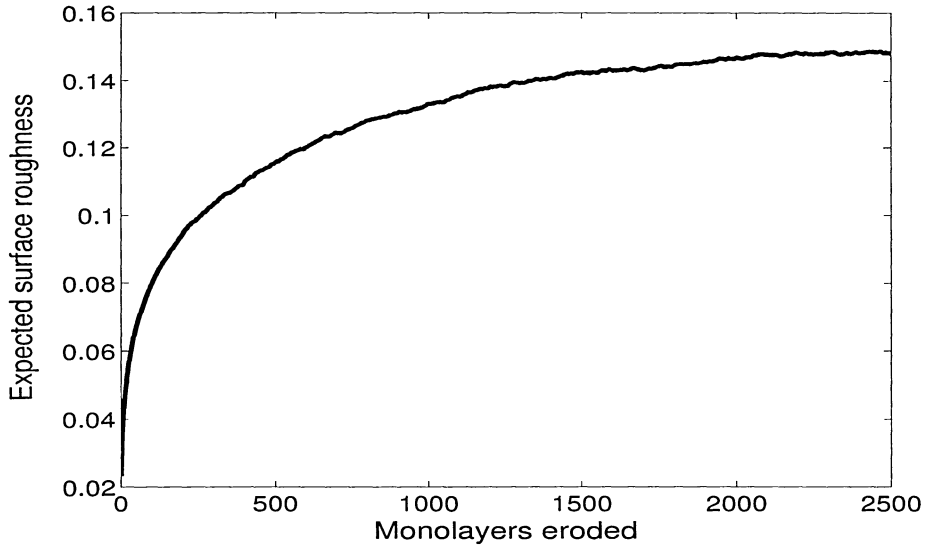

Figure 6.2: The open-loop profile of the expected surface roughness in Process 6.1 computed from the Monte-Carlo simulations.

Fig.6.3 shows the open-loop profiles of $\langle \alpha_n^2 \rangle$ for $n = 2, 3, 4$, and 5. Each profile is obtained by averaging the profiles of α_n^2 from 1000 independent Monte-Carlo simulation runs using the same simulation parameters.

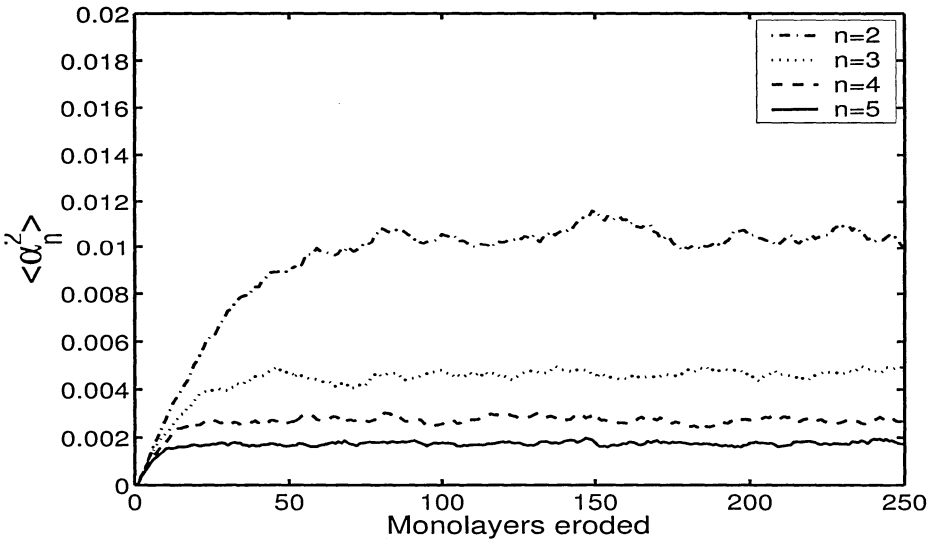

Figure 6.3: Evolution of $\langle\alpha_2^2\rangle$, $\langle\alpha_3^2\rangle$, $\langle\alpha_4^2\rangle$ and $\langle\alpha_5^2\rangle$ in Process 6.1.

Using the profiles shown in Fig.6.3, we identify the values of ν and σ of Eq.6.31 based on Eq.6.34. While $\nu < 0$, as $t \to \infty$, $\frac{1}{\langle\alpha_n(\infty)^2\rangle} = -\frac{2\nu n^2}{\sigma^2} \cdot \frac{1}{\langle\alpha_n(\infty)^2\rangle}$ versus n for $n = 2, 3, 4$, and 5 is marked in Fig.6.4 by 'o'. Using the method of least mean square, we fit the data marked in Fig.6.4 using a parabolic equation, $y = 23.07n^2$, which is plotted in Fig.6.4 by using the dotted line. Therefore, we obtain the following relationship between ν and σ:

$$-\frac{2\nu}{\sigma^2} = 23.07 \tag{6.37}$$

Furthermore, based on Eq.6.34, we can get the following equation for ν:

$$-\frac{\ln\left[\frac{2\nu n^2}{\sigma^2}\langle\alpha_n(t)^2\rangle + 1\right]}{n^2} = -2\nu t \tag{6.38}$$

Therefore, if we plot $-\ln\left[\frac{2\nu n^2}{\sigma^2}\langle\alpha_n(t)^2\rangle + 1\right]/n^2$ versus t, the slope is -2ν. This plot is shown in Fig.6.5. In Fig.6.5, 4 lines are plotted for $n = 2, 3, 4$, and 5. It is clear that these 4 lines have almost identical slopes, which means that the value of ν identified

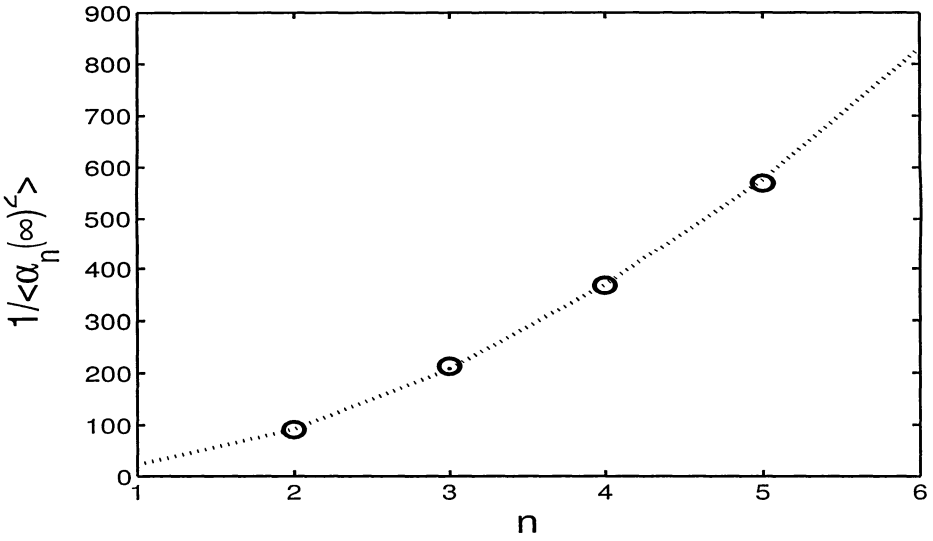

Figure 6.4: $1/\langle\alpha_n(\infty)^2\rangle$ versus n for $n = 2, 3, 4$, and 5 (marked by 'o') and the curve of $y = 23.07n^2$ (dotted line) in Process 6.1.

in this way is independent of the data set used in the identification.

From Fig.6.5, the value of ν is identified as $\nu = -1.2 \times 10^{-4}$. Then, by using Eq.6.37, $\sigma = 3.2 \times 10^{-3}$. Using the identified parameters of Eq.6.31, we compute the expected surface roughness in Process 6.1 based on Eq.6.31. An 80th order stochastic ordinary differential equation approximation of the system of Eq.6.31 is used to simulate the process (the use of higher-order approximations led to identical numerical results, thereby implying that the following simulation runs are independent of the discretization). The δ function involved in the covariances of ξ_α^n and ξ_β^n is approximated by $\frac{1}{\Delta t}$ where Δt is the integration time step. There is a small difference between the expected surface roughness profile obtained from Monte-Carlo simulations and that from the solution of the Edwards-Wilkinson equation with $\nu = -1.2 \times 10^{-4}$ and $\sigma = 3.2 \times 10^{-3}$ and this difference can be compensated by increasing the value of σ from 3.2×10^{-3} to 3.4×10^{-3}. In Fig.6.6, we compare the expected value of

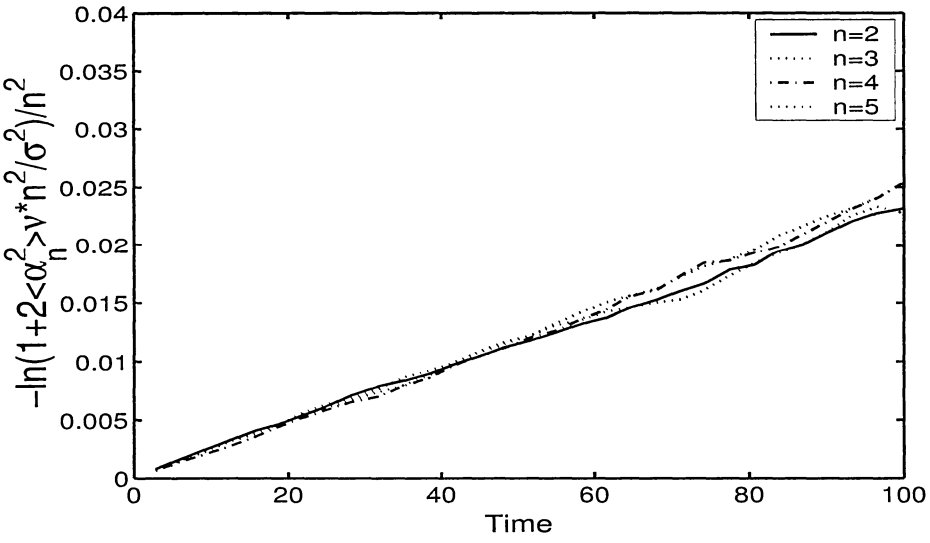

Figure 6.5: Plots of $-\ln\left[\frac{2\nu n^2}{\sigma^2}\langle\alpha_n(t)^2\rangle + 1\right]/n^2$ versus t for $n = 2, 3, 4$, and 5 in Process 6.1.

the open-loop surface roughness of Process 6.1 from the solution of the Edwards-Wilkinson equation of Eq.6.31 with $\nu = -1.2 \times 10^{-4}$ and $\sigma = 3.4 \times 10^{-3}$ to that from Monte-Carlo simulations. The two profiles are almost identical. Therefore, by using the stochastic PDE model of Eq.6.31 with the identified model parameters, we can predict the evolution of the expected surface roughness in this sputtering process. The stochastic PDE model of Eq.6.31 is used as the basis for controller design.

Feedback control design

Our control objective is to control the expected surface roughness in Process 6.1 to a desired value. We design a state feedback controller based on a $20th$ order stochastic ODE approximation constructed by using the first 20 eigenmodes of the system of Eq.6.13 with identified model parameters $\nu = -1.2 \times 10^{-4}$, $\sigma = 3.4 \times 10^{-3}$ and $\kappa = 0$. Twenty control actuators are used to control the system. The ith actuator

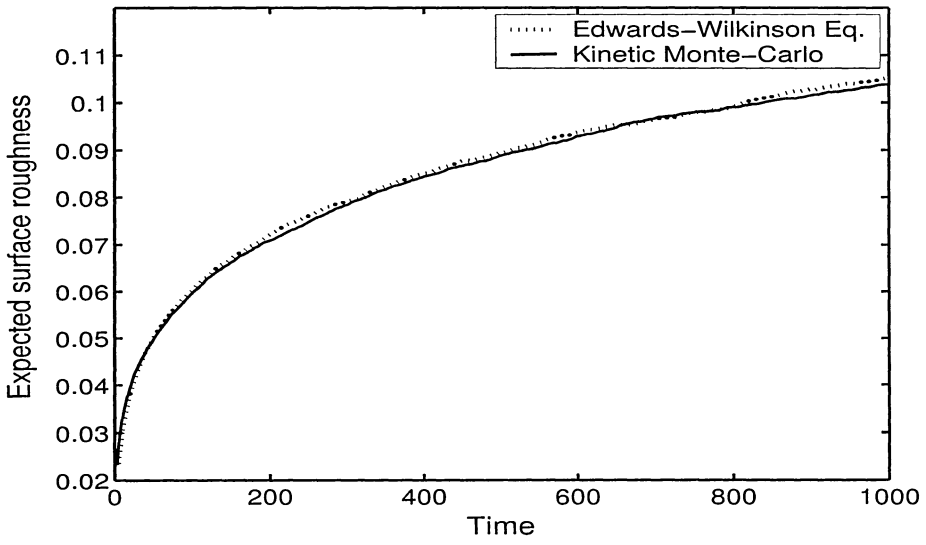

Figure 6.6: Comparison of the open-loop profile of the expected surface roughness from the kinetic Monte-Carlo simulator (solid line) and that from the solution of the Edwards-Wilkinson equation with $\nu = -1.2 \times 10^{-4}$ and $\sigma = 3.4 \times 10^{-3}$ (dotted line) in Process 6.1.

distribution function is taken to be:

$$b_i(z) = \begin{cases} \frac{1}{\sqrt{\pi}} \sin(iz); & i = 1, \cdots, 10 \\ \frac{1}{\sqrt{\pi}} \cos[(i-10)z]; & i = 11, \cdots, 20 \end{cases} \tag{6.39}$$

The desired closed-loop surface roughness is 0.053 in this simulation. Using Eq.6.28, we design the state feedback controller such that $\lambda_{c\alpha_i} = \lambda_{c\beta_i} = -0.027$, for $i = 1, \cdots, 10$. Then, we apply the designed controller to the kinetic Monte-Carlo model of Process 6.1 to control the surface roughness to the desired level. In this simulation, the controller is implemented by manipulating the bombardment rate of particles across the surface. Specifically, the bombardment rate on site i at time t is determined according to the following expression:

$$r_b(i,t) = \bar{r}_b + \left(\sum_{j=1}^{20} b_j(z_i) u_j(t) \right) / a \tag{6.40}$$

The following simulation algorithm is used to run the kinetic Monte-Carlo simulations for the closed-loop system. First, a random number is generated to pick a site among all the sites on the 1-D lattice; the probability that a surface site is picked is proportional to the bombardment rate on this site, which is computed by using Eq.6.40. Then, P_e is computed by using the box rule shown in Fig.6.1 and the center of the box is the surface particle on site i. The second random number, ζ_2 in the $(0, 1)$ interval is generated. If $\zeta_2 > 1 - P_e$ no Monte-Carlo event is executed. If $\zeta_2 < 1 - P_e$ the surface particle on site i is removed. Once a particle is removed, the first 20 states ($\alpha_1, \cdots, \alpha_{10}$ and $\beta_1, \cdots, \beta_{10}$) are updated and new control actions are computed to update the spatially distributed bombardment rate across the surface.

The closed-loop system simulation results are shown in Fig.6.7. The dashed line shows the expected surface roughness, which is the average of surface roughness profiles obtained from 200 independent runs, under feedback control. We can see that

the controller successfully drives the expected surface roughness to the desired level. The solid line shows the surface roughness profile under feedback control from one simulation run; due to the stochastic nature of the deposition process, stochastic fluctuations can be observed in the closed-loop surface roughness profile, but the surface roughness is very close to the set-point value under feedback control. For the sake of comparison, the dotted line shows a surface roughness profile from one open-loop simulation run. We can see that under feedback control, a much lower surface roughness can be achieved.

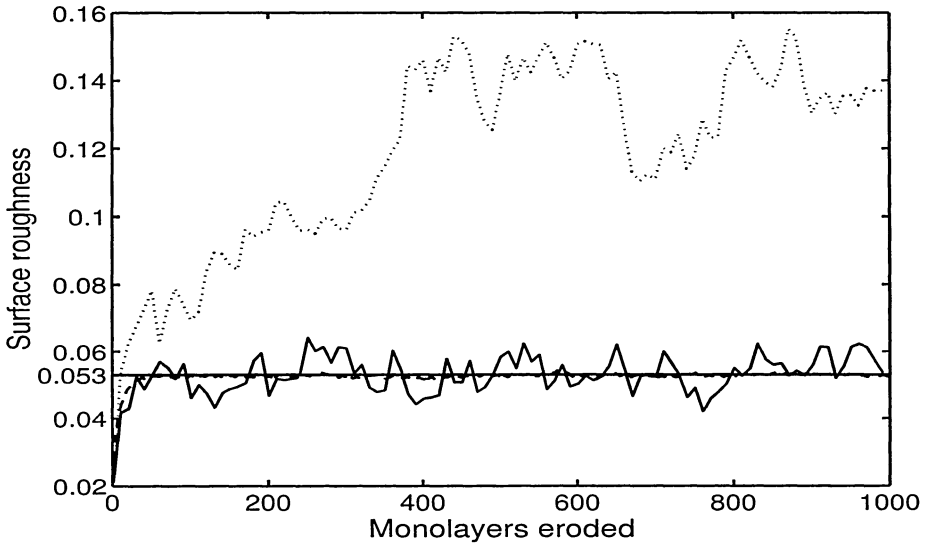

Figure 6.7: Closed-loop surface roughness profiles in Process 6.1. (a) The closed-loop surface roughness profile from one simulation run (solid line), (b) The expected closed-loop surface roughness profile obtained from 200 independent simulation runs (dashed line), and (c) the open-loop surface roughness profile from one simulation run (dotted line).

Remark 6.5 *Note that the number of control actuators needed to regulate the expected closed-loop surface roughness to a desired level, $\sqrt{r_d^2}$, depends on the value of $\sqrt{r_d^2}$. In this simulation study, twenty control actuators are used to regulate the expected closed-loop surface roughness to 0.053. However, this is not the minimum*

Table 6.1: Number of control actuators versus the lowest achievable closed-loop surface roughness.

Number of control actuators	Lowest achievable closed-loop surface roughness
2	0.099
4	0.078
6	0.066
8	0.058
10	0.053
20	0.038
30	0.031
40	0.027

number of control actuators required to achieve a closed-loop surface roughness of 0.053. For a fixed number of control actuators available, the lowest achievable closed-loop surface roughness can be computed by using Eq.6.29 and some results are listed in Table 6.1. A minimum of two control actuators are required if the desired surface roughness is 0.099 and a minimum of ten control actuators are required if the desired surface roughness is 0.053.

6.4.2 Feedback control of surface roughness in Process 6.2

Compare to Process 6.1, surface diffusion is added in Process 6.2. In this case study, $\bar{f} = 0.5$ and $J/k_bT = 2.0$. The presence of two mechanisms results to more complicated process dynamics and the open-loop surface roughness is unstable, e.g., the surface roughness goes to infinity as $t \to \infty$. In this case study, our control objective is to stabilize the closed-loop surface roughness to a finite value. We first study the dynamics of the surface roughness in this sputtering process and identify the number

of unstable modes in this process. It turns out that the number of unstable modes is finite. Then, we design a model-based state feedback controller, which employs more control actuators than the number of unstable modes, to stabilize the surface roughness to a finite value.

Open-loop dynamics

We run kinetic Monte-Carlo simulations to study the dynamics of the open-loop surface roughness and the evolution of covariance of α_n and β_n in this sputtering process. The Monte-Carlo simulation algorithm and the method to compute $\alpha_n(t)$ or $\beta_n(t)$ are as follows:

- The first random number, ζ_1 is generated to pick a site, i, among all the sites on the 1-D lattice.
- The second random number, ζ_2 in the $(0,1)$ interval, is generated to decide whether the chosen site is subject to erosion ($\zeta_2 < \bar{f}$) or diffusion ($\zeta_2 > \bar{f}$).
- If the chosen site is subject to erosion, P_e is computed by using the box rule shown in Fig.6.1 and the center of the box is the surface particle on site i. Then, another random number ζ_{e3} in the $(0,1)$ interval is generated. If $\zeta_{e3} < P_e$ the surface particle on site i is removed. Otherwise, no Monte-Carlo event is executed.
- If the chosen site is subject to diffusion, a side neighbor, j, ($j = i+1$ or $i-1$ in the case of 1-D lattice) is randomly picked and the hopping rate, $w_{i\to j}$, is computed by using Eq.6.3. Then, another random number ζ_{d3} in the $(0,1)$ interval is generated. If $\zeta_{d3} < w_{i\to j}$, the surface atom is moved to the new site. Otherwise no Monte-Carlo event is executed.

- Upon the execution of one Monte-Carlo event, α_n or β_n are updated. If the executed event is erosion, α_n or β_n can be updated by using Eq.6.36. If the executed event is diffusion from site i to site j, α_n or β_n are updated by using the following expression:

$$\alpha_n^{new} = \alpha_n^{old} + \frac{a\left\{[\psi(n, z_i - a/2) - \psi(n, z_i + a/2)] - [\psi(n, z_j - a/2) - \psi(n, z_j + a/2)]\right\}}{n}$$

$$\beta_n^{new} = \beta_n^{old} + \frac{a\left\{[\phi(n, z_i + a/2) - \phi(n, z_i - a/2)] - [\phi(n, z_j + a/2) - \phi(n, z_j - a/2)]\right\}}{n} \tag{6.41}$$

where a is the lattice size, z_i is the coordinate of the center of site i and z_j is the coordinate of the center of site j.

Fig.6.8 shows the open-loop profile of the expected surface roughness of Process 6.2 from kinetic Monte-Carlo simulations. The expected surface roughness is obtained by averaging surface roughness profiles from 1000 independent simulation runs by using the same simulation parameters. It is clear that the open-loop expected surface roughness in this sputtering process does not converge to a finite value. Our control objective is to stabilize the closed-loop surface roughness to a finite value. To do this, we identify the number of unstable modes in this process and use more control actuators than the number of unstable modes to stabilize the surface roughness in the closed-loop system.

Fig.6.9 shows the open-loop profiles of $\langle \alpha_n^2 \rangle$ for $n = 1, 5, 15$, and 20. Each profile is obtained by averaging the profile α_n^2 from 1000 independent simulation runs by using the same simulation parameters.

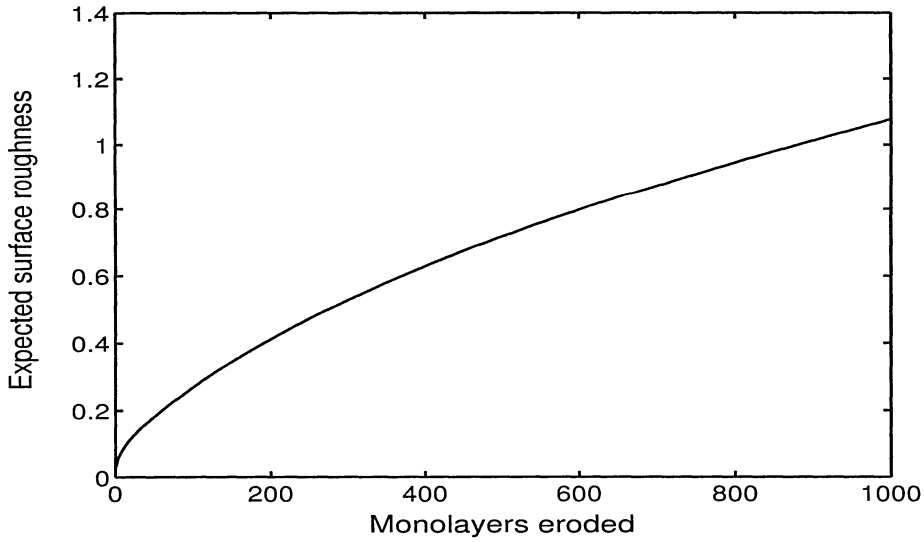

Figure 6.8: The open-loop profile of the expected surface roughness in Process 6.2 from the kinetic Monte-Carlo simulator.

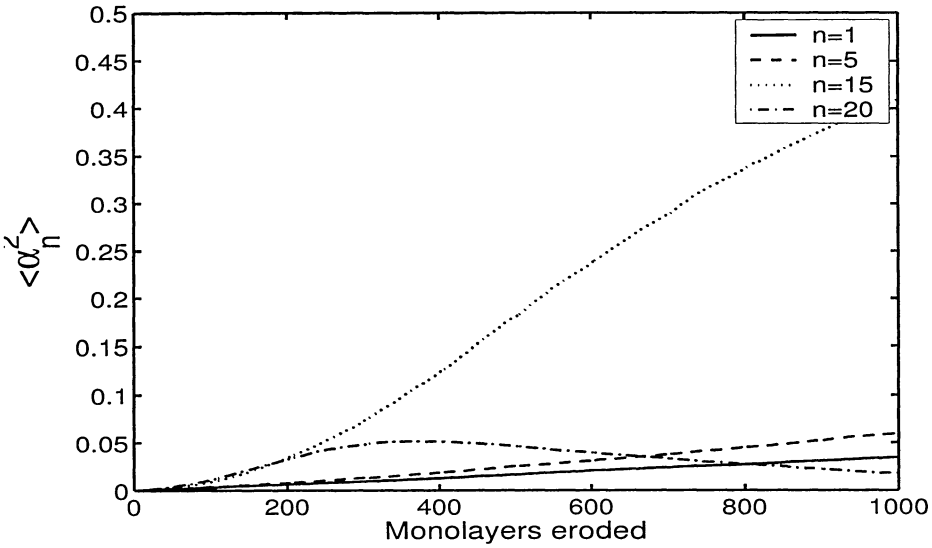

Figure 6.9: Evolution of $\langle \alpha_1^2 \rangle$, $\langle \alpha_5^2 \rangle$, $\langle \alpha_{15}^2 \rangle$ and $\langle \alpha_{20}^2 \rangle$ in Process 6.2.

Feedback control design

In Fig.6.9, it is clear that at least the first 15 modes are unstable. Although α_{20}^2 is stable, its magnitude is in the same order of that of α_1^2 or α_5^2, which is still significant. The same dynamics are also observed in the open-loop profiles of $\langle \beta_n^2 \rangle$. To this end, we design a state feedback controller based on the first 50 modes of the process (25 modes for the α_n subsystem and 25 modes for the β_n subsystem), which is sufficiently larger than the number of unstable modes (which is about 30) in the process, to stabilize the closed-loop surface roughness to a finite value. 50 control actuators are used to control the system. The ith actuator distribution function is taken to be:

$$b_i(z) = \begin{cases} \frac{1}{\sqrt{\pi}} \sin(iz); & i = 1, \cdots, 25 \\ \\ \frac{1}{\sqrt{\pi}} \cos[(i-25)z]; & i = 26, \cdots, 50 \end{cases} \tag{6.42}$$

We design the following state feedback controller to control the process:

$$u = B_s^{-1} \Lambda \tilde{x}_s \tag{6.43}$$

where $\tilde{x}_s = [\alpha_1, \ldots, \alpha_{25}, \beta_1, \ldots, \beta_{25}]^T$, $\Lambda = -0.01 \times I_{50\times 50}$ and I is an identity matrix.

Then, we apply the designed controller to the kinetic Monte-Carlo model of Process 6.2 to control the surface roughness to the desired level. In this simulation, the controller is implemented by manipulating the probability that a randomly selected site is subject to erosion rule, f. Specifically, f at site i is determined according to the following expression:

$$f(i) = \frac{\bar{f} + \left(\sum_{j=1}^{50} b_j(z_i) u_j(t) \right) / a}{1 + \left(\sum_{j=1}^{50} b_j(z_i) u_j(t) \right) / a} \tag{6.44}$$

The following simulation algorithm is used to run the kinetic Monte-Carlo simulations for the closed-loop system. First, a random number, ζ_1 is generated to pick a site, i

among all the sites on the 1-D lattice; the probability that a surface site is subject to erosion rules, $f(i)$ is determined by using Eq.6.44. Then, the second random number, ζ_2 in the $(0,1)$ interval is generated. If $\zeta_2 < f(i)$, the site i is subject to the erosion, otherwise, the site is subject to diffusion.

If the site i is subject to erosion, P_e is computed by using the box rule shown in Fig.6.1 and the center of the box is the surface particle on site i. Another random number, ζ_{e3} in the $(0,1)$ interval is generated. If $\zeta_{e3} > 1 - P_e$, no Monte-Carlo event is executed and go back to the first step of this algorithm. If $\zeta_{e3} < 1 - P_e$, the surface particle on site i is removed. Otherwise, no Monte-Carlo event is executed.

If the site i is subject to diffusion, a side-neighbor, $j = i + 1$ or $i - 1$ is randomly picked and the probability of a hopping from site i to site j, $w_{i \to j}$ is computed based on Eq.6.3. Then, another random number ζ_{d3} in the $(0,1)$ interval is generated. If $\zeta_{e3} < w_{i \to j}$, the surface particle on site i is moved to site j. Otherwise, no Monte-Carlo event is executed.

Once a Monte-Carlo event is executed, the first 50 states ($\alpha_1, \cdots, \alpha_{25}$ and $\beta_1, \cdots, \beta_{25}$) are updated and new control actions are computed to update the spatially distributed bombardment rate across the surface.

The closed-loop system simulation results are shown in Fig.6.10. The dotted line shows the expected surface roughness, which is the average of surface roughness profiles obtained from 200 independent runs, under feedback control. We can see that the controller successfully drives the expected surface roughness to a finite value. The solid line shows the surface roughness profile under feedback control from one simulation run; due to the stochastic nature of the deposition process, stochastic fluctuations can be observed in the closed-loop surface roughness profile, but the surface roughness is very close to the expected surface roughness under feedback

control. For the sake of comparison, the dashed-line shows a surface roughness profile from one open-loop simulation run. We can see that under feedback control, the surface roughness can be stabilized to a finite value.

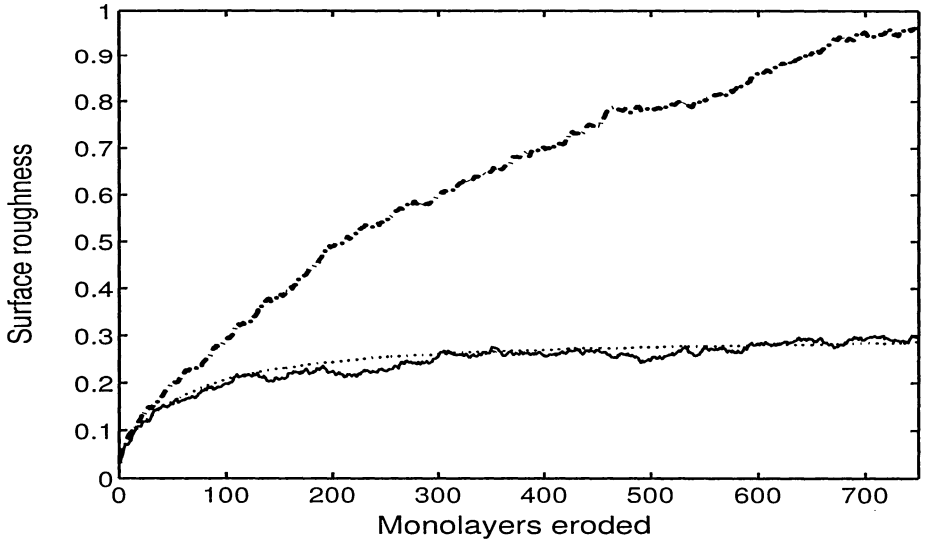

Figure 6.10: Closed-loop surface roughness profiles in Process 6.2. (a) The closed-loop surface roughness profile from one simulation run (solid line), (b) the expected closed-loop surface roughness profile (dotted line), and (c) the open-loop surface roughness profile from one simulation run (dashed line).

6.4.3 Feedback control of surface roughness in process 6.3

In this case study, our control objective is to control the surface roughness in Process 6.3 to a desired level. In Process 6.3, both erosion and diffusion are included and the sputtering yield function, $Y(\phi_i)$, is a nonlinear function of ϕ_i as shown in Eq.6.1 with $y_0 = 0.5$, $y_1 = 1.0065$ and $y_2 = -0.5065$. The evolution of surface height in this sputtering process is described by the stochastic Kuramoto-Sivashinsky equation of Eq.6.5 (Cuerno et al., 1995; Lauritsen et al., 1996). In this case study, we design a feedback controller based on the linearization of the stochastic KSE with

appropriately identified parameters. Then, we apply the designed controller to the Monte-Carlo model of this sputtering process to control the surface roughness of this process to a desired level.

Model identification

The following linearized stochastic Kuramoto-Sivashinsky equation is used as the basis for controller design:

$$\frac{\partial h}{\partial t} = -\nu \frac{\partial^2 h}{\partial x^2} - \kappa \frac{\partial^4 h}{\partial x^4} + \xi(x,t) \tag{6.45}$$

where

$$\langle \xi(x,t)\xi(x',t') \rangle = \sigma^2 \delta(x-x')\delta(t-t') \tag{6.46}$$

By expanding h in an infinite series in terms of $\phi(x)$ and $\psi(x)$ as shown in Eq.6.12, the following system of infinite stochastic ODEs is obtained:

$$\begin{aligned} \frac{d\alpha_n}{dt} &= (\nu n^2 - \kappa n^4)\alpha_n + \xi_\alpha^n(t) \\ \frac{d\beta_n}{dt} &= (\nu n^2 - \kappa n^4)\beta_n + \xi_\beta^n(t); \quad n = 1, \ldots, \infty \end{aligned} \tag{6.47}$$

Therefore,

$$\begin{aligned} \alpha_n(t) &= \alpha_n(0) e^{(\nu n^2 - \kappa n^4)t} + \int_0^t e^{(\nu n^2 - \kappa n^4)(t-\tau)} \xi_\alpha^n(\tau) d\tau \\ \beta_n(t) &= \beta_n(0) e^{(\nu n^2 - \kappa n^4)t} + \int_0^t e^{(\nu n^2 - \kappa n^4)(t-\tau)} \xi_\beta^n(\tau) d\tau; \quad n = 1, \ldots, \infty \end{aligned} \tag{6.48}$$

If the initial surface is a perfect surface, $\alpha_n(0) = 0$ and $\beta_n(0) = 0$. Using Result 6.1, the covariance of $\alpha_n(t)$ and $\beta_n(t)$ can be computed as follows:

$$\langle \alpha_n(t)^2 \rangle = \langle \beta_n(t)^2 \rangle = \sigma^2 \left[\frac{e^{2(\nu n^2 - \kappa n^4)t} - 1}{2(\nu n^2 - \kappa n^4)} \right]; \quad n = 1, \ldots, \infty \tag{6.49}$$

Based on Eq.6.49, the value of ν, κ and σ can be identified from the data of $\langle \alpha_n(t)^2 \rangle$ or $\langle \beta_n(t)^2 \rangle$, which can be obtained from kinetic Monte-Carlo simulation of the same

sputtering process. The Monte-Carlo simulation algorithm and the method to compute $\alpha_n(t)$ or $\beta_n(t)$ are as follows:

- The first random number, ζ_1 is generated to pick a site, i, among all the sites on the 1-D lattice.
- The second random number, ζ_2 in the $(0,1)$ interval, is generated to decide whether the chosen site, i, is subject to erosion ($\zeta_2 < \bar{f}$) or diffusion ($\zeta_2 > \bar{f}$).
- If the chosen site is subject to erosion, P_e and $Y(\phi_i)$ are computed. P_e is computed by using the box rule shown in Fig.6.1 and the center of the box is the surface particle on site i and $Y(\phi_i)$ is computed by using Eq.6.1. Then, another random number ζ_{e3} in the $(0,1)$ interval is generated. If $\zeta_{e3} < P_e \cdot Y(\phi_i)$ the surface particle on site i is removed. Otherwise, no Monte-Carlo event is executed.
- If the chosen site is subject to diffusion, a side neighbor, j, ($j = i+1$ or $i-1$ in the case of 1-D lattice) is randomly picked and the hopping rate, $w_{i \to j}$, is computed by using Eq.6.3. Then, another random number ζ_{d3} in the $(0,1)$ interval is generated. If $\zeta_{d3} < w_{i \to j}$, the surface atom is moved to the new site. Otherwise no Monte-Carlo event is executed.
- Upon the execution of one Monte-Carlo event, α_n or β_n are updated. If the executed event is erosion, α_n or β_n can be updated by using Eq.6.36. If the executed event is diffusion from site i to site j, α_n or β_n are updated by using the following expression:

$$\alpha_n^{new} = \alpha_n^{old} + \frac{a\{[\psi(n, z_i - a/2) - \psi(n, z_i + a/2)] - [\psi(n, z_j - a/2) - \psi(n, z_j + a/2)]\}}{n}$$

$$\beta_n^{new} = \beta_n^{old} + \frac{a\{[\phi(n, z_i + a/2) - \phi(n, z_i - a/2)] - [\phi(n, z_j + a/2) - \phi(n, z_j - a/2)]\}}{n} \tag{6.50}$$

where a is the lattice size and z_i is the coordinates of the center of site i.

Fig.6.11 shows the open-loop profile of the expected surface roughness of Process 6.3 from kinetic Monte-Carlo simulations. The expected surface roughness is obtained by averaging surface roughness profiles from 1000 independent simulation runs by using the same simulation parameters. Our control objective is to control the surface roughness in this sputtering process to a desired level. To achieve this objective, we identify the parameters of the model of Eq.6.47 so that the surface roughness predicted by Eq.6.47 is consistent to that obtained from kinetic Monte-Carlo simulations of the same sputtering process. Then, we design a feedback controller based on the process model of Eq.6.47 with the identified parameters to control the surface roughness in this process.

Fig.6.12 shows the open-loop profiles of $\langle \alpha_n^2 \rangle$ for $n = 20, 22, 25$, and 30. Each profile is obtained by averaging the profile α_n^2 from 1000 independent simulation runs by using the same simulation parameters.

Using the profiles shown in Fig.6.12, we identify the values of ν, κ and σ of Eq.6.47 based on Eq.6.49. When $\nu > 0$, $\kappa > 0$ and n is sufficient large, $\nu n^2 - \kappa n^4 < 0$. Therefore, as $t \to \infty$, $\frac{1}{\langle \alpha_n(\infty)^2 \rangle} = \frac{2(\kappa n^4 - \nu n^2)}{\sigma^2} \cdot \frac{1}{\langle \alpha_n(\infty)^2 \rangle}$ versus n for $n = 20, 21, \cdots, 30$ is marked in Fig.6.13 by '$\circ$'. Using the method of least mean square, we fit the data marked in Fig.6.13 using a $4th$ order polynomial, $y = 1.45 \times 10^{-3} n^4 - 0.26 n^2$, which is plotted in Fig.6.13 using the dotted line. Therefore, we

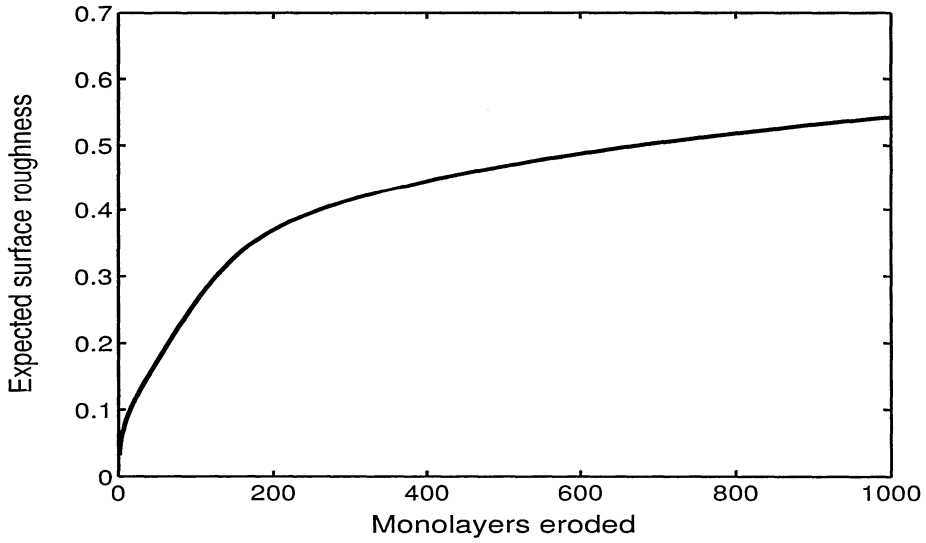

Figure 6.11: The open-loop profile of the expected surface roughness in Process 6.3 from the kinetic Monte-Carlo simulator.

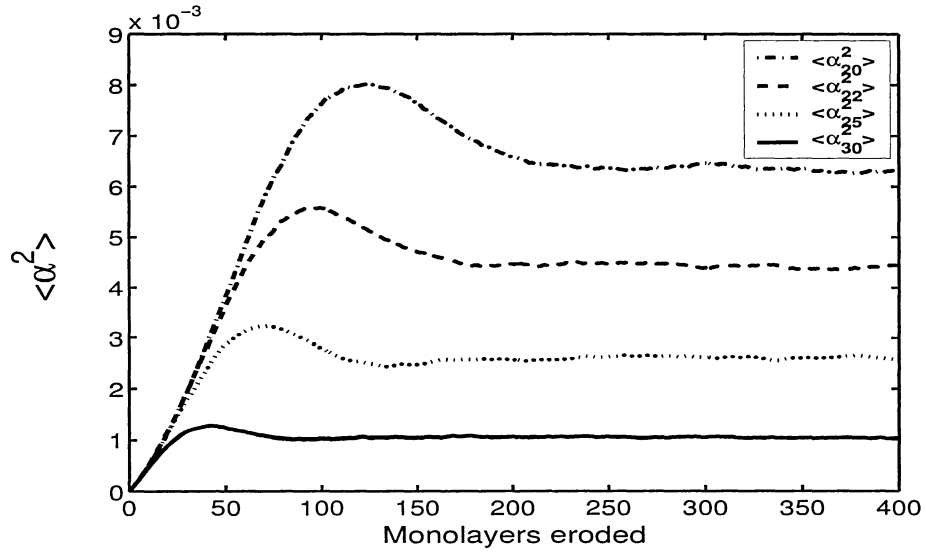

Figure 6.12: Evolution of $\langle\alpha_{20}^2\rangle$, $\langle\alpha_{22}^2\rangle$, $\langle\alpha_{25}^2\rangle$ and $\langle\alpha_{30}^2\rangle$ in Process 6.3.

obtain the following relationships between ν, σ and κ, σ:

$$\frac{2\nu}{\sigma^2} = 0.26; \quad \frac{2\kappa}{\sigma^2} = 1.45 \times 10^{-3} \tag{6.51}$$

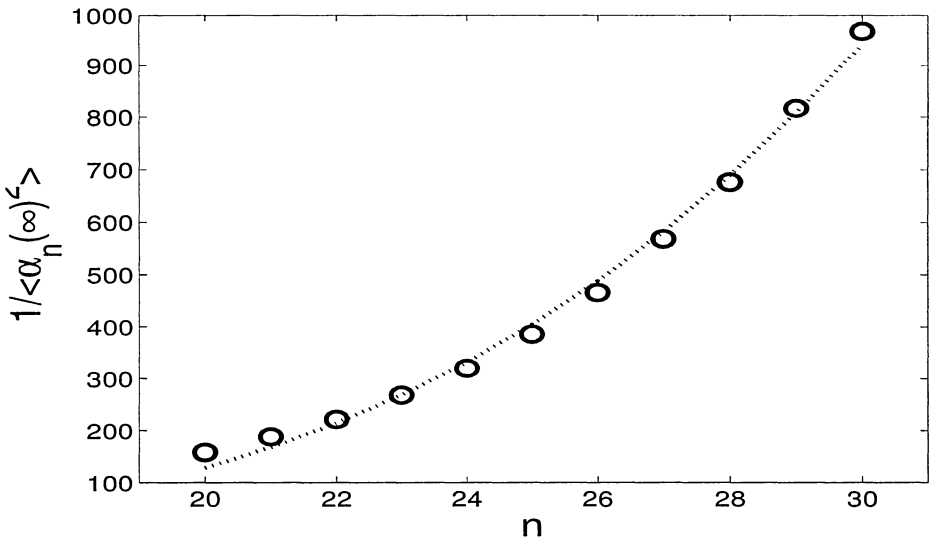

Figure 6.13: $1/\langle\alpha_n(\infty)^2\rangle$ versus n for $n = 20, 21, \cdots, 30$ (marked by '$\circ$') and the curve of $y = 1.45 \times 10^{-3}n^4 - 0.26n^2$ (dotted line) in Process 6.3.

Furthermore, based on Eq.6.49, we can get the following equations for ν and κ:

$$\frac{\ln\left[\frac{2(\nu n^2 - \kappa n^4)}{\sigma^2}\langle\alpha_n(t)^2\rangle + 1\right]}{2n^2} = (\nu - \kappa n^2)t \tag{6.52}$$

Therefore, if we plot $\ln\left[\frac{2(\nu n^2 - \kappa n^4)}{\sigma^2}\langle\alpha_n(t)^2\rangle + 1\right]/2n^2$ versus t, the slope is $\nu - \kappa n^2$. This plot is shown in Fig.6.14. In Fig.6.14, 7 lines are plotted for $n = 20, 22, 24, 26, 28,$ and 30. It is clear that there is a linear relationship between $\ln\left[\frac{2(\nu n^2 - \kappa n^4)}{\sigma^2}\langle\alpha_n(t)^2\rangle + 1\right]/2n^2$ and t.

To identify the values of ν and κ, the slopes of the lines in Fig.6.14 versus n are marked in Fig6.15 by '$\circ$'. Using the method of least mean square, we fit the data marked in Fig.6.15 using a 2^{th} order polynomial, $y = 3.27 \times 10^{-6} - 1.34 \times 10^{-8}n^2$,

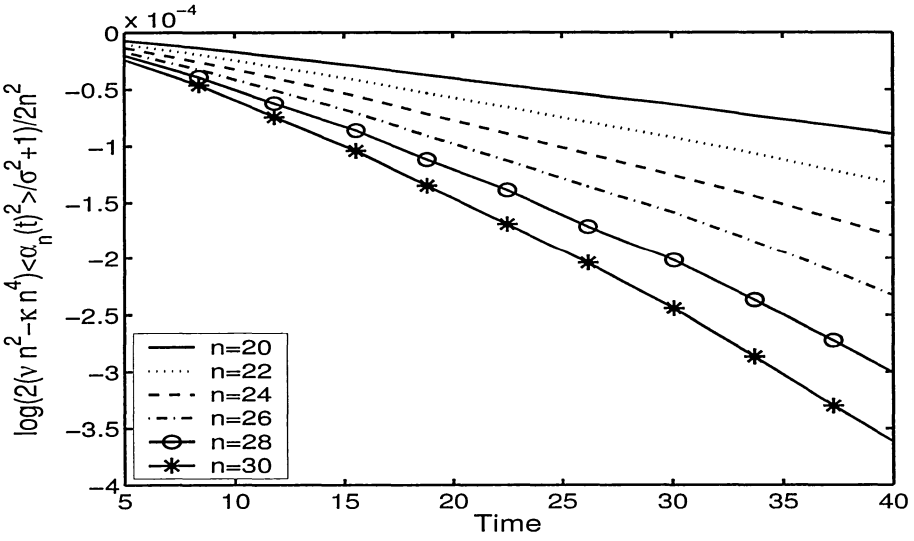

Figure 6.14: $\ln\left[\frac{2(\nu n^2-\kappa n^4)}{\sigma^2}\langle\alpha_n(t)^2\rangle+1\right]/2n^2$ versus t for $n=20,22,24,26,28$, and 30 in Process 6.3.

which is plotted in Fig.6.15 using the dotted line. Therefore, the values of ν and κ are identified as follows:

$$\nu = 3.27\times10^{-6};\quad \kappa = 1.34\times10^{-8} \tag{6.53}$$

The value of σ is determined by using Eq.6.51 and Eq.6.53. If we compute the value of σ using $\nu = 3.27\times10^{-6}$ and $\frac{2\nu}{\sigma^2} = 0.26$, we can obtain $\sigma_\nu = 5.0\times10^{-3}$. However, if we compute the value of σ using $\kappa = 1.34\times10^{-8}$ and $\frac{2\kappa}{\sigma^2} = 1.45\times10^{-3}$, we can obtain $\sigma_\kappa = 4.29\times10^{-3}$. We decide that the value of σ is the average of the value of σ_ν and σ_κ as follows:

$$\sigma = \frac{\sigma_\nu+\sigma_\kappa}{2} = 4.65\times10^{-3} \tag{6.54}$$

Using the identified parameters of Eqs.6.53 and 6.54, we compute the expected surface roughness in Process 6.3 based on Eq.6.45. An 80th order stochastic ordinary differential equation approximation of the system of Eq.6.45 is used to simulate

the process (the use of higher-order approximations led to identical numerical results, thereby implying that the following simulation runs are independent of the discretization). The δ function involved in the covariances of ξ_α^n and ξ_β^n is approximated by $\frac{1}{\Delta t}$ where Δt is the integration time step. In Fig.6.16, we compare the expected value of the open-loop surface roughness of Process 6.3 from the solution of the linearized stochastic KSE model of Eq.6.45 to that from a kinetic Monte-Carlo simulation. The two profiles are very close. Therefore, by using the linearized stochastic KSE model of Eq.6.45 with the identified model parameters, we can predict the evolution of the expected surface roughness in this sputtering process. This linearized stochastic KSE model is used as the basis for feedback controller design.

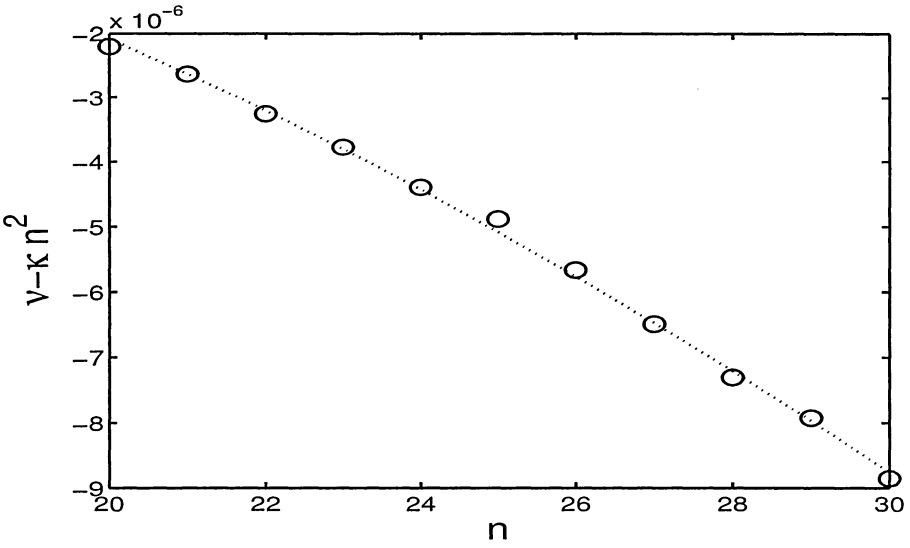

Figure 6.15: The slopes of lines in Fig.6.14 versus n for $n = 20, \cdots, 30$ (marked by 'o') and the curve of $y = 3.27 \times 10^{-6} - 1.34 \times 10^{-8} n^2$ (dotted line) in Process 6.3.

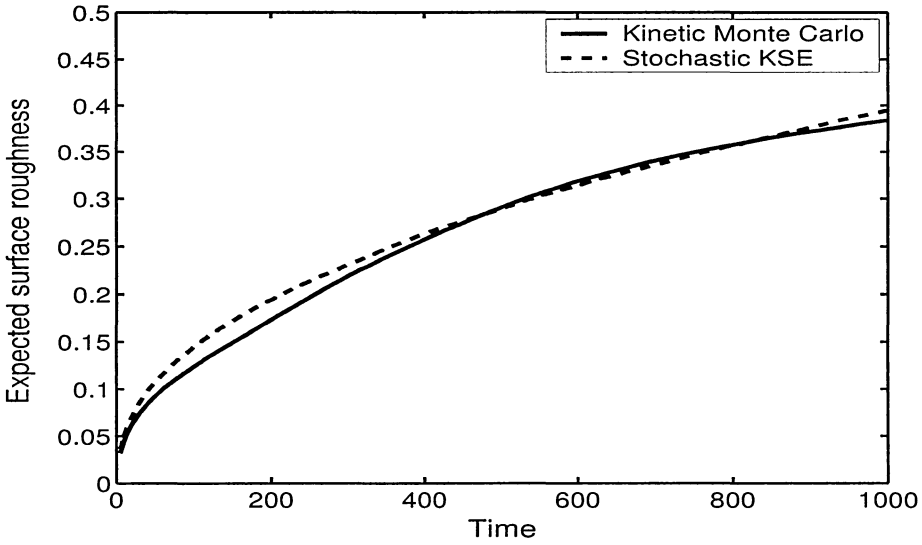

Figure 6.16: Comparison of the open-loop profile of the expected surface roughness from the kinetic Monte-Carlo simulator (solid line) and that from the solution of the linearized stochastic Kuramoto-Sivashinsky equation with $\nu = 3.27 \times 10^{-6}$, $\kappa = 1.34 \times 10^{-8}$ and $\sigma = 4.65 \times 10^{-3}$ (dotted line) in Process 6.3.

Feedback control design

Our control objective is to control the expected surface roughness in Process 6.3 to a desired value. We design a state feedback controller based on a $40th$ order stochastic ODE approximation constructed by using the first 40 eigenmodes of the system of Eq.6.47 with identified model parameters $\nu = 3.27 \times 10^{-6}$, $\sigma = 4.65 \times 10^{-3}$ and $\kappa = 1.34 \times 10^{-8}$. 40 control actuators are used to control the system. The ith actuator distribution function is taken to be:

$$b_i(z) = \begin{cases} \frac{1}{\sqrt{\pi}} \sin(iz); & i = 1, \cdots, 20 \\ \\ \frac{1}{\sqrt{\pi}} \cos[(i-20)z]; & i = 21, \cdots, 40 \end{cases} \tag{6.55}$$

The desired closed-loop surface roughness is 0.29 in this simulation. Using Eq.6.28, we design the state feedback controller such that $\lambda_{c\alpha_i} = \lambda_{c\beta_i} = -0.001$, for $i = 1, \cdots, 20$.

Then, we apply the designed controller to the Monte-Carlo model of Process 6.3 to control the surface roughness to the desired level. In this simulation, the controller is implemented by manipulating the probability that a randomly selected site is subject to erosion rule, f. Specifically, the f of site i is determined according to the following expression:

$$f(i) = \frac{\bar{f} + \left(\sum_{j=1}^{40} b_j(z_i) u_j(t) \right) / a}{1 + \left(\sum_{j=1}^{40} b_j(z_i) u_j(t) \right) / a} \tag{6.56}$$

The following simulation algorithm is used to run the kinetic Monte-Carlo simulations for the closed-loop system. First, a random number, ζ_1 is generated to pick a site i, among all the sites on the 1-D lattice; the probability that a surface site is subject to the erosion rules, $f(i)$ is determined by using Eq.6.56. Then, the second random number, ζ_2 in the $(0, 1)$ interval is generated. If $\zeta_2 < f(i)$, the site i is subject to the erosion, otherwise, the site is subject to diffusion.

If the site i is subject to erosion, P_e is computed by using the box rule shown in Fig.6.1 with the box centering the surface particle on site i and $Y(\phi_i)$ is computed by using Eq.6.1. Then, another random number, ζ_{e3} in the $(0, 1)$ interval is generated. If $\zeta_{e3} < P_e \cdot Y(\phi_i)$ the surface particle on site i is removed. Otherwise, no Monte-Carlo event is executed.

If the site i is subject to diffusion, a side-neighbor, $j = i + 1$ or $i - 1$ is randomly picked and the probability of a hopping from site i to site j, $w_{i \to j}$ is computed based on Eq.6.3. Then, another random number ζ_{d3} in the $(0, 1)$ interval is generated. If $\zeta_{e3} < w_{i \to j}$, the surface particle on site i is moved to site j. Otherwise, no Monte-Carlo event is executed. Once a Monte-Carlo event is executed, the first 40 states $(\alpha_1, \cdots, \alpha_{20}$ and $\beta_1, \cdots, \beta_{20})$ are updated and new control actions are computed to update the spatially distributed probability that a randomly selected site is subject to erosion rule.

The closed-loop system simulation results are shown in Fig.6.17. The dotted line shows the expected surface roughness, which is the average of surface roughness profiles obtained from 200 independent runs, under feedback control. We can see that the controller successfully drives the expected surface roughness to a finite value. The solid line shows the surface roughness profile under feedback control from one simulation run; due to the stochastic nature of the deposition process, stochastic fluctuations can be observed in the closed-loop surface roughness profile, but the surface roughness is very close to the expected surface roughness under feedback control. For the sake of comparison, the dashed-line shows a surface roughness profile from one open-loop simulation run. We can see that under feedback control, the surface roughness can be controlled to the desired level.

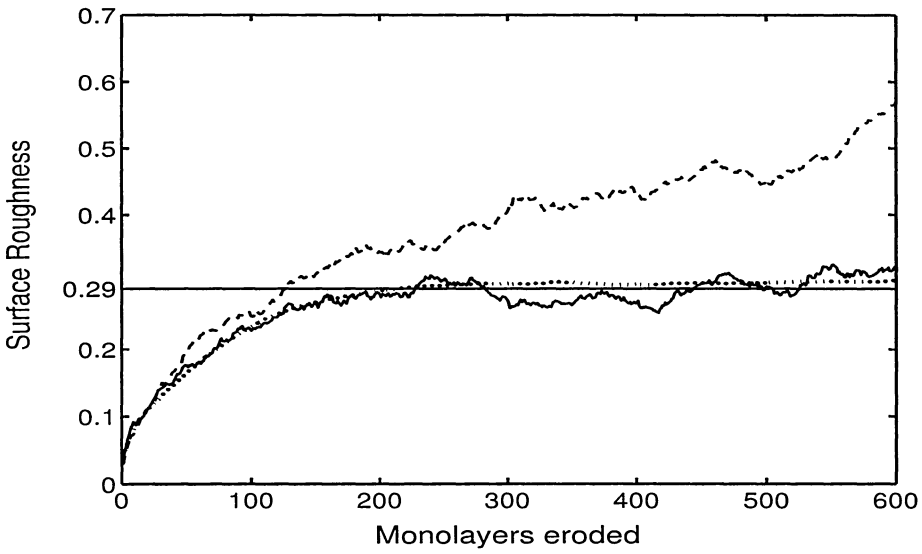

Figure 6.17: Closed-loop surface roughness profiles in Process 6.3. (a) The closed-loop surface roughness profile from one simulation run (solid line), (b) The expected closed-loop surface roughness profile obtained from 200 independent simulation runs (dotted line), and (c) the open-loop surface roughness profile from one simulation run (dashed line).

6.5 Conclusions

This chapter focused on control of surface roughness in sputtering processes using the stochastic KSE. We initially reformulated the stochastic KSE into a system of infinite stochastic ordinary differential equations by using modal decomposition. A finite-dimensional approximation of the stochastic KSE was then derived that captures the dominant mode contribution to the surface roughness. A state feedback controller was designed based on the finite-dimensional approximation to control the surface roughness. Feedback control of surface roughness in three different sputtering processes with different sputtering yield functions and different ratios of erosion and diffusion rates was studied. The parameters of the stochastic PDE models describing the sputtering processes were identified by using the surface height fluctuation data obtained from Monte-Carlo simulations so that the evolution of the surface roughness computed from the stochastic PDE models is consistent to that computed from Monte-Carlo simulations. Feedback controllers were designed and applied to Monte-Carlo models of the sputtering processes. Simulation results showed that the designed feedback controllers can successfully regulate the surface roughness to desired levels.

Chapter 7

Optimal Actuator/Sensor Placement for Nonlinear Control of the Kuramoto-Sivashinsky Equation

7.1 Introduction

The Kuramoto-Sivashinsky equation (KSE) is a nonlinear dissipative fourth-order partial differential equation (PDE) of the form:

$$\frac{\partial U}{\partial t} = -\nu \frac{\partial^4 U}{\partial z^4} - \frac{\partial^2 U}{\partial z^2} - U \frac{\partial U}{\partial z} \tag{7.1}$$

where $\nu > 0$ is the so-called instability parameter, which describes incipient instabilities in a variety of physical and chemical systems. Examples include falling liquid films (Chen and Chang, 1986), unstable flame fronts (Sivashinsky, 1977), and interfacial instabilities between two viscous fluids (Hooper and Grimshaw, 1985). Analytical and numerical studies of the dynamics of Eq.7.1 with periodic boundary conditions

(e.g., Temam, 1988; Chen and Chang, 1986) have revealed the existence of steady and periodic wave solutions, as well as chaotic behavior for very small values of ν.

In addition to the existence of complex solution patterns, the above studies have revealed that the dominant dynamics of the KSE can be adequately characterized by a small number of degrees of freedom (e.g., Temam, 1988). Motivated by this, research has focused on the design of linear/nonlinear finite-dimensional output feedback controllers (Armaou and Christofides, 2000a,b) for stabilization of the zero solution of the KSE on the basis of ordinary differential equation (ODE) approximations, obtained through linear (Armaou and Christofides, 2000a) and nonlinear (Armaou and Christofides, 2000b) Galerkin's method, that accurately describe the dominant dynamics of the KSE for a given value of the instability parameter. The global stabilization of the KSE has also been addressed via distributed static output feedback control (Christofides and Armaou, 2000). A nonlinear boundary feedback controller was also proposed in Liu and Krstić (2001) that enhances the rate of convergence to the spatially uniform steady-state of the KSE for values of ν for which this steady-state is open-loop stable. Design of fault-tolerant control systems to the KSE have been addressed in El-Farra et al. (2003) and simulation results on robust control of the linearized KSE using sliding mode controllers were presented in Orlov et al. (2004). Even though the above works lead to the systematic design of practically implementable feedback controllers for the KSE, they do not address the issue of optimal actuator/sensor placement so that the desired control objectives are achieved with minimal energy use.

The area of integration of feedback control design with optimal placement of control actuators and measurement sensors so that the desired control objectives are achieved with minimal energy use has received significant attention, especially in 70s

and early 80s (see, for example, the review paper Kubrusly and Malebranche, 1985), in the context of linear distributed parameter systems (DPS). Specifically, several results have been derived on the problem of integrating linear feedback control and optimal actuator placement for several classes of linear DPS including controllability measures and actuator placement in oscillatory systems (Arbel, 1981), as well as optimal placement of actuators for linear feedback controllers in parabolic PDEs (e.g., Demetriou, 1999) and in actively controlled structures (e.g., Choe and Baruh, 1992). Furthermore, the problem of selecting optimal locations for measurement sensors in linear distributed parameter systems has also received very significant attention (e.g., Kumar and Seinfeld, 1978; Morari and O'Dowd, 1980). Significant research efforts have also been made on the integrated optimal placement of actuators and sensors for various classes of linear DPS (Kubrusly and Malebranche, 1985). Recently, we initiated a line of work on the computation of optimal actuator/sensor locations of nonlinear controllers for spatially-distributed processes. In Antoniades and Christofides (2001), a method for the integration of nonlinear output feedback control with optimal actuator/sensor placement for transport-reaction processes described by a broad class of quasi-linear parabolic PDEs was proposed. The proposed method, based on Galerkin's method and the concept of full state-feedback linearization, allows simultaneously designing a stabilizing nonlinear output feedback controller and solving the optimal placement problem in a highly-efficient fashion.

In this chapter, we use the methodology proposed in Antoniades and Christofides (2001) to compute optimal locations of point control actuators and measurement sensors for nonlinear output feedback control of the KSE with periodic boundary conditions. We initially synthesize stabilizing nonlinear state feedback controllers via geometric techniques on the basis of finite-dimensional approximations, obtained via

Galerkin's method, that capture the dominant dynamics of the KSE. The optimal actuator location problem is subsequently formulated as the one of minimizing a meaningful cost functional that includes penalty on the response of the closed-loop system and the control action. Then, under the assumption that the number of measurement sensors is equal to the number of slow modes, we employ a procedure proposed in Christofides and Baker (1999) for obtaining estimates for the states of the approximate finite-dimensional model from the measurements. The estimates are combined with the state feedback controllers to derive output feedback controllers. The optimal location of the measurement sensors is computed by minimizing a cost function of the estimation error in the closed-loop infinite-dimensional system. The theoretical results are successfully illustrated through computer simulations of the closed-loop system using a high-order discretization of the KSE.

7.2 Preliminaries

We consider the Kuramoto-Sivashinsky equation in one spatial dimension with distributed control:

$$\begin{aligned} \frac{\partial U}{\partial t} &= -\nu\frac{\partial^4 U}{\partial z^4} - \frac{\partial^2 U}{\partial z^2} - U\frac{\partial U}{\partial z} + \sum_{i=1}^{l} b_i u_i(t) \\ y_m^\kappa &= \int_{-\pi}^{\pi} s_\kappa(z) U dz, \ \kappa = 1, \ldots, p \\ y_c^i &= \int_{-\pi}^{\pi} c_i(z) U dz, \ i = 1, \ldots, l \end{aligned} \tag{7.2}$$

subject to the periodic boundary conditions:

$$\frac{\partial^j U}{\partial z^j}(-\pi, t) = \frac{\partial^j U}{\partial z^j}(+\pi, t), \quad j = 0, \ldots, 3 \tag{7.3}$$

and the initial condition:

$$U(z, 0) = U_0(z) \tag{7.4}$$

where $U(z,t)$ is the state of the PDE, $z \in [-\pi, \pi]$ is the spatial coordinate, t is the time and 2π is the length of the spatial domain, ν is the instability parameter, and $U_0(z)$ is the initial condition. $u_i \in \mathbb{R}$ denotes the i-th manipulated input, l is the total number of manipulated inputs, $b_i(z)$ is the i-th actuator distribution function (i.e., $b_i(z)$ determines how the control action computed by the i-th control actuator, $u_i(t)$, is distributed (e.g., point or distributed actuation) in the spatial interval $[-\pi, \pi]$), $y_c^i \in \mathbb{R}$ denotes a controlled output, $c_i(z)$ is a known smooth function of z which is determined by the desired stability/performance specifications, $y_m^\kappa \in \mathbb{R}$ denotes a measured output, and $s_\kappa(z)$ is a known smooth function of z which is determined by the location and type of the measurement sensors (e.g., point/distributed sensing). We note that whenever the control action enters the system at a single point z_0, with $z_0 \in [-\pi, \pi]$ (i.e. point actuation), the function $b_i(z)$ is taken to be nonzero in a finite spatial interval of the form $[z_0 - \epsilon, z_0 + \epsilon]$, where ϵ is a small positive real number, and zero elsewhere in $[-\pi, \pi]$. Throughout the manuscript, we will consider the problem of optimal actuator/sensor placement by considering point control actuators.

To present the method that we use for output feedback controller design and optimal actuator/sensor placement, we formulate Eq.7.2 as an infinite dimensional system in the Hilbert space $\mathcal{H}([-\pi, \pi]; \mathbb{R})$, with $\mathcal{H}$ being the space of sufficiently smooth functions defined on $[-\pi, \pi]$, with inner product and norm:

$$(\omega_1, \omega_2) = \int_{-\pi}^{\pi} (\omega_1(z), \omega_2(z))_{\mathbb{R}} dz, \; ||\omega_1||_2 = (\omega_1, \omega_1)^{\frac{1}{2}} \tag{7.5}$$

where ω_1, ω_2 are two elements of $\mathcal{H}([-\pi, \pi]; \mathbb{R})$ and the notation $(\cdot, \cdot)_{\mathbb{R}}$ denotes the standard inner product in $\mathbb{R}$. Defining the state function x on $\mathcal{H}([-\pi, \pi]; \mathbb{R})$ as:

$$x(t) = U(z,t), \quad t > 0, \quad z \in [-\pi, \pi], \tag{7.6}$$

the operator $\mathcal{A}$ in $\mathcal{H}([-\pi,\pi];\mathbb{R})$ as:

$$\left.\begin{aligned}
&\mathcal{A}x = -\nu\frac{\partial^4 U}{\partial z^4} - \frac{\partial^2 U}{\partial z^2} \\
&x \in D(\mathcal{A}) = \{x \in \mathcal{H}([-\pi,\pi];\mathbb{R}) : \\
&\frac{\partial^j U}{\partial z^j}(-\pi,t) = \frac{\partial^j U}{\partial z^j}(+\pi,t), \quad j = 0,\ldots,3
\end{aligned}\right\} \tag{7.7}$$

and the input, controlled output, and measured output operators as:

$$\mathcal{B}u = \sum_{i=1}^{m} b_i u_i, \quad \mathcal{C}x = (c,x), \quad \mathcal{S}x = (s,x) \tag{7.8}$$

the system of Eqs.7.2-7.3-7.4 takes the form:

$$\begin{aligned}
\dot{x} &= \mathcal{A}x + \mathcal{B}u + f(x), \quad x(0) = x_0 \\
y_c &= \mathcal{C}x, \quad y_m = \mathcal{S}x
\end{aligned} \tag{7.9}$$

where $f(x(t)) = -U\dfrac{\partial U}{\partial z}$ and $x_0 = U_0(z)$.

For $\mathcal{A}$, we can formulate the following eigenvalue problem:

$$\mathcal{A}\phi_n = -\nu\frac{\partial^4 \phi_n}{\partial z^4} - \frac{\partial^2 \phi_n}{\partial z^2} = \lambda_n \phi_n, \quad n = 1,\ldots,\infty \tag{7.10}$$

subject to:

$$\frac{\partial^j \phi_n}{\partial z^j}(-\pi) = \frac{\partial^j \phi_n}{\partial z^j}(+\pi), \quad j = 0,\ldots,3 \tag{7.11}$$

where λ_n denotes an eigenvalue and ϕ_n denotes an eigenfunction. A direct computation of the solution of the above eigenvalue problem yields $\lambda_0 = 0$ with $\psi_0(z) = \dfrac{1}{\sqrt{2\pi}}$, and $\lambda_n = -\nu n^4 + n^2$ (λ_n is an eigenvalue of multiplicity two) with eigenfunctions $\phi_n(z) = \dfrac{1}{\sqrt{\pi}}\sin(nz)$ and $\psi_n(z) = \dfrac{1}{\sqrt{\pi}}\cos(nz)$ for $n = 1,\ldots,\infty$. We also define the eigenspectrum of $\mathcal{A}$, $\sigma(\mathcal{A})$, as the set of all eigenvalues of $\mathcal{A}$, i.e. $\sigma(\mathcal{A}) = \{\lambda_1, \lambda_2, \ldots,\}$. We note that the fact that $\mathcal{A}$ has a real pure point spectrum is a result of the fact that the spatial differential operator of the KSE with periodic boundary conditions is self-adjoint and the problem is considered in a bounded domain.

From the expression for the eigenvalues, it follows that for a fixed value of $\nu > 0$ the number of unstable eigenvalues of $\mathcal{A}$ is finite and the distance between two consecutive eigenvalues (i.e., λ_n and λ_{n+1}) increases as n increases. Furthermore, for a fixed value of $\nu > 0$, $\sigma(\mathcal{A})$ can be partitioned as $\sigma(\mathcal{A}) = \sigma_1(\mathcal{A}) \bigcup \sigma_2(\mathcal{A})$, where $\sigma_1(\mathcal{A})$ contains the first m (with m finite) "slow" eigenvalues (i.e. $\sigma_1(\mathcal{A}) = \{\lambda_1, \ldots, \lambda_m\}$) and $\sigma_2(\mathcal{A})$ contains the remaining "fast" eigenvalues (i.e., $\sigma_2(\mathcal{A}) = \{\lambda_{m+1}, \ldots, \}$ where $\lambda_{m+1} < 0$). To capture the separation between the "slow" and "fast" eigenvalues, we define the parameter $\epsilon = \dfrac{\lambda_1}{\lambda_{m+1}}$ (note that $\epsilon \to 0$ as $m \to \infty$). We note that the occurrence of a finite number of unstable eigenvalues and the separation of "slow" and "fast" eigenvalues is a common characteristic of the spectrum of spatial differential operators associated with transport-reaction processes and fluid dynamic systems (Christofides, 2001b).

The separation between the "slow" and "fast" eigenvalues suggests that the dominant dynamics of the KSE can be described by a finite-dimensional system. We apply standard Galerkin's method to the system of Eq.7.9 to derive an approximate finite-dimensional system. Let $\mathcal{H}_s$, $\mathcal{H}_f$ be modal subspaces of $\mathcal{A}$, defined as $\mathcal{H}_s = span\{\phi_1, \phi_2, \ldots, \phi_m\}$ and $\mathcal{H}_f = span\{\phi_{m+1}, \phi_{m+2}, \ldots, \}$ (the existence of $\mathcal{H}_s$, $\mathcal{H}_f$ follows from the properties of $\mathcal{A}$). Defining the orthogonal projection operators P_s and P_f such that $x_s = P_s x$, $x_f = P_f x$, the state x of the system of Eq.7.9 can be decomposed as:

$$x = x_s + x_f = P_s x + P_f x \tag{7.12}$$

Applying P_s and P_f to the system of Eq.7.9 and using the above decomposition for

x, the system of Eq.7.9 can be equivalently written in the following form:

$$\begin{aligned} \frac{dx_s}{dt} &= \mathcal{A}_s x_s + \mathcal{B}_s u + f_s(x_s, x_f) \\ \frac{\partial x_f}{\partial t} &= \mathcal{A}_f x_f + \mathcal{B}_f u + f_f(x_s, x_f) \\ y_c &= \mathcal{C} x_s + \mathcal{C} x_f, \qquad y_m = \mathcal{S} x_s + \mathcal{S} x_f, \\ x_s(0) &= P_s x(0) = P_s x_0, \;\; x_f(0) = P_f x(0) = P_f x_0 \end{aligned} \tag{7.13}$$

where $\mathcal{A}_s = P_s \mathcal{A} P_s$, $\mathcal{B}_s = P_s \mathcal{B}$, $f_s = P_s f$, $\mathcal{A}_f = P_f \mathcal{A} P_f$, $\mathcal{B}_f = P_f \mathcal{B}$ and $f_f = P_f f$ and the notation $\frac{\partial x_f}{\partial t}$ is used to denote that the state x_f belongs in an infinite-dimensional space. In the above system, $\mathcal{A}_s$ is a diagonal matrix of dimension $m \times m$ of the form $\mathcal{A}_s = diag\{\lambda_j\}$, $f_s(x_s, x_f)$ and $f_f(x_s, x_f)$ are Lipschitz vector functions, and $\mathcal{A}_f$ is an unbounded differential operator which is exponentially stable (following from the fact that $\lambda_{m+1} < 0$ and the selection of $\mathcal{H}_s, \mathcal{H}_f$). Neglecting the fast and stable infinite-dimensional x_f-subsystem in the system of Eq.7.13, the following m-dimensional slow system is obtained:

$$\begin{aligned} \frac{d\tilde{x}_s}{dt} &= \mathcal{A}_s \tilde{x}_s + \mathcal{B}_s u + f_s(\tilde{x}_s, 0) \\ \tilde{y}_c &= \mathcal{C} \tilde{x}_s, \qquad \tilde{y}_m = \mathcal{S} \tilde{x}_s \end{aligned} \tag{7.14}$$

where the bar symbol in $\tilde{x}_s$, $\tilde{y}_c$ and $\tilde{y}_m$ denotes that these variables are associated with a finite-dimensional system.

Remark 7.1 *A physical system that can be described by the KSE is the motion of a liquid film falling down on a vertical wall (Chen and Chang, 1986). In this case, $U(z,t)$ is the film height. Such a system has been found experimentally to exhibit wavy behavior of the type predicted by the KSE for values of ν smaller than 1 (see also Figure 7.2). In many instances, it is desirable to suppress wavy behavior by using control actuators that add/remove fluid mass via blowing/suction. In this case, the control input enters directly into the partial differential equation and does not appear in the boundary conditions. This physical problem is consistent with the formulation of Eq.7.2 since we consider distributed control actuation. Note that problems for which the inputs enters directly into the KSE but nonlinearly can be readily handled*

within our formulation by simply solving for u through the inversion of an algebraic nonlinear equation.

Remark 7.2 *The consideration of approximate point control is motivated by the fact that most experimental point control actuators (including the ones that add/remove fluid mass via blowing/suction) have finite (but small) support and the fact that* $b_i(z) = \delta(z - z_0)$ *(where* $\delta(\cdot)$ *is the standard Dirac function) is not an element of* $\mathcal{H}([-\pi, \pi]; \mathbb{R})$.

7.3 Integrating nonlinear control and optimal actuator placement

7.3.1 Nonlinear state feedback controller synthesis

In this section, we assume the use of point control actuators and assume that measurements of the states of the system of Eq.7.14 are available. We first address the problem of synthesizing nonlinear static state feedback control laws of the general form:

$$u = \mathcal{F}(z_a, \tilde{x}_s) \tag{7.15}$$

where $\mathcal{F}(z_a, \tilde{x}_s)$ is a nonlinear vector function and $z_a = [b_1(z_{a_1}) \cdots b_l(z_{a_l})]^T$ denotes the vector of the point actuator locations, that guarantee exponential stability of the closed-loop finite-dimensional system. To address this problem and simplify our development, we need to impose the following assumption.

Assumption 7.1 $l = m$ *(i.e., the number of control actuators is equal to the number of slow modes), and the inverse of the matrix* $\mathcal{B}_s$ *exists.*

The requirement $l = m$ is sufficient and not necessary, and it is made to simplify the synthesis of the controller and the solution of the optimal placement problem (see

also discussion in Remark 7.1 below).

Proposition 7.1 that follows provides the explicit formula for the state feedback controller that achieves the control objective (the proof can be found in Antoniades and Christofides (2001)).

Proposition 7.1 *Consider the finite-dimensional system of Eq.7.14 for which assumption 7.1 holds. Then, the state feedback controller:*

$$u = \mathcal{B}_s^{-1}\left((\Lambda_s - \mathcal{A}_s)\tilde{x}_s - f_s(\tilde{x}_s, 0)\right) \tag{7.16}$$

where Λ_s is a stable matrix, guarantees global exponential stability of the closed-loop finite-dimensional system.

Remark 7.3 *The structure of the closed-loop finite-dimensional system under the controller of Eq.7.16 has the following form:*

$$\dot{\tilde{x}}_s = \Lambda_s \tilde{x}_s \tag{7.17}$$

and thus, the response of this system depends only on the stable matrix Λ_s and the initial condition, $x_s(0)$, and is independent of the actuator locations.

Remark 7.4 *While the requirements $l = m$ and existence of $\mathcal{B}_s^{-1}$ are sufficient to design a state feedback law that fully linearizes the closed-loop finite dimensional system (Eq.7.17), it is important to note that full linearization of the closed-loop finite-dimensional system through coordinate change and nonlinear feedback can be achieved for any number of manipulated inputs (i.e., for any $l \in [1, m]$), provided that an appropriate set of involutivity conditions is satisfied by the corresponding vector fields of the system of Eq.7.14 (see (Isidori, 1989, page 165) for details).*

7.3.2 Computation of optimal actuator locations

In this subsection, we compute the actuator locations so that the state feedback controller of Eq.7.16 is near-optimal for the full KSE system of Eq.7.13 with respect

to a meaningful cost functional which is defined over the infinite time-interval and imposes penalty on the response of the closed-loop system and the control action. To this end, we initially focus on the ODE system of Eq.7.14 and consider the following cost functional:

$$\begin{aligned} J_s &= \int_0^\infty ((\tilde{x}_s(x_s(0),t), Q_s\tilde{x}_s(x_s(0),t)) \\ &\quad +u^T(\tilde{x}_s(x_s(0),t), z_a)Ru(\tilde{x}_s(x_s(0),t), z_a))dt \end{aligned} \tag{7.18}$$

where Q_s and R are positive definite matrices and the inner product in $\mathcal{H}$ notation of Eq.7.5 is used in the first term of the integrand. The cost of Eq.7.18 is well-defined and meaningful since it imposes penalty on the response of the closed-loop finite-dimensional system and the control action. However, a potential problem of this cost is its dependence on the choice of a particular initial condition, $x_s(0)$, and thus, the solution to the optimal placement problem based on this cost may lead to actuator locations that perform very poorly for a large set of initial conditions. To reduce this dependence and obtain optimality over a broad set of initial conditions, we follow (Levine and Athans, 1978) and consider an average cost over a set of m linearly independent initial conditions, $x_s^i(0)$, $i = 1, \ldots, m$, of the following form:

$$\begin{aligned} \hat{J}_s &= \frac{1}{m}\sum_{i=1}^{m}\int_0^\infty ((\tilde{x}_s(x_s^i(0),t), Q_s\tilde{x}_s(x_s^i(0),t)) \\ &\quad +u^T(\tilde{x}_s(x_s^i(0),t), z_a)Ru(\tilde{x}_s(x_s^i(0),t), z_a))dt \end{aligned} \tag{7.19}$$

Referring to the above cost, we first note that the penalty on the response of the closed-loop system:

$$\hat{J}_{xs} = \frac{1}{m}\sum_{i=1}^{m}\int_0^\infty (\tilde{x}_s(x_s^i(0),t), Q_s\tilde{x}_s(x_s^i(0),t))dt \tag{7.20}$$

is finite because the solution of the closed-loop system of Eq.7.17 is exponentially stable by appropriate choice of Λ_s. Moreover, $\hat{J}_{xs}$ is independent of the actuator locations (Remark 7.3), and thus, the optimal actuator placement problem reduces to the one of minimizing the following cost which only includes penalty on the control

action:

$$\hat{J}_{us} = \frac{1}{m}\sum_{i=1}^{m}\int_0^\infty u^T(\tilde{x}_s(x_s^i(0),t),z_a)Ru(\tilde{x}_s(x_s^i(0),t),z_a)dt \tag{7.21}$$

$\hat{J}_{us}$ is a function of multiple variables, $z_a = [z_{a1}\ z_{a2}\ \cdots\ z_{al}]$, and thus, it obtains its local minimum values when its gradient with respect to the actuator locations is equal to zero, i.e.:

$$\frac{\partial \hat{J}_{us}}{\partial z_a} = \left[\frac{\partial \hat{J}_{us}}{\partial z_{a1}}\ \cdots\ \frac{\partial \hat{J}_{us}}{\partial z_{al}}\right]^T = [\,0\ \cdots\ 0\,]^T \tag{7.22}$$

and $\nabla_{z_a z_a}\hat{J}_{us}(z_{am}) > 0$ where $\nabla_{z_a z_a}\hat{J}_{us}$ is the Hessian matrix of $\hat{J}_{us}$ and z_{am} is a solution of the system of nonlinear algebraic equations of Eq.7.22 (which includes l equations with l unknowns). The solution z_{am} for which the above conditions are satisfied and $\hat{J}_{us}$ obtains its smallest value (global minimum) corresponds to the optimal actuator locations for the closed-loop finite-dimensional system.

Remark 7.5 *Owing to the numerical complexity involved in computing the actuator locations that exactly minimize the cost of Eq.7.21 (it involves search over an infinite number of locations), we initially assume a large number, say L, of equispaced locations along the length of the spatial domain in which the control actuators are possible to be placed (i.e., locations for which $\mathcal{B}_s^{-1}$ exists and the closed-loop finite-dimensional system is stabilizable). Then, we compute the value of the cost of Eq.7.21 for all possible combinations of the actuator locations to calculate the optimal locations.*

Remark 7.6 *While the cost of Eq.7.19 is meaningful in the sense that it imposes penalty both on the system response and the control effort and standard in the context of optimal actuator placement problems, it is possible to compute optimal actuator locations with respect to cost functionals that include penalty on the rate of change of the state and of the control action in order to enforce additional control objectives. The consideration of such costs can be addressed and studied in the context of the proposed framework however, it may lead to an increase in the magnitude of the computational demand needed to solve the optimization problem.*

7.3.3 Output feedback control and sensor placement

The nonlinear controller of Eq.7.16 was derived under the assumption that measurements of the states $\tilde{x}_s$ are available, which implies that measurements of the state variable, $U(z,t)$, are available at all positions and times. However, from a practical point of view, measurements of the state variables are only available at a finite number of spatial positions. Motivated by these practical problems, we address in this section: a) the synthesis of nonlinear output feedback controllers that use measurements of the process outputs, y_m, to enforce stability in the closed-loop infinite-dimensional system, and b) the computation of optimal locations of the measurement sensors. Specifically, we consider output feedback control laws of the general form:

$$u = \mathcal{F}(y_m) \tag{7.23}$$

where $\mathcal{F}(y_m)$ is a nonlinear vector function and y_m is the vector of measured outputs. The synthesis of the controller of Eq.7.23 will be achieved by combining the state feedback controller of Eq.7.16 with a procedure proposed in Christofides and Baker (1999) for obtaining estimates for the states of the approximate ODE model of Eq.7.14 from the measurements. To this end, we need to impose the following requirement on the number of measured outputs in order to obtain estimates of the states x_s of the finite-dimensional system of Eq.7.14, from the measurements y_m^κ, $\kappa = 1, \ldots, p$.

Assumption 7.2 *$p = m$ (i.e., the number of measurements is equal to the number of slow modes), and the inverse of the operator $\mathcal{S}$ exist, so that $\hat{x}_s = \mathcal{S}^{-1} y_m$.*

We note that the requirement that the inverse of the operator S exists can be achieved by appropriate choice of the location of the measurement sensors (i.e., functions $s^\kappa(z)$). When point measurement sensors are used, this requirement can be verified by checking the invertibility of a matrix (see Eq.7.33 in the next section). The optimal

locations for the measurement sensors can be then computed by minimizing an average cost function of the estimation error of the closed-loop infinite-dimensional system of the form:

$$\hat{J}(e) = \frac{1}{m}\sum_{i=1}^{m}\int_0^{\infty}(||x_s(x_s^i(0),t) - \hat{x}_s(x_s^i(0),t)||_2)dt \tag{7.24}$$

where x_s is the slow state of the closed-loop infinite-dimensional system of Eq.7.13, $\hat{x}_s = \mathcal{S}^{-1}y_m$, and $e(t) = ||x_s - \hat{x}_s||_2$ is the estimation error. In contrast to the solution of the optimal location problem for the control actuators, the solution to this optimization problem requires the solution of the closed-loop infinite-dimensional system in order to compute x_s, and $\hat{x}_s$ (from the measurements y_m^{κ}, $\kappa = 1, 2, \ldots, p$), and thus, it is more computationally demanding.

Theorem 7.1 that follows establishes that the proposed output feedback controller enforces stability in the closed-loop infinite-dimensional system and that the solution to the optimal actuator/sensor problem, which is obtained on the basis of the closed-loop finite-dimensional system, is near-optimal in the sense that it approaches the optimal solution for the infinite-dimensional system as the separation of the slow and fast eigenmodes increases. The proof can be found in Antoniades and Christofides (2001).

Theorem 7.1 *Consider the system of Eq.7.13, and the finite-dimensional system of Eq.7.14, for which assumptions 7.1 and 7.2 hold, under the nonlinear output feedback controller:*

$$\begin{aligned} \hat{x}_s &= \mathcal{S}^{-1}y_m \\ u &= \mathcal{B}_s^{-1}\left((\Lambda_s - \mathcal{A}_s)\hat{x}_s - f_s(\hat{x}_s, 0)\right) \end{aligned} \tag{7.25}$$

Then, there exist positive real numbers μ_1, μ_2 and ϵ^* such that if $|x_s(0)| \leq \mu_1$, $||x_f(0)||_2 \leq \mu_2$, and $\epsilon \in (0, \epsilon^*]$, then the controller of Eq.7.25:
(a) guarantees exponential stability of the infinite-dimensional closed-loop system, and
(b) the locations of the point actuators and measurement sensors are near-optimal in

the sense that the cost function associated with the controller of Eq.7.25 and the system of Eq.7.13 satisfies:

$$\begin{aligned}\hat{J} &= \frac{1}{m}\sum_{i=1}^{m}\int_0^{\infty}((x_s(x_s^i(0),t),Q_s x_s(x_s^i(0),t)) \\ &\quad +(x_f(x_s^i(0),t),Q_f x_f(x_f^i(0),t)) \\ &\quad +u^T(x_s(x_s^i(0)),t,z_a)Ru(x_s(x_s^i(0)),t,z_a))dt \\ &\quad \longrightarrow \hat{J}_s \quad as \quad \epsilon \longrightarrow 0\end{aligned} \tag{7.26}$$

where $\hat{J}$ and $\hat{J}_s$ are the average cost functions of the infinite-dimensional system of Eq.7.13 and the finite-dimensional system of Eq.7.14, respectively, under the output feedback controller of Eq.7.25.

Remark 7.7 *Even though static output feedback is more sensitive to measurement noise than dynamic output feedback, we prefer to use static feedback of y_m in the controller of Eq.7.25 because the use of a state observer to obtain estimates of the slow state variables would lead to the formulation of a very computationally-demanding optimization problem for the computation of the optimal sensor locations. Furthermore, the solution to the controller design and optimal actuator/sensor placement problems for parabolic PDE systems with uncertain variables can be found in Antoniades and Christofides (2002).*

Remark 7.8 *From the definition of ϵ, it follows that $\epsilon \rightarrow 0$ as $m \rightarrow \infty$, which implies that the control design and optimal actuator/sensor placement problems for the KSE are solvable provided m is sufficiently large. While an estimate of ϵ^* can be obtained in principle from the proof of theorem 7.1, such an estimate would be in general conservative, and thus, the number of slow modes is usually determined via computer simulations.*

7.4 Numerical results

In this section, we present an application of optimal actuator/sensor placement to the KSE for $\nu = 0.2$ to achieve stabilization at the spatially-uniform steady state using a nonlinear static output feedback control law. For simplicity and in order to better present our theoretical results, we will consider the KSE in the space of odd functions with spatial zero mean. Introducing the Hilbert space $\mathcal{H}$ of sufficiently smooth odd functions that satisfy the boundary conditions of Eq.7.3 and have spatial zero mean (i.e., $\forall\ \omega \in \mathcal{H},\ \int_{-\pi}^{\pi} \omega(z)dz = 0$) and defining the state function $x \in \mathcal{H}$ as $x(t) = U(z,t), \quad \forall\ z \in [-\pi, \pi]$, the system of Eqs.7.2-7.4 can be written in the form of Eq.7.9, where the domain of definition of the spatial differential operator $\mathcal{A}$ now takes the form:

$$\begin{aligned} x \in D(\mathcal{A}) = \Big\{ & x \in \mathcal{H}([-\pi, \pi]; \mathbb{R}); \\ & \frac{\partial^j U}{\partial z^j}(-\pi, t) = \frac{\partial^j U}{\partial z^j}(\pi, t), \quad j = 0, \ldots, 3 \Big\} \end{aligned} \tag{7.27}$$

and the eigenvalue problem for $\mathcal{A}$ yields $\lambda_j = -\nu j^4 + j^2$, $\phi_j(z) = \sqrt{\frac{1}{\pi}} sin(jz)$, $j = 1, \ldots, \infty$ (note that $\psi_0(z) = \sqrt{\frac{1}{2\pi}}$ and $\psi_j(z) = \sqrt{\frac{1}{\pi}} cos(jz)$, $j = 1, \ldots, \infty$ are not considered here since we focus only on odd functions with spatial zero mean).

All the simulation runs shown below were performed for $\nu = 0.2$, using a 30-order nonlinear ordinary differential equation model obtained from the application of Galerkin's method to the system of Eq.7.2 (the use of higher-order Galerkin approximations led to identical numerical results, thereby implying that the following simulation runs are independent of the discretization). Linearizing the system around the spatially uniform steady-state for $\nu = 0.2$, we observe that the system of Eq.7.9 possesses two unstable eigenvalues. The spatiotemporal evolution of $U(z,t)$ for $\nu = 0.2$ is shown in Figure 7.1. It is clear that for $\nu = 0.2$, the spatially uniform steady-

state $U(z,t) = 0$ is unstable. Therefore, we consider the first two Galerkin modes of the KSE as the slow modes and use Galerkin's method to construct a second-order ODE system which is used for the design of a state and an output feedback controllers and the optimal placement of two control actuators and measurement sensors (assumptions 7.1 and 7.2). The resulting second-order ODE system is of the form:

$$\begin{aligned}\begin{bmatrix} (\dot{\tilde{x}}_{s1}, \phi_1) \\ (\dot{\tilde{x}}_{s2}, \phi_2) \end{bmatrix} &= \begin{bmatrix} \lambda_1 & 0 \\ 0 & \lambda_2 \end{bmatrix} \begin{bmatrix} (\tilde{x}_{s1}, \phi_1) \\ (\tilde{x}_{s2}, \phi_2) \end{bmatrix} \\ &+ \begin{bmatrix} \phi_1(z_{a1}) & \phi_1(z_{a2}) \\ \phi_2(z_{a1}) & \phi_2(z_{a2}) \end{bmatrix} \begin{bmatrix} u_1 \\ u_2 \end{bmatrix} \\ &+ \begin{bmatrix} (f_1(\tilde{x}_s, 0), \phi_1) \\ (f_2(\tilde{x}_s, 0), \phi_2) \end{bmatrix}\end{aligned} \tag{7.28}$$

where z_{a1} and z_{a2} are the locations of the two point actuators and the explicit forms of the terms $f_1(\tilde{x}_s, 0)$ and $f_2(\tilde{x}_s, 0)$ are omitted for brevity.

For the system of Eq.7.28, the nonlinear state feedback controller of Eq.7.16 takes the form:

$$\begin{aligned}\begin{bmatrix} u_1 \\ u_2 \end{bmatrix} &= \begin{bmatrix} \phi_1(z_{a1}) & \phi_1(z_{a2}) \\ \phi_2(z_{a1}) & \phi_2(z_{a2}) \end{bmatrix}^{-1} \\ &* \left(\begin{bmatrix} -\alpha - \lambda_1 & 0 \\ 0 & -\beta - \lambda_2 \end{bmatrix} \begin{bmatrix} (\tilde{x}_{s1}, \phi_1) \\ (\tilde{x}_{s2}, \phi_2) \end{bmatrix} \right. \\ &\left. - \begin{bmatrix} (f_1(\tilde{x}_s, 0), \phi_1) \\ (f_2(\tilde{x}_s, 0), \phi_2) \end{bmatrix} \right)\end{aligned} \tag{7.29}$$

Substituting the above controller into the system of Eq.7.28, we obtain the following closed-loop ODE system:

$$\begin{bmatrix} (\dot{\tilde{x}}_{s1}, \phi_1) \\ (\dot{\tilde{x}}_{s2}, \phi_2) \end{bmatrix} = \begin{bmatrix} -\alpha & 0 \\ 0 & -\beta \end{bmatrix} \begin{bmatrix} (\tilde{x}_{s1}, \phi_1) \\ (\tilde{x}_{s2}, \phi_2) \end{bmatrix} \tag{7.30}$$

where α and β are positive real numbers. Since the response of the above system depends only on the parameters α, β and the initial condition x_s, and is independent of the actuator locations, we compute the optimal actuator locations by minimizing

the following cost functional, which only includes penalty on the control action:

$$\hat{J}_{us} = \frac{1}{2}\sum_{i=1}^{2}\int_0^\infty u^T(\tilde{x}_s(x_s^i(0),t),z_a)Ru(\tilde{x}_s(x_s^i(0),t),z_a)dt \tag{7.31}$$

Using the following values for the initial conditions ${x_s}^1(0) = [\phi_1\ 0]$ and ${x_s}^2(0) = [0\ \phi_2]$, and taking R, Q_s, Q_f to be unit matrices of appropriate dimensions and $\alpha = \beta = 1$, the optimal actuator locations were found, using the procedure discussed in Remark 7.5, to be: $z_{a1} = 0.31\pi$ and $z_{a2} = 0.69\pi$. We also compute the optimal sensor locations by minimizing the following cost functional of the estimation error:

$$\hat{J}(e) = \frac{1}{2}\sum_{i=1}^{2}\int_0^\infty (||x_s(x_s^i(0),t) - \hat{x}_s(x_s^i(0),t)||_2)dt \tag{7.32}$$

where x_s is obtained from the simulation of the full-order closed-loop system of Eq.7.13, and $\hat{x}_s$ is obtained from the measured outputs of the full-order closed-loop system as shown below:

$$\begin{bmatrix} \hat{x}_{s1} \\ \hat{x}_{s2} \end{bmatrix} = \begin{bmatrix} \phi_1 & 0 \\ 0 & \phi_2 \end{bmatrix} \begin{bmatrix} \phi_1(z_{s1}) & \phi_2(z_{s1}) \\ \phi_1(z_{s2}) & \phi_2(z_{s2}) \end{bmatrix}^{-1} \begin{bmatrix} y_{m1}(z_{s1},t) \\ y_{m2}(z_{s2},t) \end{bmatrix} \tag{7.33}$$

We found the optimal location of measurement sensors to be: $z_{s1} = 0.35\pi$ and $z_{s2} = 0.64\pi$. We performed several simulation runs to evaluate the performance of the proposed method for computing optimal locations of control actuators and measurement sensors. We initially apply the state feedback controller to the 30-th order Galerkin truncation of the system of Eq.7.2 and investigate the influence of the different actuator locations on the various cost functions. Table 1 shows the values of the costs $\hat{J}_u$, $\hat{J}_x$, and $\hat{J}$ of the full-order closed-loop system under the state feedback controller, in the case of optimal actuator placement, and for the sake of comparison, the values of these costs in the case of alternative actuator placements. The cost for

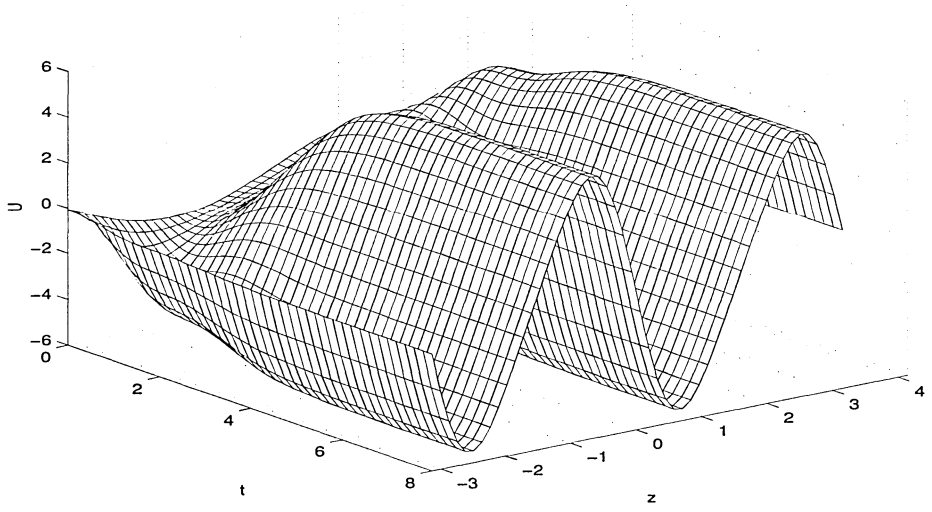

Figure 7.1: Open-loop spatiotemporal profile of $U(z,t)$ for $\nu = 0.2$.

the control action used to stabilize the KSE at $U(z,t) = 0$ when the actuators are optimally placed, is clearly smaller than the case of actuator placement based on the case 2 (by 18.9%), case 3 (by 35.5%), and case 4 (by 34.0%). Figures 7.2 and 7.3 show the norm of the control action, $||u||$, for $x_s(0) = [\phi_1\ 0]$ (Figure 7.2) and $x_s(0) = [0\ \phi_2]$ (Figure 7.3), for the optimal case (solid line), case 2 (long-dashed line), case 3 (short-dashed line), and case 4 (dotted line).

We also tested the computed optimal sensor locations $z_{s1} = 0.35\pi$ and $z_{s2} = 0.64\pi$. To this end, we implement the nonlinear output feedback controller on the 30-th order Galerkin truncation of the system of Eq.7.2 with actuator locations $z_{a1} = 0.31\pi$ and $z_{a2} = 0.69\pi$ and different sensor locations. Table 2 shows the values of the costs $\hat{J}(e)$ and $\hat{J}$ of the full-order closed-loop system under the output feedback controller, in the case of optimal sensor placement, and for the sake of comparison, the values of these costs in the case of two other sensor locations. The estimation error of the sensor locations of 0.35π and 0.64π computed by the proposed approach is smaller than the

other two cases. In Figure 7.4, we display the closed-loop estimation error ($e(t) = ||x_s - \hat{x}_s||_2$) versus time, for the optimal actuator/sensor locations, for $x_s(0) = [\phi_1\ 0]$ (solid line) and $x_s(0) = [0\ \phi_2]$ (dashed line). We can see that for both initial conditions the estimation error is very small. Finally, Figures 7.5 and 7.6 show the profiles of the KSE system, under output feedback control, for the optimal actuator/sensor locations, for $x_s(0) = [\phi_1\ 0]$ (Figure 7.5), and $x_s(0) = [0\ \phi_2]$ (Figure 7.6). We can see that the proposed controller with optimal actuator/sensor locations, stabilizes the system to the spatially uniform operating steady state very quickly, for both cases.

Finally, we tested the robustness of the output feedback control law, using the optimal actuator/sensor location, for a 25% decrease in the value of the instability parameter (i.e., ν was taken to be equal to 0.15 in the high-order discretization of the KSE but it was used as 0.2 in the controller). Figure 7.7 shows the profiles of the state (top plot) and of the manipulated inputs (bottom plot) for $x_s(0) = [\phi_1\ 0]$ and Figure 7.8 shows the profiles of the state (top plot) and of the manipulated inputs (bottom plot) for $x_s(0) = [0\ \phi_2]$. Our simulations show that the controller is capable of stabilizing the KSE at the spatially-uniform steady state solution in the presence of significant uncertainty in ν.

Remark 7.9 *Referring to the effect of ν on the actuator/sensor locations, we note that ν determines how many of the eigenvalues of the spatial differential operator are unstable, and thus, it affects the consideration of the number of slow modes. Since in our method the number of actuators and sensors is taken to be equal to the number of slow modes, it is clear that the value of the instability parameter influences the number of actuators and sensors. We also found through simulations that small variations of ν around the nominal value $\nu = 0.2$ considered in our calculations lead to slight changes in the optimal actuator locations.*

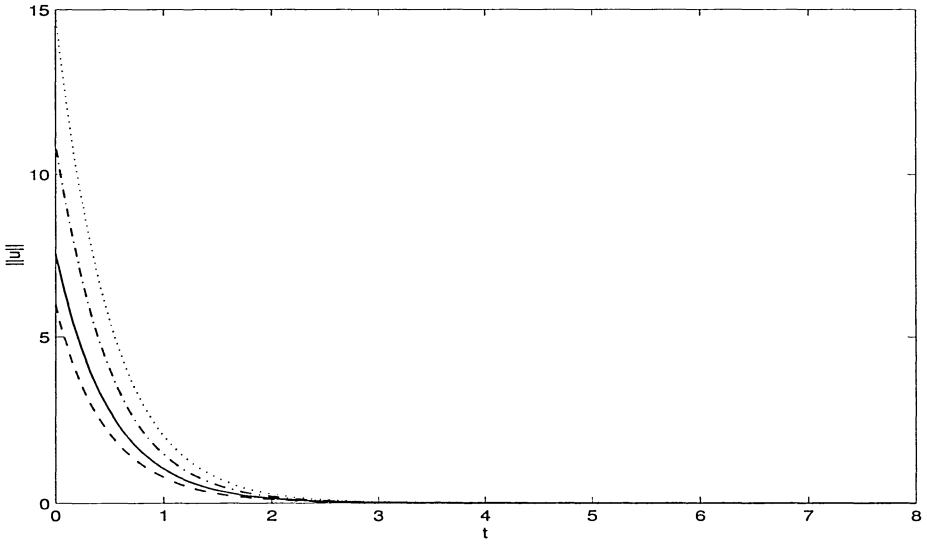

Figure 7.2: Closed-loop norm of the control effort, $\|u\|$, for $x_s(0) = [\phi_1\ 0]$, for the optimal case (solid line), case 2 (dashed-dotted line), case 3 (dashed line), case 4 (dotted line).

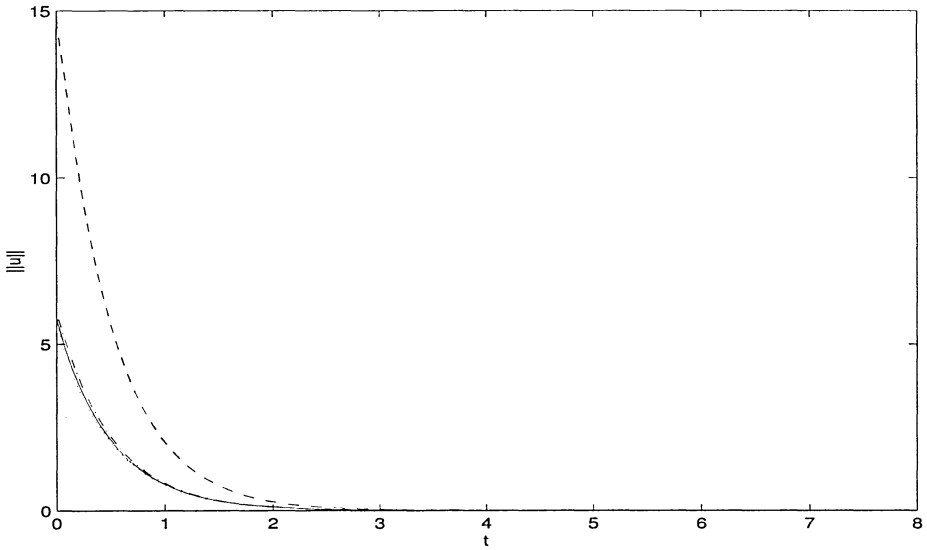

Figure 7.3: Closed-loop norm of the control effort,$\|u\|$, for $x_s(0) = [0\ \phi_2]$, for the optimal case (solid line), case 2 (dashed-dotted line), case 3 (dashed line), and case 4 (dotted line).

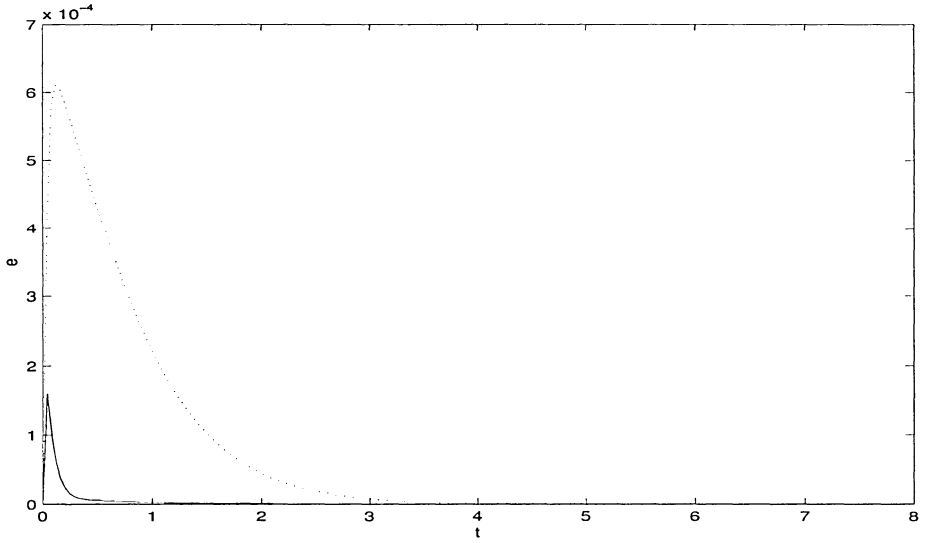

Figure 7.4: Closed-loop estimation error e versus time, for the optimal actuator/sensor locations, for $x_s(0) = [\phi_1\ 0]$ (solid line) and $x_s(0) = [0\ \phi_2]$ (dotted line).

Table 7.1: Results for two control actuators.

Case	Actuator Locations	$\hat{J}_u$	$\hat{J}_x$	$\hat{J}$
Optimal	$0.31\pi, 0.69\pi$	3.3705	0.5006	3.8711
2	$0.30\pi, 0.80\pi$	4.1536	0.5151	4.6687
3	$0.40\pi, 0.60\pi$	5.2238	0.5060	5.7298
4	$0.20\pi, 0.80\pi$	5.1089	0.5357	5.6445

Table 7.2: Results for two control actuators and measurement sensors.

Case	Sensor locations	$\hat{J}(e)$	$\hat{J}$
Optimal	$0.35\pi, 0.64\pi$	2.86e-4	3.8748
2	$0.20\pi, 0.80\pi$	1.841e-3	3.8830
3	$0.20\pi, 0.50\pi$	5.020e-3	3.9273
4	$0.45\pi, 0.55\pi$	1.508e-3	3.8803

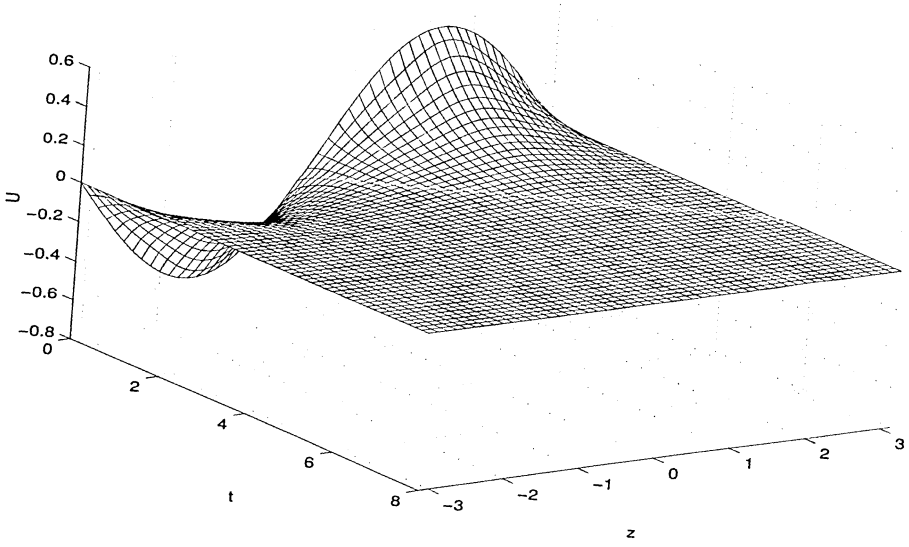

Figure 7.5: Profile of KSE under output feedback control, for the optimal actuator/sensor locations, for $x_s(0) = [\phi_1\ 0]$.

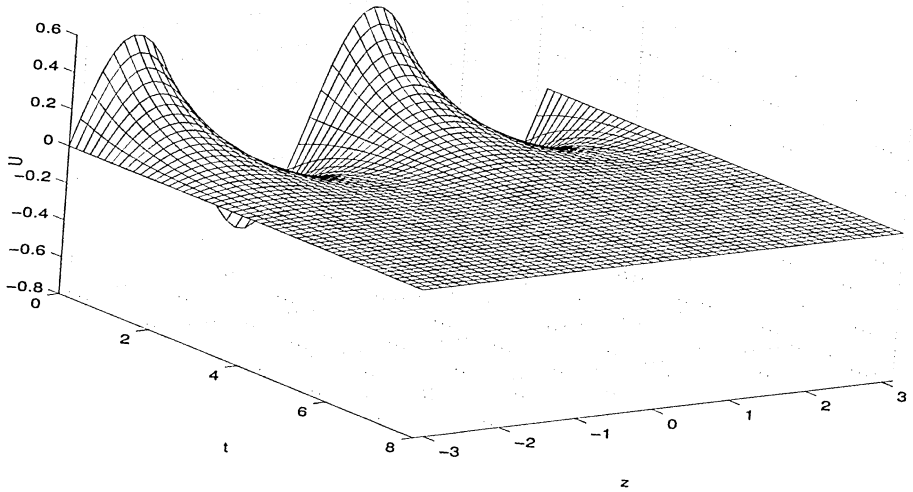

Figure 7.6: Profile of KSE under output feedback control, for the optimal actuator/sensor locations, for $x_s(0) = [0\ \phi_2]$.

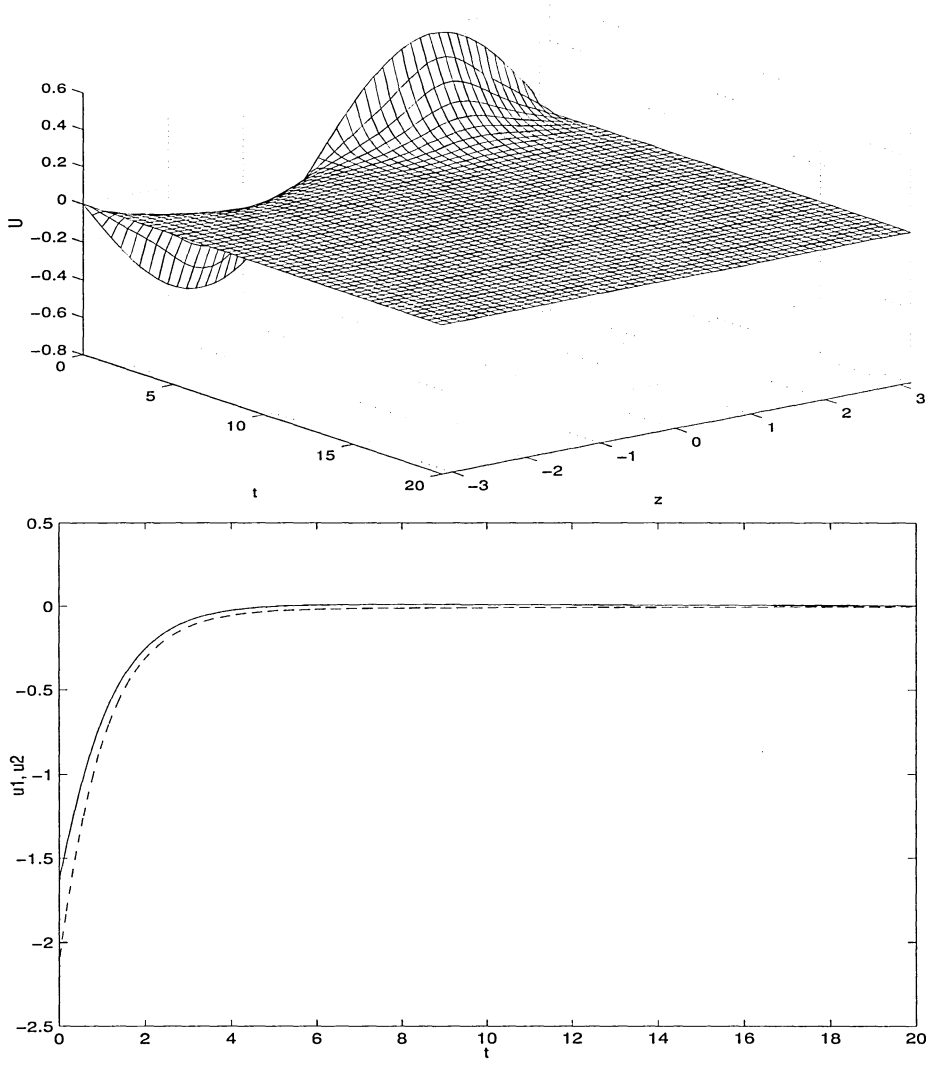

Figure 7.7: Profile of KSE under output feedback control, for the optimal actuator/sensor locations, for $x_s(0) = [\phi_1\ 0]$ and uncertainty in ν (top plot). Manipulated input profiles (bottom plot) - Solid line u_1 and dashed line u_2.

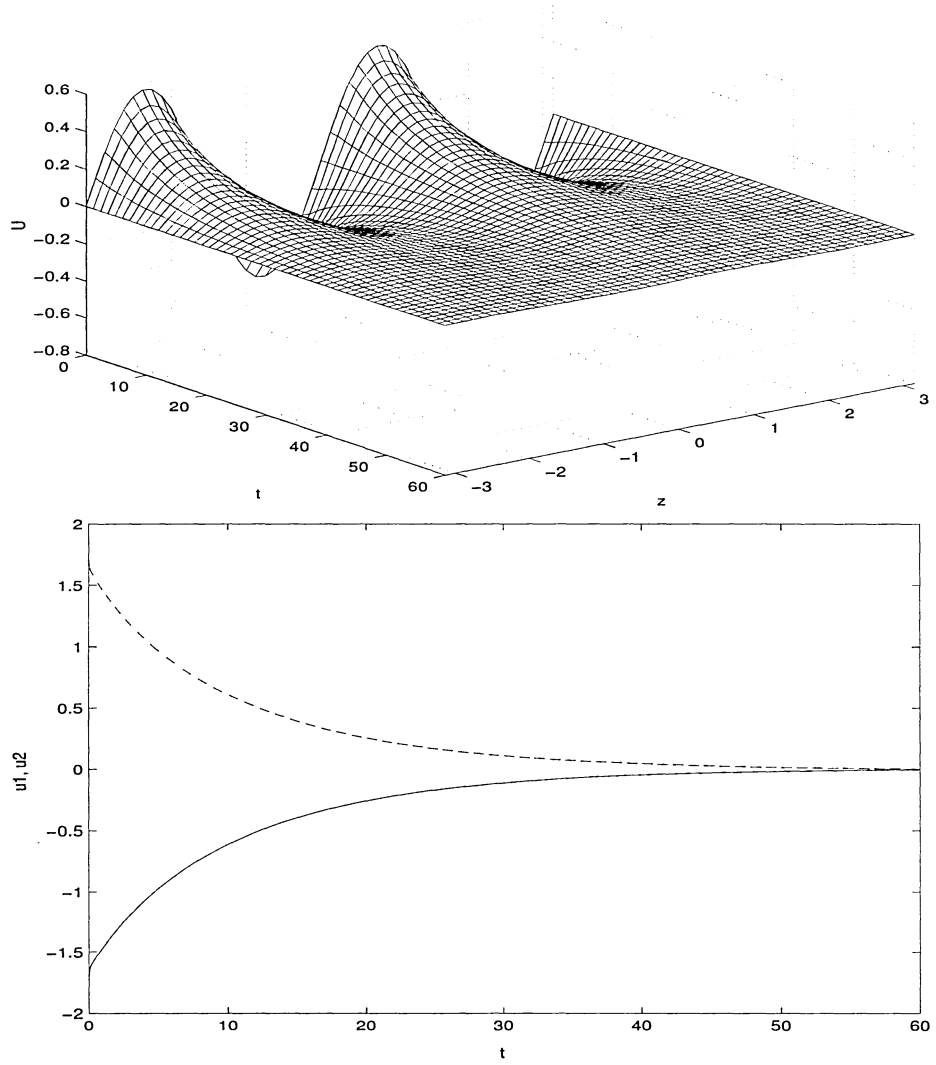

Figure 7.8: Profile of KSE under output feedback control, for the optimal actuator/sensor locations, for $x_s(0) = [0\ \phi_2]$ and uncertainty in ν (top plot). Manipulated input profiles (bottom plot) - Solid line u_1 and dashed line u_2.

7.5 Conclusions

We have computed the optimal (with respect to the costs of Eq.7.31 and Eq.7.32) locations for two control actuators and two measurement sensors, associated with a nonlinear output feedback controller that achieves stabilization of the zero solution of the KSE for $\nu = 0.2$. We have compared the optimal actuator and sensor locations with respect to alternative placements (Tables 7.1 and 7.2) and have verified the optimality of the computed locations and the robustness of the approach.

Chapter 8

Fault-Tolerant Control of Fluid Dynamic Systems via Coordinated Feedback and Switching

8.1 Introduction

The development of general and practical control algorithms for nonlinear PDEs that describe fluid flow processes (e.g., Navier-Stokes equations, Kuramoto-Sivashinsky equation (KSE)) is a fundamental problem whose practical significance ranges from feedback control of turbulence for drag reduction, to suppression of fluid mechanical instabilities in coating processes and suppression of waves exhibited by falling liquid films. For example, drag reduction through active feedback control may have a significant impact on the design and operation of underwater vehicles, airplanes and automobiles since, according to some estimates, keeping the flow over the surface of a vehicle laminar could yield up to 30% reduction in fuel consumption. Active control of fluid flow can be achieved by injection of polymers, mass transport through porous walls (e.g., blowing/suction) and application of electro-magnetic forcing.

An example fluid dynamic system, which will be used throughout paper to demonstrate the results, is the KSE. The KSE is a nonlinear dissipative partial differential equation (PDE) of the form:

$$\frac{\partial U}{\partial t} = -\nu \frac{\partial^4 U}{\partial z^4} - \frac{\partial^2 U}{\partial z^2} - U \frac{\partial U}{\partial z} \tag{8.1}$$

where $\nu > 0$ is the so-called instability parameter, which describes incipient instabilities in a variety of physical and chemical systems, including falling liquid films (Chen and Chang, 1986), unstable flame fronts (Sivashinsky, 1980), Belouzov-Zabotinskii reaction patterns (Kuramoto and Tsuzuki, 1976) and interfacial instabilities between two viscous fluids (Hooper and Grimshaw, 1985). Both the dynamics and control of the KSE with periodic boundary conditions have been the subject of significant research work. Dynamical studies have led to the discoveries of steady and periodic wave solutions, chaotic behavior for very small values of ν, and the fact that the dominant dynamics of the KSE can be adequately characterized by a small number of degrees of freedom (see, e.g., Temam, 1988; Chen and Chang, 1986; Greene and Kim, 1988; Kevrekidis et al., 1990). Control studies of the KSE have focused on a variety of problems, including the design of finite-dimensional output feedback controllers for stabilization of the zero solution of the KSE based on ODE approximations (Armaou and Christofides, 2000b), the global stabilization of the KSE via distributed static output feedback control (Christofides and Armaou, 2000), stabilization enhancement via boundary control (Liu and Krstić, 2001), adaptive stabilization (Kobayashi, 2002) and robust control (Hu and Temam, 2001).

While the above research efforts have led to a number of systematic approaches for control of the KSE and other fluid dynamic systems, a common theme of these approaches is the use of a fixed spatial arrangement (or configuration) of control actuators/measurement sensor in order to accomplish the desired control objectives.

There are many practical situations, however, where it may be desirable, and sometimes even necessary, to consider multiple actuator/sensor configurations and switch between them in a specific manner, in order to achieve the control objectives. One example is the problem of actuator failure where, upon the detection of a fault in a control actuator, it may be necessary to switch to an alternative actuator, placed at a different spatial location, in order to preserve stability of the closed-loop system. Spatially-distributed switching between control actuators in this case provides a means for fault-tolerant control. In other cases, switching between actuator configurations may be motivated by some additional performance objective, such as the desire to optimize a given performance criterion or accommodate inherently competing control objectives that cannot be reconciled using a single actuator configuration.

In El-Farra and Christofides (2004), a class of linear and quasi-linear second-order parabolic PDE systems are considered, and a method for handling control actuator failures by integrating feedback and switching among a pre-selected set of spatially-distributed control actuator configurations was developed. The developed method, based on Lyapunov techniques, provides explicit feedback laws and precise switching conditions for guaranteing closed-loop stability in the presence of actuator failures, and was successfully applied to representative examples of diffusion-reaction processes and a tubular reactor with recycle.

In this chapter, we focus on the problem of coupling feedback and switching between actuator configurations for fault-tolerant control of fluid dynamic systems modeled by highly-dissipative PDEs with constrained control actuators. The results constitute a generalization of the work of El-Farra and Christofides (2004) to higher-order (e.g., fourth in the case of the KSE) dissipative PDEs that can model fluid flows. The problem is addressed on the basis of finite-dimensional Galerkin approximations

of the PDE system and entails the integrated synthesis, via Lyapunov techniques, of stabilizing nonlinear feedback controllers together with stabilizing switching laws that orchestrate the switching between the admissible control actuator configurations, in a way that respects actuator constraints, accommodates inherently conflicting control objectives, and guarantees closed-loop stability. Precise conditions that guarantee stability of the constrained closed-loop system under switching are provided. The proposed control methodology is demonstrated through an application to the problem of suppression of wave formation, achieved via the stabilization of the zero solution, $U(z,t) = 0$, of the KSE with periodic boundary conditions, in the presence of control actuator constraints and faults.

8.2 Preliminaries

8.2.1 Mathematical description

To demonstrate the proposed fault-tolerant control methodology, we consider the one-dimensional Kuramoto-Sivashinsky equation with distributed control as our model system:

$$\frac{\partial U}{\partial t} = -\nu\frac{\partial^4 U}{\partial z^4} - \frac{\partial^2 U}{\partial z^2} - U\frac{\partial U}{\partial z} + \sum_{i=1}^{l} b_i u_i(t) \tag{8.2}$$

$$y_m^{\kappa} = \int_{-\pi}^{\pi} s_{\kappa}(z) U dz, \ \kappa = 1, \ldots, p \tag{8.3}$$

subject to the periodic boundary conditions:

$$\frac{\partial^j U}{\partial z^j}(-\pi, t) = \frac{\partial^j U}{\partial z^j}(+\pi, t), \quad j = 0, \ldots, 3 \tag{8.4}$$

and the initial condition:

$$U(z,0) = U_0(z) \tag{8.5}$$

where $U(z,t)$ is the state of the system, $z \in [-\pi, \pi]$ is the spatial coordinate, t is the time, ν is the instability parameter, $u_i \in [-u_{max}, u_{max}] \subset \mathbb{R}$ is the i-th constrained

manipulated input, l is the total number of manipulated inputs, $b_i(z)$ is the i-th actuator distribution function (i.e., $b_i(z)$ determines how the control action computed by the i-th control actuator, $u_i(t)$, is distributed (e.g., point or distributed actuation) in the spatial interval $[-\pi, \pi]$), $y_m^\kappa \in \mathbb{R}$ denotes a measured output, and $s_\kappa(z)$ is a known smooth function of z which is determined by the location and type of the measurement sensors (e.g., point/distributed sensing). Whenever the control action enters the system at a single point z_0, with $z_0 \in [-\pi, \pi]$ (i.e. point actuation), the function $b_i(z)$ is taken to be nonzero in a finite spatial interval of the form $[z_0 - \mu, z_0 + \mu]$, where μ is a small positive real number, and zero elsewhere in $[-\pi, \pi]$.

For a precise presentation of our results, we cast the system of Eq.8.2 as an infinite dimensional system in the Hilbert space $\mathcal{H}([-\pi, \pi]; \mathbb{R})$, with $\mathcal{H}$ being the space of sufficiently smooth vector functions defined on $[-\pi, \pi]$ that satisfy the boundary condition of Eq.8.4, with inner product and norm:

$$(\omega_1, \omega_2) = \int_{-\pi}^{\pi} (\omega_1(z), \omega_2(z))_{\mathbb{R}} dz, \; ||\omega_1||_2 = (\omega_1, \omega_1)^{\frac{1}{2}} \tag{8.6}$$

where ω_1, ω_2 are two elements of $\mathcal{H}([-\pi, \pi]; \mathbb{R})$ and the notation $(\cdot, \cdot)_{\mathbb{R}}$ denotes the standard inner product in $\mathbb{R}$.

Defining the state function x on $\mathcal{H}([-\pi, \pi]; \mathbb{R})$ as:

$$x(t) = U(z, t), \quad t > 0, \quad z \in [-\pi, \pi], \tag{8.7}$$

the operator $\mathcal{A}$ in $\mathcal{H}([-\pi, \pi]; \mathbb{R})$ as:

$$\mathcal{A}x = -\nu \frac{\partial^4 U}{\partial z^4} - \frac{\partial^2 U}{\partial z^2},$$

$$x \in D(\mathcal{A}) = \left\{ x \in \mathcal{H}([-\pi, \pi]; \mathbb{R}) : \frac{\partial^j U}{\partial z^j}(-\pi, t) = \frac{\partial^j U}{\partial z^j}(+\pi, t), \quad j = 0, \ldots, 3 \right\} \tag{8.8}$$

and the input, and measured output operators as:

$$\mathcal{B}u = \sum_{i=1}^{l} b_i u_i, \quad \mathcal{S}x = (s, x) \tag{8.9}$$

the system of Eqs.8.2-8.5 takes the form:

$$\begin{aligned} \dot{x} &= \mathcal{A}x + \mathcal{B}u + f(x), \quad x(0) = x_0 \\ y_m &= \mathcal{S}x \end{aligned} \tag{8.10}$$

where $f(x(t)) = -U\dfrac{\partial U}{\partial z}$ and $x_0 = U_0(z)$.

For $\mathcal{A}$, we can formulate the following eigenvalue problem:

$$\mathcal{A}\phi_n = -\nu\frac{\partial^4 \phi_n}{\partial z^4} - \frac{\partial^2 \phi_n}{\partial z^2} = \lambda_n \phi_n, \quad n = 1, \ldots, \infty \tag{8.11}$$

subject to:

$$\frac{\partial^j \phi_n}{\partial z^j}(-\pi) = \frac{\partial^j \phi_n}{\partial z^j}(+\pi), \quad j = 0, \ldots, 3 \tag{8.12}$$

where λ_n denotes an eigenvalue and ϕ_n denotes an eigenfunction. A direct computation of the solution of the above eigenvalue problem yields $\lambda_0 = 0$ with $\psi_0(z) = \dfrac{1}{\sqrt{2\pi}}$, and $\lambda_n = -\nu n^4 + n^2$ (λ_n is an eigenvalue of multiplicity two) with eigenfunctions $\phi_n(z) = \dfrac{1}{\sqrt{\pi}}\sin(nz)$ and $\psi_n(z) = \dfrac{1}{\sqrt{\pi}}\cos(nz)$ for $n = 1, \ldots, \infty$. We also define the eigenspectrum of $\mathcal{A}$, $\sigma(\mathcal{A})$, as the set of all eigenvalues of $\mathcal{A}$, i.e. $\sigma(\mathcal{A}) = \{\lambda_1, \lambda_2, \ldots\}$. We note that the fact that $\mathcal{A}$ has a real pure point spectrum is a result of the fact that the linear part of the spatial differential operator of the KSE with periodic boundary conditions is self-adjoint and the problem is considered in a bounded domain.

From the expression of the eigenvalues, it follows that for a fixed value of $\nu > 0$ the number of unstable eigenvalues of $\mathcal{A}$ is finite and the distance between two consecutive eigenvalues (i.e., λ_n and λ_{n+1}) increases as n increases. Furthermore, for a fixed value of $\nu > 0$, $\sigma(\mathcal{A})$ can be partitioned as $\sigma(\mathcal{A}) = \sigma_1(\mathcal{A}) \bigcup \sigma_2(\mathcal{A})$, where $\sigma_1(\mathcal{A})$ contains the first m (with m finite) "slow" eigenvalues (i.e. $\sigma_1(\mathcal{A}) = \{\lambda_1, \ldots, \lambda_m\}$) and $\sigma_2(\mathcal{A})$ contains the remaining "fast" eigenvalues (i.e., $\sigma_2(\mathcal{A}) = \{\lambda_{m+1}, \ldots\}$ where $\lambda_{m+1} < 0$).

To capture the separation between the "slow" and "fast" eigenvalues, we define the parameter $\epsilon = \frac{|\lambda_1|}{|\lambda_{m+1}|}$ (note that $\epsilon \to 0$ as $m \to \infty$). The separation between the "slow" and "fast" eigenvalues suggests that the dominant dynamics of the KSE can be described by a finite-dimensional system and motivates applying Galerkin's method to the system of Eq.8.10 to derive an approximate finite-dimensional system (see section 3.1 below).

Remark 8.1 *A physical system that can be described by the KSE is the motion of a liquid film falling down on a vertical wall (Chen and Chang, 1986). In this case, $U(z,t)$ is the film height. Such a system has been found experimentally to exhibit wavy behavior of the type predicted by the KSE for values of ν smaller than 1 (see also Figure 8.2). In many instances, it is desirable to suppress wavy behavior by using control actuators that add/remove fluid mass via blowing/suction. In this case, the control input enters directly into the PDE and does not appear in the boundary conditions. This physical problem is consistent with the formulation of Eq.8.2 since we consider distributed control actuation. Note that problems for which the inputs enters directly into the KSE but nonlinearly can be readily handled within our formulation by simply solving for u through the inversion of an algebraic nonlinear equation.*

Remark 8.2 *The consideration of approximate point control is motivated by the fact that most experimental point control actuators (including the ones that add/remove fluid mass via blowing/suction) have finite (but small) support and the fact that $b_i(z) = \delta(z - z_0)$ (where $\delta(\cdot)$ is the standard Dirac function) is not an element of $\mathcal{H}([-\pi, \pi]; \mathbb{R})$.*

8.2.2 Problem formulation

Consider the system of Eq.8.2, where the manipulated inputs u_i are constrained in the interval $[-u_{max}, u_{max}]$, and assume that available at our disposal is a family of N (with N finite) control actuator configurations, of which only one configuration

can be used for control at any given time instance. Each of these N configurations consists of a spatially-distinct arrangement of the control actuators, which we denote by $\bar{z}_{k(t)},\ k = 1, \cdots, N$. In this notation, the index $k(t)$ denotes the actuator configuration being active at time t, while $\bar{z}_k$ is a column vector whose components represent the corresponding spatial locations of the actuators associated with the k-th configuration. To ensure controllability of the system, we allow only a finite number of switches between configurations over finite time. The problem is how to coordinate switching between the different control actuator configurations, in the event of actuator failure, in a way that respects actuator constraints and guarantees closed-loop stability. To address this problem, we formulate the following objectives. Initially, Galerkin's method is used to derive a nonlinear finite-dimensional ODE system that captures the dominant dynamics of the KSE. Next, the ODE approximation is used as the basis for the synthesis, of bounded nonlinear output feedback controllers of the general form

$$u \ = \ p(y_m, u_{max}, \bar{z}_k) \tag{8.13}$$

that enforce asymptotic stability and reference-input tracking in the constrained closed-loop system and provide an explicit characterization of the stability region, associated with each control actuator configuration. The controller synthesis is carried out via Lyapunov-based control techniques and is inspired by the results on bounded control in Lin and Sontag (1991). Finally, a set of switching rules is derived to determine which of the N control actuator configurations can be engaged at any given time, and an upper bound on the separation between the slow and fast eigenvalues, which guarantees stability of the closed-loop infinite-dimensional system, is computed.

8.3 Fault-tolerant control system design

8.3.1 Galerkin's method

We apply Galerkin's method to the system of Eq.8.10 to derive an approximate finite-dimensional system. Let $\mathcal{H}_s$, $\mathcal{H}_f$ be modal subspaces of $\mathcal{A}$, defined as $\mathcal{H}_s = span\{\phi_1, \phi_2, \ldots, \phi_m\}$ and $\mathcal{H}_f = span\{\phi_{m+1}, \phi_{m+2}, \ldots\}$ (the existence of $\mathcal{H}_s$, $\mathcal{H}_f$ follows from the properties of $\mathcal{A}$). Defining the orthogonal projection operators P_s and P_f such that $x_s = P_s x$, $x_f = P_f x$, the state x of the system of Eq.8.10 can be decomposed as:

$$x = x_s + x_f = P_s x + P_f x \tag{8.14}$$

Applying P_s and P_f to the system of Eq.8.10 and using the above decomposition for x, the system of Eq.8.10 can be equivalently written in the following form:

$$\begin{aligned} \frac{dx_s}{dt} &= \mathcal{A}_s x_s + \mathcal{B}_s u + f_s(x_s, x_f) \\ \frac{\partial x_f}{\partial t} &= \mathcal{A}_f x_f + \mathcal{B}_f u + f_f(x_s, x_f) \\ y_m &= \mathcal{S} x_s + \mathcal{S} x_f, \\ x_s(0) &= P_s x(0) = P_s x_0, \;\; x_f(0) = P_f x(0) = P_f x_0 \end{aligned} \tag{8.15}$$

where $\mathcal{A}_s = P_s\mathcal{A}$, $\mathcal{B}_s = P_s\mathcal{B}$, $f_s = P_s f$, $\mathcal{A}_f = P_f\mathcal{A}$, $\mathcal{B}_f = P_f\mathcal{B}$ and $f_f = P_f f$ and the partial derivative notation in $\frac{\partial x_f}{\partial t}$ is used to denote that the state x_f belongs in an infinite-dimensional space. In the above system, $\mathcal{A}_s$ is a diagonal matrix of dimension $m \times m$ of the form $\mathcal{A}_s = diag\{\lambda_j\}$, $f_s(x_s, x_f)$ and $f_f(x_s, x_f)$ are Lipschitz vector functions, and $\mathcal{A}_f$ is an unbounded differential operator which is exponentially stable (following from the fact that $\lambda_{m+1} < 0$ and the selection of $\mathcal{H}_s, \mathcal{H}_f$). Neglecting the fast and stable infinite-dimensional x_f-subsystem in the system of Eq.8.15, the following m-dimensional slow system is obtained:

$$\begin{aligned} \frac{d\tilde{x}_s}{dt} &= \mathcal{A}_s \tilde{x}_s + \mathcal{B}_s u + f_s(\tilde{x}_s, 0) \\ \tilde{y}_m &= \mathcal{S} \tilde{x}_s \end{aligned} \tag{8.16}$$

where the tilde symbol in $\tilde{x}_s$ and $\tilde{y}_m$ denotes that these variables are associated with a finite-dimensional system.

8.3.2 Coordinating feedback and switching

Having obtained a finite-dimensional model that describes the dominant dynamics of the KSE, we proceed in this section to describe the proposed procedure for designing the fault-tolerant control system, on the basis of the finite-dimensional approximation in Eq.8.16. To this end, and since our objective is the stabilization of the zero solution of the KSE, we define the controlled outputs as the slow modes of the KSE, and assume, for simplicity, that the number of inputs is equal to the number of slow modes. Though not discussed in this paper explicitly, the results can be generalized to address the problem of reference-input tracking. With this in mind, the slow modes of the KSE can be described by the following m-dimensional system

$$\dot{a}_s(t) \;=\; Fa_s(t) + \bar{G}(\bar{z}_k)u(t) + \tilde{f}(a_s(t)) \tag{8.17}$$

where $a_s(t) = [a_1(t) \cdots a_m(t)]^T \in \mathbb{R}^m$, $a_i(t)$ is the amplitude of the i-th eigenmode, $\tilde{x}_s(t) = \sum_{j=1}^{m} a_j(t)\phi_j(z)$, $(x_s(t), \phi_j) = a_j(t)(\phi_j, \phi_j)$, F is an $m \times m$ diagonal matrix of the form $F = diag\{\lambda_j\}$, $\bar{G}$ is an $m \times m$ matrix whose (i,k)-th element is given by $G_{ik} = \phi_i(\bar{z}_k)$, and $\tilde{f}(\cdot)$ is a nonlinear, locally Lipschitz function of its argument. Finally, we define $\bar{f}(a_s) = Fa_s + f(a_s)$ and denote by $\bar{g}_i$ the i-th column of the matrix $\bar{G}$.

The design procedure consists of three basic steps. These include: 1) the synthesis of a stabilizing feedback controller, 2) the characterization of the constrained stability region associated with each control actuator configuration, and 3) the design of a switching law that orchestrates the re-configuration of control actuators in a way that guarantees closed-loop stability in the event of actuator failure. Below is a brief

description of each step.

1. *Feedback controller synthesis*

   The first step in designing the fault-tolerant control system is to synthesize a feedback controller that enforces closed-loop stability in the presence of input constraints. This task is carried out on the basis of the finite-dimensional slow system of Eq.8.17 using Lyapunov techniques. In particular, using a quadratic Lyapunov function of the form $V = a_s^T \Phi a_s$, where Φ is a positive-definite symmetric matrix that satisfies the inequality $F^T\Phi + \Phi F - \Phi \bar{G}\bar{G}^T\Phi < 0$, we synthesize the following bounded nonlinear feedback law (the detailed calculations for controller synthesis and the construction of the stability region can be found in El-Farra and Christofides (2003a)):

$$u = -r(a_s, u_{max}^k, \bar{z}_k) \left(L_{\bar{G}} V\right)^T (\bar{z}_k) \tag{8.18}$$

   where

$$r(a_s, u_{max}^k, \bar{z}_k) = \frac{L_{\bar{f}}^* V + \sqrt{(L_{\bar{f}}^* V)^2 + \left(u_{max}^k |(L_{\bar{G}} V)^T(\bar{z}_k)|\right)^4}}{|(L_{\bar{G}} V)^T(\bar{z}_k)|^2 \left[1 + \sqrt{1 + (u_{max}^k |(L_{\bar{G}} V)^T(\bar{z}_k)|)^2}\right]} \tag{8.19}$$

   where $\bar{z}_k = [\bar{z}_{k_1} \ \bar{z}_{k_2} \ \cdots \ \bar{z}_{k_m}]^T$, $k = 1, \cdots, N$, $L_{\bar{f}}^* V = L_{\bar{f}} V + \rho |a_s|^2$, $\rho > 0$, $L_{\bar{G}} V$ is a row vector of the form $[L_{\bar{g}_1} V \cdots L_{\bar{g}_m} V]$. The notation u_{max}^k is used to indicate the magnitude of actuator constraints associated with the k-th configuration. This number is allowed to vary from one configuration to another. The scalar function $r(\cdot)$ in Eqs.8.18-8.19 can be thought of as a nonlinear controller gain. This Lyapunov-based gain, which depends on both the magnitude of actuator constraints, u_{max}^k, and the actuator configuration used, $\bar{z}_k$, is shaped in a way that guarantees constraint satisfaction and asymptotic closed-loop stability within a well-characterized region in the state space. The characterization of this region is discussed in the next step.

2. *Characterization of stability regions*

Given that actuator constraints place fundamental limitations on both the initial conditions and actuator locations that can be used for stabilization, it is important for the control system designer to explicitly characterize these limitations by identifying, for each actuator configuration, the set of feasible initial conditions starting from where the constrained closed-loop system is asymptotically stable. As will be discussed in step 3 below, this characterization is necessary for the design of an appropriate switching scheme that ensures fault-tolerance. The control law designed in step 1 provides such a characterization. Specifically, for this control law, one can show (see (El-Farra and Christofides, 2003a) for a detailed proof) that the set described by

$$\Theta(u_{max}^k, \bar{z}_k) \quad = \quad \{a_s \in \mathbb{R}^m : L_{\tilde{f}}^* V \leq u_{max}^k |(L_{\tilde{G}} V)^T(\bar{z}_k)|\} \tag{8.20}$$

represents a set where the control action satisfies the constraints and the time-derivative of the Lyapunov function is negative-definite along the trajectories of the closed-loop system of Eq.8.17. Note that the size of this set depends, as expected, on the magnitude of the constraints. In particular, the set becomes smaller as the constraints become tighter (smaller u_{max}^k). Note also that the set $\Theta(u_{max}^k, \bar{z}_k)$ is parameterized by the actuator locations because the matrix $\bar{G}$ in Eq.8.17 depends on the actuator locations. Therefore, for a given actuator configuration (fixed $\bar{z}_k$), one can use the above inequality to estimate the stability region associated with this configuration. This is done by constructing the largest invariant subset of Θ, which we denote by $\Omega(u_{max}^k, \bar{z}_k)$. Confining the initial conditions within the set $\Omega(u_{max}^k, \bar{z}_k)$ ensures that the closed-loop trajectory stays within the region defined by $\Theta(u_{max}^k, \bar{z}_k)$, and thereby V continues to decay monotonically, for all times that the k-th actuator configuration is active.

3. *Switching logic for actuator re-configuration*

Having designed the feedback control law in step 1, and characterized the stability region associated with each actuator configuration in step 2, the final step in the control system design procedure is to derive a switching rule that orchestrates the re-configuration of the control actuators in the event of actuator failure. This rule determines which of the backup actuator configurations can be activated, in the event of actuator failure, in order to preserve closed-loop stability. The need for a switching rule stems from the fact that, even if the controller enforces closed-loop stability for each actuator configuration individually, closed-loop stability of the switched system is not guaranteed unless restrictions are placed on the switching logic. In particular, owing to the limitations imposed by input constraints on the stability region for each actuator configuration, switching from the current malfunctioning actuator configuration to a well-functioning, but arbitrarily selected, backup configuration will not help preserve closed-loop stability if the state of the system, at the time of actuator failure, lies outside the stability region of the chosen backup configuration. In this case, stabilization using this configuration would require more control action than is allowed by its constraints. This observation underscores the main idea of the proposed switching logic, which is to switch to the actuator configuration for which the closed-loop state resides within the stability region at the time of actuator failure. Without loss of generality, let the initial actuator configuration be $k(0) = 1$ and let T be the time when this configuration fails, then the switching rule given by

$$k(T) \;=\; j \;\; if \;\; a_s(T) \;\in\; \Omega(u^j_{max}, \bar{z}_j), \;\; j \in \{2, 3, \cdots, N\} \tag{8.21}$$

guarantees closed-loop asymptotic stability. The implementation of the above

switching law requires monitoring the closed-loop state trajectory with respect to the stability regions associated with the various actuator configurations.

Remark 8.3 *While the fault-tolerant control approach outlined above has been developed on the basis of the finite-dimensional system of Eq.8.17, the large separation between the slow and fast eigenmodes of the spatial differential operator of the KSE allows the application of this approach to the infinite-dimensional system. In particular, one can show (using the singular perturbation formulation of Galerkin's method; see (Christofides, 2001b)) that the proposed feedback and switching scheme guarantees asymptotic closed-loop stability for the infinite-dimensional system of Eq.8.2, provided that* ϵ *is sufficiently small. Note that from the definition of* ϵ*, it follows that* $\epsilon \longrightarrow 0$ *as* $m \longrightarrow \infty$*, which implies that stability of the infinite-dimensional closed-loop system is guaranteed provided that* m *is sufficiently large. Even though an estimate of how small* ϵ *needs to be can, in principle, be obtained using singular perturbation methods, such an estimate may be conservative in general and, therefore, the appropriate number of slow modes is usually tested via closed-loop simulations.*

Remark 8.4 *The stability region associated with each set of actuators is derived on the basis of the approximate ODE model that describes the evolution of the slow modes (with the fast modes neglected). This region describes the set of initial slow states starting from where the reduced-order model can be stabilized for a given set of constrained control actuators. Due to the error introduced by neglecting the fast modes, this region is not exactly the same as the set of initial slow states starting from where the full system can be stabilized. However, if the separation between the slow and fast modes is large enough, the stability region of the approximate system will approach that of the slow part of the full system. The discrepancy between the two regions can be made small by including additional modes in constructing the reduced-order model. Alternatively, for a given choice of the order of the approximation (that is adequate for stabilization), one can treat the effect of the fast states as a disturbance to the approximate slow system and use this to further constrain the size of the nom-*

inal stability region originally derived by neglecting the fast states (e.g., see El-Farra and Christofides, 2003a, for a discussion on the construction of stability regions for constrained nonlinear systems with disturbances).

Remark 8.5 *The control objective in this work is to achieve fault-tolerant stabilization of the infinite-dimensional system without using an unnecessarily large number of control actuators. Therefore, from a stability point of view, only a small set (depending on the value of ν) of well-functioning control actuators is needed at any given time to ensure closed-loop stability (which is equal to the number of slow modes being controlled). From a performance standpoint, however, the use of multiple sets of actuators at a given time, simultaneously, could be useful. On the other hand, this can increase the total cost of control implementation and may not always yield appreciable performance improvement. Furthermore, the simultaneous use of multiple actuator sets, to improve performance, may not be feasible in some cases due to the fundamental limitations of actuator constraints that restrict the stability region of each actuator set. Therefore, even though a given set of actuators may be non-failing, it may not be possible to use the actuators of that set at a given time if, at this time, the state of the system is outside the corresponding stability region. Using this set in conjunction with the set of operating actuators may in fact lead to instability (see section 4 for examples).*

Remark 8.6 *Owing to the spatially-distributed nature of the KSE control problem, the switching scheme proposed in this paper differs from the schemes proposed in hybrid controller design for lumped-parameter systems. For lumped systems, with no spatial variation, the idea is to achieve the control objectives by switching between members of an a priori specified family of feedback functions, whereas in the approach that we follow in this work, we seek to achieve the control objectives by switching between members of an a priori specified family of spatially-distributed control actuator configurations, using the same feedback function (parameterized by $\bar{z}_k$). The area of switched and hybrid controller design for lumped systems is currently an active area of*

research (e.g., see Bemporad and Morari, 1999; Liberzon and Morse, 1999; El-Farra and Christofides, 2003b, and the references therein for results in this area).

Remark 8.7 *Under the assumption that the number of measurements is equal to the number of slow modes and that the inverse of the operator $\mathcal{S}$ exists (which can be ensured via appropriate selection of the measurement sensors' locations), an output feedback controller can be designed by combining the state feedback controller of Eqs.8.18-8.19 with an estimator that provides estimates for the states of the approximate ODE model of Eq.8.16 from the measurements. While the estimation error leads to some loss in the size of the stability region obtained under state feedback, this loss can be made small by increasing the order of the ODE approximation and including more measurements. This approach therefore allows us to asymptotically (as $\epsilon \to 0$) recover the state feedback stability region associated with each control actuator configuration.*

8.4 Simulation results

In this section, we demonstrate how the integrated feedback and switching scheme outlined in section 3.2 can be used to deal with the problem of actuator failure, in the context of stabilizing the zero solution of the one-dimensional KSE with periodic boundary conditions and input constraints. For simplicity, we will consider the KSE in the space of odd functions with spatial zero mean. Introducing the Hilbert space $\mathcal{H}$ of sufficiently smooth odd functions that satisfy the boundary conditions of Eq.8.4 and have spatial zero mean (i.e., $\forall\ \omega \in \mathcal{H},\ \int_{-\pi}^{\pi} \omega(z)dz = 0$) and defining the state function $x \in \mathcal{H}$ as $x(t) = U(z,t), \quad \forall\ z \in [-\pi, \pi]$, the system of Eqs.8.2-8.5 can be written in the form of Eq.8.10, where the domain of definition of the spatial differential operator $\mathcal{A}$ now takes the form:

$$x \in D(\mathcal{A}) = \left\{ x \in \mathcal{H}([-\pi,\pi];\mathbb{R});\ \frac{\partial^j U}{\partial z^j}(-\pi,t) = \frac{\partial^j U}{\partial z^j}(\pi,t), \quad j = 0,\ldots,3 \right\} \tag{8.22}$$

and the eigenvalue problem for $\mathcal{A}$ yields $\lambda_j = -\nu j^4 + j^2$, $\phi_j(z) = \sqrt{\frac{1}{\pi}} sin(jz)$, $j = 1, \ldots, \infty$ (note that $\psi_0(z) = \sqrt{\frac{1}{2\pi}}$ and $\psi_j(z) = \sqrt{\frac{1}{\pi}} cos(jz)$, $j = 1, \ldots, \infty$ are not considered here since we focus only on odd functions with spatial zero mean).

Linearizing the system around the spatially uniform steady-state, we observe that, for $\nu = 0.2$, the system possesses two unstable eigenvalues. Using a 30-th order Galerkin discretization of the KSE, we simulate the open-loop system with $\nu = 0.2$ (higher-order discretizations led to identical results). The resulting spatiotemporal evolution of $U(z,t)$ is depicted in Fig.8.1 and clearly shows that the spatially uniform steady-state, $U(z,t) = 0$, is unstable for $\nu = 0.2$. The control objective, therefore, is to stabilize the system at this unstable steady state. To achieve this objective, we consider the first two eigenvalues to be the dominant ones and use standard Galerkin's method to derive the following second-order model (to be used for controller design) that describes the temporal evolution of the amplitudes of the first two eigenmodes

$$\begin{bmatrix} \dot{a}_1(t) \\ \dot{a}_2(t) \end{bmatrix} = \begin{bmatrix} \lambda_1 & 0 \\ 0 & \lambda_2 \end{bmatrix} \begin{bmatrix} a_1(t) \\ a_2(t) \end{bmatrix} + \begin{bmatrix} \phi_1(\bar{z}_1) & \phi_1(\bar{z}_2) \\ \phi_2(\bar{z}_1) & \phi_2(\bar{z}_2) \end{bmatrix} \begin{bmatrix} u_1 \\ u_2 \end{bmatrix} + \begin{bmatrix} f_1(a_1, a_2) \\ f_2(a_1, a_2) \end{bmatrix} \tag{8.23}$$

where $(\dot{\tilde{x}}_s, \phi_i) = a_i(t)(\phi_i, \phi_i)$, $i = 1, 2$. $\bar{z}_1$ and $\bar{z}_2$ are the locations of the two point actuators used for stabilization. The explicit forms of the terms $f_1(a_1, a_2)$ and $f_2(a_1, a_2)$ are omitted for brevity. Before proceeding with controller synthesis on the basis of the above system, we first demonstrate that the first two modes indeed capture the dominant dynamics of the nonlinear KSE. To this end, we simulate the open-loop system, using the high (30-th) order Galerkin discretization, for two values of the instability parameter, $\nu = 1.2$ and $\nu = 0.2$. For each value, we plot the norm of the vector of "fast" modes, $a_f = [a_3 \cdots a_{30}]$ and the amplitude of the first two modes on a three-dimensional plot. The results are shown in Fig.8.2, where the top plot shows the result for $\nu = 1.2$ (where the zero steady-state is globally asymptotically

stable), while the bottom plot shows the result for $\nu = 0.2$ (where the zero steady-state is unstable and the system moves to a spatially non-uniform steady-state; see Fig.8.1). In the bottom plot, for convenience, the results are presented in terms of the deviation from the stable, spatially non-uniform steady-state in order to shift the equilibrium state to the origin, i.e. $a_f^d = [a_3^d \cdots a_{30}^d]$ where $a_i^d = a_i - a_{i,s}$, $i = 3, \cdots, 30$, and $a_{i,s}$ is the steady-state value of the i-th mode that corresponds to the spatially non-uniform stable steady-state of the KSE with $\nu = 0.2$. In both plots, it is clear that the dynamics of the high-order system converge quickly to the subspace described by the first two modes, implying that the first two modes are the dominant ones. In particular, note that the norm of the modes $a_f = [a_3 \cdots a_{30}]$ drops quickly to zero and that beyond this point the entire system evolution is basically captured by the evolution of the first two modes. These results motivate the use of the system of Eq.8.23 for the synthesis of the controller, using Eqs.8.18-8.19, and the switching law, using Eqs.8.20-8.21. The controller and switching laws are then implemented on a high-order Galerkin discretization (30-th order) of the nonlinear KSE (further increase in the order of the approximation led to identical results). The closed-loop high-order system is then integrated numerically, forward in time, using explicit Euler method.

To illustrate different aspects of the proposed fault-tolerant control scheme, we consider the following two problems where switching is needed to preserve closed-loop stability. In the first problem, two pairs of point control actuators, placed at $(\bar{z}_1 = 0.3\pi, \bar{z}_2 = 0.7\pi)$ (configuration A) and $(\bar{z}_1 = 0.1\pi, \bar{z}_2 = 0.9\pi)$ (configuration B) are assumed to be available. Both pairs have the same constraints of $u_{max}^A = u_{max}^B = 2.0$, but only one configuration can be used for control at any given moment. The question to be addressed here is: when is it feasible to switch to configuration B given

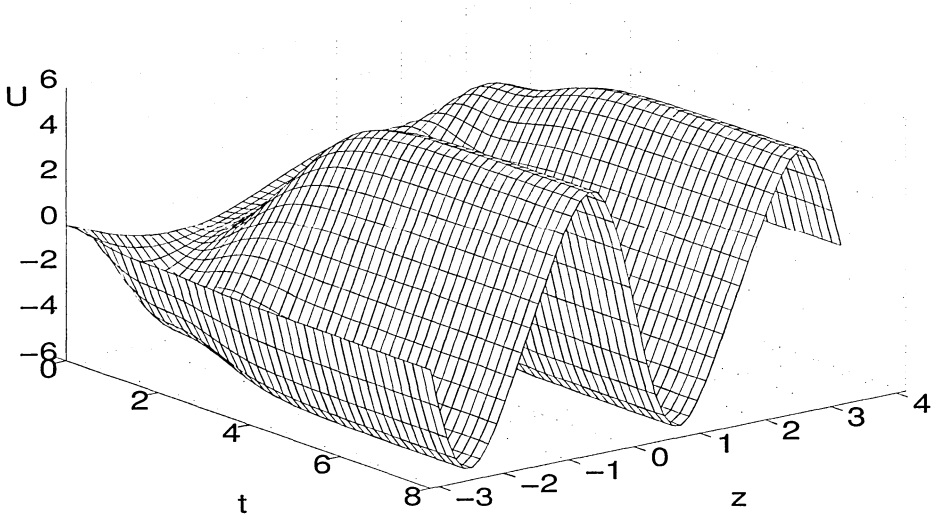

Figure 8.1: Open-loop spatiotemporal profile of $U(z,t)$ for $\nu = 0.2$.

that a fault is detected in the actuators of configuration A. In the second problem, we assume that a third pair of actuators, located at ($\bar{z}_1 = 0.2\pi, \bar{z}_2 = 0.8\pi$) (Configuration C) with constraints of $u^C_{max} = 0.5$, is also available (in addition to configurations A and B). Again, only one of the three configurations can be active at any given moment. The problem here is to decide which of the two "fall-back" actuator configurations (B or C) should be activated, once the actuators of configuration A fail. Basically, the first problem deals with the issue of identifying the appropriate switching times for a fixed re-configuration strategy, while second problem addresses the issue of how to select the appropriate actuator re-configuration strategy, among a family of possible choices, in order to provide the necessary fault-tolerance.

The simulation results under state feedback control are presented first. For the first problem, we initially use Eq.8.20 with $\rho = 0.001$ to compute the stability regions for configurations A and B. To simplify the presentation of our results, we show in Fig.8.3a the set of admissible initial conditions for the amplitudes, $a_1(0)$ and $a_2(0)$,

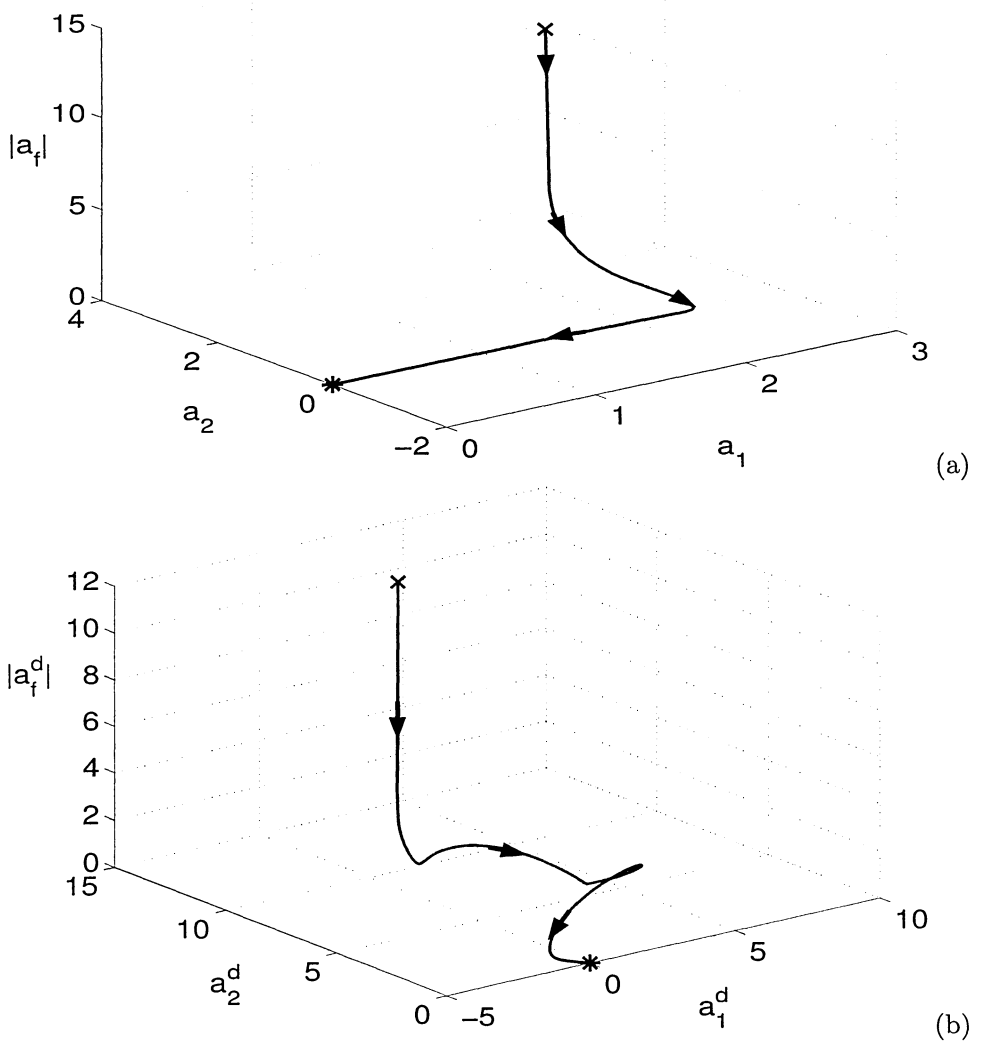

Figure 8.2: (a) Evolution of the norm of the fast modes, $a_f = [a_3, \cdots, a_{30}]$, and of the two dominant modes, a_1 and a_2, for $\nu = 1.2$. (b) Evolution of the norm of the fast modes (in deviation variable form), $a_f^d = [a_3^d, \cdots, a_{30}^d]$, and of the two dominant modes, a_1^d and a_2^d, for $\nu = 0.2$ (all modes are in deviation variable form).

of the first two eigenmodes, respectively, for configuration A (solid ellipse) and configuration B (dashed ellipse) (note that $x_s(0) = a_1(0)\phi_1(z) + a_2(0)\phi_2(z)$). From this figure, it is clear that for an initial condition $(a_1(0), a_2(0)) = (0.2, 1.5)$, only configuration A can be used initially since the initial condition is outside the stability region for configuration B. Figures 8.3b-c depict, respectively, the closed-loop state and manipulated input profiles corresponding to this initial condition and using configuration A. Clearly, the controller successfully stabilizes the KSE at the desired steady-state. Now, suppose that sometime after starting from this initial condition, a fault is detected in configuration A. From Fig.8.3a, we see that switching to configuration B may or may not solve the problem depending on when the failure of A actually occurs. For example, consider the case when A fails at $t = 3.5$. By monitoring the slow state evolution over time, we find that the state is outside the stability region for B at this time, as shown by point X on the solid trajectory in Fig.8.3a. Therefore, switching to configuration B will not preserve closed-loop stability (note that the solid trajectory settles at another steady-state after switching at point X). This is also confirmed by the unstable closed-loop state profile in Fig.8.4a. The corresponding profiles for both manipulated inputs are shown in Fig.8.4b which show that the inputs stay saturated. Suppose now that configuration A fails at $t = 5$. In this case, we see from the dashed trajectory in Fig.8.3a that the state at this time is within the stability region for configuration B (point Y) and, according to our switching scheme, closed-loop stability can be maintained by switching to configuration B at this time (note that the dashed trajectory in Fig.8.3a converges to the origin when configuration B is activated at point Y). This is also demonstrated in Fig.8.5 which shows that the controller successfully stabilizes the KSE when configuration B is activated at $t = 5$.

We now turn our attention to the second problem. The stability regions for con-

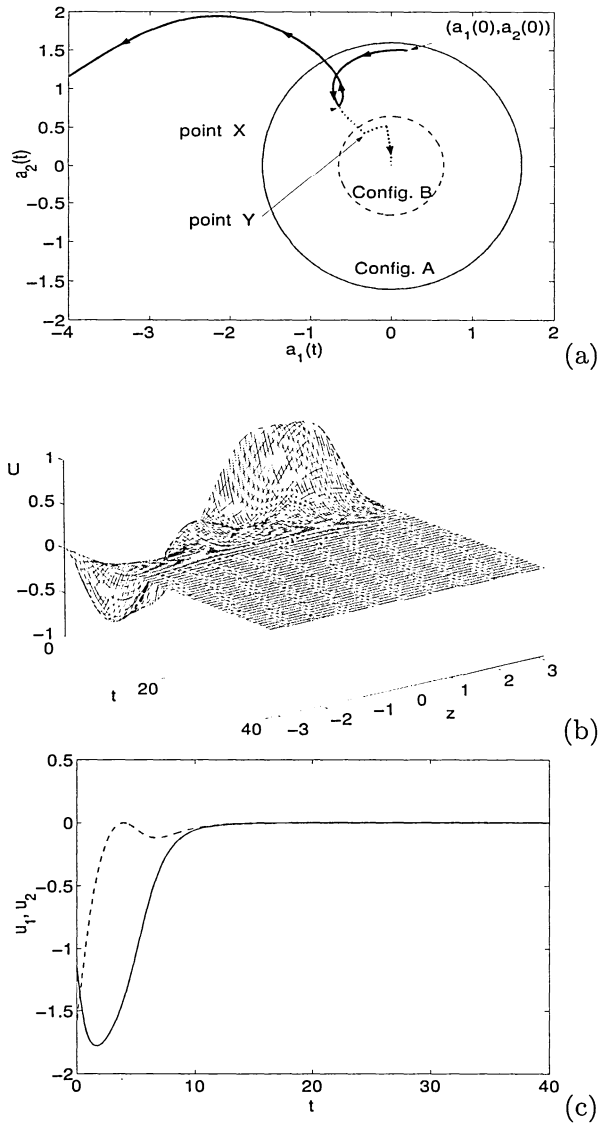

Figure 8.3: (a) Stability regions for configuration A ($u_{max} = 2.0$, $z_1 = 0.3\pi$, $z_2 = 0.7\pi$) (solid ellipse) and for configuration B ($u_{max} = 2.0$, $z_1 = 0.1\pi$, $z_2 = 0.9\pi$) (dashed ellipse), (b) Closed-loop state profile (state feedback) for $(a_1(0), a_2(0)) = (0.2, 1.5)$ using configuration A without switching, (c) Corresponding manipulated input profiles for u_1 (solid) and u_2 (dashed).

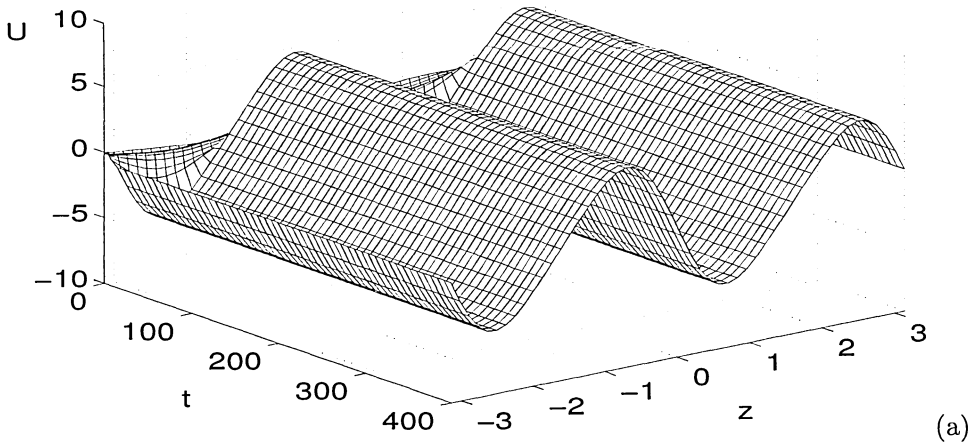

(a)

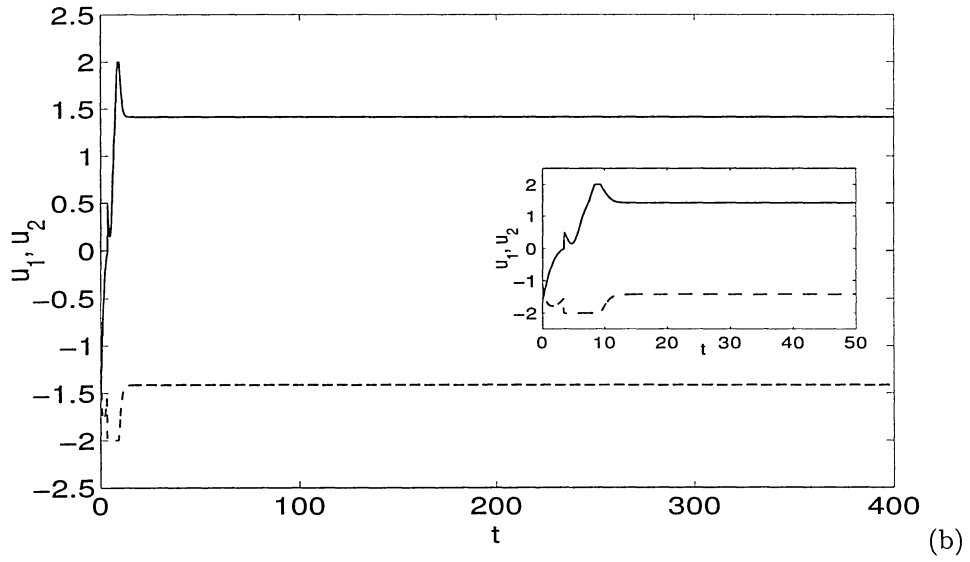

(b)

Figure 8.4: (a) Closed-loop state profile (state feedback) for $(a_1(0), a_2(0)) = (0.2,\ 1.5)$ when configuration A fails at $t = 3.5$ and configuration B is activated, (b) Corresponding manipulated input profiles for u_1 (solid) and u_2 (dashed).

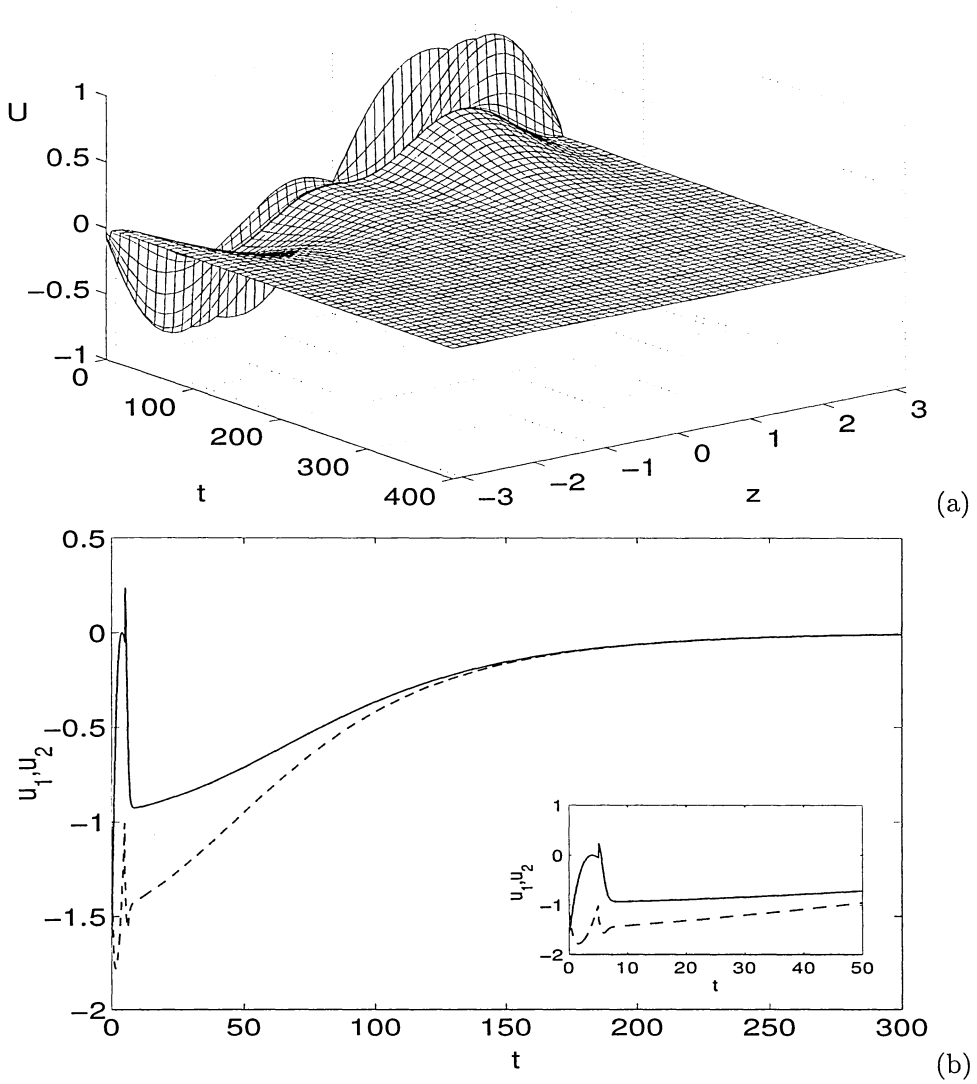

Figure 8.5: (a) Closed-loop state profile (state feedback) for $(a_1(0), a_2(0)) = (0.2,\ 1.5)$ when configuration A fails at $t = 5$ and configuration B is activated, (b) Corresponding manipulated input profiles for u_1 (solid) and u_2 (dashed).

figurations A, B, and C are depicted in Fig.8.6a by the solid, dashed, and dotted ellipses, respectively. From this figure, it is easy to see that for the initial condition $(a_1(0), a_2(0)) = (0.2, 1.5)$, only configuration A is feasible initially. Suppose that sometime after starting from this initial condition, say $t = 3.5$, a fault is detected in configuration A and it becomes necessary to switch to either configuration B or C. Without using the switching rule of Eq.8.21, it is not clear which of the two configurations should be activated at this time. Figures 8.6b-c depict, respectively, the resulting closed-loop state and manipulated input profiles when configuration C is chosen. We see in this case that the controller is unable to stabilize the closed-loop system at the desired steady-state. This is expected since the state, at the time of switching, lies outside the stability region for configuration C (see point X on the solid trajectory in Fig.8.6a). In contrast, by using the switching logic of the fault-tolerant control scheme proposed in section 3, we conclude that it is configuration B, not C, that should be activated because the closed-loop trajectory at this time is inside the stability region of B (see dashed trajectory in Fig.8.6a). Figure 8.7 depicts the results for this case which show that the controller successfully stabilizes the closed-loop system when B is activated instead of C. The switching law therefore allows us to choose the appropriate actuator re-configuration scheme.

For the case of output feedback control, measurements from a pair of point sensors, located at $z_1 = 0.35\pi$ and $z_2 = 0.65\pi$, are used to obtain estimates of the first two eigenmodes. The estimates are then used in the implementation of the output feedback controller. Owing to the slight discrepancy between the stability regions obtained under state and output feedback control (see Remark 8.7), the switching law proposed in Eq.8.21 is used only as an approximate guide. The simulation results for this case are consistent with the state feedback results for both problems. We

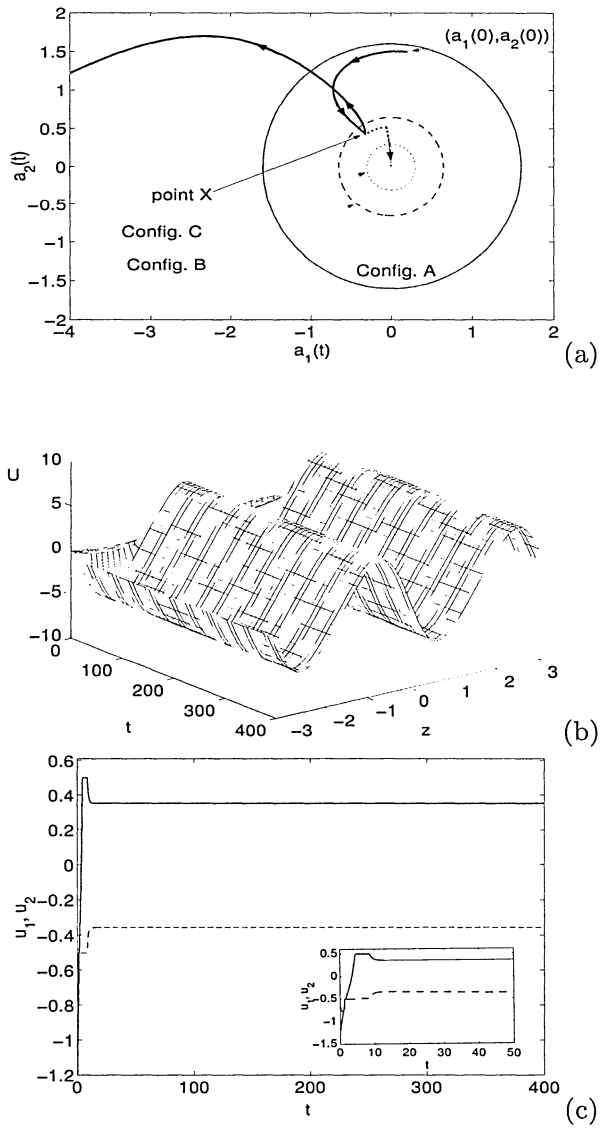

Figure 8.6: (a) Stability regions for configuration A ($u_{max} = 2.0$, $z_1 = 0.3\pi$, $z_2 = 0.7\pi$) (solid ellipse), configuration B ($u_{max} = 2.0$, $z_1 = 0.1\pi$, $z_2 = 0.9\pi$) (dashed ellipse), and configuration C ($u_{max} = 0.5$, $z_1 = 0.2\pi$, $z_2 = 0.8\pi$), (b) Closed-loop state profile (state feedback) for $(a_1(0), a_2(0)) = (0.2, 1.5)$ when configuration A fails at $t = 3.5$ and configuration C is activated, (b) Corresponding manipulated input profiles for u_1 (solid) and u_2 (dashed).

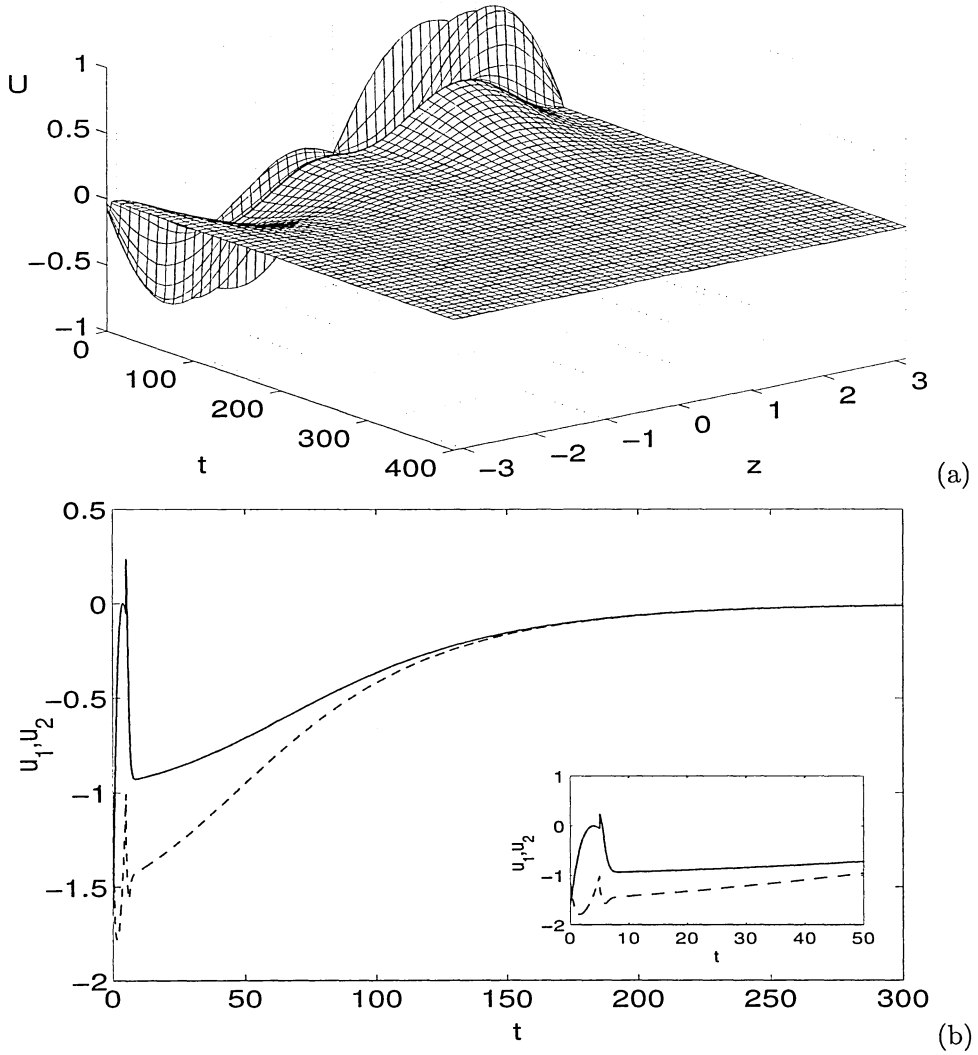

Figure 8.7: (a) Closed-loop state profile (state feedback) for $(a_1(0), a_2(0)) = (0.2,\ 1.5)$ when configuration A fails at $t = 3.5$ and configuration B is activated, (b) Corresponding manipulated input profiles for u_1 (solid) and u_2 (dashed).

present only the results for the first problem. These are given in Figs.8.8-8.9 which, respectively, show that the closed loop system becomes unstable when configuration A fails at $t = 3.5$ and configuration B is activated, whereas closed-loop stability is maintained by activating configuration B when A fails at $t = 5.0$.

Remark 8.8 *The fact that the fast stable modes were neglected in the controller design can result in some degradation in the control performance when the controller is implemented on the full (high-order) system. If these modes die out sufficiently fast, then such degradation would be minimal. However, since the control objective is to achieve stabilization of the PDE system, a second-order model that describes the evolution of the first two modes (which are unstable) was found to be sufficient to design a controller that stabilizes the zero solution of the KSE. Nonetheless, it is possible to enhance the performance further by keeping more modes in the reduced-order model in order to obtain a better approximation of the full system.*

Remark 8.9 *It should be noted that, while the KSE was used in this paper to demonstrate the design and implementation of the proposed fault-tolerant control scheme, the proposed approach can also be applied to other dissipative PDEs that can model fluid dynamic systems, such as the Burger's equation (Baker et al., 2000), the Korteweg-de Vries Burgers equation (Armaou and Christofides, 2000b) and various forms of the Navier-Stokes equations (such as equations that describe two-dimensional transitional flow in a channel (e.g., see Baker et al., 2000)).*

8.5 Conclusions

In this chapter, a fault-tolerant control system design methodology was proposed for fluid dynamic systems modeled by highly-dissipative partial differential equations (PDEs) with constrained control actuators. The central idea of the proposed method is that of coordinating feedback controller synthesis and switching between multi-

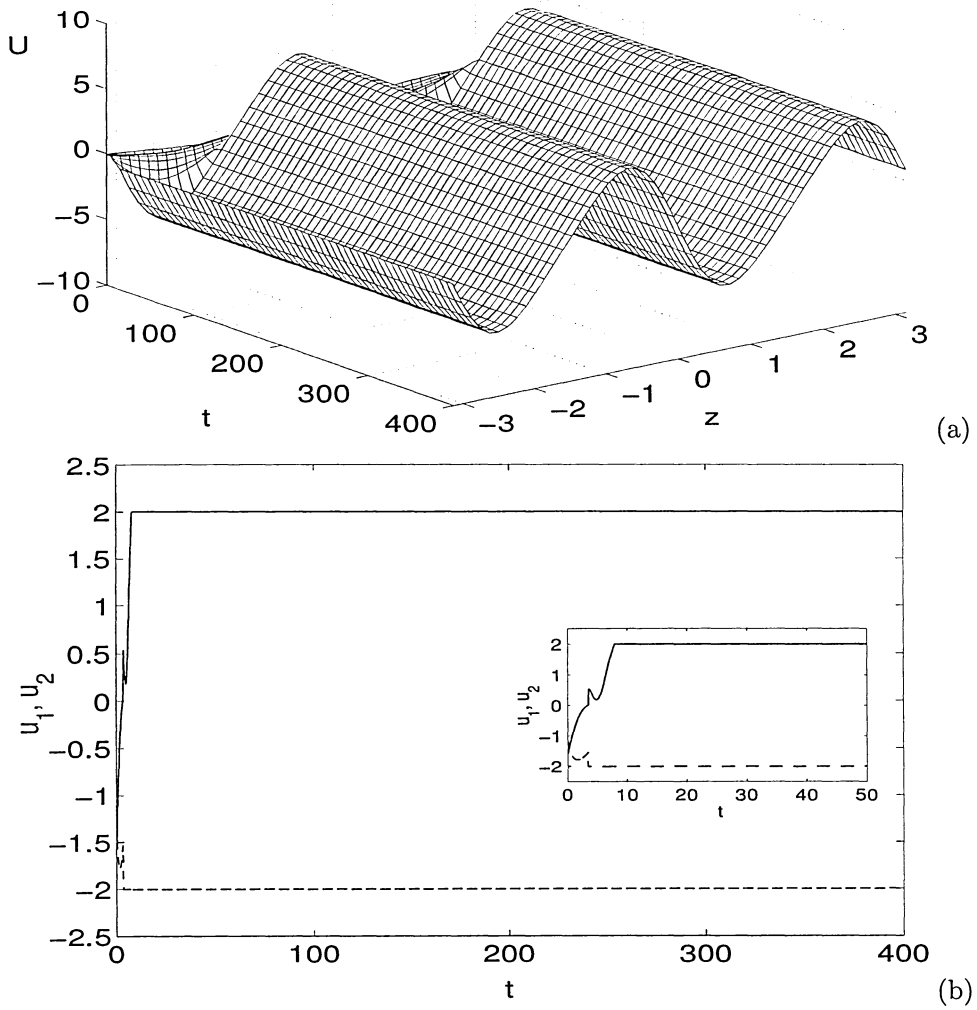

Figure 8.8: (a) Closed-loop state profile (output feedback) for $(a_1(0), a_2(0)) = (0.2, 1.5)$ when configuration A fails at $t = 3.5$ and configuration B is activated, (b) Corresponding manipulated input profiles for u_1 (solid) and u_2 (dashed).

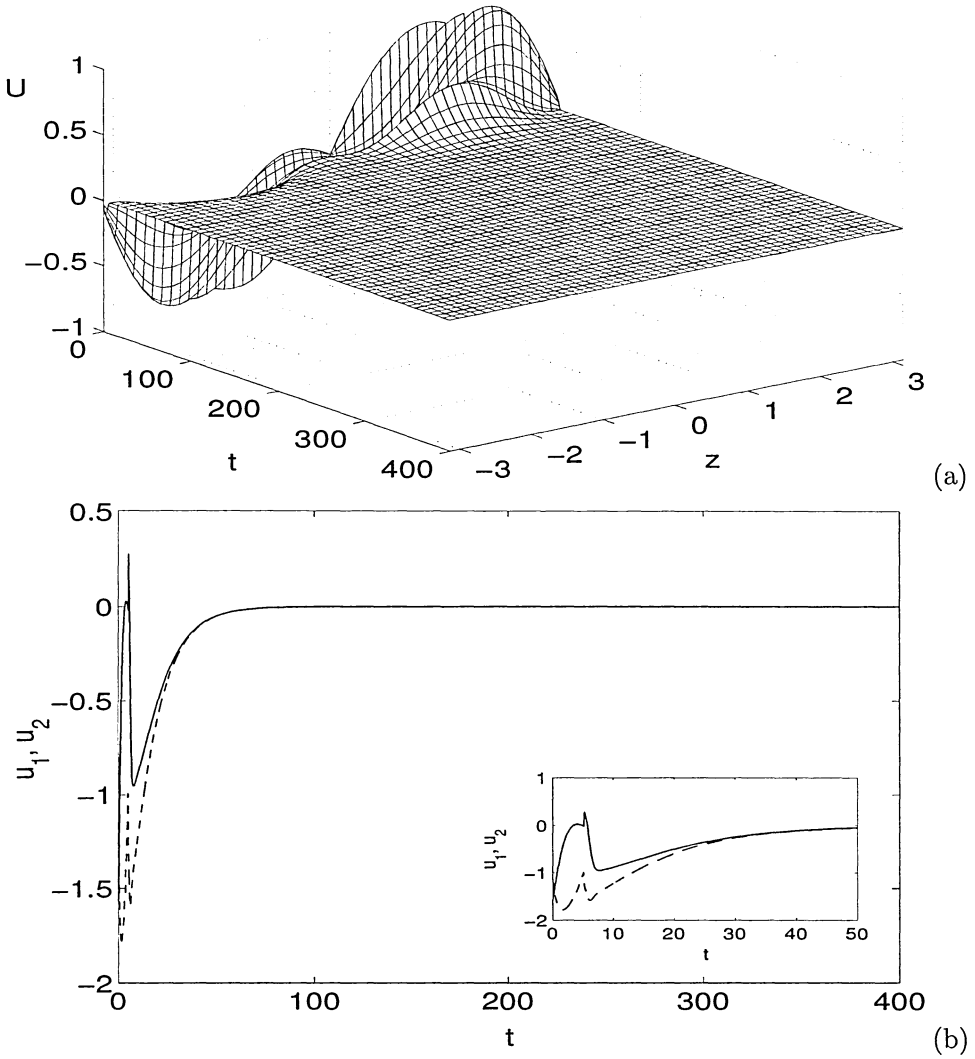

Figure 8.9: (a) Closed-loop state profile (output feedback) for $(a_1(0), a_2(0)) = (0.2, 1.5)$ when configuration A fails at $t = 5$ and configuration B is activated, (b) Corresponding manipulated input profiles for u_1 (solid) and u_2 (dashed).

ple, spatially-distributed control actuator configurations. Using appropriate finite-dimensional approximations of the PDE system, a stabilizing feedback controller was designed for a given actuator configuration, and an explicit characterization of the constrained stability region was obtained. Switching laws were then derived, on the basis of these stability regions, to orchestrate the transition between the control actuator configurations, in a way that guarantees constraint satisfaction and preserves closed-loop stability of the infinite-dimensional system in the event of actuator failures. The results were applied to the problem of suppressing wave formation in falling liquid films via the stabilization of the zero solution of the one-dimensional Kuramoto-Sivashinsky equation, with periodic boundary conditions, subject to actuator constraints and failures.

Chapter 9

Robust Stabilization of Infinite-Dimensional Systems Using Sliding-Mode Output Feedback Control

9.1 Introduction

Sliding-mode control has long been recognized as a powerful control method to counteract non-vanishing external disturbances and unmodelled dynamics (Utkin, 1992). This method is based on the deliberate introduction of sliding motions into the control system and consists of two steps. First, a manifold is designed such that if confined to this manifold the system has desired dynamic properties. Second, a switched control law, which drives the system to the manifold, is synthesized. The controller, thus constructed, asymptotically stabilizes the system and since the motion along the manifold proves to be uncorrupted by matched disturbances, the closed-loop system is additionally guaranteed to have strong robustness properties against matched dis-

turbances. Due to these advantages and simplicity of implementation, sliding-mode controllers have widely been used in various applications (Utkin et al., 1999).

Motivated by technological advances, significant interest has emerged in extending this discontinuous control method to distributed parameter systems (DPS). The earlier works (Orlov and Utkin, 1987; Zolezzi, 1989) on extensions of discontinuous control algorithms to infinite-dimensional systems ran into a major difficulty, caused by the presence of an unbounded infinitesimal operator in the plant equation, and called for further theoretical investigations. Presently, the discontinuous control synthesis in the infinite-dimensional setting is well documented (Levaggi, 2002a,b; Orlov, 2000; Orlov and Dochain, 2002). This synthesis retains robustness features, similar to those possessed by its counterpart in the finite-dimensional case. Being complementary to the H_∞-design (Curtain and Zwart, 1995; Foias et al., 1996; van Keulen, 1993), it constitutes an alternative approach to control of infinite-dimensional systems.

However, the existing results on discontinuous control of infinite-dimensional systems are based on the assumption that distributed sensing and actuation is available over the entire spatial domain. Although due to recent advances in Micro-Electro-Mechanical-Systems (MEMS) technology, manufacturing large arrays of micro sensors and actuators with integrated control circuitry has become feasible (see Ho and Tai, 1998, and references quoted therein), implementation of distributed sensors and actuators is hardly possible in many real-life applications where the available number of sensors and actuators is typically small. Thus, the development of discontinuous control methods for infinite-dimensional systems with finite-dimensional sensing and actuation is a fundamental problem of relevance to various practical applications.

In this chapter, an output feedback control method based on sliding modes is developed for a class of linear infinite-dimensional systems with finite-dimensional

unstable part using finite-dimensional sensing and actuation. For these systems, our main results include: 1) the discontinuous output feedback controller synthesis based on sliding modes in the infinite-dimensional setting, and 2) the justification of the implementation of the discontinuous sliding-mode controller via its continuous approximation.

Initially, the class of infinite-dimensional system is precisely formulated. Modal decomposition is then used to decompose the original infinite-dimensional system into an interconnection of a finite-dimensional (possibly unstable) system and an infinite-dimensional stable system. A sliding mode-based stabilizing state feedback controller is constructed on the basis of the finite-dimensional system. Subsequently, an infinite-dimensional Luenberger state observer, which utilizes a finite-number of measurements, is constructed to provide estimates of the state of the infinite-dimensional system. Finally, an output feedback controller design is completed by coupling the infinite-dimensional Luenberger state observer and the sliding mode-based state feedback controller. In order to obtain the fully practical finite-dimensional framework for controller synthesis, a finite-dimensional approximation of the Luenberger observer as well as a continuous approximation of the sliding-mode controller are carried out at the implementation stage.

Implementation, performance and robustness issues of the sliding-mode output feedback control design are illustrated in a simulation study of a distributed parameter system governed by the linearization of the Kuramoto-Sivashinsky equation around the spatially-uniform steady-state solution with periodic boundary conditions. While being unforced, the KSE describes incipient instabilities in a variety of physical and chemical systems and a control problem that occurs here is to avoid the appearance of the instabilities in the closed-loop system (Christofides and Armaou, 2000) (see also

Christofides, 2001b, for other results on control of PDE systems). We also note several recent works on control of the Kuramoto-Sivashinsky equation including boundary control (Liu and Krstić, 2001), as well as methods for robust (Hu and Temam, 2001) and adaptive (Kobayashi, 2002) stabilization.

9.2 Preliminaries

We consider infinite-dimensional systems, defined in a Hilbert space H, of the form:

$$\dot{x} = Ax + Bu \tag{9.1}$$

$$y = Cx, \tag{9.2}$$

where $x \in H$ is the state, $u \in R^m$ is the control input, $y \in R^p$ is the measured output, A is an infinitesimal operator which generates a C_0 (strongly continuous) semigroup $T_A(t)$, $B \in \mathcal{L}(R^m, H)$ and $C \in \mathcal{L}(H, R^p)$. Hereinafter, the notation is fairly standard. Particularly, given Hilbert spaces U and H, the symbol $\mathcal{L}(U, H)$ stands for the set of linear bounded operators from U to H. All relevant background material on infinite-dimensional dynamic systems in a Hilbert space can be found, e.g., in Curtain and Zwart (1995).

Given an initial condition

$$x(0) = x^0 \in H, \tag{9.3}$$

it is well-known that the Hilbert space-valued differential equation (9.1) with a continuously differentiable control input $u(x)$ has a unique local mild solution $x(t)$ (Pazy, 1983). By default, only mild solutions are under study in the present work. The precise meaning of the solution of (9.1), for inputs which are only piece-wise continuously differentiable, is defined as a limiting result obtained through the following regularization procedure.

Let the control input $u(x)$ undergo discontinuities on the hyperplane

$$\sigma x = 0,\ \sigma \in \mathcal{L}(H, R^m) \tag{9.4}$$

and let $u(x)$ be continuously differentiable beyond this hyperplane. Then the trajectories of (9.1) are defined in the conventional sense whenever they are beyond the discontinuity hyperplane (9.4) whereas in a vicinity of this hyperplane the original system is replaced by a related system, which takes into account all possible imperfections in the new control input $u^\delta(x)$ (e.g., delay, hysteresis, saturation, etc.) and for which there exists a conventional solution. A motion along the discontinuity hyperplane, if any, is then obtained by making the characteristics of the new system approach those of the original one. Such a motion is further referred to as a sliding mode that has become standard in the literature. The rigorous introduction of the solution concept is as follows (Orlov and Dochain, 2002).

Definition 9.1 *An absolutely continuous function $x^\delta(t)$, defined on some interval $[0, \tau)$, is said to be an approximate δ-solution of system (9.1) if it is a conventional solution of*

$$\dot{x}^\delta = Ax^\delta + Bu^\delta(x^\delta)$$

with some $u^\delta(x)$ such that

$$\|u^\delta(x) - u(x)\| \leq \delta \ for\ all\ x \in H\ subject\ to\ \|\sigma x\| \geq \delta. \tag{9.5}$$

Definition 9.2 *An absolutely continuous function $x(t)$, defined on some interval $[0, \tau)$, is said to be a solution of system (9.1) if there exists a family of δ-solutions $x^\delta(t)$ of the system such that*

$$\lim_{\delta \to 0} \|x^\delta(t) - x(t)\| = 0\ uniformly\ in\ t \in [0, \tau).$$

Thus, by definition the sliding motion, which is in general non-unique, does not depend on the precise specification of the discontinuous input on the discontinuity

hyperplane. Moreover, an equivalent control value $u_{eq}(x)$, maintaining the system motion on this hyperplane, is imposed by the original system itself. If the $m \times m$-matrix (σB) is non-singular there exists a unique solution of the equation $\sigma\dot{x} = 0$, i.e., $\sigma Ax + \sigma Bu = 0$ with respect to u and this solution

$$u_{eq}(x) = -(\sigma B)^{-1}\sigma Ax \tag{9.6}$$

is accepted as the equivalent control value because (9.6) is the only controller maintaining system (9.1) with appropriate initial conditions on the hyperplane $\sigma x = 0$. According to the infinite-dimensional extension (Orlov, 2000; Orlov and Dochain, 2002) of the equivalent control method (Utkin, 1992), the so-called sliding mode equation

$$\dot{x} = [A - B(\sigma B)^{-1}\sigma A]x, \tag{9.7}$$

governing the system motion on the discontinuity hyperplane $\sigma x = 0$, is then obtained by substituting the equivalent control value (9.6) into (9.1) for u. The following result is extracted from (Orlov, 2000, Theorem 1).

Theorem 9.1 *Consider the dynamic system (9.1) subject to the above assumptions and solution formulation. Let $T(x^0) \geq 0$ be a finite time, which depends on the initial condition (9.3), in which the system starts evolving in the discontinuity hyperplane (9.4) and let the operator $\tilde{A} = A - B(\sigma B)^{-1}\sigma A$ generate an exponentially stable semigroup. Then the initial value problem (9.1), (9.3) has a unique solution, and this solution is governed by the sliding mode equation (9.7) for $t \geq T(x^0)$.*

For convenience of the reader, we recall the definition of the generator of an exponentially stable semigroup as well as that of the exponential stabilizability/detectability (see, e.g., Curtain and Zwart, 1995, for details).

Definition 9.3 *The operator $\tilde{A}$ generates an exponentially stable semigroup $\tilde{S}(t)$ iff the initial value problem $\dot{x} = \tilde{A}x$, $x(0) = x^0$ has a unique solution $x(t) = \tilde{S}(t)x^0$, and $\|\tilde{S}(t)\| \leq \omega e^{-\alpha t}$ for all $t \geq 0$ and some positive ω, α.*

Definition 9.4 *System (9.1), (9.2), or equivalently, the pair $\{A, B\}$ is said to be exponentially stabilizable if there exists $D \in \mathcal{L}(H, R^m)$ such that the operator $A + BD$ generates an exponentially stable semigroup.*

Definition 9.5 *System (9.1), (9.2), or equivalently, the pair $\{A, C\}$ is said to be exponentially detectable if there exists $L \in \mathcal{L}(R^p, H)$ such that the operator $A + LC$ generates an exponentially stable semigroup.*

The following assumption is made throughout.

Assumption 9.1 *System (9.1), (9.2) is exponentially stabilizable and detectable.*

Assumption 1 implies that the system (9.1), (9.2) can be exponentially stabilized via linear dynamic output feedback control of the form:

$$u(\tilde{x}) = D\tilde{x} \tag{9.8}$$

$$\dot{\tilde{x}} = A\tilde{x} + Bu(\tilde{x}) - L(y - C\tilde{x}) \tag{9.9}$$

where the internal state $\tilde{x} \in H$, and the operators D and L satisfy the condition of the stabilizability/detectability definitions.

Moreover, under the assumption of exponential stabilizability and detectability, H can be decomposed as $H = H_1 \oplus H_2$, and the state equation (9.1) can be rewritten in terms of $x_1 \in H_1$ and $x_2 \in H_2$, as follows (Curtain and Zwart, 1995, Section 5.2):

$$\dot{x}_1 = A_1 x_1 + B_1 u \tag{9.10}$$

$$\dot{x}_2 = A_2 x_2 + B_2 u \tag{9.11}$$

$$y = C_1 x_1 + C_2 x_2 \tag{9.12}$$

where $H_1 = R^n$ is a finite-dimensional subspace, $A_j = A|_{H_j}$, and $C_j = C|_{H_j}$ are the operator restrictions on H_j, $j = 1, 2$, $B_j = P_j B$ and P_j is the projector on H_j. From Assumption 9.1, the matrix pairs $\{A_1, B_1\}$ and $\{A_1, C_1\}$ are controllable and observable, respectively, and the operator $A_2 = A|_{H_2}$ generates an exponentially stable semigroup $S_{A_2}(t)$ on H_2.

The decomposition (9.10)-(9.11) of the original system (9.1) into a finite-dimensional possibly unstable part (9.10) and an infinite-dimensional stable part (9.11) has long been recognized as providing the framework for the design of stabilizing controllers for linear infinite-dimensional systems (see the notes and references quoted in (Curtain and Zwart, 1995, Chapter 5)). Using the decomposition of (9.10)-(9.11), the synthesis of dynamic output feedback control laws is obtained as follows:

$$u(\tilde{x}_1) = D_1 \tilde{x}_1 \tag{9.13}$$

$$\dot{\tilde{x}}_1 = A_1 \tilde{x}_1 + B_1 u(\tilde{x}_1) - L_1(y - C_1 \tilde{x}_1 - C_2 \tilde{x}_2) \tag{9.14}$$

$$\dot{\tilde{x}}_2 = A_2 \tilde{x}_2 + B_2 u(\tilde{x}_1) \tag{9.15}$$

where $D_1 = D|_{H_1}$, $L_1 = P_1 L$ are such that the $n \times n$- matrices $A_1 + B_1 D_1$ and $A_1 + L_1 C_1$ are Hurwitz. Although the finite-dimensional state estimate $\tilde{x}_1(t)$ is only required in the control law (9.13), the Luenberger observer design is carried out in the infinite-dimensional setting (9.14), (9.15) to avoid the appearance of the destabilizing spill-over effect in the closed-loop system (see also proof of Theorem 9.4). The implementation of the above observer can then be performed by obtaining a finite-dimensional approximation of the $\tilde{x}_2$-subsystem of sufficiently high-order.

It is worth noting that there is a body of literature focusing on the construction of the associated Luenberger observers for stabilization of infinite-dimensional systems (see, e.g., Curtain and Zwart, 1995, Chapter 5 and references therein). Such a treatment, based on a finite-dimensional approximation of the original infinite-

dimensional system, becomes attractive in practice if instabilities due to spill-over effect can be prevented; it additionally ensures strong robustness properties against unmodelled dynamics and parameter variations. In order to enhance performance the approximation-based treatment will subsequently be accompanied by sliding-mode output feedback synthesis, potentially capable of providing this desired robustness feature.

Remark 9.1 *We note that under Assumption 9.1, the eigenspectrum of the operator A of system (9.1) could have hyperbolic-like or parabolic-like structure. As an example, in Fig. 9.1, we show the eigenspectrum of the linearized Korteweg-de Vries-Burgers (KdVB) equation (left plot), which is a third-order PDE with a hyperbolic-like spectrum and that of the linearized Kuramoto-Sivashinsky equation (KSE) (right plot), which is a fourth-order PDE with a parabolic-like spectrum. Specifically, the linearized KdVB equation takes the form:*

$$\begin{aligned} \frac{\partial x}{\partial t} &= -\frac{\partial^3 x}{\partial z^3} + a_1 \frac{\partial^2 x}{\partial z^2} \\ \frac{\partial^j x}{\partial z^j}(0,t) &= \frac{\partial^j x}{\partial z^j}(+\pi,t), \quad j = 0,\ldots,2 \end{aligned} \tag{9.16}$$

and the linearized KSE takes the form:

$$\begin{aligned} \frac{\partial x}{\partial t} &= -\nu \frac{\partial^4 x}{\partial z^4} - \frac{\partial^2 x}{\partial z^2} \\ \frac{\partial^j x}{\partial z^j}(-\pi,t) &= \frac{\partial^j x}{\partial z^j}(+\pi,t), \quad j = 0,\ldots,3 \end{aligned} \tag{9.17}$$

Both the linearized KdVB and KS partial differential equations belong in the class of linear infinite-dimensional systems considered in this work and satisfy Assumption 9.1 (see (Armaou and Christofides, 2000b) for results on finite-dimensional control design for the KdVB equation and the KSE).

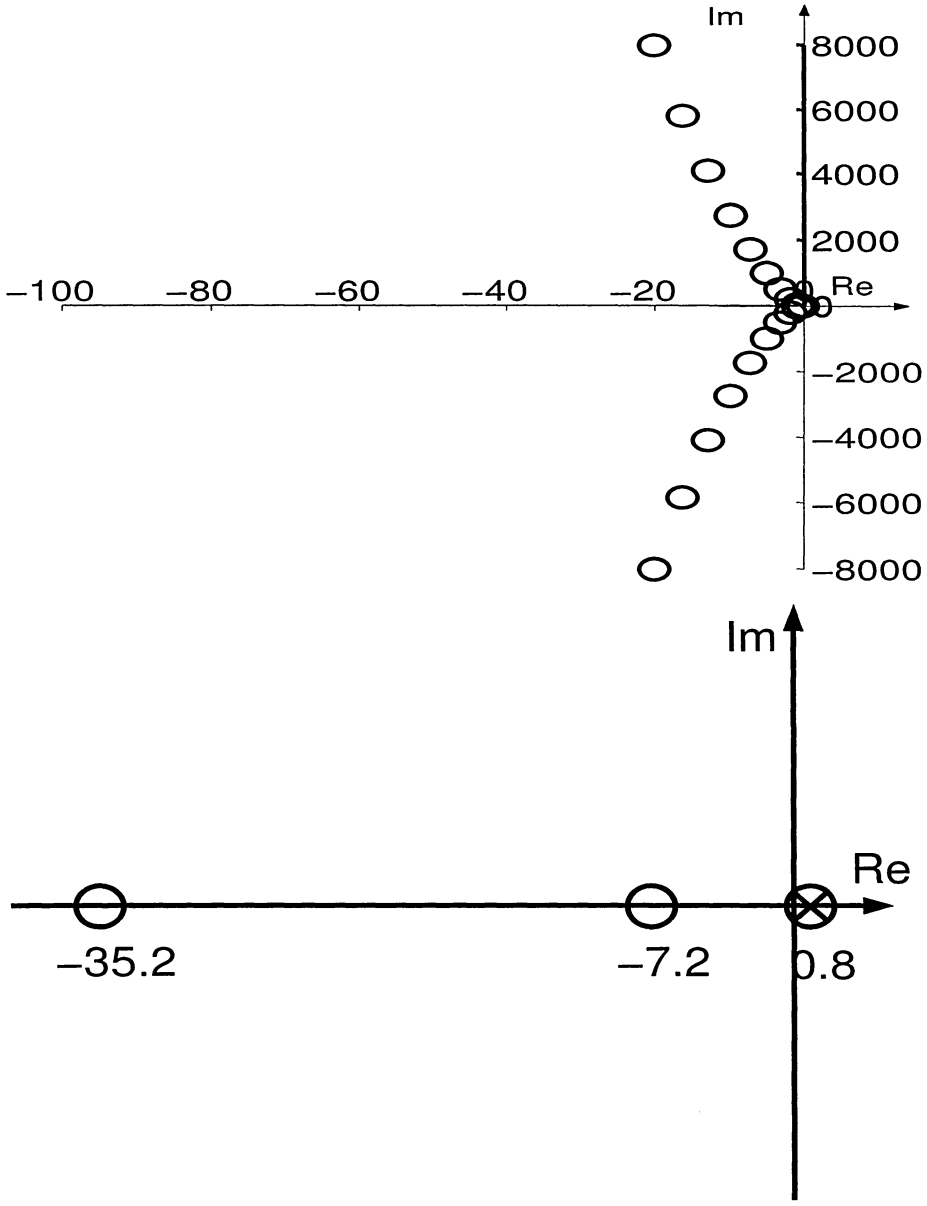

Figure 9.1: Eigenspectrum of the linearized KdVB equation with $a_1 = 0.05$ (left plot) and that of the linearized KSE with $\nu = 0.2$ (right plot).

9.3 Sliding-Mode Feedback Synthesis

The aim of this section is to demonstrate how the approximation-based approach can be used to globally exponentially stabilize the infinite-dimensional system (9.1), (9.2) by means of discontinuous output feedback control. First, a discontinuous state feedback controller is constructed and then the Luenberger observer (9.14), (9.15) of the unstable modes is involved to synthesize a stabilizing output feedback law.

9.3.1 State Feedback Design

The stabilizing discontinuous state feedback controller to be developed is based on the deliberate introduction of sliding modes into the finite-dimensional subsystem (9.10). Taking into account that the infinite-dimensional subsystem (9.11) is stable and does not require to be stabilized, the discontinuous state feedback, stabilizing subsystem (9.10), is subsequently shown to simultaneously stabilize the infinite-dimensional closed-loop system (9.10), (9.11). Thus, the discontinuous stabilization of the infinite-dimensional system (9.10), (9.11) is reduced to the sliding-mode finite-dimensional treatment which is as follows (Utkin, 1992).

The stabilization problem for the finite-dimensional system (9.10) is solved in the space of the new state variable

$$\xi = Mx_1 \in R^n \tag{9.18}$$

where $M \in R^{n\times n}$ is a non-singular matrix such that

$$MB_1 = (0, B_{12})^T \tag{9.19}$$

with a non-singular matrix $B_{12} \in R^{m\times m}$. To satisfy (9.19), the first $n - m$ rows of M are composed of $n - m$ linearly independent vectors, orthogonal to the control

subspace, whereas B_1^T forms the remaining m rows of M so that the matrix $B_{12} = B_1^T B_1$ is nonsingular.

System (9.10), rewritten in terms of the components $\xi_1 = P_{11}\xi \in R^{n-m}$, $\xi_2 = P_{12}\xi \in R^m$ of the new state variable $\xi = (\xi_1, \xi_2)^T$, is given by

$$\dot{\xi}_1 = A_{11}\xi_1 + A_{12}\xi_2 \tag{9.20}$$

$$\dot{\xi}_2 = A_{21}\xi_1 + A_{22}\xi_2 + B_{12}u \tag{9.21}$$

where P_{11} and P_{12} are the projectors on the subspaces spanned by the first $n-m$ state components and the remaining m components, respectively. By construction, the matrix pair $\{A_1, B_1\}$ is controllable, because the pair $\{A, B\}$, otherwise, would not be exponentially stabilizable. Due to Lemma of (Utkin, 1992, p.101), it follows that the matrix pair $\{A_{11}, A_{12}\}$ is also controllable. Then, by an appropriate choice of $K \in R^{m\times(n-m)}$, the matrix $A_{11} + A_{12}K$ can be made Hurwitz with an a priori fixed location of the eigenvalues.

The unit signal-based control law can be synthesized in the following form:

$$u(\xi) = -[\gamma_0 + \gamma_1\|\xi\|]B_{12}^{-1}U(\sigma\xi) \tag{9.22}$$

with nonnegative γ_0,

$$\gamma_1 > \|A_{21} - KA_{11}\| + \|A_{22} - KA_{12}\|, \tag{9.23}$$

$$\sigma\xi = \xi_2 - K\xi_1, \tag{9.24}$$

and

$$U(\sigma\xi) = \frac{\sigma\xi}{\|\sigma\xi\|} \tag{9.25}$$

to drive the system (9.20), (9.21) to the discontinuity hyperplane $\sigma\xi = 0$. In the above control law, γ_0 and γ_1 are constants, the norm of the unit component $U(\sigma\xi)$ is equal

to one everywhere but on the hyperplane $\sigma\xi = 0$, where this component is permitted to be multivalued and take any value from the unit ball $B_1^m = \{u \in R^m : \|u\| \leq 1\}$.

It should be pointed out that the standard sliding-mode control would also be synthesized to steer the system to the same hyperplane (Utkin, 1992). However, this standard approach would result in several switching points as one coordinate after the other hits the hyperplane and in order to design such a controller one would need to additionally follow the hierarchy of the control components that ensures the existence of the sliding motion. In order to simplify the stability analysis and avoid extra computations, required by the hierarchy procedure, the unit feedback controller (9.22) is synthesized in such a manner that the motion of the closed-loop system never passes through the discontinuity hyperplane. The system stability is thus analyzed beyond the hyperplane. Once the trajectory is on the discontinuity hyperplane, smooth closed-loop system dynamics can be restored and standard Lyapunov theory can be used.

The linear boundedness of controller (9.22) prevents the state of the closed-loop system (9.20), (9.21), (9.22) from escaping to infinity in finite time. Subject to the lower bound (9.23), this controller dominates the rest, $(A_{21} - KA_{11})\xi_1 + (A_{22} - KA_{12})\xi_2$, of the right-hand side of the equation

$$\sigma\dot{\xi} = (A_{21} - KA_{11})\xi_1 + (A_{22} - KA_{12})\xi_2 + B_{12}u(\xi), \tag{9.26}$$

thereby providing the flow of the closed-loop system to be directed toward the discontinuity hyperplane $\sigma\xi = 0$. Since the sliding mode equation $\sigma\dot{\xi} = 0$, or equivalently,

$$\dot{\xi}_1 = (A_{11} + A_{12}K)\xi_1 \tag{9.27}$$

is exponentially stable due to a special choice of K, the finite-dimensional system (9.20), (9.21), driven by the discontinuous control law (9.22)-(9.25), can be proven to

be asymptotically (when $\gamma_0 > 0$) or exponentially stable (when $\gamma_0 = 0$).

The following result is inspired from the standard sliding-mode control theory (Utkin, 1992, Chapter 7, Section 6).

Lemma 9.1 *Let the finite-dimensional system (9.20), (9.21), be driven by the unit control law (9.22)-(9.25). Then, given an initial condition $\xi(0) = \xi^0 \in R^n$, the closed-loop system (9.20)-(9.25) has a unique solution, globally defined for all $t \geq 0$, and this system is globally asymptotically stable when $\gamma_0 > 0$ and it is globally exponentially stable when $\gamma_0 = 0$.*

Proof: We break up the proof into 3 simple steps.

1) By Theorem of (Utkin, 1992, p. 16) a unique solution of the finite-dimensional system (9.20)-(9.25) exists locally for all initial conditions. By the same theorem, a system motion on the discontinuity hyperplane $\sigma\xi = 0$, if any, is governed by the sliding mode equation (9.27). While being governed by the linear equation (9.27), such a motion is apparently uniformly bounded on an arbitrary finite time interval and globally continuable on the right. The same is also true for a motion, initialized beyond the discontinuity hyperplane.

Indeed, beyond this hyperplane the right-hand side of the state equation (9.20)-(9.25) is linearly bounded in the state variable so that

$$\|\xi(t)\| \leq \|\xi^0\| + \int_0^t [\gamma_0 + L\|\xi(\tau)\|]d\tau, \tag{9.28}$$

for some constant $L > 0$. It follows that

$$\|\xi(t)\| \leq [\|\xi^0\| + \gamma_0 T] + L\int_0^t \|\xi(\tau)\|d\tau, \ 0 \leq t < T. \tag{9.29}$$

By applying the Bellman-Gronwall lemma to inequality (9.29), any solution of this equation is uniformly bounded

$$\|\xi(t)\| \leq [\|\xi^0\| + \gamma_0 T]e^{LT} \tag{9.30}$$

on an arbitrary time interval $[0, T)$ before possible getting on the discontinuity hyperplane where it has been shown to remain uniformly bounded on any finite time interval. Thus, given an arbitrary initial condition, there exists a unique solution of (9.20)-(9.25), which turns out to be globally continuable on the right.

2) Let us now assume that $\gamma_0 > 0$ and let us demonstrate that the closed-loop system in this case is globally asymptotically stable. For this purpose, we introduce the quadratic function

$$V(\sigma\xi) = (\sigma\xi)^T \sigma\xi \tag{9.31}$$

and compute its time derivative along the trajectories of the closed-loop system (9.20)-(9.25):

$$\begin{aligned} \dot{V}(t) &= 2(\sigma\xi)^T \{(A_{21} - KA_{11})\xi_1 + (A_{22} - KA_{12})\xi_2 - [\gamma_0 + \gamma_1 \|\xi\|] U(\sigma\xi)\} \\ &\leq -2(\sigma\xi)^T \{\gamma_0 + [\gamma_1 - \|A_{21} - KA_{11}\| - \|A_{22} - KA_{12}\|] \|\xi\|\} \frac{\sigma\xi}{\|\sigma\xi\|}. \end{aligned} \tag{9.32}$$

Due to (9.23), it follows that

$$\dot{V}(t) \leq -2\gamma_0 \|\sigma\xi\| = -2\gamma_0 \sqrt{V(t)}, \tag{9.33}$$

thereby yielding the finite time convergence of $V(t)$ to zero. In order to reproduce this conclusion, one should note that for all $t \geq 0$, an arbitrary solution $V(t)$ to the latter inequality is dominated, i.e., $V(t) \leq V_0(t)$, by the solution to the differential equation $\dot{V}_0(t) = -2\gamma_0 \sqrt{V_0(t)}$, initialized with the same initial condition $V_0(0) = \|\sigma\xi^0\|^2$. Since $V_0(t) = 0$ for all $t \geq \gamma_0^{-1} \|\sigma\xi^0\|$, $V(t)$ vanishes after a finite time moment $T \leq T_0 = \gamma_0^{-1} \|\sigma\xi^0\|$, i.e., $\sigma\xi(t) = 0$ for all $t \geq T$.

Thus, starting from the finite time moment $T \leq \gamma_0^{-1} \|\sigma\xi^0\|$ the closed-loop system evolves in the sliding mode on the m-dimensional hyperplane $\sigma\xi = 0$. By Theorem of (Utkin, 1992, p. 16) this motion is governed by the sliding mode equation (9.27) which is globally exponentially stable due to a special choice of the matrix K. While

being governed on the time interval $t \in [0, T)$ by the ordinary differential equations (9.20), (9.21) with a smooth right-hand side, the initial stage of the trajectory, before it hits the discontinuity hyperplane $\sigma\xi = 0$, continuously depends on the initial conditions. Coupled to the exponential stability of the sliding motion after the time moment T, this ensures the closed-loop system (9.20)-(9.25) with $\gamma_0 > 0$ to be globally asymptotically stable on the semi-infinite time interval $[0, \infty)$.

3) Setting $\gamma_0 = 0$ in the control algorithm (9.22), the derivative estimate (9.32) for the quadratic function (9.31) takes the form

$$\dot{V}(t) \leq -2\gamma \|\xi(t)\| \sqrt{V(t)} \tag{9.34}$$

where $\gamma = \gamma_1 - \|A_{21} - KA_{11}\| - \|A_{22} - KA_{12}\|$ is positive by virtue of (9.23).

In contrast to (9.33), equality (9.34) cannot guarantee that $V(t) = 0$ starting from a finite time moment because (9.33) is now violated for $\|\xi(t)\| \to 0$. However, if for some $\zeta \in (0, 1)$ the following state estimate

$$\|\xi(t)\| > \zeta \|\xi^0\| \tag{9.35}$$

could be guaranteed on the time interval $t \in (0, T)$ with

$$T = \frac{\|\sigma\xi^0\|}{\gamma\zeta\|\xi^0\|}, \tag{9.36}$$

then in analogy to (9.33), the trajectory of the closed-loop system (9.20)-(9.25), corresponding to $\gamma_0 = 0$, would also enter the hyperplane $\sigma\xi = 0$ in a finite time $\tau_0 \leq T$, and starting from τ_0 the system would evolve in the sliding mode on this hyperplane.

If hypothesis (9.35) fails to hold on the entire time interval $(0, \tau_0)$, then there exists a time moment $t_1 \in (0, \tau_0)$ such that

$$\|\xi(t_1)\| = \zeta \|\xi^0\|. \tag{9.37}$$

Taking into account the earlier obtained state estimate (9.30) subject to $\gamma_0 = 0$, it follows that

$$\|\xi(t)\| \leq \|\xi^0\| e^{LT} \; for \; t \in (0, t_1). \tag{9.38}$$

Now regarding t_1 as the new initial time moment and following the same line of reasoning as before, one can obtain that either the state vector enters the hyperplane $\sigma\xi = 0$ at time instant $\tau_1 < t_1 + T$ and then it evolves in the sliding mode on this hyperplane, or $\|\xi(t_2)\| = \zeta^2 \|\xi^0\|$ for some $t_2 \in (t_1, \tau_1)$ and

$$\|\xi(t)\| \leq \zeta \|\xi^0\| e^{LT} \; for \; t \in (t_1, t_2). \tag{9.39}$$

Thus, by iterating on i, one concludes that either the state vector enters the hyperplane $\sigma\xi = 0$ in a finite time and after that it never leaves this hyperplane, or $\|\xi(t_{i+1})\| = \zeta^{i+1} \|\xi^0\|$ for some $t_{i+1} \in (t_i, \tau_i)$, $i = 0, 1, \ldots$ and

$$\|\xi(t)\| \leq \zeta^i \|\xi^0\| e^{LT} \; for \; t \in (t_i, t_{i+1}) \tag{9.40}$$

where $t_0 = 0$.

In the latter case, inequalities (9.40), coupled together for $i = 0, 1, \ldots$, ensure that for all $t \geq 0$ there exists a decaying exponential state estimate

$$\|\xi(t)\| \leq L_0 \|\xi^0\| e^{-\mu t} \tag{9.41}$$

with $\mu = -T^{-1} \ln \zeta > 0$ and $L_0 = e^{LT} > 0$.

In turn, in the former case, inequalities (9.41) are also satisfied before the instant of hitting the hyperplane $\sigma\xi = 0$ whereas after this instant the sliding motion on $\sigma\xi = 0$ is governed by the globally exponentially stable equation (9.27). Thus, in any case the closed-loop system (9.20)-(9.25) with $\gamma_0 = 0$ proves to be globally exponentially stable. Lemma 1 is completely proven.

One can be surprised that according to Lemma 1, feedback (9.22) with $\gamma_0 > 0$ can only guarantee asymptotic stability of the closed-loop system whereas the less powerful feedback (9.22) with $\gamma_0 = 0$ exponentially stabilizes the system. To explain this, one should take into account that the peaking phenomenon (Sussman and Kokotovic, 1991) in the initial stage of the trajectory, before it hits the discontinuity hyperplane, is capable of destroying exponential stability of the system, but it can only occur when $\gamma_0 > 0$ (cf. the general upper estimate (9.30) and the particular upper estimate (9.41), corresponding to $\gamma_0 = 0$).

Remark 9.2 *It is worth noting that the sign of the time derivative (9.32) of the quadratic function (9.31), computed along the trajectories of the closed-loop system (9.20)-(9.25) with $\gamma_0 > 0$, remains negative even in the case when sufficiently small matched disturbances $d(x,t) \in R^m$, which satisfy $\|d(\xi,t)\| < \gamma_0$ for all $\xi \in R^n$ and all $t > 0$, affect the system. Thus, the line of reasoning, used in the proof of Lemma 1, applies to such a perturbed system as well, so that the matched disturbances are rejected by the unit controller (9.22)-(9.25) with γ_0 exceeding a norm bound of these disturbances (see also example in subsection 9.4.2).*

Remark 9.3 *The main drawback of the use of the unit controller (9.22)-(9.25) with positive γ_0 is that of fast switching of the control action in a practical implementation of such a controller; this may excite unmodelled high-frequency dynamics of the closed-loop system that may severely limit the achievable closed-loop performance. A continuous version of this controller can be obtained for $\gamma_0 = 0$ (note that in the particular case, where the number of the control inputs, m, equals to the dimension of the system, n, the resulting controller will also be linear). While being continuous in the origin, this controller reduces the amplitude of undesired oscillations around the equilibrium solution, however, in contrast to its counterpart with positive γ_0, it cannot reject non-vanishing disturbances.*

In what follows, we demonstrate that the same control law (9.22)-(9.25) globally

stabilizes (asymptotically (when $\gamma_0 > 0$) or exponentially (when $\gamma_0 = 0$)) the closed-loop infinite-dimensional system (9.1).

Theorem 9.2 *Consider an infinite-dimensional system (9.1) for which Assumption 9.1 holds and let the unit control signal (9.22)-(9.25) be constructed via the finite-dimensional approximation (9.10) of the system and its equivalent representation (9.18)-(9.21). Then, given an initial condition $x(0) = x^0 \in H$, the closed-loop system (9.1), (9.22)-(9.25), has a unique solution, which is globally defined for all $t \geq 0$, and this system is globally asymptotically stable when $\gamma_0 > 0$ and it is globally exponentially stable when $\gamma_0 = 0$.*

Proof: The proof follows the same path as in Lemma 1.

1) By Lemma 1, a unique solution of the finite-dimensional system (9.20)-(9.25) exists for all initial conditions and this solution is globally defined for all $t \geq 0$. While this system remains beyond the discontinuity hyperplane $\sigma\xi = 0$, the control function $u(t)$, computed according to (9.22) on the trajectories of (9.20), (9.21), is continuously differentiable in t. Thus, before the solution of the finite-dimensional system (9.20)-(9.25) hits the discontinuity hyperplane, the infinite-dimensional system (9.11), driven by this control signal, satisfies (Pazy, 1983, p.109, Corollary 2.10). By this corollary, system (9.11), (9.22) has a unique solution under arbitrary initial conditions (9.3) at least till a time instant when system (9.20)-(9.25) enters the hyperplane $\sigma\xi = 0$.

As shown in the proof of Lemma 1, any solution of the finite-dimensional system (9.20)-(9.25), entering the discontinuity hyperplane in a finite time $T > 0$, never leaves it. In order to describe the behavior of the infinite-dimensional system (9.11), (9.22) on the hyperplane $\sigma\xi = 0$, one should use the infinite-dimensional extension of the equivalent control method that has recently been justified in Orlov (2000).

According to this extension, the equivalent control value

$$u_{eq} = B_{12}^{-1}(KA_{11} + KA_{12}K - A_{21} - A_{22}K)\xi_1, \tag{9.42}$$

a unique solution of the equation $\dot{\sigma}(\xi(t)) = 0$ with respect to u, is substituted into (9.11) for u. By (Orlov, 2000, Theorem 1), the equation

$$\dot{x_2} = A_2 x_2 + B_2 B_{12}^{-1}(KA_{11} + KA_{12}K - A_{21} - A_{22}K)\xi_1, \ t \geq T, \tag{9.43}$$

thus obtained, describes the motion of the infinite-dimensional subsystem (9.11) while the finite-dimensional subsystem (9.10) evolves in the sliding mode on the discontinuity hyperplane $\sigma\xi = 0$.

Apparently, the equivalent control function (9.42), computed along the sliding modes (9.27), is continuously differentiable in t, and hence, the infinite-dimensional sliding mode equation (9.43) satisfies (Pazy, 1983, p.109, Corollary 2.10), too. By applying this corollary to (9.43), we conclude that the solutions of the infinite-dimensional part (9.11), (9.22) of the closed-loop system (9.1), (9.22)-(9.25) are globally continuable on the right, even if the finite-dimensional system enters the discontinuity hyperplane $\sigma\xi = 0$ in a finite time.

2) If $\gamma_0 > 0$ then, as shown in the proof of Lemma 1, after the finite time $T \leq \gamma_0^{-1}\|\sigma\xi^0\|$ the finite-dimensional system (9.20)-(9.25) evolves in the sliding mode on the hyperplane $\sigma\xi = 0$. While being governed on the time interval $[0, T)$ by the differential equations (9.11), (9.20), (9.21), subject to the smooth control input (9.22), the initial stage of the trajectory $x(t)$, before it hits the discontinuity hyperplane $\sigma\xi = 0$, continuously depends on the initial data x^0.

In turn, for $t \geq T$ the closed-loop system (9.1), (9.22)-(9.25) is maintained on the hyperplane $\sigma\xi = 0$ and it is governed by the sliding mode equations (9.27), (9.43). Due to a special choice of K, the solution of the former equation is exponentially

decaying

$$\|\xi_1(t)\| \leq \omega \|\xi_1(T)\| e^{-\beta(t-T)}, \ t \geq T \tag{9.44}$$

with some $\omega > 0$ and $\beta > 0$. Since the semigroup $S_{A_2}(t)$ generated by the infinitesimal operator A_2 is exponentially stable, i.e., $\|S_{A_2}(t-T)\| \leq \omega_0 e^{-\alpha(t-T)}$ for all $t \geq T$ and some $\alpha, \omega_0 > 0$, the solution of the latter equation, given by

$$x_2(t) = S_{A_2}(t-T)x_2(T) + \int_T^t S_{A_2}(t-T-\tau)B_2 B_{12}^{-1}(KA_{11} + KA_{12}K - A_{21} - A_{22}K)\xi_1(\tau)d\tau, \tag{9.45}$$

is estimated as follows

$$\|x_2(t)\| \leq \omega_0 \|x_2(T)\| e^{-\alpha(t-T)} + \kappa \|\xi_1(T)\| [e^{-\beta(t-T)} + e^{-\alpha(t-T)}], \ t \geq T \tag{9.46}$$

where

$$\kappa = \frac{\omega_0 \omega e^{\alpha T}}{|\alpha - \beta|} \|B_2 B_{12}^{-1}(KA_{11} + KA_{12}K - A_{21} - A_{22}K)\| > 0$$

and inequality (9.44) has been used. By taking into account (9.44) and employing that $\sigma\xi = 0$, or equivalently, $\xi_2(t) = K\xi_1(t)$ for $t \geq T$, it follows that

$$\|x(t)\| \leq \omega_1 \|x(T)\| e^{-\nu_1(t-T)}, \ t \geq T \tag{9.47}$$

for some $\omega_1 > 0$ and $\nu_1 > 0$. Coupled to the afore-mentioned property of the initial stage of the solution to continuously depend on the initial data, the exponential decay (9.47) after the finite time moment T ensures the global asymptotic stability of the closed-loop system (9.1), (9.22)-(9.25) with $\gamma_0 > 0$.

3) If $\gamma_0 = 0$ then apart from the exponential decay (9.47) on the discontinuity hyperplane $\sigma\xi = 0$, a similar state estimate takes place at the initial stage preceding a sliding motion on this hyperplane. Indeed, by Lemma 1, the finite-dimensional component $\xi(t)$ of the closed-loop system (9.1), (9.22)-(9.25) with $\gamma_0 = 0$ is globally

exponentially stable whereas the solution

$$x_2(t) = S_{A_2}(t)x_2(0) - \gamma_1 \int_0^t \|\xi(\tau)\| S_{A_2}(t-\tau)B_2 B_{12}^{-1} \frac{\sigma\xi(\tau)}{\|\sigma\xi(\tau)\|} d\tau,\ 0 \le t < T \quad (9.48)$$

of the infinite-dimensional part (9.11), before $\xi(t)$ hits the hyperplane $\sigma\xi = 0$, is estimated as follows

$$\|x_2(t)\| \le \omega_0 \|x_2(0)\| e^{-\alpha t} + \kappa_1 \|\xi^0\| [e^{-\mu t} + e^{-\alpha t}],\ 0 \le t < T \quad (9.49)$$

where

$$\kappa_1 = \frac{L_0 \omega_0 \gamma_1}{|\alpha - \mu|} \|B_2 B_{12}^{-1}\| > 0,$$

and inequality (9.41) has been used. By taking into account (9.41), it follows that

$$\|x(t)\| \le \omega_2 \|x^0\| e^{-\nu_2 t},\ 0 \le t < T \quad (9.50)$$

for some $\omega_2 > 0$ and $\nu_2 > 0$. Since relation (9.50), coupled to (9.47), ensures that

$$\|x(t)\| \le \Omega \|x^0\| e^{-\nu t},\ t \ge 0 \quad (9.51)$$

for $\Omega = \max\{\omega_1, \omega_2, \omega_1\omega_2\} > 0$ and $\nu = \min\{\nu_1, \nu_2\} > 0$, regardless of whether the closed-loop system enters the discontinuity hyperplane $\sigma\xi = 0$ in a finite time $T < \infty$ or it never hits this hyperplane, the global exponential stability of (9.1), (9.22)-(9.25) with $\gamma_0 = 0$ is guaranteed. Thus, Theorem 9.2 is completely proven.

The implementation of the discontinuous unit feedback (9.25) can be performed through its continuous approximation $U^\delta(\sigma\xi)$, e.g.,

$$U^\delta(\sigma\xi) = \frac{\sigma\xi}{\|\sigma\xi\| + \delta^3}, \quad (9.52)$$

such that condition (9.5) holds with $u(x) = \frac{\sigma\xi}{\|\sigma\xi\|}$ and $u^\delta(x) = U^\delta(\sigma\xi)$. Undesirable high frequency state oscillations that would be excited by fast switching in the discontinuous controller are thus avoided, and the resulting closed-loop system, corresponding to a sufficiently small δ, can be shown to be practically stable (i.e., all

the trajectories converge to an ϵ-vicinity of the equilibrium solution). Theorem 9.3 summarizes the main result.

Theorem 9.3 *Let a continuous approximation (9.52) of the discontinuous unit feedback signal (9.25) be substituted into the control law (9.22) for $U(\sigma x)$. Then, given an initial condition (9.3) and sufficiently small $\delta > 0$, the closed-loop system (9.1), (9.22)-(9.24), (9.52) has a unique solution $x^{\delta}(t)$, globally defined for all $t \geq 0$. Moreover, this system is Lyapunov stable, and for arbitrary $\epsilon > 0$ there exist $\delta_0(\epsilon)$ and $T_0(x^0, \epsilon) > 0$ such that*

$$\|x^{\delta}(t)\| < \epsilon \text{ for all } t \geq T_0(x^0, \epsilon) \text{ and } \delta \in (0, \delta_0). \tag{9.53}$$

Proof: By Theorem 9.2 system (9.1), (9.3), driven by the discontinuous controller (9.22)-(9.25), has a unique solution $x(t)$, globally defined for all $t \geq 0$, and $x(t) \to 0$ as $t \to \infty$. The latter guarantees that for arbitrary $\epsilon > 0$ there exists $T_0(x^0, \epsilon) > 0$ such that

$$\|x(t)\| \leq \frac{\epsilon}{2} \text{ for all } t \geq T_0(x^0, \epsilon). \tag{9.54}$$

In turn, the smoothed system (9.1), (9.3), driven by the continuous, piece-wise smooth controller (9.22)-(9.24), (9.52), is well-known (Pazy, 1983) to have a unique solution $x^{\delta}(t)$, locally defined on some time interval $(0, \tau)$. Then Theorem 1 and Definition 2, coupled together, ensure that

$$\|x(t) - x^{\delta}(t)\| \leq \frac{\epsilon}{2} \text{ for all } t \in (0, \tau),\ \delta \in (0, \delta_0), \tag{9.55}$$

and some $\delta_0(\epsilon) > 0$. Thus, the solutions $x^{\delta}(t)$ are uniformly bounded on $(0, \tau)$ for all $\delta \in (0, \delta_0)$, and these solutions are therefore uniquely continuable on the right so that inequality (9.55) remains in force for $t \geq \tau$. By virtue of (9.54), it follows stability of the closed-loop system (9.1), (9.22)-(9.24), (9.52) and validity of (9.53). Theorem 9.3 is proven.

We note that Remarks 9.1 and 9.2 apply to the infinite-dimensional system (9.1) as well. In Section 4, these conclusions will be supported by numerical simulations.

9.3.2 Output Feedback Design

In this subsection, we proceed with the design of the discontinuous output feedback controller by coupling the discontinuous state feedback law (9.22) with the Luenberger observer (9.14), (9.15). For this purpose, we first represent (9.22) in terms of the state component x_1:

$$u(x_1) = -[\gamma_0 + \gamma_1 \|Mx_1\|] B_{12}^{-1} \frac{(P_{12} - KP_{11})Mx_1}{\|(P_{12} - KP_{11})Mx_1\|} \tag{9.56}$$

Then, we substitute x_1 by the observer output $\tilde{x}_1$ in (9.56) and modify the gain $\gamma_0 + \gamma_1 \|M\tilde{x}_1\|$ by adding the error term $\gamma_2 \|y - C\tilde{x}\|$ with

$$\gamma_2 > \|(P_{12} - KP_{11})L_1\|. \tag{9.57}$$

The reason for the gain modification is to ensure that the observer-based controller is capable of steering the trajectories of the closed-loop system to the discontinuity manifold $(P_{12} - KP_{11})M\tilde{x}_1 = 0$ in spite of the observer error, thereby imposing on the system a desired stability property similar to that obtained under the state feedback controller. By Theorem 9.4, stated below, the resulting discontinuous output feedback control law, which yields a proper solution to the stabilization problem in question, takes the following form:

$$u(y, \tilde{x}) = -[\gamma_0 + \gamma_1 \|M\tilde{x}_1\| + \gamma_2 \|y - C\tilde{x}\|] B_{12}^{-1} \frac{(P_{12} - KP_{11})M\tilde{x}_1}{\|(P_{12} - KP_{11})M\tilde{x}_1\|} \tag{9.58}$$

Theorem 9.4 *Let the infinite-dimensional system (9.1) for which Assumption 9.1 holds be driven by the observer-based dynamic output feedback controller (9.14), (9.15), (9.58) with gain parameters γ_0, γ_1, γ_2, satisfying (9.23) and (9.57), respectively. Then, given initial conditions $x(0) = x^0 \in H$, $\tilde{x}(0) = \tilde{x}^0 \in H$, the closed-loop*

system (9.1), (9.14), (9.15), (9.58) has a unique solution, globally defined for all $t \geq 0$, *and this system is globally asymptotically stable when* $\gamma_0 > 0$ *and it is globally exponentially stable when* $\gamma_0 = 0$.

Proof: The proof parallels that of Theorem 9.2.

1) First let us represent the over-all system (9.1), (9.14), (9.15), (9.58) in terms of the observer error $e = (e_1, e_2)^T$, $e_i = x_i - \tilde{x}_i$, $i = 1, 2$, and the observer state components $\tilde{\xi} = (\tilde{\xi}_1, \tilde{\xi}_2)^T$, $\tilde{\xi}_i = P_{1i} M \tilde{x}_1$ and $\tilde{x}_2$:

$$\begin{aligned}
\dot{e}_1 &= (A_1 + L_1 C_1) e_1 + L_1 C_2 e_2 \\
\dot{e}_2 &= A_2 e_2 \qquad (9.59) \\
\dot{\tilde{\xi}}_1 &= A_{11} \tilde{\xi}_1 + A_{12} \tilde{\xi}_2 - P_{11} L_1 C e \qquad (9.60) \\
\dot{\tilde{\xi}}_2 &= A_{21} \tilde{\xi}_1 + A_{22} \tilde{\xi}_2 + B_{12} u(y, \tilde{\xi}, \tilde{x}_2) - P_{12} L_1 C e \qquad (9.61) \\
\dot{\tilde{x}}_2 &= A_2 \tilde{x}_2 + B_2 u(y, \tilde{\xi}, \tilde{x}_2) \qquad (9.62)
\end{aligned}$$

where

$$u(y, \tilde{\xi}, \tilde{x}_2) = -[\gamma_0 + \gamma_1 \|\tilde{\xi}\| + \gamma_2 \|y - C_1 M^{-1} \tilde{\xi} - C_2 \tilde{x}_2\|] B_{12}^{-1} \frac{\sigma\tilde{\xi}}{\|\sigma\tilde{\xi}\|} \qquad (9.63)$$

and $\sigma\tilde{\xi} = \tilde{\xi}_2 - K\tilde{\xi}_1$.

Since the semigroup $S_{A_2}(t)$ generated by the infinitesimal operator A_2 is exponentially stable and $A_1 + L_1 C_1$ is a Hurwitz matrix by construction, the observer error equation (9.59) has a unique globally defined solution under arbitrary initial conditions $e_1(0) = e_1^0 \in R^n$, $e_2(0) = e_2^0 \in H$ and this solution is given by

$$\begin{aligned}
e_1(t) &= e^{(A_1 + L_1 C_1)t} e_1^0 + \int_0^t e^{(A_1 + L_1 C_1)(t-\tau)} L_1 C_2 S_{A_2}(\tau) e_2^0 d\tau \qquad (9.64) \\
e_2(t) &= S_{A_2}(t) e_2^0, \; t \geq 0. \qquad (9.65)
\end{aligned}$$

The following observer error estimate

$$\|e(t)\| \leq \kappa_0 \|e(0)\| e^{-\beta_0 t}, \; t \geq 0, \; i = 1, 2, \qquad (9.66)$$

is then straightforwardly obtained for some positive κ_0, β_0.

It follows that subsystem (9.60) - (9.63) is enforced by the exponentially decaying inputs $P_{11}L_1Ce(t)$ and $P_{12}L_1Ce(t)$. While subsystem (9.60) - (9.63) remains beyond the discontinuity hyperplane $\sigma\tilde{\xi} = 0$, the control function $u(t)$, computed according to (9.63) on the trajectories of (9.60) - (9.62), is continuously differentiable in t. Thus, before the subsystem hits the discontinuity hyperplane, it satisfies (Pazy, 1983, p.109, Corollary 2.10). By this corollary, subsystem (9.60) - (9.63) has a unique solution under arbitrary initial conditions at least till a time instant when the subsystem enters the hyperplane $\sigma\tilde{\xi} = 0$.

It should be noted that if subsystem (9.60) - (9.63) enters the discontinuity hyperplane then it never leaves it because the time derivative of the quadratic function

$$V(\sigma\tilde{\xi}) = (\sigma\tilde{\xi})^T\sigma\tilde{\xi} \tag{9.67}$$

remains negative on the trajectories of the system beyond this hyperplane:

$$\dot{V}(t) =\leq -2(\sigma\tilde{\xi})^T(\gamma_0 + \gamma\|\tilde{\xi}\| + \tilde{\gamma}\|e\|)\frac{\sigma\tilde{\xi}}{\|\sigma\tilde{\xi}\|}. \tag{9.68}$$

where constants $\gamma = \gamma_1 - \|A_{21} - KA_{11}\| - \|A_{22} - KA_{12}\|$ and $\tilde{\gamma} = (\gamma_2 - \|(P_{12} - KP_{11})L_1\|)\|C\|$ are positive by virtue of (9.23), (9.57).

In order to describe the behavior of subsystem (9.60) - (9.63) on the hyperplane $\sigma\tilde{\xi} = 0$, one should use the infinite-dimensional extension of the equivalent control method (Orlov, 2000). According to this extension, the equivalent control value

$$u_{eq} = B_{12}^{-1}[(KA_{11} + KA_{12}K - A_{21} - A_{22}K)\tilde{\xi}_1 + (P_{12} - KP_{11})L_1Ce], \tag{9.69}$$

a unique solution of the equation $\dot{\sigma}(\tilde{\xi}(t)) = 0$ with respect to u, is substituted into (9.61), (9.62) for u. By (Orlov, 2000, Theorem 1), the equations

$$\dot{\tilde{\xi}}_1 = (A_{11} + KA_{12})\tilde{\xi}_1 - P_{11}L_1Ce, \tag{9.70}$$

$$\dot{\tilde{x}}_2 = A_2\tilde{x}_2 + B_2B_{12}^{-1}(KA_{11} + KA_{12}K - A_{21} - A_{22}K)\tilde{\xi}_1$$
$$+B_2B_{12}^{-1}(P_{12} - KP_{11})L_1Ce, \tag{9.71}$$

thus obtained, describe the motion of subsystem (9.60) - (9.63) after a time instant when the subsystem hits the discontinuity hyperplane $\sigma\tilde{\xi} = 0$.

While being governed by the linear equation (9.70) subject to (9.66), the finite-dimensional component $\tilde{\xi}(t)$ of the sliding motion is apparently uniformly bounded on an arbitrary finite time interval and globally continuable on the right. The same is also true for a motion, initialized beyond the discontinuity hyperplane.

Indeed, beyond this hyperplane the right-hand side of (9.60), (9.61), (9.63) is linearly bounded in the state variable so that

$$\|\tilde{\xi}(t)\| \leq \|\tilde{\xi}^0\| + \int_0^t [\gamma_0 + N_1\|\tilde{\xi}(\tau)\| + N_2\|e(\tau)\|]d\tau \tag{9.72}$$

for some constants $N_1, N_2 > 0$. Taking into account (9.66), it follows that

$$\|\tilde{\xi}(t)\| \leq [\|\tilde{\xi}^0\| + \frac{\kappa_0 N_2}{\beta_0}\|e^0\| + \gamma_0 T] + N_1\int_0^t \|\tilde{\xi}(\tau)\|d\tau \tag{9.73}$$

By applying the Bellman-Gronwall lemma to inequality (9.73), any solution of this equation is uniformly bounded

$$\|\tilde{\xi}(t)\| \leq [\|\tilde{\xi}^0\| + \frac{\kappa_0 N_2}{\beta_0}\|e^0\| + \gamma_0 T]e^{N_1 T} \tag{9.74}$$

on an arbitrary time interval $[0, T)$ before possible getting on the discontinuity hyperplane where it has been shown to remain uniformly bounded on any finite time interval. Thus, given arbitrary initial conditions $e^0 \in H, \tilde{\xi}^0 \in R^n$, there exists a unique solution of (9.59)-(9.61), (9.63), which turns out to be globally continuable on the right.

Moreover, the equivalent control function (9.69), computed along the sliding modes (9.70), is continuously differentiable in t, and hence, the infinite-dimensional sliding

mode equation (9.71) satisfies (Pazy, 1983, p.109, Corollary 2.10). By applying this corollary to (9.71), one concludes that the solutions of the infinite-dimensional part (9.62), (9.63) of the closed-loop system (9.59)-(9.63) are unambiguously globally continuable on the right, even if the finite-dimensional system enters the discontinuity hyperplane $\sigma\tilde{\xi} = 0$ in a finite time.

Since (9.59)-(9.63) is nothing else than a representation of the original closed-loop system (9.1), (9.14), (9.15), (9.58) in terms of the observer error and observer state, a solution of the original system is globally uniquely defined, too.

2) If $\gamma_0 > 0$ then the time derivative estimate (9.33) of the quadratic function (9.67) is now guaranteed by (9.68). As shown in the proof of Lemma 1, this estimate ensures that $V(t) = 0$ for all $t \geq \gamma_0^{-1}\|\sigma\tilde{\xi}^0\|$, i.e., after a finite time moment $T \leq \gamma_0^{-1}\|\sigma\tilde{\xi}^0\|$ the finite-dimensional system (9.60), (9.61), (9.63) evolves in the sliding mode on the hyperplane $\sigma\tilde{\xi} = 0$. While being governed on the time interval $t \in [0, T)$ by the differential equations (9.59)-(9.62) subject to the smooth control input (9.63), the initial stage of the trajectory of the system, before it hits the discontinuity hyperplane $\sigma\tilde{\xi} = 0$, continuously depends on the initial conditions.

In turn, for $t \geq T$ the closed-loop system (9.59)-(9.63) is maintained on the hyperplane $\sigma\tilde{\xi} = 0$ and it is governed by the sliding mode equations (9.70), (9.71). Taking into account the observer error estimate (9.66) and employing that $A_{11} + KA_{12}$ is a Hurwitz matrix due to a special choice of K, the solution of the former equation is proven to exponentially decay with some $\omega > 0$ and $\beta > 0$:

$$\|\tilde{\xi}_1(t)\| \leq \omega\|\tilde{\xi}_1(T)\|e^{-\beta(t-T)}, \ t \geq T. \tag{9.75}$$

Since the semigroup $S_{A_2}(t)$ generated by the infinitesimal operator A_2 is exponentially stable, i.e., $\|S_{A_2}(t-T)\| \leq \omega_0 e^{-\alpha(t-T)}$ for all $t \geq T$ and some $\alpha, \omega_0 > 0$, the solution

of the latter equation, given by

$$\tilde{x}_2(t) = S_{A_2}(t-T)\tilde{x}_2(T) + \int_T^t S_{A_2}(t-T-\tau)B_2B_{12}^{-1}(P_{12}-KP_{11})L_1Ce(\tau)d\tau + \int_T^t S_{A_2}(t-T-\tau)B_2B_{12}^{-1}(KA_{11}+KA_{12}K-A_{21}-A_{22}K)\xi_1(\tau)d\tau, \tag{9.76}$$

is estimated as follows

$$\|\tilde{x}_2(t)\| \leq \omega_0\|\tilde{x}_2(T)\|e^{-\alpha(t-T)} + \tilde{\kappa}\|e(T)\|[e^{-\beta_0(t-T)} + e^{-\alpha(t-T)}] + \kappa\|\xi_1(T)\|[e^{-\beta(t-T)} + e^{-\alpha(t-T)}],\ t \geq T \tag{9.77}$$

where

$$\tilde{\kappa} = \frac{\omega_0\kappa_0 e^{\alpha T}}{|\alpha-\beta_0|}\|B_2B_{12}^{-1}(P_{12}-KP_{11})L_1C\| > 0,$$

$$\kappa = \frac{\omega_0\omega e^{\alpha T}}{|\alpha-\beta|}\|B_2B_{12}^{-1}(KA_{11}+KA_{12}K-A_{21}-A_{22}K)\| > 0,$$

and inequalities (9.66), (9.75) have been used. By taking into account (9.66) and (9.75), and employing that $\sigma\tilde{\xi} = 0$, or equivalently, $\tilde{\xi}_2(t) = K\tilde{\xi}_1(t)$ for $t \geq T$, it follows that in the case when $\gamma_0 > 0$ the closed-loop system (9.59)-(9.63) is exponentially decaying for $t \geq T$. Coupled to the afore-mentioned property of the initial stage of the solution to continuously depend on the initial conditions, this ensures the global asymptotic stability of (9.59)-(9.63) as well as that of the original closed-loop system (9.1), (9.14), (9.15), (9.58) whenever $\gamma_0 > 0$.

3) For later use, we present the following extension of Lemma 1.

Lemma 9.2 *Let the finite-dimensional system (9.60), (9.61) be enforced by the unit controller (9.63) subject to* $\gamma_0 = 0$ *and let the exponential estimate (9.66) hold for the input signal. Then, the closed-loop system is globally exponentially stable.*

Proof is nearly the same as that of Lemma 1 and it is therefore omitted.

If $\gamma_0 = 0$ then apart from the exponential decaying of the closed-loop system (9.59)-(9.63) on the discontinuity hyperplane $\sigma\tilde{\xi} = 0$, this is also true at the initial stage preceding a sliding motion on this hyperplane. Indeed, by Lemma 2, the finite-dimensional component $\tilde{\xi}(t)$ of (9.59)-(9.63) with $\gamma_0 = 0$ is globally exponentially stable:

$$\|\tilde{\xi}(t)\| \leq L_0\|\tilde{\xi}(0)\|e^{-\mu t},\ t \geq 0 \tag{9.78}$$

for some $\mu > 0$ and $L_0 > 0$, whereas the solution

$$\tilde{x}_2(t) = S_{A_2}(t)\tilde{x}_2(0) - \int_0^t [\gamma_1\|\tilde{\xi}(\tau)\| + \gamma_2\|Ce(\tau)\|]S_{A_2}(t-\tau)B_2B_{12}^{-1}\frac{\sigma\tilde{\xi}(\tau)}{\|\sigma\tilde{\xi}(\tau)\|}d\tau,\ 0 \leq t < T \tag{9.79}$$

of the infinite-dimensional part (9.15), before the time instant T when $\tilde{\xi}(t)$ hits the hyperplane $\sigma\tilde{\xi} = 0$, is estimated as follows

$$\|\tilde{x}_2(t)\| \leq \omega_0\|\tilde{x}_2(0)\|e^{-\alpha t} + \kappa_1\|\tilde{\xi}(0)\|[e^{-\mu t} + e^{-\alpha t}] + \kappa_2\|e(0)\|[e^{-\beta_0 t} + e^{-\alpha t}]\ 0 \leq t < T \tag{9.80}$$

where

$$\kappa_1 = \frac{L_0\omega_0\gamma_1}{|\alpha - \mu|}\|B_2B_{12}^{-1}\| > 0,\ \kappa_2 = \frac{\kappa_0\omega_0\gamma_2}{|\alpha - \beta_0|}\|B_2B_{12}^{-1}\|\|C\| > 0$$

and inequalities (9.66) and (9.78) have been used. As in the proof of Theorem 1, relations (9.77) and (9.80), coupled together, ensure that the infinite-dimensional part (9.15) is also exponentially stable, regardless of the closed-loop system (9.59)-(9.63) enters the discontinuity hyperplane $\sigma\tilde{\xi} = 0$ in a finite time $T < \infty$ or it never hits this hyperplane. Thus, the global exponential stability of (9.59)-(9.63) and consequently that of the original closed-loop system (9.1), (9.14), (9.15), (9.58) is guaranteed whenever $\gamma_0 = 0$. This completes the proof of Theorem 9.4.

Remark 9.4 *In contrast to the state feedback design (cf. Remark 9.1), the observer-based controller (9.58) is only robust against vanishing disturbances because the ob-*

server model (9.14), (9.15) is only capable of tracking the state of the system up to a certain estimation error, which decreases as the disturbance magnitude decreases.

Remark 9.5 *As in the state feedback design (cf. Remark 9.2), the output feedback controller (9.58) with $\gamma_0 = 0$ is continuous at the origin, thereby eliminating around the equilibrium solution undesired high-frequency state oscillations caused by fast switching in the control signal.*

In analogy to the state feedback design, the implementation of the discontinuous output feedback (9.63) can be performed through its continuous version

$$u(y, \tilde{\xi}, \tilde{x}_2) = -[\gamma_0 + \gamma_1 \|\tilde{\xi}\| + \gamma_2 \|y - C_1 M^{-1} \tilde{\xi} - C_2 \tilde{x}_2\|] B_{12}^{-1} \frac{\sigma \tilde{\xi}}{\|\sigma \tilde{\xi}\| + \delta^3}. \quad (9.81)$$

As opposed to the discontinuous feedback (9.63), its continuous approximation (9.81) does not excite undesirable high frequency state oscillations, whereas the resulting closed-loop system is practically stabilized in the following sense.

Theorem 9.5 *Let system (9.1) and observer (9.14), (9.15) be enforced by a continuous approximation (9.81) of the discontinuous dynamic output feedback (9.63) subject to (9.23), (9.57). Then, given initial conditions $x(0) = x^0$, $\tilde{x}_1(0) = \tilde{x}_1^0$, $\tilde{x}_2(0) = \tilde{x}_2^0$ and sufficiently small $\delta > 0$, the closed-loop system (9.1), (9.14), (9.15), (9.63) has a unique solution $x^\delta(t), \tilde{x}_1^\delta(t), \tilde{x}_2^\delta(t)$, which is globally defined for all $t \geq 0$. Moreover, this system is Lyapunov stable, and for arbitrary $\epsilon > 0$ there exist $\delta_0(\epsilon) > 0$ and $T_0(x^0, \tilde{x}_1^0, \tilde{x}_2^0, \epsilon) > 0$ such that*

$$\|x^\delta(t)\|, \|\tilde{x}_1^\delta(t)\|, \|\tilde{x}_2^\delta(t)\| < \epsilon \text{ for all } t \geq T_0(x^0, \tilde{x}_1^0, \tilde{x}_2^0, \epsilon) \text{ and } \delta \in (0, \delta_0). \quad (9.82)$$

Proof The proof is similar to that of Theorem 9.3 and it is therefore omitted.

9.4 Numerical results

In this section, we present applications of the discontinuous output feedback controller design to the linearization of the one-dimensional KSE around its spatially-uniform

steady state. The KSE describes incipient instabilities in a variety of physical and chemical systems and a control problem that occurs here is to avoid the appearance of the instabilities in the closed-loop system (Armaou and Christofides, 2000b). In order to smooth the response of the system the sliding mode-based controller is approximated by its continuous $\delta-$counterparts, (9.52) in the state feedback case and (9.81) in the output feedback case. The objectives of the numerical simulations are to illustrate that: (1) the proposed $\delta-$sliding-mode distributed output feedback controller is able to practically stabilize the linearized KSE at the spatially-uniform steady state solution with good robustness with respect to significant uncertainty in the instability parameter, ν, and (2) in the presence of non-vanishing external disturbance, the proposed $\delta-$sliding-mode controller is superior to a linear feedback controller in terms of closed-loop performance. The two points are demonstrated in subsections 9.4.1 and 9.4.2, respectively.

The linearized KSE with external disturbance is of the form:

$$\begin{aligned} \frac{\partial x}{\partial t} &= -\nu\frac{\partial^4 x}{\partial z^4} - \frac{\partial^2 x}{\partial z^2} + \sum_{i=1}^{m} b_i u_i(t) + d(z,t) \\ y_\kappa &= \int_{-\pi}^{\pi} s_\kappa(z) x dz, \ \kappa = 1, \ldots, p \end{aligned} \tag{9.83}$$

subject to the periodic boundary conditions:

$$\frac{\partial^j x}{\partial z^j}(-\pi, t) = \frac{\partial^j x}{\partial z^j}(+\pi, t), \quad j = 0, \ldots, 3 \tag{9.84}$$

and the initial condition:

$$x(z, 0) = x_0(z) \tag{9.85}$$

where $x(z,t)$ is the state of the KSE, $z \in (-\pi, \pi)$ is the spatial coordinate, t is the time and 2π is the length of the spatial domain, ν is the instability parameter, and $x_0(z)$ is the initial condition. $u_i \in R$ denotes the i-th manipulated input, m is the total number of manipulated inputs, $b_i(z) \in L_2(-\pi, \pi)$ is a square integrable

function that represents the distribution function of the $i-$th control actuator, p is the total number of measurement sensors, $y_\kappa \in R$ denotes a measured output, $s_\kappa(z) \in L_2(-\pi, \pi)$ is a square integrable function of z which is determined by the location and type of the measurement sensors, and $d(z,t)$ is an unknown uniformly bounded external disturbance to be rejected.

To simplify the presentation of our numerical results, we formulate (9.83)-(9.85) as an infinite-dimensional system in the Hilbert space of odd functions with spatial zero mean in the interval $(-\pi, \pi)$. This requires that the initial condition $x_0(z)$, the actuator distribution functions $b_i(z)$, $i = 1, \ldots, m$, and the external disturbance $d(z,t)$ are odd functions in the spatial variable z (this assumption imposes certain practical constraints on the shape of the actuator distribution functions, which will be discussed below in subsection 9.4.1). Under this assumption, we formulate (9.83)-(9.85) as an infinite-dimensional system in the Hilbert space $L_2^{odd}(-\pi, \pi)$. To this end, we introduce the operator

$$Ax = -\nu \frac{\partial^4 x}{\partial z^4} - \frac{\partial^2 x}{\partial z^2} \tag{9.86}$$

with the dense domain

$$\begin{aligned} \mathcal{D}(A) = \Big\{ & x \in L_2^{odd}(-\pi, \pi) : \frac{\partial^4 x}{\partial z^4}(z) \in L_2^{odd}(-\pi, \pi), \\ & \frac{\partial^j x}{\partial z^j}(-\pi) = \frac{\partial^j x}{\partial z^j}(+\pi), \; j = 0, \ldots, 3 \Big\} \end{aligned} \tag{9.87}$$

and the input and measured output operators

$$Bu = \sum_{i=1}^{l} b_i u_i, \quad Cx = \int_{-\pi}^{\pi} \mathcal{S}(z) x(z) dz, \tag{9.88}$$

where $\mathcal{S}(z) = (s_1(z), \ldots, s_p(z))^T$. Then, the system (9.83)-(9.85) can be written as follows

$$\begin{aligned} \dot{x} &= Ax + Bu + d, \quad x(0) = x_0 \\ y &= Cx. \end{aligned} \tag{9.89}$$

in the Hilbert space $L_2^{odd}(-\pi,\pi)$ where the operators $B : R^m \rightarrow L_2^{odd}(-\pi,\pi)$ and $C : L_2^{odd}(-\pi,\pi) \rightarrow R^p$ are bounded, and A is an unbounded operator (Pazy, 1983).

In order to decompose the system (9.89) according to (9.10)-(9.11) into stable and unstable parts we formulate the following eigenvalue problem for A:

$$A\phi_n = -\nu\frac{\partial^4\phi_n}{\partial z^4} - \frac{\partial^2\phi_n}{\partial z^2} = \lambda_n\phi_n, \quad n = 1,\ldots,\infty \tag{9.90}$$

subject to:

$$\frac{\partial^j\phi_n}{\partial z^j}(-\pi) = \frac{\partial^j\phi_n}{\partial z^j}(+\pi), \quad j = 0,\ldots,3 \tag{9.91}$$

where λ_n denotes an eigenvalue and ϕ_n denotes an odd eigenfunction. A direct computation of the solution of the above eigenvalue problem yields $\lambda_n = -\nu n^4 + n^2$ with odd eigenfunctions $\phi_n(z) = \frac{1}{\sqrt{\pi}}\sin(nz)$, $n = 1,\ldots,\infty$. The spectrum $\{\lambda_1,\lambda_2,\ldots,\}$ of A is defined as the set of all eigenvalues of A. We note that the fact that A has a real pure point spectrum is a result of the fact that the spatial differential operator of the linearization of KSE with periodic boundary conditions is self-adjoint and the problem is considered in a bounded domain.

From the expression of the eigenvalues, it follows that for a fixed value of $\nu > 0$ the number of unstable eigenvalues of A is finite and the distance between two consecutive eigenvalues (i.e., λ_n and λ_{n+1}) increases as n increases. From these properties of the eigenspectrum of A, it follows that A generates an analytic semigroup (Curtain and Zwart, 1995; Temam, 1988).

By expanding the solution of the system (9.83) in an infinite series in terms of the odd eigenfunctions of the operator (9.90), we obtain:

$$x(z,t) = \sum_{n=1}^{\infty}\alpha_n(t)\phi_n(z) \tag{9.92}$$

where $\alpha_n(t)$ is time-varying coefficient and $\phi_n(z) = (1/\sqrt{\pi})\sin(nz)$. Substituting the above expansion for the solution, $x(z,t)$, into the system and taking the inner product

in $L_2^{odd}(-\pi,\pi)$ with the eigenfunction $\phi_n(z)$, the following infinite-dimensional system of ODEs is obtained:

$$\begin{aligned}\dot{\alpha_n} &= (-\nu n^4 + n^2)\alpha_n + \sum_{i=1}^{m} b_{\alpha i}^n u_i(t) + d_\alpha^n(t), n = 1,\ldots,\infty, \\ y_\kappa &= \int_{-\pi}^{\pi} s_\kappa(z)(\sum_{n=1}^{\infty}\alpha_n(t)\phi_n(z))dz, \kappa = 1,\ldots,p\end{aligned} \tag{9.93}$$

where

$$b_{\alpha i}^n = \textstyle\int_{-\pi}^{\pi} b_i(z)\phi_n(z)dz \tag{9.94}$$

and

$$d_\alpha^n(t) = \textstyle\int_{-\pi}^{\pi} d(z,t)\phi_n(z)dz. \tag{9.95}$$

All simulation runs were performed for $\nu = 0.2$, using a 30-order linear ordinary differential equation model obtained from the application of modal decomposition to the system (9.83) (the use of higher-order approximations led to identical numerical results, thereby implying that the following simulation runs are independent of the discretization).

9.4.1 Application to the linearized KSE without external disturbance

In this subsection, we demonstrate that the proposed sliding-mode distributed feedback controller is capable of stabilizing of the spatially-uniform steady state of the linearized KSE when there is no external disturbance (i.e., $d(z,t) \equiv 0$). We observe that the system (9.93) possesses two unstable eigenvalues, and thus for $\nu = 0.2$, the spatially uniform steady-state $x(z,t) = 0$ is unstable. Therefore, we consider the first two modes of the linearization of KSE as the slow modes and use modal decomposition to construct a second-order ODE system. Two actuators are used to guarantee the exponential stabilizability of the system. At this point, it is important to point out that our choice to consider the linearized KSE as an infinite-dimensional system

in the Hilbert space of odd functions with spatial zero mean in order to simplify the presentation of the controller synthesis formulas imposes certain practical constraints on the shape of the actuator distribution functions; it requires, for example, that $b_i(z)$ are odd functions, e.g., $b_i(z) = \phi_i(z)$, $i = 1, 2$. While it is possible to proceed with a such choice for $b_i(z)$, from a practical point of view as well as to study the effect of the control action on the fast modes (not accounted in the model used for controller design, i.e., "spillover" effect), it is preferable to consider the use of point control actuators. Therefore, we assume that we have available for the control of the KSE two point control actuators, placed at $z_{a1} = 0.31\pi$ and $z_{a2} = 0.69\pi$ (Lou and Christofides, 2003c) with following actuator distribution functions:

$$b_i(z) = \begin{cases} \dfrac{1}{\varepsilon_b} & if \;\; z_{a_i} - \dfrac{\varepsilon_b}{2} < z < z_{a_i} + \dfrac{\varepsilon_b}{2} \\ 0 & if \;\; otherwise \end{cases}, \; i = 1, \ldots, m. \tag{9.96}$$

where ε_b is a constant representing the width of control actuation in the spatial interval $(-\pi, \pi)$ (note that the above selection of $b_i(z)$ ensures that $b_i(z) \in L_2(-\pi, \pi)$). In this work, $\varepsilon_b = 0.1$ in all closed-loop simulations.

The second-order ODE system resulting from the application of modal decomposition to the linearized KSE is of the form:

$$\begin{bmatrix} \dot{\alpha_1} \\ \dot{\alpha_2} \end{bmatrix} = \begin{bmatrix} \lambda_1 & 0 \\ 0 & \lambda_2 \end{bmatrix} \begin{bmatrix} \alpha_1 \\ \alpha_2 \end{bmatrix} + \begin{bmatrix} b^1_{\alpha 1} & b^1_{\alpha 2} \\ b^2_{\alpha 1} & b^2_{\alpha 2} \end{bmatrix} \begin{bmatrix} u_1 \\ u_2 \end{bmatrix} \tag{9.97}$$

where $b^n_{\alpha i}$ $(i, n = 1, 2)$ are computed by using (9.94).

The first simulation run was performed to evaluate the ability of the sliding-mode state feedback controller to stabilize the system (9.83). The continuous approximation of the sliding-mode state feedback controller (9.22), (9.52) takes the following form:

$$\begin{bmatrix} u_1 \\ u_2 \end{bmatrix} = -\left(\gamma_0 + \gamma_1 \left\|\xi\right\|\right) B_{12}^{-1} \frac{\xi}{\left\|\xi\right\| + \delta_c^3} \tag{9.98}$$

where $\xi = \begin{bmatrix} b^1_{\alpha 1} & b^1_{\alpha 2} \\ b^2_{\alpha 1} & b^2_{\alpha 2} \end{bmatrix}^T \begin{bmatrix} \alpha_1 \\ \alpha_2 \end{bmatrix}$ and $B_{12} = \begin{bmatrix} b^1_{\alpha 1} & b^1_{\alpha 2} \\ b^2_{\alpha 1} & b^2_{\alpha 2} \end{bmatrix}^T \begin{bmatrix} b^1_{\alpha 1} & b^1_{\alpha 2} \\ b^2_{\alpha 1} & b^2_{\alpha 2} \end{bmatrix}$. The controller parameters used in the simulation are $\gamma_0 = 5.0$, $\gamma_1 = 5.0$, and $\delta^3_c = 0.005$.

The system is assumed to be at the initial condition:

$$x_0 = 1.35 \sin(z) \in L_2^{odd}(-\pi, \pi). \tag{9.99}$$

The closed-loop spatio-temporal profile of $x(z,t)$ and the profiles of the two manipulated inputs are shown in Fig. 9.2. It is clear that the controller stabilizes the state of the system at $x(z,t) = 0$.

The second simulation run was performed to evaluate the ability of the sliding-mode output feedback controller to stabilize the system (9.83). Two point measurement sensors are used in this simulation to guarantee the exponential detectability of the system. The measurement sensors are placed at $z_{s1} = 0.35\pi$ and $z_{s2} = 0.64\pi$ (Lou and Christofides, 2003c). Based on the two measurements, $[\ y_1 \quad y_2\ ]^T$, and the 30-order approximation of the infinite-dimensional system (9.93), the state observer is of the following form:

$$\begin{aligned} \begin{bmatrix} \dot{\tilde{\alpha}}_1 \\ \dot{\tilde{\alpha}}_2 \end{bmatrix} &= \begin{bmatrix} \lambda_1 & 0 \\ 0 & \lambda_2 \end{bmatrix} \begin{bmatrix} \tilde{\alpha}_1 \\ \tilde{\alpha}_2 \end{bmatrix} + \begin{bmatrix} b^1_{\alpha 1} & b^1_{\alpha 2} \\ b^2_{\alpha 1} & b^2_{\alpha 2} \end{bmatrix} \begin{bmatrix} u_1 \\ u_2 \end{bmatrix} \\ &\quad -L_1 \left(\begin{bmatrix} y_1 \\ y_2 \end{bmatrix} - C_1 \begin{bmatrix} \tilde{\alpha}_1 \\ \tilde{\alpha}_2 \end{bmatrix} - C_2 \begin{bmatrix} \tilde{\alpha}_3 \\ \vdots \\ \tilde{\alpha}_{30} \end{bmatrix} \right) \\ \begin{bmatrix} \dot{\tilde{\alpha}}_3 \\ \vdots \\ \dot{\tilde{\alpha}}_{30} \end{bmatrix} &= \begin{bmatrix} \lambda_3 & \cdots & 0 \\ \vdots & \ddots & \vdots \\ 0 & \cdots & \lambda_{30} \end{bmatrix} \begin{bmatrix} \tilde{\alpha}_3 \\ \vdots \\ \tilde{\alpha}_{30} \end{bmatrix} + \begin{bmatrix} b^3_{\alpha 1} & b^3_{\alpha 2} \\ \vdots & \vdots \\ b^{30}_{\alpha 1} & b^{30}_{\alpha 2} \end{bmatrix} \begin{bmatrix} u_1 \\ u_2 \end{bmatrix} \end{aligned} \tag{9.100}$$

where

$$C_1 = \begin{bmatrix} c^1_1 & c^2_1 \\ c^1_2 & c^2_2 \end{bmatrix} \tag{9.101}$$

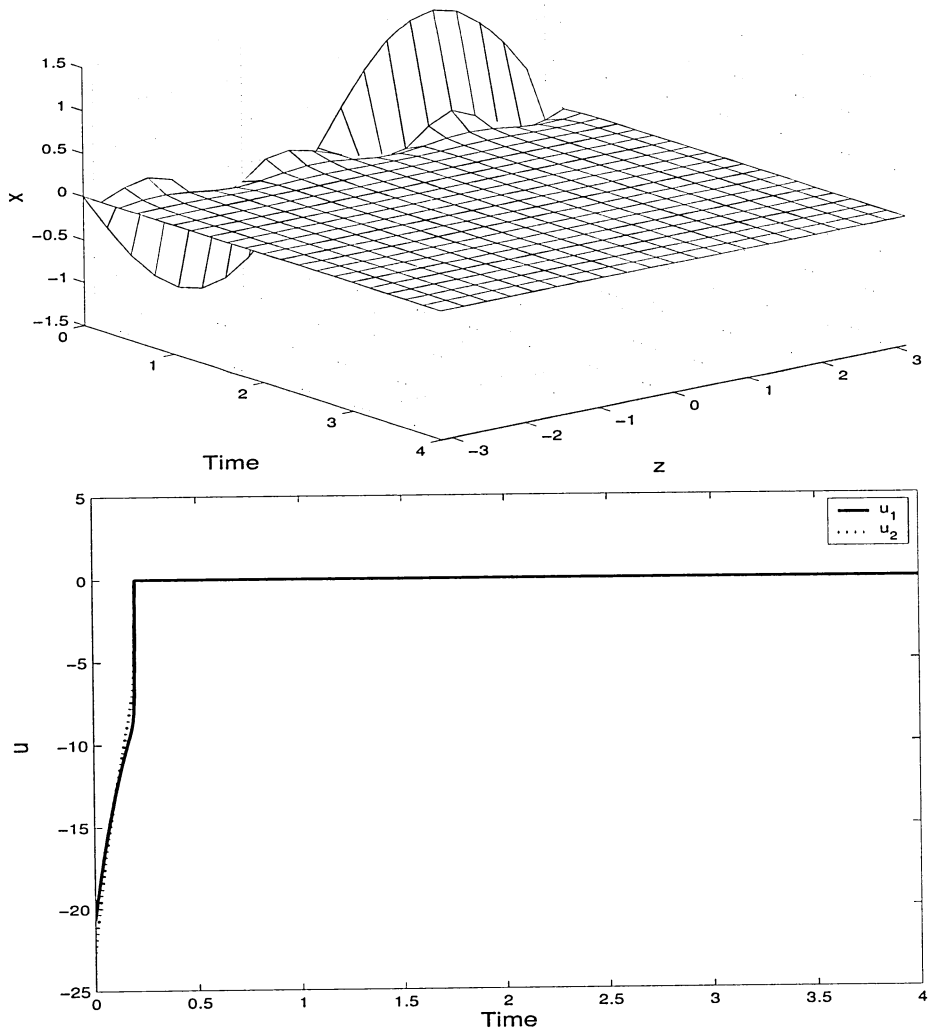

Figure 9.2: Closed-loop spatio-temporal profile of $x(z,t)$ (left figure) and manipulated input profiles (right figure) under $\delta-$sliding-mode state feedback control.

$$C_2 = \begin{bmatrix} c_1^3 & \cdots & c_1^{30} \\ c_2^3 & \cdots & c_2^{30} \end{bmatrix} \tag{9.102}$$

c_κ^n is given by:

$$c_\kappa^n = \int_{-\pi}^{\pi} s_\kappa(z)\phi_n(z)dz, \tag{9.103}$$

the function $s_\kappa(z)$ is of the following form:

$$s_\kappa(z) = \begin{cases} \dfrac{1}{\varepsilon_s} & if \;\; z_{s_\kappa} - \dfrac{\varepsilon_s}{2} < z < z_{s_\kappa} + \dfrac{\varepsilon_s}{2} \\ 0 & if \;\; otherwise \end{cases}, \; \kappa = 1, \cdots, p. \tag{9.104}$$

z_{s_κ} is the location of the κ-th measurement sensor and ε_s is a constant representing the width of the distributed sensing in the spatial interval $(-\pi, \pi)$. In this work, $\varepsilon_s = 0.1$ in all closed-loop simulations.

L_1 is set to be:

$$L_1 = -10 \begin{bmatrix} c_1^1 & c_1^2 \\ c_2^1 & c_2^2 \end{bmatrix}^{-1} \tag{9.105}$$

The observer outputs are used to compute the control action via the following continuous sliding-mode controller (based on (9.63) and (9.81)):

$$\begin{bmatrix} u_1 \\ u_2 \end{bmatrix} = -\left(\gamma_0 + \gamma_1 \left\|\tilde{\xi}\right\| + \gamma_2 \left\|\tilde{\zeta}\right\|\right) B_{12}^{-1} \frac{\tilde{\xi}}{\left\|\tilde{\xi}\right\| + \delta_c^3} \tag{9.106}$$

where $\tilde{\xi} = \begin{bmatrix} b_{\alpha 1}^1 & b_{\alpha 2}^1 \\ b_{\alpha 1}^2 & b_{\alpha 2}^2 \end{bmatrix}^T \begin{bmatrix} \tilde{\alpha}_1 \\ \tilde{\alpha}_2 \end{bmatrix}$, $\tilde{\zeta} = \begin{bmatrix} y_1 \\ y_2 \end{bmatrix} - C_1 \begin{bmatrix} \tilde{\alpha}_1 \\ \tilde{\alpha}_2 \end{bmatrix} - C_2 \begin{bmatrix} \tilde{\alpha}_3 \\ \vdots \\ \tilde{\alpha}_{30} \end{bmatrix}$ and $B_{12} = \begin{bmatrix} b_{\alpha 1}^1 & b_{\alpha 2}^1 \\ b_{\alpha 1}^2 & b_{\alpha 2}^2 \end{bmatrix}^T \begin{bmatrix} b_{\alpha 1}^1 & b_{\alpha 2}^1 \\ b_{\alpha 1}^2 & b_{\alpha 2}^2 \end{bmatrix}$. The following values are used for the parameters of the controller of Eq.9.106: $\gamma_0 = 5.0$, $\gamma_1 = 5.0$, $\gamma_2 = 5.0$, and $\delta_c^3 = 0.005$.

The initial condition for the system is the same to that in (9.99) and the initial condition for the state observer is given as:

$$\tilde{x}_0 = 1.0\sin(z) + \frac{0.1}{\sqrt{\pi}} \sum_{n=2}^{30} \sin(nz) \in L_2^{odd}(-\pi, \pi) \tag{9.107}$$

The closed-loop spatio-temporal profile of $x(z,t)$ and the profiles of the two manipulated inputs are shown in Fig. 9.3. It is clear that the proposed sliding-mode output feedback controller stabilizes the state of the system at $x(z,t) = 0$.

The third simulation run was performed to test the robustness of the output feedback control law (9.100)-(9.106), for a 25% decrease in the value of the instability parameter (i.e., ν was taken to be equal to 0.15 in the high-order discretization of the linearization of KSE but it was used as 0.2 in the controller and state observer); this corresponds to a vanishing disturbance since, $x(z,t) = 0$, for the uncertain system, continues to be an equilibrium solution. Figure 9.4 shows the closed-loop spatio-temporal profile of the state and profiles of the two manipulated inputs, using initial conditions for the system and for the state observer same to those in (9.99) and (9.107), respectively. Our simulation clearly shows that the proposed sliding-mode output feedback controller is capable of stabilizing the linearized KSE at the spatially-uniform steady state solution in the presence of significant uncertainty in ν.

9.4.2 Application to the linearized KSE with non-vanishing external disturbance

In this subsection, we demonstrate that in the presence of external non-vanishing disturbance, the proposed sliding-mode feedback controller is superior to a linear feedback controller in terms of closed-loop performance. All the simulation runs shown in this subsection were performed for $\nu = 0.2$, using a 30-order linear ordinary differential equation model obtained from the application of modal decomposition to the system (9.83) (the use of higher-order approximations led to identical numerical results, thereby implying that the following simulation runs are independent of the discretization). We consider the first five modes of the linearization of KSE as the

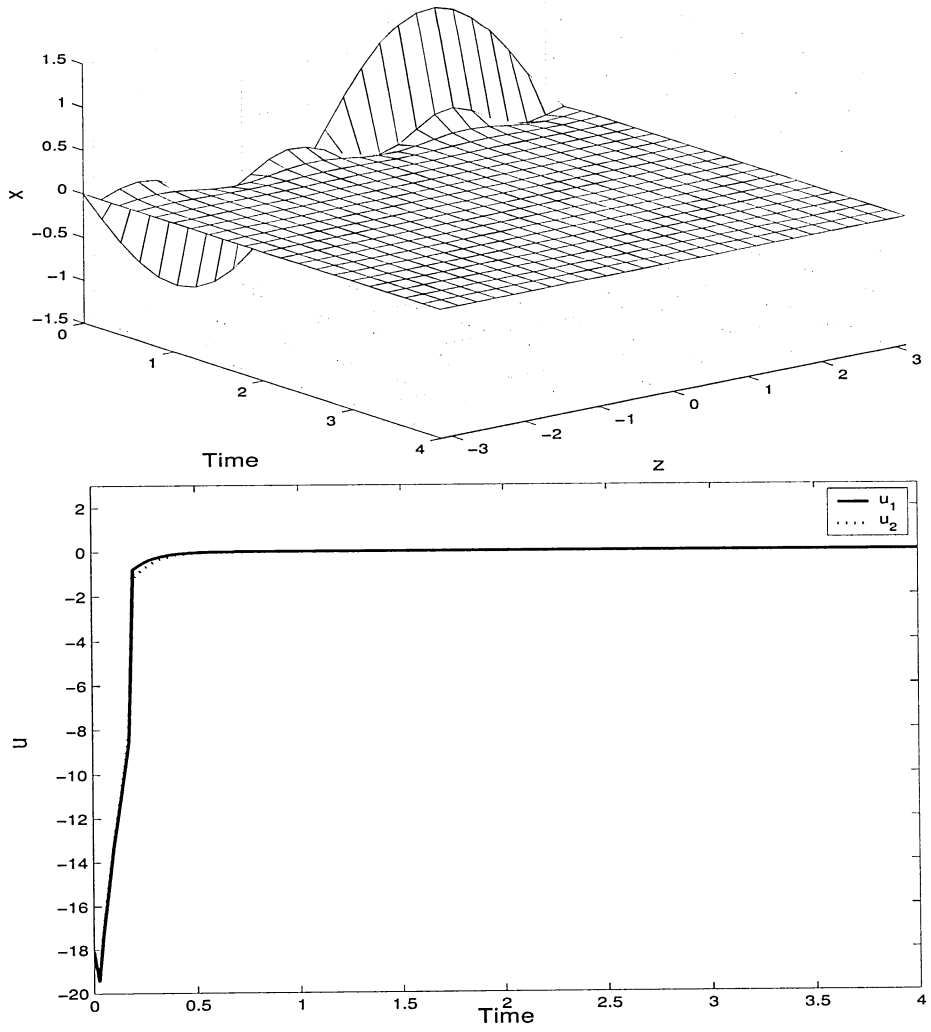

Figure 9.3: Closed-loop spatio-temporal profile of $x(z,t)$ (left figure) and manipulated input profiles (right figure) under $\delta-$sliding-mode output feedback control.

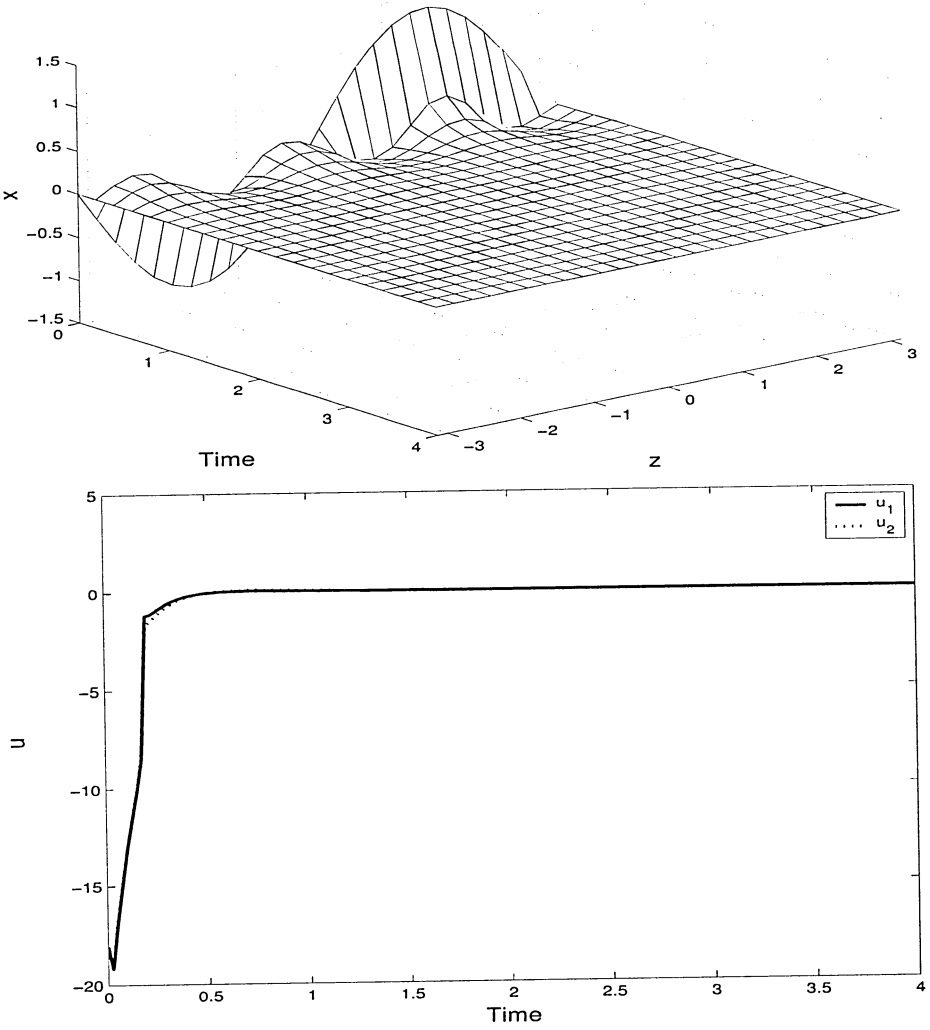

Figure 9.4: Closed-loop spatio-temporal profile of $x(z,t)$ (left figure) and manipulated input profiles (right figure) under $\delta-$sliding-mode output feedback control for 25% uncertainty in ν.

slow modes and use modal decomposition to construct a fifth-order ODE system. Five actuators are used to control the system. The resulting fifth-order ODE system is of the following form:

$$\begin{bmatrix} \dot{\alpha}_1 \\ \vdots \\ \dot{\alpha}_5 \end{bmatrix} = \begin{bmatrix} \lambda_1 & \dots & 0 \\ \vdots & \ddots & \vdots \\ 0 & \dots & \lambda_5 \end{bmatrix} \begin{bmatrix} \alpha_1 \\ \vdots \\ \alpha_5 \end{bmatrix} + \begin{bmatrix} b^1_{\alpha 1} & \cdots & b^1_{\alpha 5} \\ \vdots & \ddots & \vdots \\ b^5_{\alpha 1} & \cdots & b^5_{\alpha 5} \end{bmatrix} \begin{bmatrix} u_1 \\ \vdots \\ u_5 \end{bmatrix} + \begin{bmatrix} d^1_\alpha \\ \vdots \\ d^5_\alpha \end{bmatrix} \tag{9.108}$$

where $b^n_{\alpha i}$ $(i, n = 1, \cdots, 5)$ are computed by using (9.94) with the actuator distribution functions, $b_i(z)$, of the form as shown in (9.96) and d^i_α $(i = 1, \cdots, 5)$ are computed by using (9.95) with $d(z,t)$ of the following form:

$$d(z,t) = \frac{1}{\sqrt{\pi}} \sin(z)[4 + \sin(10t)] \tag{9.109}$$

The first simulation run was performed to compare the closed-loop performance under the sliding-mode state feedback control and that under linear state feedback control in the presence of non-vanishing external disturbance (9.109). For the system (9.108), the continuous approximation (9.52) of the discontinuous sliding-mode state feedback controller (9.22) takes the form:

$$\begin{bmatrix} u_1 \\ \vdots \\ u_5 \end{bmatrix} = -\left(\gamma_0 + \gamma_1 \left\|\xi_d\right\|\right) B_d^{-1} \frac{\xi_d}{\left\|\xi_d\right\| + \delta_c^3} \tag{9.110}$$

where $\xi_d = \begin{bmatrix} b^1_{\alpha 1} & \cdots & b^1_{\alpha 5} \\ \vdots & \ddots & \vdots \\ b^5_{\alpha 1} & \cdots & b^5_{\alpha 5} \end{bmatrix}^T \begin{bmatrix} \alpha_1 \\ \vdots \\ \alpha_5 \end{bmatrix}$ and

$$B_d = \begin{bmatrix} b^1_{\alpha 1} & \cdots & b^1_{\alpha 5} \\ \vdots & \ddots & \vdots \\ b^5_{\alpha 1} & \cdots & b^5_{\alpha 5} \end{bmatrix}^T \begin{bmatrix} b^1_{\alpha 1} & \cdots & b^1_{\alpha 5} \\ \vdots & \ddots & \vdots \\ b^5_{\alpha 1} & \cdots & b^5_{\alpha 5} \end{bmatrix}.$$

To reject the non-vanishing external disturbance, we assume that the upper bound of the external disturbance is known and the parameter γ_0 in (9.110) is larger than the upper bound of the external disturbance. The controller parameters used in this simulation are the same to those used in subsection 9.4.1.

The linear state feedback controller is designed as follows:

$$\begin{bmatrix} u_1 \\ \vdots \\ u_5 \end{bmatrix} = -k \begin{bmatrix} b^1_{\alpha 1} & \cdots & b^1_{\alpha 5} \\ \vdots & \ddots & \vdots \\ b^5_{\alpha 1} & \cdots & b^5_{\alpha 5} \end{bmatrix}^{-1} \begin{bmatrix} \alpha_1 \\ \vdots \\ \alpha_5 \end{bmatrix} \tag{9.111}$$

where the gain value $k = 9.503$ is selected for the simulation.

To compare the closed-loop performance of the two controllers, we use a performance index of the following form:

$$J(t_f) = \int_0^{t_f} \int_{-\pi}^{\pi} x^2(z,t) dz dt \tag{9.112}$$

where $x(z,t)$ is the state of the closed-loop system and t_f is the total simulated time. Throughout, this time is set to $t_f = 4$.

The initial condition of the system is the same to (9.99) and the locations of the five actuators are $z_{a_1} = 0.15\pi$, $z_{a_2} = 0.31\pi$, $z_{a_3} = 0.5\pi$, $z_{a_4} = 0.69\pi$ and $z_{a_5} = 0.85\pi$.

Figure 9.5 shows the spatio-temporal profile of $x(z,t)$ and profiles of the five manipulated inputs under the sliding-mode state feedback controller (9.110). It is clear that this controller is capable of stabilizing the state of the system as $x(z,t) = 0$ in the presence of non-vanishing external disturbance. The value of the performance index, corresponding to (9.110), is $J(t_f) = 0.5731$.

Figure 9.6 shows the spatio-temporal profile of $x(z,t)$ and profiles of the five manipulated inputs under linear state feedback control. We can see that the linear state feedback controller is not able to drive the state of the system to $x(z,t) = 0$ in the presence of non-vanishing external disturbance. Moreover, the value of the performance index is $J(t_f) = 1.3263$ which is much larger than that under the $\delta-$sliding-mode state feedback controller (9.110).

Remark 9.6 *We note that the superior closed-loop performance achieved by the proposed $\delta-$sliding-mode feedback controller is not due to the poor tuning of the linear*

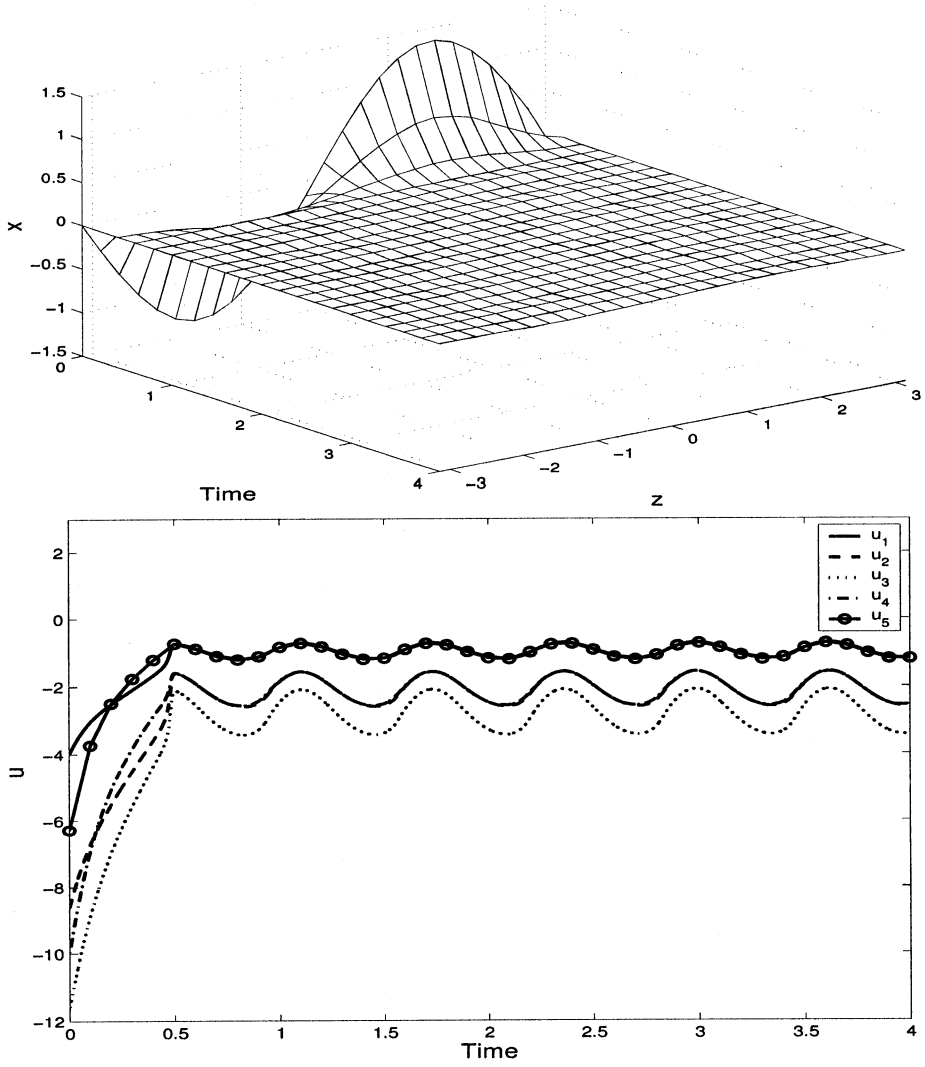

Figure 9.5: Closed-loop spatio-temporal profile of $x(z,t)$ (left figure) and manipulated input profiles (right figure) under $\delta-$sliding-mode state feedback control with external disturbance $(d(z,t) = \frac{1}{\sqrt{\pi}}\sin(z)[4+\sin(10t)])$.

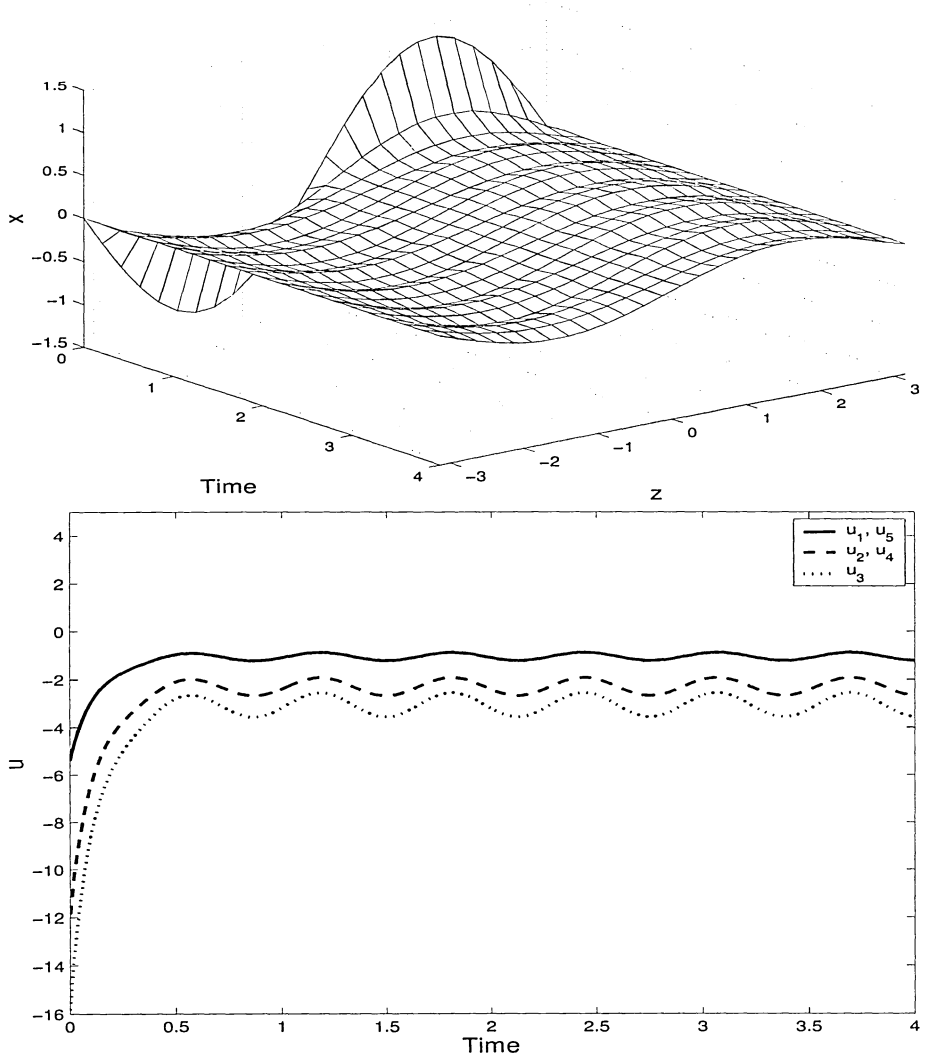

Figure 9.6: Closed-loop spatio-temporal profile of $x(z,t)$ (left figure) and manipulated input profiles (right figure) under linear state feedback control with external disturbance ($d(z,t) = \frac{1}{\sqrt{\pi}}\sin(z)[4+\sin(10t)]$).

feedback controller. The gain k of the linear state feedback controller (9.111) is tuned such that the performance under this linear controller is the same to that under the $\delta-$sliding-mode state feedback controller (9.110) with respect to the performance index defined in (9.112), when there is no external disturbance. Figures 9.7 and 9.8 show the closed-loop spatio-temporal profile of $x(z,t)$ and the profiles of the five manipulated inputs under the linear state feedback controller and the $\delta-$sliding-mode state feedback controller without external disturbance. $J(t_f) = \int_0^{t_f}\int_{-\pi}^{\pi} x^2(z,t)dzdt = 0.3567$ in both cases. Comparing Figs.9.7 and 9.8 to Figs.9.6 and 9.5, we can see that while both controllers (9.110) and (9.111) can achieve the same performance without the presence of external disturbance, the closed-loop performance is significantly deteriorated by the non-vanishing disturbance under the linear state feedback control law (9.111) but it is not deteriorated under the $\delta-$sliding-mode state feedback control law (9.110).

Finally, we compare the closed-loop performance under the sliding-mode output feedback controller and the linear output feedback controller in the presence of non-vanishing external disturbance. Two measurement sensors are used in this simulation. The sensors are placed at $z_{s1} = 0.35\pi$ and $z_{s2} = 0.64\pi$ (Lou and Christofides, 2003c). Based on the two measurements, $[\ y_1 \quad y_2\ ]^T$, and the 30-order approximation of the infinite-dimensional system (9.93), the state observer is of the following form:

$$\begin{bmatrix} \dot{\tilde{\alpha}}_1 \\ \vdots \\ \dot{\tilde{\alpha}}_5 \end{bmatrix} = \begin{bmatrix} \lambda_1 & \dots & 0 \\ \vdots & \ddots & \vdots \\ 0 & \dots & \lambda_5 \end{bmatrix} \begin{bmatrix} \tilde{\alpha}_1 \\ \vdots \\ \tilde{\alpha}_5 \end{bmatrix} + \begin{bmatrix} b^1_{\alpha 1} & \cdots & b^1_{\alpha 5} \\ \vdots & \ddots & \vdots \\ b^5_{\alpha 1} & \cdots & b^5_{\alpha 5} \end{bmatrix} \begin{bmatrix} u_1 \\ \vdots \\ u_5 \end{bmatrix}$$

$$-L_{d1}\left(\begin{bmatrix} y_1 \\ y_2 \end{bmatrix} - C_{d1} \begin{bmatrix} \tilde{\alpha}_1 \\ \vdots \\ \tilde{\alpha}_5 \end{bmatrix} - C_{d2} \begin{bmatrix} \tilde{\alpha}_6 \\ \vdots \\ \tilde{\alpha}_{30} \end{bmatrix} \right) \tag{9.113}$$

$$\begin{bmatrix} \dot{\tilde{\alpha}}_6 \\ \vdots \\ \dot{\tilde{\alpha}}_{30} \end{bmatrix} = \begin{bmatrix} \lambda_6 & \cdots & 0 \\ \vdots & \ddots & \vdots \\ 0 & \cdots & \lambda_{30} \end{bmatrix} \begin{bmatrix} \tilde{\alpha}_6 \\ \vdots \\ \tilde{\alpha}_{30} \end{bmatrix} + \begin{bmatrix} b^6_{\alpha 1} & \cdots & b^6_{\alpha 5} \\ \vdots & \ddots & \vdots \\ b^{30}_{\alpha 1} & \cdots & b^{30}_{\alpha 5} \end{bmatrix} \begin{bmatrix} u_1 \\ \vdots \\ u_5 \end{bmatrix}$$

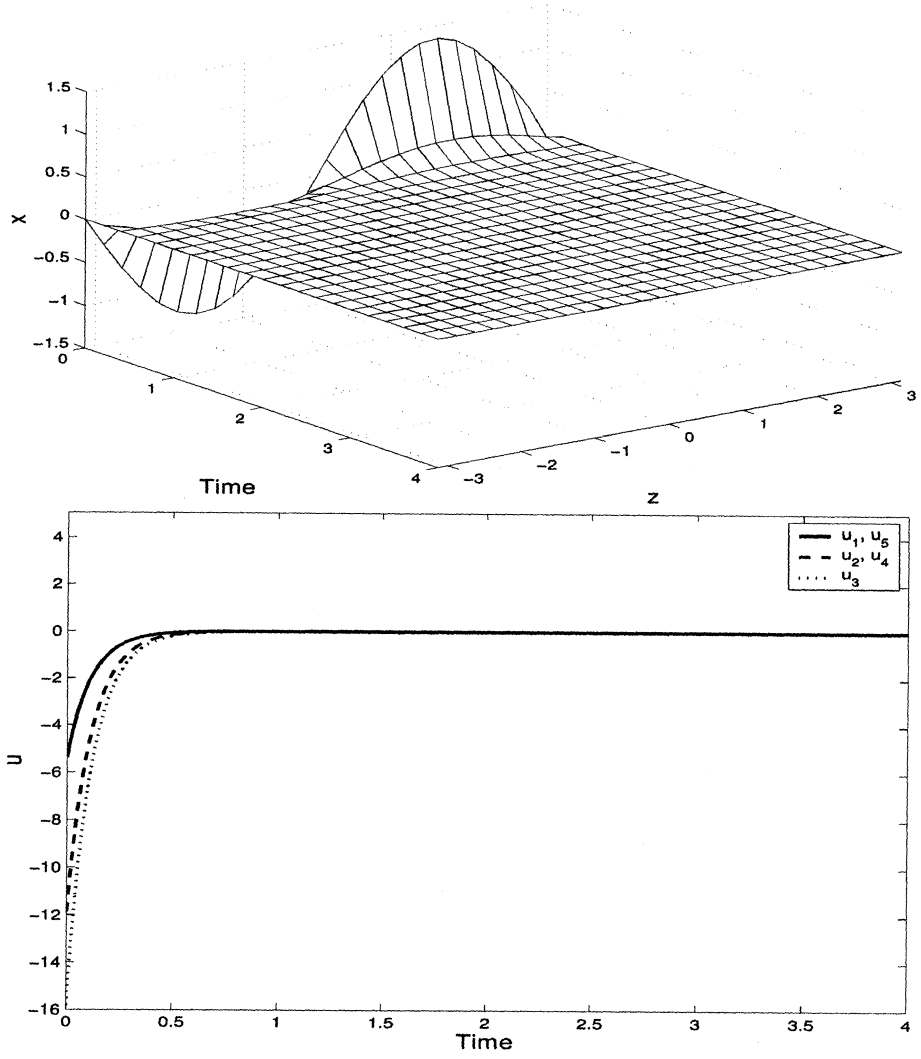

Figure 9.7: Closed-loop spatio-temporal profile of $x(z,t)$ (left figure) and manipulated input profiles (right figure) under linear state feedback control without external disturbance; $J(t_f) = \int_0^{t_f} \int_{-\pi}^{\pi} x^2(z,t) dz dt$=0.3567.

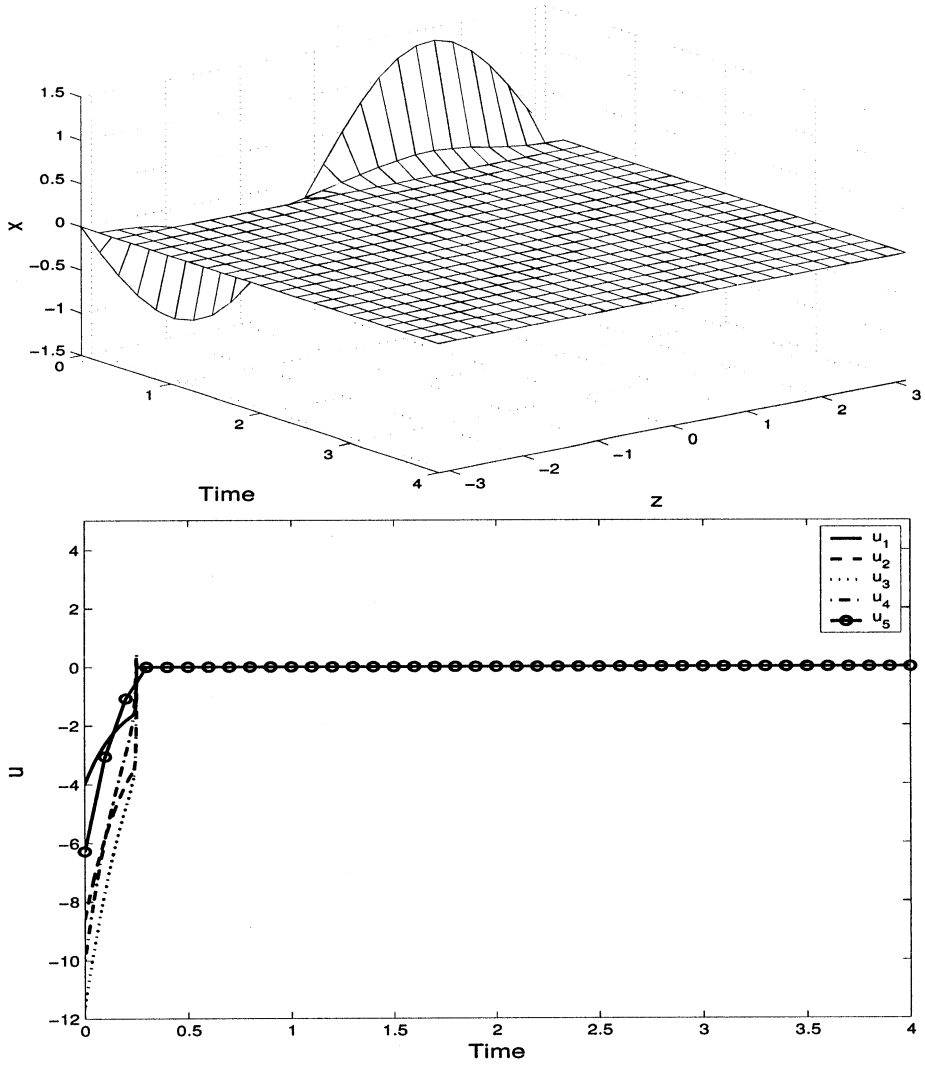

Figure 9.8: Closed-loop spatio-temporal profile of $x(z,t)$ (top figure) and manipulated input profiles (bottom figure) under $\delta-$sliding-mode state feedback control without external disturbance; $J(t_f) = \int_0^{t_f} \int_{-\pi}^{\pi} x^2(z,t) dz dt$ =0.3567.

where

$$C_{d1} = \begin{bmatrix} c_1^1 & \cdots & c_1^5 \\ c_2^1 & \cdots & c_2^5 \end{bmatrix} \tag{9.114}$$

$$C_{d2} = \begin{bmatrix} c_1^6 & \cdots & c_1^{30} \\ c_2^6 & \cdots & c_2^{30} \end{bmatrix} \tag{9.115}$$

c_κ^n ($\kappa = 1, 2$ and $n = 1, \ldots, 30$) is given by (9.103). L_{d1} is set to be:

$$L_{d1} = \begin{bmatrix} -61.503 & -45.274 & 11.395 & 52.714 & 47.944 \\ -64.149 & 44.218 & 17.044 & -56.905 & 42.524 \end{bmatrix}^T \tag{9.116}$$

The state estimates of (9.113) are used in the following $\delta-$sliding-mode controller:

$$\begin{bmatrix} u_1 \\ \vdots \\ u_5 \end{bmatrix} = -\left(\gamma_0 + \gamma_1 \left\|\tilde{\xi}_d\right\| + \gamma_2 \left\|\tilde{\zeta}_d\right\|\right) B_d^{-1} \frac{\tilde{\xi}_d}{\left\|\tilde{\xi}_d\right\| + \delta_c^3} \tag{9.117}$$

where $\tilde{\xi}_d = \begin{bmatrix} b_{\alpha 1}^1 & \cdots & b_{\alpha 5}^1 \\ \vdots & \ddots & \vdots \\ b_{\alpha 1}^5 & \cdots & b_{\alpha 5}^5 \end{bmatrix}^T \begin{bmatrix} \tilde{\alpha}_1 \\ \vdots \\ \tilde{\alpha}_5 \end{bmatrix}$, $\tilde{\zeta} = \begin{bmatrix} y_1 \\ y_2 \end{bmatrix} - C_{d1} \begin{bmatrix} \tilde{\alpha}_1 \\ \vdots \\ \tilde{\alpha}_5 \end{bmatrix} - C_{d2} \begin{bmatrix} \tilde{\alpha}_6 \\ \vdots \\ \tilde{\alpha}_{30} \end{bmatrix}$

and $B_d = \begin{bmatrix} b_{\alpha 1}^1 & \cdots & b_{\alpha 5}^1 \\ \vdots & \ddots & \vdots \\ b_{\alpha 1}^5 & \cdots & b_{\alpha 5}^5 \end{bmatrix}^T \begin{bmatrix} b_{\alpha 1}^1 & \cdots & b_{\alpha 5}^1 \\ \vdots & \ddots & \vdots \\ b_{\alpha 1}^5 & \cdots & b_{\alpha 5}^5 \end{bmatrix}$. The values of γ_0, γ_1, γ_2 and δ_c^3 are the same to those used in subsection 9.4.1.

In turn, the state estimates (9.113) are also used in the following linear controller:

$$\begin{bmatrix} u_1 \\ \vdots \\ u_5 \end{bmatrix} = -k \begin{bmatrix} b_{\alpha 1}^1 & \cdots & b_{\alpha 5}^1 \\ \vdots & \ddots & \vdots \\ b_{\alpha 1}^5 & \cdots & b_{\alpha 5}^5 \end{bmatrix}^{-1} \begin{bmatrix} \tilde{\alpha}_1 \\ \vdots \\ \tilde{\alpha}_5 \end{bmatrix} \tag{9.118}$$

where the gain value $k = 9.503$ is the same as before.

Using as initial condition for the system the same to that in (9.99) and initial condition for the state observer the same to that in (9.107), the closed-loop spatio-temporal profile of $x(z,t)$ and the profiles of the five manipulated inputs under sliding-mode output feedback controller (9.113)-(9.117) are shown in Fig. 9.9. We can

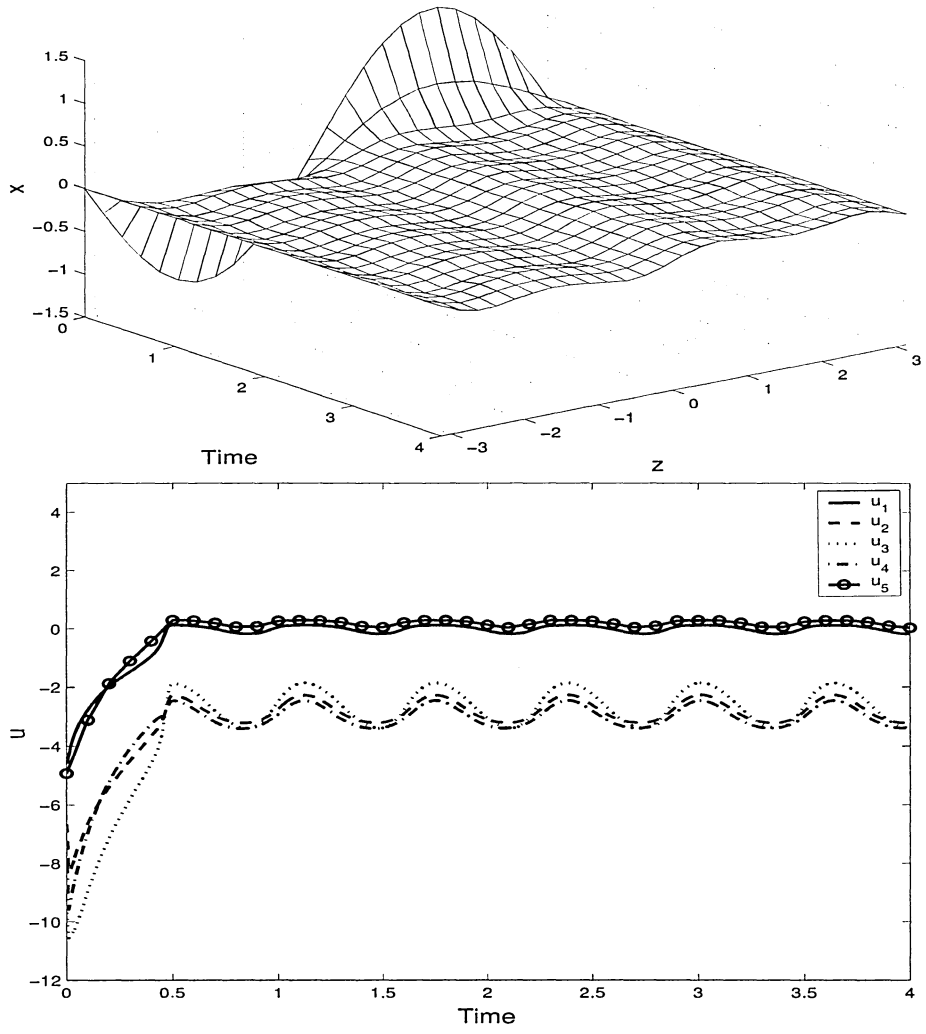

Figure 9.9: Closed-loop spatio-temporal profile of $x(z,t)$ (top figure) and manipulated input profiles (bottom figure) under $\delta-$sliding-mode output feedback control with external disturbance.

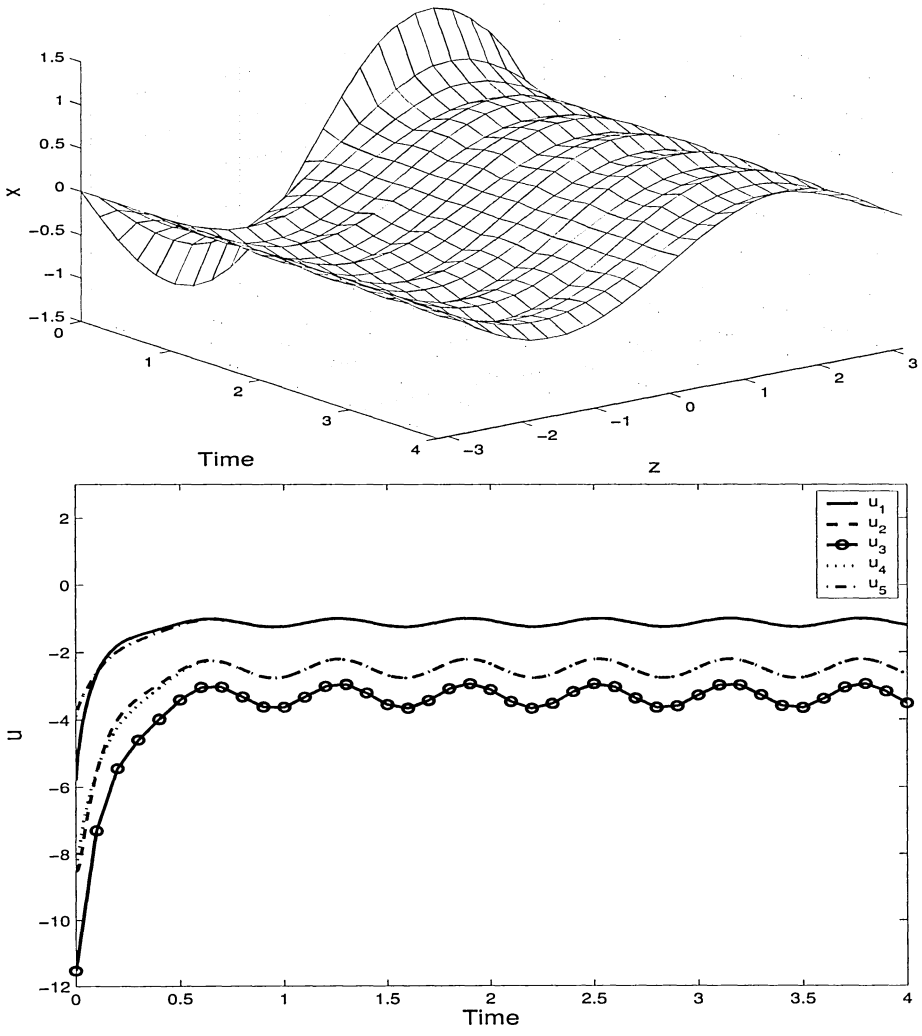

Figure 9.10: Closed-loop spatio-temporal profile of $x(z,t)$ (top figure) and manipulated input profiles (bottom figure) under linear output feedback control with external disturbance.

clearly see that the $\delta-$sliding-mode output feedback controller (9.113)-(9.117) is able to efficiently suppress the influence of the non-vanishing external disturbance to the state of the system and drive the state of the system very close to $x(z,t) = 0$ achieving, at the same time, very good performance (performance index $J(t_f) = 0.7522$). Figure 9.10 shows the closed-loop spatio-temporal profile of $x(z,t)$ and the profiles of the five manipulated inputs under the linear output feedback controller (9.113)-(9.116), (9.118). The performance index under the linear output feedback control law is $J(t_f) = 4.0886$, which is much larger than that under the $\delta-$sliding-mode output feedback controller.

Remark 9.7 *We note that it is important to implement the designed state/output feedback sliding-mode controllers (Eqs.9.22 and 9.58) by using their continuous approximations so that fast switching in the control actions can be avoided. To demonstrate the presence of fast switching in discontinuous sliding-mode controllers, we run a simulation to stabilize the system (9.83) using the discontinuous output feedback sliding-mode controller of Eq.(9.63). The design of the output feedback controller and the state observer follows the development in Eqs.(9.100)-(9.107) except that the δ_c^3 term is removed from the denominator of the controller. In Fig. 9.11, we show the closed-loop spatio-temporal profile of $x(z,t)$ and the profiles of the two manipulated inputs. Comparing Fig. 9.11 and Fig. 9.3, we can see that the closed-loop profiles of x from both simulations are very close, but the manipulated inputs from the δ-sliding-mode output feedback controller are much smoother than those from the discontinuous sliding-mode output feedback controller. Therefore, the δ-sliding-mode controllers are preferable from a practical implementation point of view.*

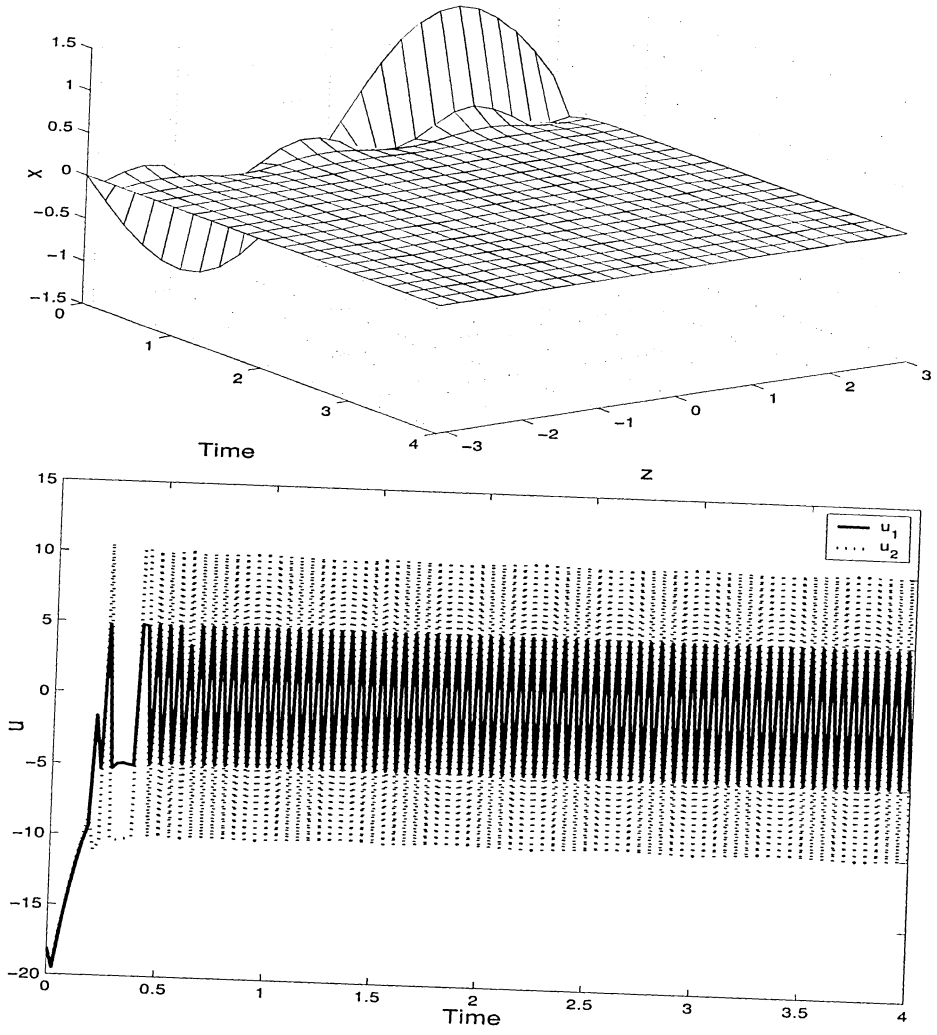

Figure 9.11: Closed-loop spatio-temporal profile of $x(z,t)$ (left figure) and manipulated input profiles (right figure) under sliding-mode output feedback control.

9.5 Conclusions

Sliding-mode controllers have been widely used in practice due to simplicity of their implementation and strong robustness properties against unmodelled dynamics and parameter variations. In the infinite-dimensional setting the sliding mode-based synthesis has only been developed under the restrictive assumption that distributed sensing over the entire spatial domain is available. In this chapter, a fully practical framework is proposed for the synthesis of sliding-mode output feedback controllers for linear infinite-dimensional systems with finite-dimensional unstable part when finite-dimensional sensing and actuation are only available. The proposed framework involves a finite-dimensional approximation of the infinite-dimensional Luenberger observer and a continuous approximation of the sliding-mode controller. Although the case of bounded control and observation operators is only studied, the extension to unbounded point actuators and sensors seems possible. The proposed control method was used to stabilize the linearization of the Kuramoto-Sivashinsky equation around the spatially-uniform steady state solution in the presence of vanishing and non-vanishing disturbances. The sliding-mode controller was found to be superior to a linear feedback controller in terms of closed-loop performance in the presence of non-vanishing disturbances.

Chapter 10

Conclusions and Future Work

10.1 Conclusions

This thesis developed a framework of feedback control of thin film micro-structure using multiscale distributed systems. The research on feedback control of thin film growth is motivated by the strong dependence of the electrical and mechanical properties of thin films on their micro-structure and the desire to produce high quality thin films to meet the increasingly stringent requirements on the quality of such films. Specifically, we have made the following contributions in this thesis:

A methodology for feedback control of thin film growth using kinetic Monte-Carlo models has been developed in Chapter 2. The methodology leads to the design of (a) real-time roughness estimators by using multiple small lattice kinetic Monte-Carlo simulators, adaptive filters and measurement error compensators, and (b) feedback controllers based on the real-time roughness estimators. Application of the proposed estimator/controller structure to the multiscale process model demonstrated successful regulation of the surface roughness at the desired value. The method was also successfully applied to control surface roughness in a $GaAs$ deposition process using

an experimentally determined kinetic Monte-Carlo process model in Chapter 4.

The problem of multivariable feedback control of surface roughness and growth rate in thin film growth was studied in Chapter 3. We have examined the nature of this multivariable control problem and developed a systematic method for the design of a multivariable feedback control system, which can be implemented in real-time. Using the method for real-time estimator design presented in Chapter 2, a surface roughness and growth rate estimator was constructed that allowed computing estimates of the surface roughness and growth rate at a time-scale comparable to the real-time evolution of the process. The interactions between the inputs (substrate temperature and inlet precursor mole fraction) and outputs (growth rate and surface roughness) in the closed-loop system were studied and found to be significant. A multivariable feedback controller, which used the state estimator and explicitly compensated for the effect of input/output interactions, was designed to simultaneously regulate the growth rate and surface roughness by manipulating substrate temperature and inlet precursor mole fraction. The proposed control system was applied to the multiscale process model and successful regulation of the surface roughness and growth rate to the desired set-point values was demonstrated through computer simulations.

The desire to design feedback controllers directly on the basis of deposition process models motivated research on feedback control of deposition processes based on stochastic PDE models of thin film growth. In Chapter 5, a method for feedback control of surface roughness in deposition processes, based on stochastic PDEs which describe the fluctuation of surface height in the spatial domain, was developed. We formulated the stochastic PDE into a system of infinite stochastic ordinary differential equations (ODEs) by using modal decomposition. A finite-dimensional approxima-

tion of the stochastic PDE model was then derived that captured the dominant mode contribution to the surface roughness. A state feedback controller was designed based on the finite-dimensional approximation to control the surface roughness. Analysis of the closed-loop system showed that the controller can drive the surface roughness governed by the infinite-dimensional system to desired levels.

The method developed in Chapter 5 was used to control surface roughness of sputtering processes using the stochastic Kuramoto-Sivashinsky equation (KSE) in Chapter 6. To obtain model parameters, Monte-Carlo simulations were first performed to simulate the evolution of the surface height fluctuation in three sputtering processes. Then, the parameters of the stochastic KSE models describing the sputtering processes were identified by using the surface height fluctuation data obtained from Monte-Carlo simulations so that the evolution of the surface roughness computed from the stochastic KSE models is consistent to that computed from Monte-Carlo simulations. Feedback controllers were designed and applied to Monte-Carlo models of the sputtering processes to control the surface roughness to desired levels.

10.2 Future work

A method for model-based state feedback controller design for thin film micro-structure based on stochastic PDE models has been developed. The developed method has been successfully applied to control surface roughness of a deposition process described by the Edwards-Wilkinson equation, a second order stochastic PDE, and sputtering processes described by the stochastic Kuramoto-Sivashinsky equation.

Although available measurement techniques make it possible to obtain real-time measurement of thin film states over the whole spatial domain, from a practical point of view, it is often that measurements of the state variables are only available at a

finite number of spatial positions. Motivated by these practical problems, design of output feedback controllers for thin film micro-structure based on stochastic PDE models has practical significance and can be achieved by coupling the designed state-feedback controller and a state observer.

In our control problem formulation of feedback controller design based on the stochastic PDE models, the surface roughness control problem is formulated as a covariance control problem of the system of infinite stochastic ODEs and the controller is design based on the solution of the corresponding Lyapunov equation. In our control problem formulation, by appropriately choosing the actuator distribution function, all matrices involved in the Lyapunov equation are diagonal matrices. Therefore, the feedback controller can be readily designed by using the analytical solution of the Lyapunov equation. However, the Lyapunov equation cannot be solved, in general, analytically. In the case that analytical solution of the Lyapunov equation cannot be obtained, a general controller design method to assign the covariance matrix of the system of infinite stochastic ODEs to desired level is necessary to control the surface roughness of processes described by stochastic PDE models.

Covariance control problem for linear finite-dimensional stochastic systems has been extensively studied by Skelton and co-workers (see, for example, Hotz and Skelton, 1987; Skelton and Ikeda, 1989; Grigoriadis and Skelton, 1994, 1997). However, few results are available for covariance control of linear infinite-dimensional stochastic systems. Therefore, theoretical investigation of covariance control theory for stochastic infinite-dimensional systems can benefit the research on feedback control of thin film micro-structure.

Bibliography

Åström, K. J. (1970). *Introduction to Stochastic Control Theory.* Academic Press, New York.

Adams, C. D., Srolovitz, D. J., and Atzmon, M. (1993). Monte Carlo simulation of phase separation during thin-film codeposition. *Journal of Applied Physics*, 74:1707–1715.

Adomaitis, R. A., Choo, J. O., Rubloff, G. W., Henn-Lecordier, L., and Liu, Y. (2003). Spatially controllable CVD: The programmable reactor project. In *A.I.Ch.E Annual Meeting, paper 177f, San Francisco, CA.*

Akiyama, Y., Imaishi, N., Shin, Y. S., and Jung, S. C. (2002). Macro- and micro-scale simulation of growth rate and composition in MOCVD of yttria-stabilized zirconia. *Journal of Crystal Growth*, 241:352–362.

Antoniades, C. and Christofides, P. D. (2001). Integrating nonlinear output feedback control and optimal actuator/sensor placement for transport-reaction processes. *Chemical Engineering Science*, 56:4517–4535.

Antoniades, C. and Christofides, P. D. (2002). Integrated robust control and optimal actuator/sensor placement for uncertain transport-reaction processes. *Computers & Chemical Engineering*, 26:187–203.

Arbel, A. (1981). Controllability measures and actuator placement in oscillatory systems. *International Journal of Control*, 33:565–574.

Armaou, A. and Christofides, P. D. (1999). Plasma-enhanced chemical vapor deposition: Modeling and control. *Chemical Engineering Science*, 54:3305–3314.

Armaou, A. and Christofides, P. D. (2000a). Feedback control of the Kuramoto-Sivashinsky equation. *Physica D.*, 137:49–61.

Armaou, A. and Christofides, P. D. (2000b). Wave suppression by nonlinear finite-dimensional control. *Chemical Engineering Science*, 55:2627–2640.

Armaou, A., Siettos, C. I., and Kevrekidis, I. G. (2004). Time-steppers and 'coarse' control of distributed microscopic processes. *International Journal of Robust and Nonlinear Control*, 14:89–111.

Baker, J., Armaou, A., and Christofides, P. D. (2000). Nonlinear control of incompressible fluid flow: Application to Burgers' equation and 2D channel flow. *Journal of Mathematical Analysis and Applications*, 252:230–255.

Baker, J. and Christofides, P. D. (1999). Output feedback control of parabolic PDE systems with nonlinear spatial differential operators. *Industrial & Engineering Chemistry Research*, 38:4372–4380.

Bemporad, A. and Morari, M. (1999). Control of systems integrating logic, dynamics and constraints. *Automatica*, 35:407–427.

Blakemore, J. S. (1982). Semiconducting and other major properties of gallium arsenide. *Journal of Applied Physics*, 53:R123–R181.

Busch, B. W., Pluchery, O., Chabal, Y. J., Muller, D. A., Opila, R. L., Kwo, J. R., and Garfunkel, E. (2002). Materials characterization of alternative gate dielectrics. *MRS Bulletin*, 3:206–211.

Chang, J. P., Lin, Y. S., Berger, S., Kepten, A., Bloom, R., and Levy, S. (2001). Ultrathin zirconium oxide films as alternative gate dielectrics. *Journal of Vacuum Science & Technology B*, 19:2137–2143.

Chen, L. H. and Chang, H. C. (1986). Nonlinear waves on liquid film surfaces-II. Bifurcation analyses of the long-wave equation. *Chemical Engineering Science*, 41:2477–2486.

Chen, S., Merriman, B., Kang, M., Caflisch, R. E., Ratsch, C., Cheng, L. T., Gyure, M., Fedkiw, R. P., Anderson, C., and Osher, S. (2001). A level set method for thin film epitaxial growth. *Journal of Computational Physics*, 167:475–500.

Chen, Z. Y., Bogaerts, A., Depla, D., and Ignatova, V. (2003). Dynamic Monte Carlo simulation for reactive sputtering of aluminium. *Nuclear Instruments and Methods in Physics Research B*, 207:415–423.

Choe, K. and Baruh, H. (1992). Actuator placement in structural control. *Journal of Guidance Control and Dynamics*, 15:40–48.

Christofides, P. D. (1998). Robust control of parabolic PDE systems. *Chemical Engineering Science*, 53:2449–2465.

Christofides, P. D. (2001a). Control of nonlinear distributed process systems: Recent developments and challenges. *A.I.Ch.E. Journal*, 47:514–518.

Christofides, P. D. (2001b). *Nonlinear and Robust Control of PDE Systems: Methods and Applications to Transport-Reaction Processes*. Birkhäuser, Boston.

Christofides, P. D. and Armaou, A. (2000). Global stabilization of the Kuramoto-Sivashinsky equation via distributed output feedback control. *Systems & Control Letters*, 39:283–294.

Christofides, P. D. and Baker, J. (1999). Robust output feedback control of quasi-linear parabolic PDE systems. *Systems & Control Letters*, 36:307–316.

Christofides, P. D. and Daoutidis, P. (1997). Finite-dimensional control of parabolic PDE systems using approximate inertial manifolds. *Journal of Mathematical Analysis and Applications*, 216:398–420.

Coltrin, M. E., Kee, R. J., and Evans, G. H. (1989). Mathematical model of the fluid mechanics and gas-phase chemistry in a rotating disk chemical vapor deposition reactor. *Journal of the Electrochemical Society*, 136:819–829.

Cuerno, R. and Lauritsen, K. B. (1995). Renormalization-group analysis of a noisy Kuramoto-Sivashinsky equation. *Physical Review E*, 52:4853–4859.

Cuerno, R., Makse, H. A., Tomassone, S., Harrington, S. T., and Stanley, H. E. (1995). Stochastic model for surface erosion via ion sputtering: Dynamical evolution from ripple morphology to rough morphology. *Physical Review Letters*, 75:4464–4467.

Cui, J., Ozeki, M., and Ohashi, M. (1998). Dynamical approach to the surface reaction of triisobutylgallium (TIBGa) on GaAs(001) by using molecular beam scattering. *Journal of Crystal Growth*, 188:137–143.

Curtain, R. F. and Zwart, H. J. (1995). *An Introduction to Infinite-Dimensional Linear Systems Theory*. Springer-Verlag, New York.

Curtis, R., Mitsui, T., and Ganz, E. (1997). An ultrahigh vacuum high speed scanning tunneling microscope. *Review of Scientific Instruments*, 68:2790–2796.

Demetriou, M. (1999). Numerical investigation on optimal actuator/sensor location of parabolic PDEs. In *Proceedings of the American Control Conference*, pages 1722–1726, San Diego, CA.

Drotar, J. T., Zhao, Y. P., Lu, T. M., and Wang, G. C. (1999). Numerical analysis of the noisy Kuramoto-Sivashinsky equation in 2+1 dimensions. *Physical Review E*, 59:177–185.

Duan, J. Q. and Ervin, V. J. (2001). On the stochastic Kuramoto-Sivashinsky equation. *Nonlinear Analysis*, 44:205–216.

Edwards, S. F. and Wilkinson, D. R. (1982). The surface statistics of a granular aggregate. *Proceedings of the Royal Society of London Series A - Mathematical Physical and Engineering Sciences*, 381:17–31.

El-Farra, N. H. and Christofides, P. D. (2003a). Bounded robust control of constrained multivariable nonlinear processes. *Chemical Engineering Science*, 58:3025–3047.

El-Farra, N. H. and Christofides, P. D. (2003b). Coordinated feedback and switching for control of hybrid nonlinear processes. *A.I.Ch.E. Journal*, 49:2079–2098.

El-Farra, N. H. and Christofides, P. D. (2004). Coordinated feedback and switching for control of spatially-distributed processes. *Computers & Chemical Engineering*, 28:111–128.

El-Farra, N. H., Lou, Y., and Christofides, P. D. (2003). Fault-tolerant control of fluid dynamic systems via coordinated feedback and switching. *Computers & Chemical Engineering*, 27:1913–1924.

Feller, W. (1975). *An Introduction to Probability Theory and Its Applications*. Wiley, New York.

Fichthorn, K. A. and Weinberg, W. H. (1991). Theoretical foundations of dynamical Monte Carlo simulations. *Journal of Chemical Physics*, 95:1090–1096.

Foias, C., Ozbay, H., and Tannenbaum, A. (1996). *Robust Control of Infinite Dimensional Systems: Frequency Domain Methods*. Springer-Verlag, London.

Fu, Q., Li, L., and Hicks, R. F. (2000). Ab initio cluster calculations of hydrogenated GaAs(001) surfaces. *Physical Review B*, 61:11034–11040.

Gadgil, P. N. (1993). Single wafer processing in stagnation point flow CVD reactor: prospects, constraints and reactor design. *Journal of Electronic Materials*, 22:171–177.

Gallivan, M. A. and Murray, R. M. (2003). Model reduction and system identification of master equation control systems. In *Proceedings of American Control Conference*, pages 3561–3566, Denver, Colorado.

Gillespie, D. T. (1976). A general method for numerically simulating the stochastic time evolution of coupled chemical reactions. *Journal of Computational Physics*, 22:403–434.

Gillespie, D. T. (1992). A rigorous derivation of the chemical master equation. *Physica A*, 188:404–425.

Gilmer, G. H. and Bennema, P. (1972). Simulation of crystal growth with surface diffusion. *Journal of Applied Physics*, 43:1347–1360.

Gilmer, G. H., Huang, H., de la Rubia, T. D., Torre, J. D., and Baumann, F. (2000). Lattice Monte Carlo models of thin film deposition. *Thin Solid Films*, 365:189–200.

Granneman, E. H. (1993). Thin films in the integrated circuit industry: requirements and deposition methods. *Thin Solid Films*, 228:1–11.

Greene, J. M. and Kim, J. S. (1988). The steady-states of the Kuramoto-Sivashinsky equation. *Physica D.*, 33:99–120.

Grigoriadis, K. M. and Skelton, R. E. (1994). Alternating convex projection methods for covariance control design. *International Journal of Control*, 60:1083–1106.

Grigoriadis, K. M. and Skelton, R. E. (1997). Minimum-energy covariance controllers. *Automatica*, 33:569–578.

Gummalla, M., Tsapatsis, M., Watkins, J. J., and DG, D. G. V. (2004). Multiscale hybrid modeling of film deposition within porous substrates. *A.I.Ch.E. Journal*, 50:684–695.

Hansen, U., Rodgers, S., and Jensen, K. F. (2000). Modeling of metal thin film growth: Linking angstrom-scale molecular dynamics results to micron-scale film topographies. *Physical Review B*, 62:2869–2878.

Haselwandter, C. and Vvedensky, D. D. (2002). Fluctuations in the lattice gas for Burgers' equation. *Journal of Physics A: Mathematical and General*, 35:L579–L584.

Heyn, C., Franke, T., and Anton, R. (1999). Modelling of compound semiconductor epitaxy. *Journal of Crystal Growth*, 201:67–72.

Ho, C. M. and Tai, Y. C. (1998). Micro-electro-mechanical-systems (MEMS) and fluid flows. *Annual Reviews of Fluid Mechanics*, 30:579–612.

Hooper, A. P. and Grimshaw, R. (1985). Nonlinear instability at the interface between two viscous fluids. *Physics of Fluids*, 28:37–45.

Hotz, A. and Skelton, R. E. (1987). Covariance control theory. *International Journal of Control*, 46:13–32.

Hu, C. B. and Temam, R. (2001). Robust control of the Kuramoto-Sivashinsky equation. *Dynamics of Continuous Discrete and Impulsive Systems Series B*, 8:315–338.

Insepov, Z., Yamada, I., and Sosnowski, M. (1997). Surface smoothing with energetic cluster beams. *Journal of Vacuum Science & Technology A - Vacuum Surfaces and Films*, 15:981–984.

Ishii, A. and Kawamura, T. (1999). Monte Carlo simulation of homoepitaxial growth on two-component compound semiconductor surfaces. *Surface Science*, 436:38–50.

Isidori, A. (1989). *Nonlinear Control Systems: An Introduction.* Springer-Verlag, Berlin-Heidelberg, second edition.

Ito, T. and Shiraishi, K. (1996). A Monte Carlo study on the structural change of the GaAs(001) surface during MBE growth. *Surface Science*, 357:486–489.

Itoh, M. (2001). Atomic-scale homoepitaxial growth simulations of reconstructed III-V surfaces. *Progress in Surface Science*, 66:53–153.

Itoh, M., Bell, G. R., Joyce, B., and Vvedensky, D. (2000). Transformation kinetics of homoepitaxial islands on GaAs(001). *Surface Science*, 464:200–210.

Jansen, A. P. J. (1995). Monte Carlo simulations of chemical reactions on a surface with time-dependent reaction-rate constants. *Computer Physics Communications*, 86:1–12.

Kasu, M. and Kobayashi, N. (1997). Surface kinetics of metalorganic vapor-phase epitaxy: surface diffusion, nucleus formation, sticking at steps. *Journal of Crystal Growth*, 174:513–521.

Kersch, A., Morokoff, W., and Werner, C. (1994). Self-consistent simulation of sputter-deposition with the Monte-Carlo method. *Journal of Applied Physics*, 75:2278–2285.

Kevrekidis, I. G., Nicolaenko, B., and Scovel, J. C. (1990). Back in the saddle again: A computer assisted study of the Kuramoto-Sivashinsky equation. *SIAM Journal on Applied Mathematics*, 50:760–790.

Kobayashi, T. (2002). Adaptive stabilization of the Kuramoto-Sivashinsky equation. *International Journal of Systems Science*, 33:175–180.

Kubrusly, C. S. and Malebranche, H. (1985). Sensors and controllers location in distributed systems-a survey. *Automatica*, 21:117–128.

Kumar, S. and Seinfeld, J. (1978). Optimal location of measurements for distributed parameter estimation. *IEEE Transactions on Automatic Control*, AC-23:690–698.

Kuramoto, Y. and Tsuzuki, T. (1976). Persistent propagation of concentration waves in dissipative media far from thermal equilibrium. *Progress of Theoretical Physics*, 55:356–369.

Lam, R. and Vlachos, D. G. (2001). Multiscale model for epitaxial growth of films: Growth mode transition. *Physical Review B*, 64:035401.

Lauritsen, K. B., Cuerno, R., and Makse, H. A. (1996). Noisy Kuramote-Sivashinsky equation for an erosion model. *Physical Review E*, 54:3577–3580.

Law, D. C., Li, L., Begarney, M. J., and Hicks, R. F. (2000). Analysis of the growth modes for gallium arsenide metalorganic vapor-phase epitaxy. *Journal of Applied Physics*, 88:508–512.

Lee, Y. H., Kim, Y. S., Ju, B. K., and Oh, M. H. (1999). Roughness of $ZnS : Pr, Ce/Ta_2O_5$ interface and its effects on electrical performance of alternating current thin-film electroluminescent devices. *IEEE Transactions on Electron Devices*, 46:892–896.

Levaggi, L. (2002a). Infinite dimensional systems sliding motions. *European Journal of Control*, 8:508–518.

Levaggi, L. (2002b). Sliding modes in banach spaces. *Differential Integral Equations*, 15:167–189.

Levine, W. S. and Athans, M. (1978). On the determination of the optimal constant output feedback gains for linear multivariable system. *IEEE Transactions on Automatic Control*, 15:44–48.

Liberzon, D. and Morse, A. S. (1999). Basic problems in stability and design of switched systems. *IEEE Control Systems Magazine*, 19:59–70.

Lin, Y. and Sontag, E. D. (1991). A universal formula for stabilization with bounded controls. *Systems & Control Letters*, 16:393–397.

Liu, W.-J. and Krstić, M. (2001). Stability enhancement by boundary control in the Kuramoto-Sivashinsky equation. *Nonlinear Analysis: Theory, Methods & Applications*, 43:485–507.

Lou, Y. and Christofides, P. D. (2003a). Estimation and control of surface roughness in thin film growth using kinetic Monte-Carlo models. *Chemical Engineering Science*, 58:3115–3129.

Lou, Y. and Christofides, P. D. (2003b). Feedback control of growth rate and surface roughness in thin film growth. *A.I.Ch.E. Journal*, 49:2099–2113.

Lou, Y. and Christofides, P. D. (2003c). Optimal actuator/sensor placement for nonlinear control of the Kuramoto-Sivashinsky equation. *IEEE Transactions on Control Systems Technology*, 11:737–745.

Lou, Y. and Christofides, P. D. (2004a). Feedback control of surface roughness in sputtering processes using the stochastic Kuramoto-Sivashinsky equation. *Computers & Chemical Engineering,* submitted.

Lou, Y. and Christofides, P. D. (2004b). Feedback control of surface roughness of GaAs (001) thin films using kinetic Monte-Carlo models, in press. *Computers & Chemical Engineering;* presented also at 2004 American Control Conference, pp. 940–945, Boston, MA.

Lou, Y. and Christofides, P. D. (2004c). Feedback control of surface roughness using stochastic PDEs, in press. *A.I.Ch.E. Journal;* presented also at 7th IFAC Symposium on Dynamics and Control of Process Systems, 6 pages, Boston, MA.

Makeev, M. A., Cuerno, R., and Barabasi, A. L. (2002). Morphology of ion-sputtered surfaces. *Nuclear Instruments and Methods in Physics Research B*, 197:185–227.

Melsa, J. L. and Sage, A. P. (1973). *An Introduction to Probability and Stochastic Processes.* Prentice-Hall, Englewood Cliffs.

Meng, B. and Weinberg, W. H. (1996). Dynamical Monte Carlo studies of molecular beam epitaxial growth models: interfacial scaling and morphology. *Surface Science*, 364:151–163.

Morari, M. and O'Dowd, J. (1980). Optimal sensor location in the presence of nonstationary noise. *Automatica*, 16:463–480.

Ni, D. and Christofides, P. D. (2004a). Dynamics and control of thin film surface microstructure in a complex deposition process. *Chemical Engineering Science;* submitted.

Ni, D. and Christofides, P. D. (2004b). Predictive control of thin film microstructure in a complex deposition process. In *Proceedings of 7th IFAC Symposium on Dynamics and Control of Process Systems*, Boston, MA.

Ni, D., Lou, Y., Christofides, P. D., Sha, L., Lao, S., and Chang, J. P. (2004). Real-time carbon content control for PECVD ZrO_2 thin-film growth. *IEEE Transactions on Semiconductor Manufacturing*, 17:221–230.

Orlov, Y. (2000). Discontinuous unit feedback control of uncertain infinite-dimensional systems. *IEEE Transactions on Automatic Control*, 45:834–843.

Orlov, Y. and Dochain, D. (2002). Discontinuous feedback stabilization of minimum-phase semilinear infinite-dimensional systems with application to chemical tubular reactor. *IEEE Transactions on Automatic Control*, 47:1293–1304.

Orlov, Y., Lou, Y., and Christofides, P. D. (2004). Robust stabilization of infinite-dimensional systems via sliding-mode output feedback control, in press. *International Journal of Control;* presented also at 2003 Conference on Control & Decision, pp. 845–850, Maui, Hawaii.

Orlov, Y. and Utkin, V. I. (1987). Sliding mode control in infinite-dimensional systems. *Automatica*, 23:753–757.

Palasantzas, G. (1993). Roughness spectrum and surface width of self-affine fractal surfaces via the K-correlation model. *Physical Review B*, 48:14472–14478.

Pazy, A. (1983). *Semigroups of Linear Operators and Applications to Partial Differential Equations.* Springer-Verlag, New York.

Pickering, C. (2001). Spectroscopic ellipsometry for monitoring and control of surfaces, thin layers and interfaces. *Surface and Interface Analysis*, 31:927–937.

Plapp, M. and Karma, A. (2000). Multiscale finite-difference-diffusion Monte-Carlo method for simulating dendritic solidification. *Journal of Computational Physics*, 165:592–619.

Qi, H. J., Huang, L. H., Tang, Z. S., Cheng, C. F., Shao, J. D., and Fan, Z. X. (2003). Roughness evolution of ZrO_2 thin films grown by reactive ion beam sputtering. *Thin Solid Films*, 444:146–152.

Raimondeau, S. and Vlachos, D. G. (2000). Low-dimensional approximations of multiscale epitaxial growth models for microstructure control of materials. *Journal of Computational Physics*, 160:564–576.

Reese, J. S., Raimondeau, S., and Vlachos, D. G. (2001). Monte Carlo algorithms for complex surface reaction mechanisms: Efficiency and accuracy. *Journal of Computational Physics*, 173:302–321.

Renaud, G., Lazzari, R., Revenant, C., Barbier, A., Noblet, M., Ulrich, O., Leroy, F., Jupille, J., Borensztein, Y., Henry, C. R., Deville, J. P., Scheurer, F., Mane-Mane, J., and Fruchart, O. (2003). Real-time monitoring of growing nanoparticles. *Science*, 300:1416–1419.

Sharma, O. P. and Sirignano, W. A. (1969). Ignition of stagnation point flow by a hot body. *Combustion Science and Technology*, 1:95–104.

Shiraishi, K. (1996). First-principles calculations of surface adsorption and migration on GaAs surfaces. *Thin Solid Films*, 272:345–363.

Shiraishi, K. (2001). Monte Carlo simulation of recovery process after MBE growth on GaAs(100). *Surface Science*, 493:438–446.

Shitara, T., Vvedensky, D. D., Wilby, M. R., Zhang, J., Neave, J. H., and Joyce, B. A. (1992b). Misorientation dependence of epitaxial growth on vicinal GaAs(001). *Physical Review B*, 46:6825–6833.

Shitara, T., Vvedensky, D. D., Wilby, M. R., Zhang, J., Neave, J. H., and Joyce, B. A. (1992a). Step-density variations and reflection high-energy electron-diffraction intensity oscillations during epitaxial growth on vicinal GaAs(001). *Physical Review B*, 46:6815–6824.

Siettos, C. I., Armaou, A., Makeev, A. G., and Kevrekidis, I. G. (2003). Microscopic/stochastic timesteppers and "coarse" control: a kMC example. *A.I.Ch.E. Journal*, 49:1922–1926.

Sinha, S. K., Sirota, E. B., Garoff, S., and Stanley, H. B. (1988). X-ray and neutron scattering from rough surfaces. *Physical Review B*, 38:2297–2311.

Sivashinsky, G. I. (1977). Nonlinear analysis of hydrodynamic instability in laminar flames - I. Derivation of basic equations. *Acta Astronautica*, 4:1177–1206.

Sivashinsky, G. I. (1980). On flame propagation under conditions of stoichiometry. *SIAM Journal on Applied Mathematics*, 39:67–82.

Skelton, R. E. and Ikeda, M. (1989). Covariance controllers for linear continuous-time systems. *International Journal of Control*, 49:1773–1785.

Sussman, H. J. and Kokotovic, P. V. (1991). The peaking phenomenon and the global stabilization of nonlinear systems. *IEEE Trans. Automat.Contr.*, 36:424–440.

Tanenbaum, D. M., Laracuente, A. L., and Gallagher, A. (1997). Surface roughening during plasma-enhanced chemical-vapor deposition of hydrogenated amorphous silicon on crystal silicon substrates. *Physical Review B*, 56:4243–4250.

Tejedor, P., Šmilauer, P., Roberts, C., and Joyce, B. A. (1999). Surface-morphology evolution during unstable homoepitaxial growth of GaAs(110). *Physical Review B*, 59:2341–2345.

Temam, R. (1988). *Infinite-Dimensional Dynamical Systems in Mechanics and Physics*. Springer-Verlag, New York.

Theodoropoulou, A., Adomaitis, R. A., and Zafiriou, E. (1999). Inverse model based real-time control for temperature uniformity of RTCVD. *IEEE Transactions on Semiconductor Manufacturing*, 12:87–101.

Tirtowidjojo, M. and Pollard, R. (1988). Elementary processes and rate-limiting factors in MOVPE of GaAs. *Journal of Crystal Growth*, 93:108–114.

Utkin, V. I. (1992). *Sliding Modes in Control Optimization.* Springer-Verlag, Berlin.

Utkin, V. I., Guldner, J., and Shi, J. (1999). *Sliding modes in electromechanical systems.* Taylor and Francis, London.

Van Kampen, N. G. (1992). *Stochastic Processes in Physics and Chemistry.* North-Holland, Amsterdam.

van Keulen, B. (1993). *H_∞-Control for Distributed Parameter Systems: A State-Space Approach.* Birkhäuser, Boston.

Vanhove, J. M., Lent, C. S., Pukite, P. R., and Cohen, P. I. (1983). Damped oscillations in reflection high-energy electron-diffraction during GaAs MBE. *Journal of Vacuum Science & Technology B*, 1:741–746.

Villain, J. (1991). Continuum models of crystal growth from atomic beams with and without desorption. *Journal De Physique I*, 1:19–42.

Vlachos, D. G. (1996). Homogeneous-heterogeneous oxidation reactions over platinum and inert surfaces. *Chemical Engineering Science*, 51:2429–2438.

Vlachos, D. G. (1997). Multiscale integration hybrid algorithms for homogeneous-heterogeneous reactors. *A.I.Ch.E. Journal*, 43:3031–3041.

Voigtländer, B. (2001). Fundamental processes in Si/Si and Ge/Si studied by scanning tunneling microscopy during growth. *Surface Science Reports*, 43:127–254.

Vvedensky, D. D. (2003). Edwards-Wilkinson equation from lattice transition rules. *Physical Review E*, 67:025102(R).

Vvedensky, D. D., Zangwill, A., Luse, C. N., and Wilby, M. R. (1993). Stochastic equations of motion for epitaxial growth. *Physical Review E*, 48:852–862.

Wallace, R. M. and Wilk, G. D. (2002). High-κ gate dielectric materials. *MRS Bulletin*, 3:192–197.

Yun, J. H. and Rhee, S. W. (1997). Simplified simulation of step coverage in chemical vapor deposition with a hemispherical vapor source model. *Journal of the Electrochemical Society*, 144:1803–1807.

Zapien, J. A., Messier, R., and Collin, R. W. (2001). Ultraviolet-extended real-time spectroscopic ellipsometry for characterization of phase evolution in BN thin films. *Applied Physics Letters*, 78:1982–1984.

Ziff, R. M., Gulari, E., and Barshad, Y. (1986). Kinetic phase transitions in an irreversible surface-reaction model. *Physical Review Letters*, 56:2553–2556.

Zolezzi, T. (1989). Variable structure control of semilinear evolution equations. *Partial differential equations and the calculus of variations, Essays in honor of Ennio De Giorgi, Birkhäuser, Boston*, 2:997–1018.